N^o d'ordre : 3354

THÈSE

en cotutelle

entre

L'UNIVERSITÉ BORDEAUX I

ÉCOLE DOCTORALE DES SCIENCES DU VIVANT,
GÉOSCIENCES, SCIENCES DE L'ENVIRONEMENT

et

L'UNIVERSITÉ POLYTECHNIQUE DE CATALOGNE

présentée à

L'UNIVERSITÉ POLYTECHNIQUE DE CATALOGNE

par Roland GARNIER

POUR OBTENIR LE GRADE DE

DOCTEUR

SPÉCIALITÉ: OCÉANOGRAPHIE, PALÉO-OCÉANOGRAPHIE

Modélisation non linéaire d'instabilités morphodynamiques en zone de surf

---

Nonlinear modelling of surf zone morphodynamical instabilities

---

Soutenue le : 21 mars 2007

Après avis de :

Giovanni Coco	Professeur, NIWA, Nouvelle Zélande	Rapporteur
Nick Dodd	Professeur, Université de Nottingham, RU	Rapporteur

Devant la commission d'examen formée de :

Huib de Swart	Professeur, Université de Utrecht, Pays Bas	Président
Philippe Bonneton	Directeur de recherche CNRS, UBI, France	Directeur
Thierry Garlan	Docteur, SHOM, France	Rapporteur
Daniel Calvete	Docteur, UPC, Espagne	Examinateur
Yolanda Ciriano	Docteur, UPC, Espagne	Examinateur

Membres invités :

Albert Falqués	Professeur, UPC, Espagne	Directeur
Raphael Certain	Docteur, Université de Perpignan, France	Suppléant

- 2007 -

Universitat Politècnica de Catalunya
Applied Physics Department

Nonlinear modelling of surf zone morphodynamical instabilities

PhD thesis presented by

Roland Garnier

for the degree of DOCTOR

Director:

Pr. Albert Falqués Serra
Universitat Politècnica de Catalunya

Co-director:

Pr. Philippe Bonneton
Université Bordeaux I

Barcelona, December 2006

Je remercie / Agradezco / Thanks to ...

a mi director de tesis, Albert Falqués, por haberme dado la posibilidad de hacer esta tesis, por su pasión por la ciencia y el mar que sabe muy bien transmitir, por su disponibilidad y accesibilidad a pesar de todo el trabajo que hace, por el interés que porta a mi trabajo, por su ayuda, su eficacia, su paciencia, por las 'campañas' en el Delta del Ebro y su facultad para detectar barras de arena!

a todos los morf@s, del grupo de morfodinámica costanera dirigido por Albert Falqués, por sus competencias, su ayuda, su amistad, y por todos los momentos pasados dentro y fuera de la universidad. He tenido mucha suerte de llegar en un grupo tan bueno, tanto al nivel científico como humano. Para cada un@, tengo un profundo respeto. En concreto, a Daniel Calvete por el tiempo dedicado, su disponibilidad, sus consejos, su eficacia y su confianza, ha sido como mi segundo director español, y le debo mucho. También gracias por los trámites administrativos. A Cesca Ribas y Yolanda Ciriano, por haber sido ejemplos para mi, por sus tesis las cuales han sido una gran fuente de inspiración, por las conversaciones, por sus compañías, por las comidas en la terraza en los viejos tiempos, por haberme aprendido a disfrutar de los congresos, por su energía y su alegría. Recuerdo tambien la llamada de Cesca, buscandome, para la oferta de la beca, gracias! A Miquel Caballeria quien ha sido a la origen de esta tesis por haber desarrollado y confiado su modelo, por sus resultados, por su ayuda siempre que la necesité.

mon directeur français, Philippe Bonneton, pour sa gentillesse et ses competences, qui m'a introduit dans le milieu de l'Océanographie, en particulier, grâce à qui j'ai pu connaitre le groupe de l'UPC. Merci aussi pour les démarches administratives.

Nick Dodd, for inviting me in his group in Nottingham, for his interest in my work, for his collaboration, for his sympathy, for reviewing this thesis.

a Giovanni Coco, por los momentos pasados en Barcelona y en los congresos, por los futuros momentos en Nueva Zelanda (espero!), por el interés que porta a mi trabajo, por su revisión de esta tesis durante la llegada del pequeño Mattia Miles.

Huib de Swart, for his enthusiasm, his interest in my work, for the discussions during his stays in Barcelona.

the scientists who have accepted to be member of my PhD committee: Miguel A. Losada, Philippe Bonneton, Daniel Calvete, Thierry Garlan, Huib de Swart, Raphael Certain, Yolanda Ciriano.

James Kirby and Fengyan Shi for sharing the REF/DIF model and for their help.

the Catalan Government for my IQUC grant. The funding of the Ministerio de Ciencia y Tecnologia of Spain through the PUDEM project under contract REN2003-06637-C02-01/MAR. The HUMOR project, sponsored by the EU under contract MAS3-CT97-0081.

a todos los miembros del departamento de física aplicada, en particular a los miembros de la administración, nuevos y antiguos, a Esther, a Silvia, a Roser y a Angel, también quería agradecer a Xavier Massó y la unidad del tercer ciclo. A los informáticos, de talento, imprescindibles, a Tony, quien he necesitado mucho los últimos años, a Fernando y a Juan Ramon. A todos los miembros de mecánica de fluidos, a Isabel (por su ayuda como responsable del programa de doctorado, por su playa que tengo que descubrir), a Arantxa (por los partidos de tenis), a Oriol (por su ayuda con linux, y con el cluster), al director del departamento Paco, a Alvaro (experto en Matlab y café), a Vicente (por el Phillips), a Juan y Marta, a Josema Redondo (por los seminarios en Villanova), a Alexei, a Alex, a los otros estudiantes de doctorado, a Vero, a Fernando (por los mementos de kite que tendríamos que acabar), a Marc, a Robert, a mi ultimo compañero de despacho Ferran. Por compartir comidas y de cafés en la UPC y por los momentos pasados fuera.

a los otros grupos de la UPC, al grupo del LIM, al secretaria y a los investigadores, en particular a Tonatiu (por el mini-surf en San Diego) y a Jose Maria quienes he conocido en Plymouth. Al grupo del BSC, Hadrien, Bea, Guillaume, Mariano, Manolo...

al grupo del ICM, en particular a Jorge Guillén y Elena Ojeda (y Cesca!), por las colaboraciones, y por sus imágenes ARGUS, muy útiles para el trabajo y el surf.

a los otros grupos españoles, en particular, a todo el grupo de Granada dirigido por Miguel Losada (a los científicos y a la administración), y al grupo de Santander.

les groupes français, en particulier l'équipe METHYS du DGO de Bordeaux, Natalie (et Philippe) Bonneton, Bruno Castelle, Fabien Marche, Vincent Marieu, Nadia Senechal, Aldo Sottolichio (pour son rapport). L'administration de l'Université Bordeaux 1. L'équipe du Trefle. Le SHOM (Fabrice Ardhuin et Thierry Garlan). L'IFREMER (Pierre Le Hir, Benoît Waeles). Virginie Lafon, Daniela Apoluceno. Les scientifiques français ou travaillant en France, que j'ai connus durant l'ASF à Bordeaux, Génie Civil - Génie Côtier á Brest (je tiens aussi a remercier le comité d'organisation), les conférences internationales ou les cours d'été: le BRGM, en particulier, Deborah Idier que j'ai retrouvée lors de presque tous mes séjours à l'étranger, Rodrigo Pedreros (pour le cata !), l'EDF (Michel Benoit et Florence Lafon), le groupe d'Anglet, les Perpignanais, Raphael Certain et Pierre Ferrer, Philippe Laroudé, le franco-suedois-japonais Benoît

Camenen (toujours présent !), les rochelois, Nans Bujan, Rodrigo Cienfuegos...

the organising commitee and all the staff of the summer schools of (1) Hydro- and morphodynamic processes in coastal seas, in Renesse, Netherlands, June 2003 and (2) Mathematical methods for coastal engineering, Plymouth, UK, June 2005.

all the scientists that visit us in Barcelona and that I have met during the two summer schools, the conferences or the workshops. Among them (I am sorry for those I forget): the Dutch researchers: Nicolette Vis-Star, Marije Smith, Mark Klein, Pieter Ross, Rianne, Daniëlle, Saskia... The group of Nottingham that I have recently joined. Pr Howell Peregrine. The ragazzi italiani, Giovanni Besio, Matteo Antuono, Emanuele Terrile, for the trip in Baja California. A los mexicanos por su amistad y su alegria, Adrian Pedrozo-Acuña por su hospitalidad, su generosidad, la organización de los cursos en Plymouth, Vanessa Magar, Ismael Mariño, Gabriel, Christian y los demás.

les amis que j'ai rencontrés, ou qui on fait partie de ma vie à Barcelone, pendant ces 5 années. Le cousin le grand Pat, avec qui j'ai découvert cette ville, grâce a qui j'ai eu envie de m'y installer, et avec qui j'ai partagé 5 ans de vie commune, tellement de bons souvenirs ! L'ex-nouveau colloc Hadrien, qui était là depuis le début, pour tous les moments passés. Flo, Guillermo (le presque gabach), Eglantine, Paxi, Anso, la bande de Gracia et tous les autres. La grande Carmen (la Vascacha), David et Aaron, Titi. A España, en particular, Euskadi, Asturias y Cadix, y sobre todo Catalunya y Barcelona. A los barrios de La Barceloneta, del Gótico, de Gracia, de Sagrada Famila, y los otros. A las playas y las olas de La Barceloneta, Montgat, Masnou, Sitges, Castelldefels, Empuriapage. A los españoles y los catalanes. A los jugadores del Barça: a Carles Puyol, y Ronaldiño. A Bisbal y Manu Chao. Monsieur Solide. Le Duc (Dude). Les trips aux Maroc, au Portugal et en Espagne. Les plages océanes de La Teste, et Bisca. Le Bassin d'Arcachon. Les Munks. DAMNATUR Asso. Les bonnes sessions. Tous mes potes de Buch et du bassin, les très très solides: Arpi, Ben, Bouta, Dieg, Eric, Fede, Foin, Jux, Lolo, Manu, Me, Niac, Nico, Rems, Ryl, Vince, Yogui, et leur compagne, et tous les autres.

Ana, pour les trois merveilleuses années qu'on vient de passer ensemble, et pour ce qu'il nous reste à partager. Merci aussi a ses parents: Mariana et Hector.

Ma famille, et en particulier ma soeur Anne, ma mère Catherine (et Lul) et ma grand mère Denise, pour leur amour et leur soutient.

Nottingham, February 2007

Contents

Chapter 1

Introduction

1.1 Nearshore dynamics

1.1.1 The nearshore zone

Due to various phenomena, beaches inevitably change at a time scale which varies from seconds to centuries, depending on the kind of beaches and on the external forcing. In this thesis we concentrate our efforts on beach changes on a time scale of hours to days, in the particular case of sandy beaches where the external forcing is made by wind or swell waves. Our area of interest is precisely the nearshore zone in which we will predominantly focus in the surf zone. As the beach profile in figure 1.1 shows, the nearshore zone is the part of the beach, bounded shoreward by the shoreline, and seaward by the offshore boundary. Waves form in the offshore zone and arrive in the nearshore zone where the reducing depth causes their transformation. Their amplitude increases in the shoaling zone until they reach their breaking point from where they dissipate in the surf zone. The swash zone is the zone where waves totally dissipate by the run-up; this is the boundary between the surf zone and the dry beach.

The nearshore zone is a complex dynamical system where many phenomena interact at different time and length scales. The smaller ones are at the origin of beach changes; in particular, each morphological change starts from the motion of individual sand grains. In order to understand the behaviour of larger scale sand packets, these smaller scale phenomena must be parameterized, by considering approximations which inevitably cause discrepancy from the real behaviour of beaches. In this thesis, we study the evolution of sand packets with the length scale from one metre to tens of metres. We consider that these packets may organize and can explain the large scale behaviour of beaches (length scale of hundreds of metres). We assume that the external forcing responsible for the moving of beaches comes from waves. In the surf zone, the waves break, dissipating and

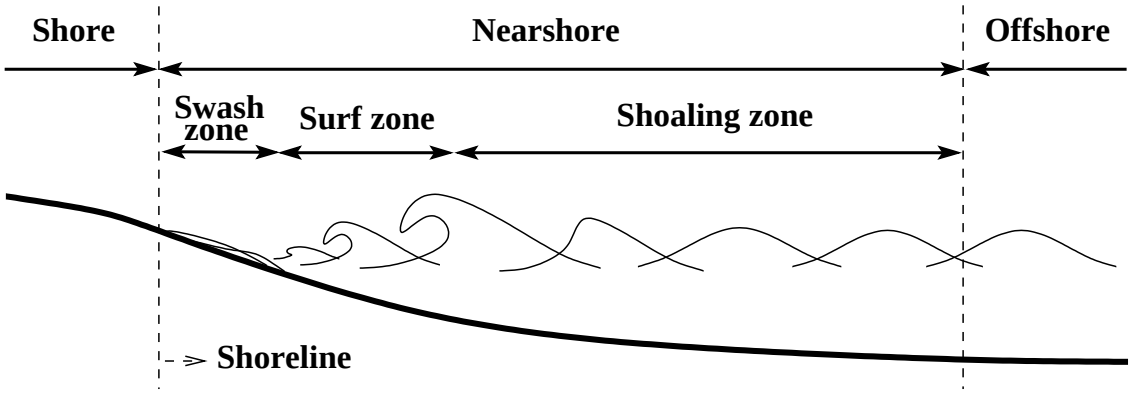

Figure 1.1: The nearshore zone.

transforming a large amount of energy into different scale processes such as turbulent motions and mean currents. For given offshore incident wave conditions, the transformation of waves may be understood in the nearshore zone but the parameterization of turbulent motions is necessary. Thus, understanding large scale beach changes is limited due to the approximations made for describing the smaller scale phenomena.

Furthermore, a new problem occurs if we are interested in the prediction of these beach changes because of the uncertainty in wave forecast. Since a prediction of the wave conditions for one week is not reliable, a longer term forecast is impossible. This makes any exact prediction of large scale morphological changes unfeasible. An approximative method consists in determining characteristic conditions of the studied zone, based on past events.

Because beaches are always evolving, the concept of beach equilibrium may be contested. Nevertheless, for two events characterized by similar incident wave conditions, we observe that the beach response is similar. Besides, if the event is sufficiently regular and lengthy, the beach system trends tend to a certain state, that we call equilibrium state. On open sandy beaches, which are characterized by a coastline almost rectilinear, sometimes with undulations, and which are devoid of human intervention, an average in the longshore direction leads to particular profiles that we call equilibrium profile. This profile essentially depends on the sediment grain size and on the wave conditions. We basically find two kinds of equilibrium profiles: (1) the planar beach profiles if there is no longshore bar (they usually occur on beaches with coarse sand), and (2) the barred beach profiles if there is one or more longshore bars. These longshore bars may appear, disappear and migrate depending on wave conditions.

1.1.2 Human interventions

Human interventions in the nearshore zone inevitably change the natural structure of the beach, i.e. perturb its equilibrium. One of the most common interventions is the beach restoration, as in most cases, a touristic interest. There are basically two ways to restore beaches, but each way presents unpleasantness.

Figure 1.2: Photography of Montgat beach, Cataluña, Spain. Example of beach regeneration. Left: year 1986, the dashed line corresponds to the sediment imported area. Right: year 1987. 2 million cubic metres of sand have been imported. The totality of the imported sand will gone.

The simplest way is the beach nourishment and consists in importing sand from another place. Even if the goal of this technique seems reached, the dry beach area having been extended, this sediment import technique presents two problems. Without mentioning the expenses of such a project, the expected results are good only for a short time. Indeed, most of the time, after storms, the beach recovers its initial position (see figure 1.2). Fortunately because this technique is used for touristic interests it is mainly useful in the summer period when wave conditions are weak. Thus, in general it should not be repeated more than once a year. We will talk about "annual regeneration of beaches". The second problem is linked to the place where the sediment has been taken off. Indeed it is difficult to find such an amount of sand in dry areas. In most cases, the sediment is taken from the sea in a close area, where the sediment transport may be important. Thus, in this situation, the equilibrium of the beach may be perturbed.

The second technique used to restore beaches is the beach protection by the construction of structures called breakwaters. They may have different shapes and may be constructed at different locations. Among them, we find breakwaters parallel to the beach (see figures 1.3 and 1.4). Their interest is to create a natural import of sand behind them, by blocking the wave breaking. We can also find breakwater perpendicular to the coast, useful when there is an ambient longshore current: we observe a deposit of sand at the side exposed to the current. The back side of this technique is that the sediment naturally imported does not come from the offshore zone, but from a nearby area also located in the surf zone. Other beaches are therefore affected. For instance, in the case of those parallel to the coast breakwaters, the beach area between two consecutive structures is clearly eroded.

The dredging is the opposite intervention. At the entrance of harbours or deep areas such as river mouthes, accumulation may be a problem for shipping. Dredging is therefore needed. An example of bad dredging feedback has been seen in the Mundaka beach, Spain (see figure 1.5). In this place, a world championship surfing tour takes place each year. But the wave quality has been strongly damaged due to strong dredging in the nearby river mouth which affected the beach morphology, so the tour was cancelled

Figure 1.3: Photographs of Sea Palling, UK. Breakwater series.

Figure 1.4: Photography of Norfolk beach, Virginia, USA. Breakwater series.

Figure 1.5: Photography of the Mundaka waves, Euskady, Spain.

in 2005.

As with many other human interventions, these examples show the lack of knowledge in the predictions about the evolution of beaches. Even if some uncertainty in these predictions is inevitable, an improvement seems possible by a better understanding of the physics governing the phenomena, particularly the organization processes. To this end, we need to understand the fundamental processes, for instance the processes behind the most natural morphological changes such as the nearshore rhythmic features.

1.1.3 Nearshore rhythmic features

Even in open beaches the structure of beaches is complex. In particular, we observe bumps and troughs that break the alongshore uniformity of beaches. If a regular spacing between a series of bumps or troughs is found, we talk about rhythmic features. There are several kinds of rhythmic features, depending on their cross-shore location, or on their properties, and a classification has been made. Here, we present the main rhythmic features that will be evoked in this thesis. In particular, we will deal with surf zone features that are called bars. This type of rhythmic morphological system was first systematically described in the literature by Evans (1938) and has been reported from many sites, either in low energy beaches (Niederoda & Tanner, 1970; Falqués, 1989) or in moderate energy environments (Guilcher *et al.*, 1952; Hunter *et al.*, 1979; Pedreros *et al.*, 1996; Konicki & Holman, 2000; Lafon *et al.*, 2002). These bars can be subtidal or intertidal systems (Lafon *et al.*, 2002; Castelle, 2004).

Transverse bar systems are an example of rhythmic nearshore morphology. They may be attached to the beach and have a characteristic length of some tens of metres. They may be linked to the oscillation of the coastline and may coexist with a longshore bar being associated with the seaward facing horns of a crescentic bar. However, they can also occur in absence of any longshore bar (see review in Ribas *et al.*, 2003). They sometimes appear in the intertidal zone. They sometimes have a short cross-shore extension that is why it may be difficult to make the distinction with beach cusps, which form in

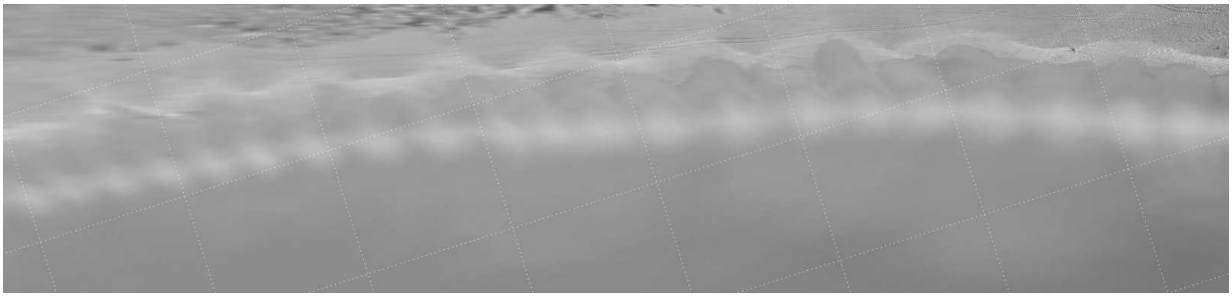

Figure 1.6: Plan view of time exposure image of the Trafalgar beach, Cadiz, Spain. The offshore boundary is at the bottom. Left, oblique down-current oriented bars (wave length $\sim$ 20 m). Right, transverse bars (wave length $\sim$ 30 m).

the swash zone. These short-extended transverse bar patterns have been observed in Trafalgar beach, Cadiz, Spain (see left photo in figure 1.6). If they have an oblique orientation with respect to the coastline, these bars are called oblique bars, they appear on the right photo in figure 1.6, in the part of the beach where wave incidence angle is bigger. The transverse/oblique bars are often described as the same kind of features because they have similar wave lengths and growth times.

The so-called ridge and runnel systems are similar to oblique bar systems but with a bigger characteristic length (of about hundreds of metres). They are very persistent in the French Atlantic Coast (De Melo Apoluceno, 2002; De Melo Apoluceno *et al.*, 2002; Castelle, 2004; Lafon *et al.*, 2002, 2004). They appear in the intertidal zone and they are partially or totally discovered at low tide (left photo in figure 1.7).

This coast is also known for the crescentic bars. They are another well-known type of rhythmic morphology. Their length scale is about a hundred metres, but this depends on their cross-shore location. They are probably the most persistent rhythmic features and appear in all the barred beaches and develop on the longshore bar. For instance, in the French Atlantic coast, we can distinguish two kinds of crescentic bars. (1) the larger ones are the more persistent and appear on the offshore (subtidal) bar; they may be seen (because of water transparency) in the left photo of figure 1.7. (2) the smaller ones may develop in the intermediate zone or in the intertidal zone. Right photo of figure 1.7) displays series of shoals and horns which appear on the intertidal longshore bar, at the same cross-shore location and with the same spacing as the ridge and runnel systems, this may suggest a link between these two kinds of features. In this thesis, we consider these rhythmic features as crescentic bars, however, other studies called them low tide terraces or parallel ridge and runnel systems (Short, 1999; Castelle *et al.*, 2007).

Probably the best way to observe the subtidal rhythmic features in the surf zone is the remote sensing technique, the ARGUS images, for instance. This technique is based on the correlation between the white foam produced by breaking waves and the underlying topographic features. For instance, a clear crescentic pattern is seen in photo 1.8. Moreover, by using this technique, figure 1.6 shows the extension of the transverse/oblique bars in the cross-shore direction until the subtidal zone, which differentiate them from the beach cusps.

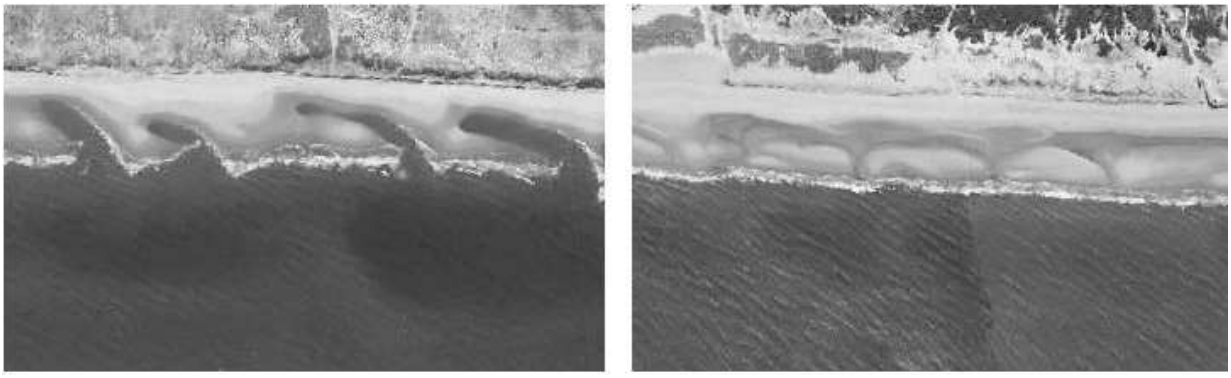

Figure 1.7: Photographies of the French Atlantic coast, France. Left, ridge and runnel system in the intertidal zone (wave length $\sim$ 200 m), crescentic bar system in the subtidal zone (wave length $\sim$ 750 m). Right, crescentic bar system (low tide terraces) on the intertidal longshore bar (wave length $\sim$ 200 m).

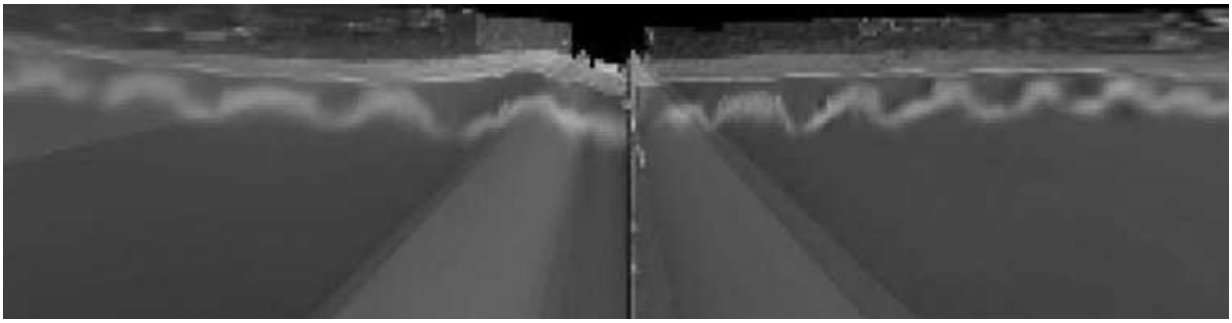

Figure 1.8: Plan view of time exposure image of the Duck coast, USA. The offshore boundary is at the bottom. Crescentic bar system (wave length $\sim$ 500 m)

The study of these rhythmic bars has a strong scientific interest because they are the simplest and the most natural representations of surf zone morphological changes. Understanding the formation and the evolution of theses bars is therefore essential to validate the large scale morphological theories: it is proof that smaller scale processes are well approximated/parameterized. The study of rhythmic bars has also direct practical interests. Firstly, they may be directly linked to the erosion of the coastline. Secondly, for beach nourishment, it is essential to know if the human deposition will be redistributed in bars. Thirdly, for beach safety, these bars may induce very strong seaward cross-shore currents called rip-currents. Fourthly, for a more recreational interest they may generate a progressive wave breaking essential for surfing.

1.2 Nearshore numerical models

1.2.1 Self-organization mechanisms

Most nearshore numerical models are used for coastal engineering applications which define the final goal of such models. To satisfy the demand, these numerical models are often applied to concrete beaches which are often very complex. In an ideal situation, the numerical models should be able to predict the beach evolutions, but, due to the complexity of the beach dynamics, and particularly due to the sediment transport most studies are limited to the hydrodynamics that still constitute a difficult challenge. We need to be aware that a number of approximations are needed to realise morphodynamical studies.

Many morphodynamical studies may be considered as stability studies. Both in the case of existing beaches, or future designed beaches, the goal of morphodynamical modelling is often to give information on the stability of the beach. The challenge would be to learn, in the former case, the equilibrium of the beach given off-shore conditions, and in the latter case, how the initial equilibrium may be affected by the man made structure.

The first step to validate a morphodynamical stability model should be by using the simplest existing beach system: a longitudinally uniform beach. Particularly, nearshore rhythmic features should be described. Because they appear in open beaches, they are not usually forced neither by offshore bathymetric features nor by man made structures. Thus, their origin has been an intriguing research problem for decades. Two general explanations for their generation have been given. The first theory considers that they appear by forced-response mechanisms, i.e., they come from a passive response of the bed to the hydrodynamical forcing. The second theory is based on self-organization mechanisms, i.e., they emerge from free instability of the system due to a positive feedback between the flow and the bed. Numerous linear and nonlinear models are based on this second theory which is the main hypothesis of our work.

1.2.2 Linear stability analysis

In general, the linear stability analysis gives the initial tendency to grow or decay of the various coupled flow-morphology patterns. Thus, it is useful to identify positive feedback mechanisms between flow and morphology giving rise to the observed bed patterns and to give an indication of the relevant time and space scales. However, the assumption of infinitesimal amplitude of the linear analysis precludes any fully reliable comparison with field observations, since it was never verified by the observed bars. When the finite amplitude of the features is accounted for in a nonlinear stability analysis the conclusion is sometimes that some of the predictions (shape, spacing, etc.) of the linear stability prevail for the finite amplitude regime, and sometimes not (Calvete & de Swart, 2003). Thus, while the linear stability gives a suggestion, any true verification that morphodynamical instability is responsible for the formation of bars actually needs nonlinear stability analysis. In particular, any information on the final amplitude of the bars essentially needs a nonlinear analysis.

1.2.3 Nonlinear stability analysis

Nonlinear stability analysis of marine morphodynamical systems to model emerging patterns can be done with approximated semi-analytical methods based on power expansions in a small parameter. This typically leads to Ginzburg-Landau type equations and, although these methods are valid for finite amplitude of the features, the conditions must be only slightly above critical so that they are known as weakly nonlinear analysis. They have been applied, for instance, to sand ripples by Blondeaux (1990) sand banks and sand waves by Komarova & Newell (2000) and Idier & Astruc (2003). Removing the assumption of small amplitude commonly requires the use of numerical models known as fully nonlinear models. This has been carried out in recent years with various techniques. The more traditional method considers the basic physical principles (momentum, water mass, sediment conservation) as partial differential equations, then discretizes them either by finite differences or by spectral methods and finally solves them. This method has been applied to the formation of crescentic bars by Damgaard *et al.* (2002) and by Reniers *et al.* (2004) in case of shore-normal wave incidence. In a similar context and with a similar method, Caballeria *et al.* (2002) examined the finite amplitude dynamics of both crescentic and transverse bars. Following a similar approach but with spectral methods, Nemeth (2003) investigated the formation of tidal sand waves. A second method still considers those governing partial differential equations but discretizes them by using expansions in the linear stability modes. This procedure has been applied by Schuttelaars (1997) and Schramkowski *et al.* (2004) to tidal embayment dynamics and by Calvete & de Swart (2003) to the formation of shoreface-connected sand ridges. Finally, a third method uses abstract rules to describe the basic physics of the system instead of using the partial differential equations (e.g., cellular automata). This procedure has been pursued by Werner & Fink (1993) and Coco *et al.* (2000) for the formation of beach cusps and by Ashton *et al.* (2001) to the formation of large scale shoreline sand waves.

As has been summarised in the last paragraph, nonlinear stability analysis has been

applied to many morphodynamical systems. However, while those nonlinear models describe the growth of morphological features up to finite amplitude, the saturation process at some final amplitude is particularly difficult to describe. An exception is the study of the formation of shoreface-connected sand ridges up to finite amplitude along with its final nonlinear dynamics by Calvete & de Swart (2003) and Roos *et al.* (2004). It was suggested that the saturation takes place as a balance between the instability mechanism and the damping due to gravitational downslope sediment transport but a fully comprehensive explanation was not given. The instability source in that context was the positive feedback between the growing bed features and the perturbations on the current thereinafter called 'bedflow' interaction. However, the corresponding situation in the surf zone is much more complex due to the presence of the breaking waves leading to the so-called 'bedsurf' coupling, namely, the coupling between the growing bed features and the wave field. Thus, in the existing models (Damgaard *et al.*, 2002; Caballeria *et al.*, 2002; Reniers *et al.*, 2004; Fachin & Sancho, 2004*a*) the saturation of the growth of bars either has not been reached or has not been discussed. Therefore, the finite amplitude dynamics of surf zone bars still remains largely unexplored.

1.2.4 Previous surf zone bars modelling

The surf zone bar systems have been the object of many modelling studies, but these studies only describe the initial behaviour of the bars. In particular neither the initial formation nor the final behaviour of ridge and runnel systems has been studied.

The transverse/oblique surf zone bar modelling has been suggested by river studies. The fact that waves incoming obliquely to the coast drive a longshore current that may be quite strong suggests that such bars could form as dunes or free bars in rivers do, i.e., as a morphodynamical instability of the coupling of flow and morphology through the sediment transport. This classical hypothesis was first formulated by Sonu (1968) and has been explored since then by means of linear stability analysis in different model contexts. The recent paper of Ribas *et al.* (2003) summarises and discusses the earlier linear stability analysis of Barcilon & Lau (1973), Hino (1974), Christensen *et al.* (1994) and Falqués *et al.* (1996), based on self-organization processes.However, the emerging patterns are quite sensitive to the mean beach profile, either barred or unbarred, and to the sediment transport description (Klein & Schuttelaars, 2005; Ribas, 2004). Several instability modes can appear and, in particular, the growing bars may be up-current or down-current oriented. This means that they may open an acute angle against the current or with the current, respectively (Evans, 1938; Short, 1994). In general, all the models predict a down-current migration of the bars. Thus, the previous studies only describe the formation of transverse bar systems, by the linear stability analysis, or by using a nonlinear model (Caballeria *et al.*, 2002; Fachin & Sancho, 2004*a*). Investigations on their finite amplitude dynamics is therefore needed.

Most surf zone bar modelling studies deal with crescentic bar systems. They seem to appear by the same mechanisms than for transverse bars, but they are located on the longshore bar. We find linear stability analysis (Deigaard *et al.*, 1999; Klein *et al.*, 2002;

Ribas *et al.*, 2003; Calvete *et al.*, 2005) and nonlinear studies (Caballeria *et al.*, 2002; Damgaard *et al.*, 2002; Castelle, 2004; Reniers *et al.*, 2004). Notice that in some studies, crescentic bar systems may appear in planar beaches, but it seems that this is due to the regular wave breaking parameterization, i.e. to the single breaking point hypothesis, that in fact would simulate the effect produced by the longshore bar. As for the transverse bars systems, the nonlinear studies only describe the initial step of the morphological evolution.

No numerical model has been able to simulate the formation of ridge and runnel systems. Some conceptual models based on observations taken in the French Atlantic coast explain that ridge and runnel system may form by deformation of the intertidal crescentic bars (De Melo Apoluceno, 2002; Castelle, 2004). Thus, numerical modelling needs to be explored.

1.3 Outline of the thesis

The main goal of this thesis is to gain insight on the stability (self-organization) of beaches, particularly, by extending the work on the surf zone rhythmic bars to the nonlinear regime. To this end, the finite difference numerical model MORFO55 that is an extension of MORFO50 (Caballeria *et al.*, 2002) has been used, developed and tested.

The research questions that summarise the objective of the thesis are presented here:

1. Is it possible to model finite amplitude (long term) evolution of morphodynamical instabilities ?
2. Is there any physical reason which explains why existing nonlinear numerical models could not describe the finite amplitude (long term) evolution of morphodynamical instabilities ?
3. What are the gains that may be obtained by modelling finite amplitude (long term) evolution of morphodynamical instabilities ?
4. Does an equilibrium state with rhythmic bars exist ?
5. Do the ridge and runnel systems appear by morphodynamical self-organization ?
6. How realistic are the model results on surf zone rhythmic bars ?

The remaining part of the thesis is divided into 7 chapters with the following contents:

Chapter 2 describes the MORFO55 model by explaining the improvements made from its previous version: MORFO50. Firstly, the main assumption are evoked. Then, the governing equations, the parameterization and the boundary conditions are expressed. The numerical method is also presented. Finally the different options available are summarised.

Chapter 3 is dedicated to the morphological study of complex (longitudinally non-uniform) beaches trough three real cases, in order to test the model. Part of this chapter has been taken from Garnier *et al.* (2004); Dodd *et al.* (2007).

Chapter 4 deals with morphodynamical instabilities of planar beaches. Particularly the nonlinear evolution of oblique/transverse bar systems is studied and extends the work on their formation (Ribas *et al.*, 2003; Caballeria *et al.*, 2002) to the finite amplitude dynamics. These results have been presented in Garnier *et al.* (2006*b*, 2005*b*); Garnier (2005); Garnier *et al.* (2005*a*).

Chapter 5 deals with morphodynamical instabilities of barred beaches. This is an extension to the nonlinear regime of the previous works of Caballeria *et al.* (2002); Calvete *et al.* (2005) on the formation of crescentic bars. This chapter is partly based on Garnier *et al.* (2006*c*,*a*).

Chapter 6 explains the physical mechanisms behind the evolution of surf zone bar system. The mechanisms governing the formation of bar systems (Falqués *et al.*, 1996; Caballeria *et al.*, 2002; Ribas *et al.*, 2003; Calvete *et al.*, 2005) are applied in our cases. They are extended to the nonlinear evolution. The general results are taken from Garnier *et al.* (2006*b*).

Chapter 7 is a discussion on the nonlinear modelling of surf zone bar systems.

Chapter 8, the conclusion responds to the research questions and exposes the further research.

Chapter 2

The MORFO55 model

2.1 Introduction

The MORFO55 nonlinear numerical model is a depth-averaged shallow-water equations solver with sediment transport and bed updating. We can define it as a stability model as its main goal is to study hydrodynamical and morphodynamical instabilities which can be generated by self-organization mechanisms. In the surf zone, many phenomena interact at different time and length scales. The emerging instability patterns have a length scale from tens to hundreds of metres, whereas, for instance, turbulent processes have a much smaller length scale. Many approximations/parameterizations are therefore necessary.

MORFO55 has been built in parallel with a linear stability model: MORFO60, based on the same equations (Calvete *et al.*, 2005). This model has been a very useful tool to compare the initial steps of the growing instabilities. It has been made in order to extend the initial development of instabilities to the finite-amplitude dynamics (Garnier *et al.*, 2006*b*).

The first version of MORFO55 was MORFO50. Its complete formulation was presented in Caballeria (2000). Its main application was to simulate the initial formation of transverse and crescentic bars (Caballeria *et al.*, 2002). The two objectives of the development of MORFO55 are:

- to overcome the limitation of MORFO50 that was not able to describe the strongly nonlinear regime,

- to improve the formulation, mainly by including a more realistic wave transformation and sediment transport formulation.

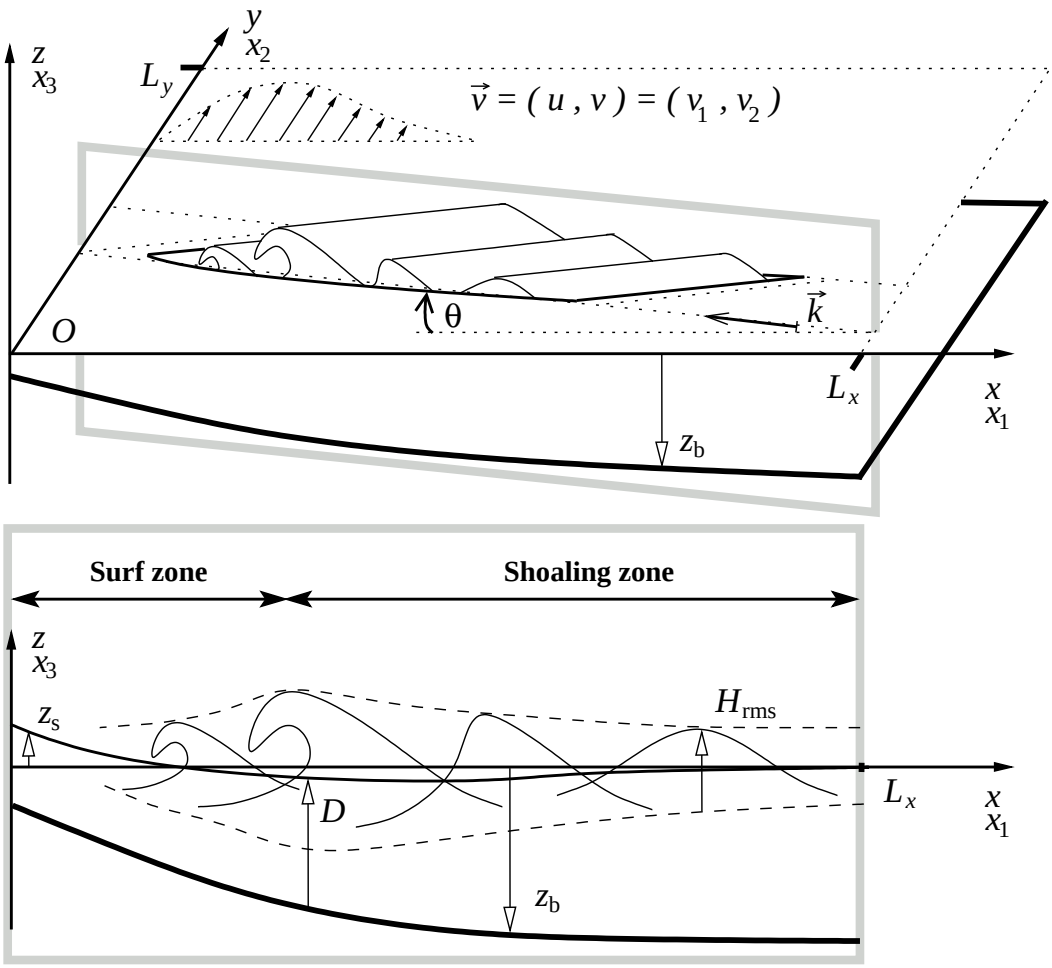

Figure 2.1: Physical system. Frame of reference.

In section 2.2 we present the basic assumptions. Then the general formulation is exposed, first the governing equations (section 2.3), second the boundary conditions (section 2.4) and third the parameterizations (section 2.5). Section 2.6 deals with the numerical methods. Finally, the main model options are listed in section 2.7.

2.2 Model assumptions

2.2.1 Physical system

The domain of study is confined into the nearshore zone (see figure 1.1), more precisely it is composed by the surf zone and the shoaling zone (see figure 2.1). The offshore zone is out of study, i.e. the processes of the wind wave generation and of the tide are not taken into account. Moreover the swash zone dynamics is not included. Because the surf zone is more dynamical than the shoaling zone, we will often classify the MORFO55 as a surf zone model.

As figure 2.1 shows, a rectangular domain is considered. The origin O of the Cartesian coordinate system (O, x_1, x_2, x_3) is situated at an arbitrary point of the boundary which separates the swash zone and the surf zone. This boundary which will be sometimes (improperly) called the coastline is assumed to be rectilinear. The x_1-axis standing for the seaward cross-shore direction is also called the x-axis. The rectilinear offshore boundary is located at $x = L_x$. The x_2-axis, or y-axis, represents the longshore direction. The two lateral boundaries are located at: $y = 0$ and $y = L_y$. The x_3-axis (or z-axis) is the vertical direction and increases upwards. Its origin corresponds with the position of the sea water level in the case of still water, i.e. it corresponds to the tide level given offshore.

2.2.2 Dynamical unknowns

Depending on the four independent variables: x_1, x_2, x_3, and t^*, where t^* is the instantaneous time, the dynamics of the surf zone may be represented by some instantaneous variables: the instantaneous sea water level: $\tilde{z_s}(x_1, x_2, t^*)$, the instantaneous bed level: $\tilde{z_b}(x_1, x_2, t^*)$, and the components of the three-dimensional flow velocity vector: $\tilde{u}_i(x_1, x_2, x_3, t^*)$, where the index i ($i = 1, 2, 3$) corresponds to the projection of the vector on the x_i-axis. Numerous simplifications are necessary to describe large-scale evolutions. They consist in introducing mean variables that can characterize the dynamics of our morphodynamical system. The theory is described in detail in the literature (Pedlosky, 1987; Mei, 1989; Ribas, 2004).

In order to describe long-term morphodynamical evolutions (from minutes to days), the fastest phenomena as the wave orbital motion or the turbulent motions are filtered. To this end, these variables will be time-averaged over a wave period T (i.e. wave-averaged). The corresponding mean quantities, depending on the slower time t, are computed by using the formula:

$$f(t) = \left\langle \tilde{f}(t^*) \right\rangle = \frac{1}{T} \int_{t-T/2}^{t+T/2} \tilde{f}(t^*)\, dt^* \quad . \tag{2.1}$$

The wave-averaged variables are defined as: $z_s(x_1, x_2, t) = \langle \tilde{z_s}(x_1, x_2, t^*) \rangle$, $z_b(x_1, x_2, t) = \tilde{z_b}(x_1, x_2, t^*)$, and $u_i(x_1, x_2, x_3, t) = \langle \tilde{u}_i(x_1, x_2, x_3, t^*) \rangle$ ($i = 1, 2, 3$). Notice that we consider the instantaneous bed level and the wave-averaged bed level as the same quantities, because the morphological characteristic time is much larger than the hydrodynamical one.

In order to simplify our physical system, we use the shallow water theory, considering that the horizontal scales are much larger than the vertical scales. In these conditions, we can define the wave- and depth-averaged horizontal velocity:

$$v_i(x_1, x_2, t) = \frac{1}{D} \left\langle \int_{z_b}^{\tilde{z_s}} \tilde{u}_i(x_1, x_2, x_3, t^*)\, dx_3 \right\rangle \quad , \qquad i = 1, 2 \quad , \tag{2.2}$$

where $D(x_1, x_2, t)$ is the total mean depth defined as $D = z_s - z_b$. The two component of the vector $\vec{v}$ are also called u, and v: $\vec{v} = (v_1, v_2) = (u, v)$.

The wave orbital motion has been filtered by time-averaging, however, waves are the only forcing of our dynamical system. Thus, wave transformation must be described. If we consider a sinusoidal monochromatic wave train, we can write the fluctuating contribution of the instantaneous sea level, due to wave orbital motion as:

$$z_s{}'(x_1, x_2, t^*) = \frac{H}{2} e^{i\tilde{\Phi}} \quad , \tag{2.3}$$

where $H(x_1, x_2, t)$ is the wave height ($H = 2A$, where A is the wave amplitude), $\tilde{\Phi}(x_1, x_2, t^*)$ is the instantaneous wave phase. We define the time-averaged wave phase as: $\Phi(x_1, x_2, t) = \left\langle \tilde{\Phi}(x_1, x_2, t^*) \right\rangle$. We can describe the wave propagation by using the two variables H and Φ.

In place of using the wave height H as a characteristic variable, it may be convenient to use the wave energy density $E(x_1, x_2, t)$ which stands for:

$$E = \frac{1}{8} \rho g H^2 \quad , \tag{2.4}$$

where g is the acceleration due to gravity and ρ the water density. In the open sea, a wave field coming from different random events is nor regular and has wave heights randomly distributed. Longuet-Higgins (1952) has made a statistical description of random waves by introducing a new formulation of the wave energy density, depending on the root-mean-square average of the wave height $H_{rms}(x_1, x_2, t)$:

$$E = \frac{1}{8} \rho g H_{rms}^2 \ . \tag{2.5}$$

Whereas the formula 2.4 is used to simulate regular waves from a laboratory experiments, in the next of the thesis, as only beach cases will be evoked, we will use the formula 2.5.

The wave phase Φ gives two main informations about the wave field: the wave vector $\vec{k}(x_1, x_2, t)$ and the wave frequency $\omega(x_1, x_2, t)$,

$$\vec{k} = \vec{\nabla}\Phi \quad , \tag{2.6}$$

$$\omega = -\frac{\partial \Phi}{\partial t} \quad , \tag{2.7}$$

where $\vec{\nabla}$ is the horizontal gradient operator ($\vec{\nabla} = (\nabla_1, \nabla_2) = (\partial/\partial x_1 \, , \, \partial/\partial x_2)$). Moreover, from the wave vector, we deduce the wavenumber $k(x_1, x_2, t) = |\vec{k}|$ and the wave angle $\theta(x_1, x_2, t) = \arctan(-k_2/k_1)$. As shown figure 2.1, θ is chosen positive clockwise.

In place of describing the mean bed level $z_b(x_1, x_2, t)$, it is possible to deal with $h(x_1, x_2, t)$, the deviation of the bed with respect to the initial topography $z_b^0(x_1, x_2)$ (see figure 2.2). These variables are related by:

$$h(x_1, x_2, t) = z_b(x_1, x_2, t) - z_b^0(x_1, x_2) \ . \tag{2.8}$$

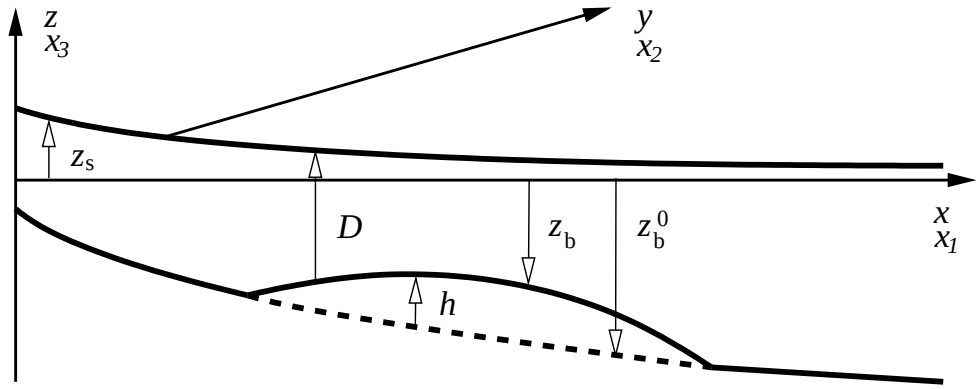

Figure 2.2: Bed perturbation with respect to the initial topography.

Thus, the dynamical unknowns read:

- $z_{\mathrm{s}}(x_1, x_2, t)$, the mean (time-averaged) sea level,
- $\vec{v}(x_1, x_2, t)$, the mean (time- and depth-averaged) horizontal velocity vector,
- $E(x_1, x_2, t)$, the wave energy density, or,
  $H_{\mathrm{rms}}(x_1, x_2, t)$ the root-mean-square average of the wave height
- $\Phi(x_1, x_2, t)$, the mean (time-averaged) wave phase, or,
  $\vec{k}(x_1, x_2, t)$, the wave vector, and $\omega(x_1, x_2, t)$, the wave frequency,
- $z_{\mathrm{b}}(x_1, x_2, t)$, the mean (time-averaged) bed level, or,
  $h(x_1, x_2, t)$, the bed perturbation.

2.3 Governing equations

The governing equations of the MORFO55 model are presented in figure 2.3. They solve the dynamical unknowns presented at the end of the last section. The water mass conservation equation, the two momentum conservation equations (for each component of the horizontal velocity vector), the wave transformation equations and the sediment conservation equations are fully coupled.

The main improvement from MORFO50 (Caballeria, 2000) concerning the governing equations stays in the wave transformation equations in order to include or improve processes such as wave-current interaction, irregular waves, wave refraction and wave diffraction. Particularly, three options are available in MORFO55 (figure 2.3), each of them consider wave-current interaction and irregular waves which were not included in MORFO50. In particular, the time-dependent energy equation (section 2.3.3) is used in options (W1) and (W2). In option (W1) the wave phase is governed by the Eikonal equation (section 2.3.5), while in option (W2) it is governed by the dispersion relation

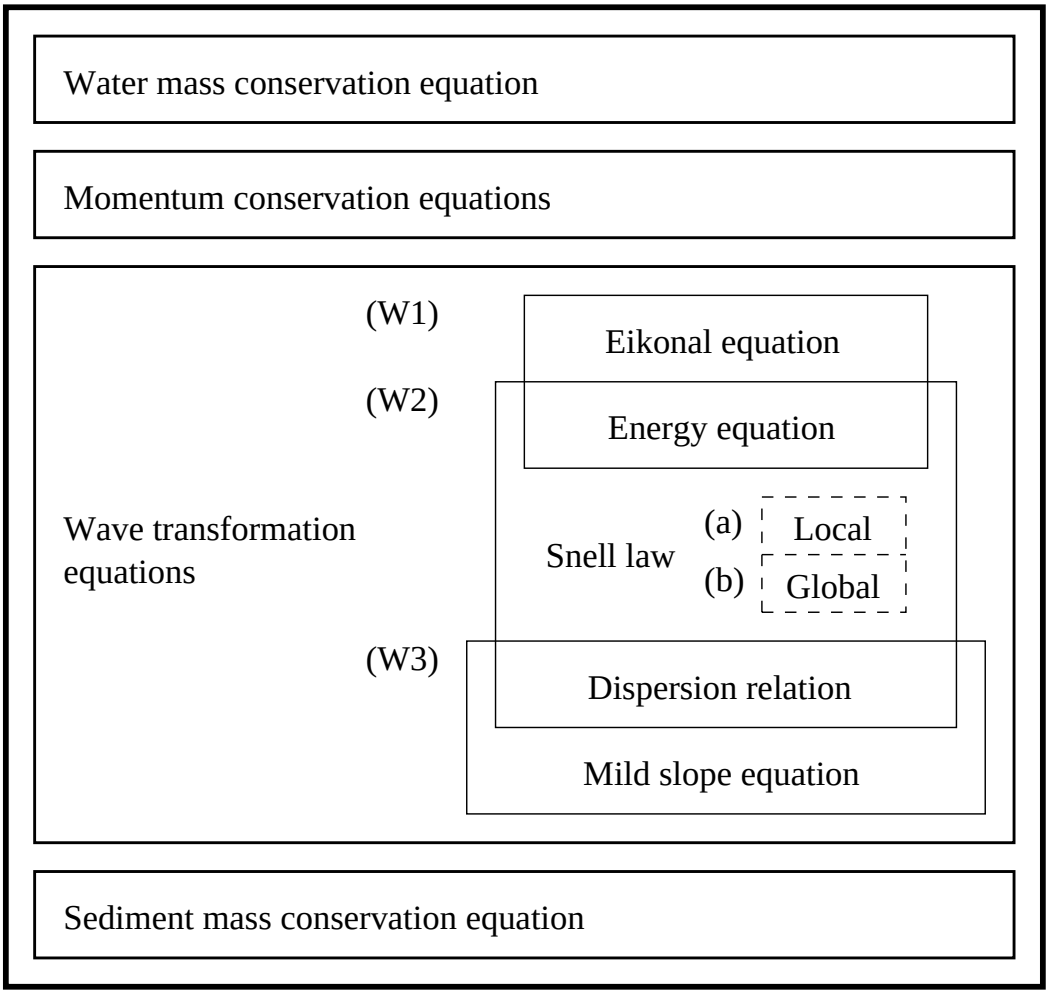

Figure 2.3: Model sketch. The fully coupled governing equations. Three different options for the wave transformation are available: (W1) the wave energy and the wave phase are governed by the time-dependent energy equation and Eikonal equation, respectively, (W2) the time-dependent Eikonal equation of case (W1) is substituted by the Snell law and the dispersion relation, (W3) the wave energy and the wave angle are governed by the parabolic mild slope equation from REF/DIF 1 (Kirby & Dalrymple, 1994), the wavenumber is given by the dispersion relation.

(section 2.3.4) and the Snell law (section 2.3.6). In option (W3), the wave energy and the wave phase are deduced from the complex amplitude given by the mild slope equation (section 2.3.7), the wavenumber is given by the dispersion relation (section 2.3.4) . The main differences between these three options concern wave refraction and wave diffraction; they are discussed in section 2.7. In next chapters, option (W2) will be used.

2.3.1 Water mass conservation equation

The water mass conservation equation reads (Mei, 1989):

$$\frac{\partial D}{\partial t} + \frac{\partial}{\partial x_j}(D\, v_j) = 0 \ , \tag{2.9}$$

where D is the total mean depth ($D = z_\mathrm{s} - z_\mathrm{b}$) as said in section 2.2.2.

2.3.2 Momentum conservation equations

The momentum conservation equations are (Mei, 1989):

$$\frac{\partial v_i}{\partial t} + v_j \frac{\partial v_i}{\partial x_j} = -g\frac{\partial z_\mathrm{s}}{\partial x_i} - \frac{1}{\rho\, D}\frac{\partial}{\partial x_j}(S'_{ij} - S''_{ij}) - \frac{\tau_{\mathrm{b}i}}{\rho\, D} \quad , \qquad i = 1, 2 \ , \tag{2.10}$$

The wave radiation stress tensor, $\bar{\bar{S}}'$, the turbulent Reynolds stress tensor, $\bar{\bar{S}}''$, and the bed shear stress vector, $\vec{\tau}_\mathrm{b}$, will be described in section 2.5.

2.3.3 Energy equation

One hydrodynamical improvement with respect to MORFO50 (Caballeria *et al.*, 2002) has been the introduction of the wave energy density conservation equation including wave-current interaction and irregular waves, relaxing the assumption of a single breaking-point (Mei, 1989; Ribas *et al.*, 2003):

$$\frac{\partial E}{\partial t} + \frac{\partial}{\partial x_j}\left((v_j + c_{\mathrm{g}j})E\right) + S'_{ij}\frac{\partial v_j}{\partial x_i} = -\varepsilon \ , \tag{2.11}$$

where the energy density E is defined in function of the root-mean-square average of the wave height H_rms to take into account irregular (random) waves ($E = \rho\, g\, H_\mathrm{rms}^2/8$). Moreover, $\vec{c_\mathrm{g}}$ is the group velocity vector of the waves and ε is the dissipation rate due to wave breaking and bottom friction described in section 2.5.

2.3.4 Dispersion relation

From the linear wave theory, valid in the case of slow-varying current and water depth, we obtain the dispersion relation (Mei, 1989):

$$\sigma^2 = g\, k\, \tanh(k\, D) \ , \tag{2.12}$$

where σ is the intrinsic frequency, that is, the frequency in a frame moving with the current $\vec{v}$. The relation between the intrinsic frequency σ and the absolute frequency ω is given by:

$$\omega = \sigma + v_i k_i \ . \tag{2.13}$$

2.3.5 Eikonal equation

The wave phase Φ is governed by the Eikonal equation (Mei, 1989; Ribas, 2004):

$$\frac{\partial \Phi}{\partial t} + v_j \frac{\partial \Phi}{\partial x_j} = -\sqrt{g \sqrt{\frac{\partial \Phi}{\partial x_i} \frac{\partial \Phi}{\partial x_i}} \tanh\left(D \sqrt{\frac{\partial \Phi}{\partial x_i} \frac{\partial \Phi}{\partial x_i}}\right)} \ . \tag{2.14}$$

This equation has been obtained by combining equations 2.6 and 2.7 with the dispersion relation (equation 2.12).

2.3.6 Snell law

2.3.6.1 Global Snell law

For parallel depth contours, by neglecting the wave-current interactions, the global Snell law may be obtained from the Eikonal equation (Mei, 1989; Caballeria *et al.*, 2002):

$$k \sin\theta = k^0 \sin\theta^0 \ , \tag{2.15}$$

where k^0 and θ^0 are the wavenumber magnitude and the wave angle at the seaward boundary. In case of non-alongshore uniform topography, the global Snell law may be used, but taking into account that wave refraction is crudely approximated.

2.3.6.2 Local Snell law

The local Snell law is supposed to extend the global Snell law to the case of non parallel depth contours, however, their curvature should be small (Mei, 1989; Caballeria *et al.*, 2002):

$$\frac{d}{dx^*}(k \sin\theta^*) = 0 \ , \tag{2.16}$$

where θ^* is the angle between the wave rays and the x^*-axis, that is, the normal to the perturbed depth contours. The main inconvenience of this local Snell law is that it is conducive to model break down due to the existence of a limit angle (Caballeria *et al.*, 2002).

2.3.7 Mild slope equation

The REF/DIF 1 code (Kirby & Dalrymple, 1994) has been integrated in the MORFO55 model. It solves a parabolic version of the mild slope equation (Mei, 1989; Kirby & Dalrymple, 1994; Dingemans, 1997; Kirby *et al.*, 2002, 2004). The complete form of the parabolic equation used in REF/DIF 1 is written in Kirby & Dalrymple (1994).

Here, we only present a similar but simpler equation to illustrate the wave dissipation model, in order to understand the REF/DIF 1 model outputs:

$$\frac{\partial \bar{A}}{\partial x} = -\frac{\varepsilon}{2\, c_{\mathrm{g}}\, E}\, \bar{A} \ . \tag{2.17}$$

$\bar{A}$ is the complex amplitude related to the water-surface displacement by:

$$z_{\mathrm{s}}{}'(x_1, x_2, t^*) = \mathrm{Re}\left(\bar{A}\, e^{i(kx-\omega t^*)}\right) \ , \tag{2.18}$$

where the symbol Re mean real part. If we consider an irregular (random) wave train, the rms wave height is given by twice the modulus of the complex amplitude:

$$H_{\mathrm{rms}} = 2\,|\bar{A}| \ . \tag{2.19}$$

The components of the wave vector are given by:

$$k_1 = k + \frac{\partial}{\partial x} \arg \bar{A} \ , \tag{2.20}$$

$$k_2 = \frac{\partial}{\partial y} \arg \bar{A} \ , \tag{2.21}$$

where $\arg \bar{A}$ means the argument of $\bar{A}$. In 2.20, the wavenumber k is given by the dispersion relation 2.12.

2.3.8 Sediment mass conservation equation

To couple the bottom level with the hydrodynamical variables, the sediment mass conservation equation is used:

$$\frac{\partial z_{\mathrm{b}}}{\partial t} + \frac{1}{1-p}\, \frac{\partial q_j}{\partial x_j} = 0 \ , \tag{2.22}$$

where p is the sediment porosity ($p = 0.4$) and $\vec{q}$ is the horizontal sediment flux vector.

2.4 Boundary conditions

To solve the time-dependent governing equations 2.9, $2.10_{i=1,2}$, 2.11, 2.14 and 2.22, boundary conditions must be given at the shoreline, the offshore boundary and the lateral boundary, for the variables D, u, v, H_{rms}, Φ and z_{b} (Caballeria, 2000).

2.4.1 Shore boundary

The shore boundary is characterized by: $x = 0$. In order to avoid the complications of the swash zone dynamics, an artificial vertical absorbing wall is assumed. The cross-shore

component of the velocity vector therefore vanishes:

$$u(0, y, t) = 0 \ , \tag{2.23}$$

and also the cross-shore component of the sediment flux vector:

$$q_x(0, y, t) = 0 \ . \tag{2.24}$$

Since we are considering a viscous flow, the longshore component of the velocity vector also vanishes:

$$v(0, y, t) = 0 \ . \tag{2.25}$$

The variables $D(0, y, t)$, $H_{\mathrm{rms}}(0, y, t)$, $\Phi(0, y, t)$ and $z_{\mathrm{b}}(0, y, t)$ are assumed to be free according to their respective equations 2.9, 2.11 and 2.22.

2.4.2 Offshore boundary

The offshore boundary is characterized by: $x = L_x$. The wave conditions are imposed at this boundary: $H_{\mathrm{rms}}(Lx, y, t) = H^0_{\mathrm{rms}}$ and $\theta(Lx, y, t) = \theta^0$. $\Phi(Lx, y, t)$ is determined from equation 2.6.

A radiation boundary condition is applied to the flow components u and v that imposes a seaward exponential decay:

$$\kappa_x \frac{\partial u}{\partial x} + u = 0 \quad , \quad x = L_x \ , \tag{2.26}$$

$$\kappa_y \frac{\partial v}{\partial x} + v = 0 \quad , \quad x = L_x \ . \tag{2.27}$$

corresponding to,

$$u(x, y, t) = u(L_x, y, t) \exp \frac{L_x - x}{\kappa_x} \quad , \quad x \geq L_x \ , \tag{2.28}$$

$$v(x, y, t) = v(L_x, y, t) \exp \frac{L_x - x}{\kappa_y} \quad , \quad x \geq L_x \ , . \tag{2.29}$$

Finally, the variables $D(L_x, y, t)$ and $z_{\mathrm{b}}(L_x, y, t)$ are obtained by linear extrapolation.

2.4.3 Lateral boundaries

The two lateral boundaries are characterized by: $y = 0$ and $y = L_y$.

For the variables D, u, v, H_{rms} and z_{b}, and for its first y-derivatives, we impose periodic boundary conditions, for instance:

$$z_{\mathrm{b}}(x, 0, t) = z_{\mathrm{b}}(x, L_y, t) \ , \tag{2.30}$$

$$\frac{\partial}{\partial x} z_{\mathrm{b}}(x, 0, t) = \frac{\partial}{\partial x} z_{\mathrm{b}}(x, L_y, t) \ . \tag{2.31}$$

These periodic boundary conditions are also applied to the y-component of the wave vector $\vec{k}$ that allows to construct Φ on the lateral boundaries.

2.5 Parameterization

As it is common, only the processes we are interested in are described dynamically in the present study and the processes at smaller scale are parameterized. The former are the formation and evolution of the bars, the currents and the low frequency waves. The latter consist of wind waves, turbulence, bed shear stress and sediment transport.

The more sensitive and unknown point concerns probably the sediment transport formulation. Among many existing formulae we have chosen two. Option (S1) is based on the Bailard formula (section 2.5.6). Option (S2) is more compact; it is based on on the Soulsby and Van Rijn formula (2.5.7) They are discussed in section 2.7.

2.5.1 Radiation stress tensor

The momentum input due to wind waves has been parameterized in the momentum equations 2.10 using the radiation stress tensor from the linear wave theory (Longuet-Higgins & Stewart, 1964):

$$S'_{ij} = E\left(\frac{c_\mathrm{g}}{c}\frac{k_i k_j}{k^2} + \left(\frac{c_\mathrm{g}}{c} - \frac{1}{2}\right)\delta_{ij}\right) \quad , \tag{2.32}$$

with δ_{ij} being the Kronecker delta symbol, c_g the modulus of the group velocity vector $\vec{c_\mathrm{g}}$ and c the modulus of the phase velocity vector $\vec{c}$. The phase and group velocity magnitudes are:

$$c = \sqrt{\frac{g}{k}\tanh kD} \quad , \tag{2.33}$$

$$c_\mathrm{g} = \frac{c}{2}\left(1 + \frac{2kD}{\sinh 2kD}\right) \quad , \tag{2.34}$$

and the components of the corresponding vectors are:

$$c_i = \frac{k_i}{k}\,c \quad , \tag{2.35}$$

$$c_{\mathrm{g}i} = \frac{k_i}{k}\,c_\mathrm{g} \quad . \tag{2.36}$$

2.5.2 Wave dissipation rate

In the wave energy equation 2.11 or in the mild slope equation 2.17, both the dissipation rate by bottom friction and by breaking, $\varepsilon = \varepsilon_\mathrm{f} + \varepsilon_\mathrm{b}$, is accounted for. According

to Horikawa (1988), the dissipation due to bottom friction, ε_{f}, is:

$$\varepsilon_{\mathrm{f}} = \frac{4}{3\pi}\,\rho\,c_{\mathrm{d}}\,\frac{\pi^3\,{H_{\mathrm{rms}}}^3}{T^3}\,\frac{1}{\sinh^3 kD}\ , \tag{2.37}$$

where c_{d} is the hydrodynamical drag coefficient (default value: $c_{\mathrm{d}} = 0.01$).

For the dissipation due to wave breaking the expression (Thornton & Guza, 1983)

$$\varepsilon_{\mathrm{b}} = \frac{3\sqrt{\pi}}{16}\,B^3\,f_{\mathrm{p}}\,\rho\,g\,\frac{{H_{\mathrm{rms}}}^5}{{\gamma_{\mathrm{b}}}^2\,D^3}\,\left(1 - \frac{1}{(\,1 + (H_{\mathrm{rms}}\,/\,\gamma_{\mathrm{b}}\,D)^2\,)^{\,5/2}}\right) \tag{2.38}$$

is obtained by considering the Rayleigh distribution as the probability distribution for the wave height and taking into account that the largest waves are more likely to break. Here, B is a breaking related coefficient (default value: $B = 1.0$), f_{p} is the intrinsic frequency peak of the wave field, $f_{\mathrm{p}} = \sigma/2\pi$, and γ_{b} is the breaker index (default value: $\gamma_{\mathrm{b}} = 0.42$ (Thornton & Guza, 1983)).

2.5.3 Reynolds stress tensor

The momentum input from turbulence is described through the turbulent Reynolds stress tensor:

$$S''_{ij} = \rho\,\nu_{\mathrm{t}}\,D\,(\frac{\partial v_i}{\partial x_j} + \frac{\partial v_j}{\partial x_i})\ , \tag{2.39}$$

where ν_{t} is the turbulent momentum horizontal diffusivity proposed by Battjes (1975):

$$\nu_{\mathrm{t}} = M\left(\frac{\varepsilon}{\rho}\right)^{\frac{1}{3}}\,H_{\mathrm{rms}}\ , \tag{2.40}$$

M is the turbulence parameter (default value: $M = 1$).

2.5.4 Undertow

To take into account the undertow effect, we approximate the near bed mean current vector $\vec{U}$ (Mei, 1989; Ribas *et al.*, 2003) as:

$$\vec{U} = \vec{v} - \frac{E}{\rho\,c\,D}\,\frac{\vec{k}}{k}\ . \tag{2.41}$$

This near-bed mean current will be used in the parameterization of the bed shear stress 2.5.5 and of the sediment transport 2.5.6. These two parameterizations should be coherent themselves. For instance, if the selected sediment transport formulation does not describe the cross-shore sediment transport, the bed shear stress must not take into account the undertow.

In the case that the undertow effect vanishes, we consider that :

$$\vec{U} = \vec{v}\ . \tag{2.42}$$

2.5.5 Bed shear stress vector

The bed shear stress in the momentum equations is an analytical approximation of the average over the Rayleigh distributed wave height and over the wave period of the instantaneous bed shear stress vector given by Mei (1989):

$$\vec{\tau_{\mathrm{b}}} = \rho\, c_{\mathrm{d}}\, |\vec{u_{\mathrm{B}}}|\, \vec{u_{\mathrm{B}}} \ , \tag{2.43}$$

where $\vec{u_{\mathrm{B}}}$ is the instantaneous total flow velocity at the bed (from both currents and waves).

The time-average method and the analytical approximation is given in appendices B and A, respectively. The bed shear stress vector is:

$$\begin{aligned} \vec{\tau_{\mathrm{b}}} &= \rho\, c_{\mathrm{d}}\, U\, \vec{U} + \rho\, \frac{c_{\mathrm{d}}}{\sqrt{\pi}}\, \frac{u_{\mathrm{b}}\, \vec{U}}{1 + 1.6\, \hat{U} + 2.5\, \hat{U}^2} \\ &+ \rho\, \frac{c_{\mathrm{d}}}{\sqrt{\pi}}\, \frac{(u_{\mathrm{b}}\, U + U^2)\, \cos\Psi}{1.081 - 0.043\, \Psi + (0.351 + 0.55\, \Psi)\, \hat{U} + (1.26 - 0.098)\, \Psi)\, \hat{U}^2}\, \frac{\vec{k}}{k} \ , \end{aligned} \tag{2.44}$$

where c_{d} is the hydrodynamical drag coefficient (default value: $c_{\mathrm{d}} = 0.01$), U is the modulus of $\vec{U}$: $U = |\vec{U}|$, $\hat{U}$ is defined as: $\hat{U} = |\vec{U}|/u_{\mathrm{b}}$, u_{b} is the root-mean-square wave orbital velocity amplitude at the bottom and Ψ is the angle between the current and the propagation direction. The root-mean-square wave orbital velocity amplitude at the bottom stands:

$$u_{\mathrm{b}} = \frac{\omega H_{\mathrm{rms}}}{2 \sinh(kD)} = \frac{\pi H_{\mathrm{rms}}}{T\, \sinh(kD)} \ . \tag{2.45}$$

2.5.6 Bailard sediment transport

The depth- and wave-averaged horizontal sediment flux in the sediment mass conservation equation 2.3.8 is first described by using a complete formula combining the Bailard formulation (Bailard, 1981) with a contribution driven by the waves from Plant *et al.* (2001). The depth- and wave-averaged horizontal sediment flux is computed as:

$$\vec{q} = \vec{q_{\mathrm{bl}}} + \vec{q_{\mathrm{sl}}} + \vec{q_{\mathrm{g}}} + \vec{q_{\mathrm{w}}} \ , \tag{2.46}$$

where,

- $\vec{q_{\mathrm{bl}}}$ is the bedload transport without the gravitational contribution and without the contribution driven by the waves alone in absence of current. This will be calculated by the formula of Bailard (1981),
- $\vec{q_{\mathrm{sl}}}$ is the suspended load transport without the gravitational contribution and without the contribution driven by the waves alone in absence of current. This will be calculated by the formula of Bailard.

- $\vec{q_{\rm g}}$ is the downslope gravitational transport. This will be computed by using the corresponding terms in the Bailard formulae for bedload and suspended load,

- $\vec{q_{\rm w}}$ is the contribution driven by the waves alone because of skewness and correlations between sediment concentration and wave oscillatory motion. This will be parameterized by comparison with the cross-shore transport parameterization of Plant *et al.* (2001).

2.5.6.1 Bailard bedload transport

According to Bailard (1981), the instantaneous bedload transport without the gravitational contribution and without the contribution driven by the waves alone in absence of current is:

$$\vec{q_{\rm bl}} \;=\; \frac{\epsilon_{\rm b}\, c_{\rm D}}{g(s-1)\tan\phi_{\rm c}} |\vec{u_{\rm B}}|^2\, \vec{u_{\rm B}} \;\;, \tag{2.47}$$

where $c_{\rm D}$ is the morphodynamical frictional drag coefficient fixed as the hydrodynamical coefficient ($c_{\rm D} = c_{\rm d}$), $\phi_{\rm c}$ is the angle of repose of the sediment, $\epsilon_{\rm b} \simeq 0.13$ is an efficiency and s is the relative density of the sediment ($s \simeq 2.7$). The original formula of Bailard has been divided by $\rho_{\rm s} g$ in order to express $\vec{q}$ as volume instead of weight per time and length units, with account of $\rho_{\rm s} = s\rho$.

From the auxiliary integrals given in appendix A, we deduce its time average over the Rayleigh distribution (appendix C):

$$\vec{q_{\rm bl}} \;=\; \frac{\epsilon_{\rm b}\, c_{\rm D}}{g(s-1)\tan\phi_{\rm c}} \left((U^2 + \frac{u_{\rm b}^2}{2})\, \vec{U} \;+\; u_{\rm b}^2\, U\, \cos\psi\, \frac{\vec{k}}{k} \right) \;\;. \tag{2.48}$$

2.5.6.2 Bailard suspended load transport

Again, according to Bailard (1981), the instantaneous suspended load transport without the gravitational contribution and without the contribution driven by the waves alone in absence of current is:

$$\vec{q_{\rm sl}} = \frac{\epsilon_{\rm s}\, c_{\rm D}}{g(s-1)w_{\rm s}} |\vec{u_{\rm B}}|^3\, \vec{u_{\rm B}} \;\;, \tag{2.49}$$

where $\epsilon_{\rm s}$ is the efficiency for suspended load and $w_{\rm s}$ is the fall celerity of the sediment. By comparison with sediment transport prediction with more sophisticated models, Deigaard (1997) suggests $\epsilon_{\rm s} \simeq 0.02$ while Bailard & Inman (1981) indicated $\epsilon_{\rm s} \simeq 0.01$. The rest of the symbols have the same meaning as in section 2.5.6.1.

According to the analytical approximation given in appendix A, we show in ap-

pendix C that the (mean) suspended load transport is:

$$\begin{aligned} \vec{q_{\rm sl}} &= \frac{\epsilon_{\rm s}\, c_{\rm D}}{g(s-1)\, w_{\rm s}} \left(U^3 + (1.47 - 0.52\psi) u_{\rm b}^2 U + \frac{0.56\, u_{\rm b}^3}{1 + 2.7\hat{U}}\right) \vec{U} \\ &+ \frac{\epsilon_{\rm s}\, c_{\rm D}}{g(s-1)\, w_{\rm s}} \left(1.7 + \frac{0.0663 - 0.453\hat{U} + 1.53\hat{U}^2}{1+\hat{U}}\right) u_{\rm b}^3 U \cos\psi \;\; \frac{\vec{k}}{k} \;\; . \end{aligned} \tag{2.50}$$

2.5.6.3 Bailard downslope gravitational transport

According to Bailard (1981), the gravitational contribution of the instantaneous bedload transport is (appendix C):

$$\vec{\tilde{q}_{\rm g}} = -\tilde{\gamma_{\rm g}}\, \vec{\nabla} z_{\rm b} \;\; , \tag{2.51}$$

where $\tilde{\gamma_{\rm g}}$ is the instantaneous Bailard bedslope coefficient:

$$\tilde{\gamma_{\rm g}} = \frac{c_{\rm D}}{g(s-1)} \left(\frac{\epsilon_{\rm b}}{\tan\phi_{\rm c}^2} + \left(\frac{\epsilon_{\rm s}}{w_{\rm s}}\right)^2 |\vec{u_{\rm B}}|^2 \right) |\vec{u_{\rm B}}|^3 \;\; . \tag{2.52}$$

From appendices A and C, the (mean) downslope gravitational transport is:

$$\vec{q_{\rm g}} = -\gamma_{\rm g}\, \vec{\nabla} z_{\rm b} \;\; , \tag{2.53}$$

where, $\gamma_{\rm g}$ is called the (mean) Bailard bedslope coefficient and reads:

$$\begin{aligned} \gamma_{\rm g} &= \frac{c_{\rm D}}{g(s-1)} \frac{\epsilon_{\rm b}}{(\tan\phi_{\rm c})^2} \left(U^3 \, + \, (1.47 - 0.52\psi)\, u_{\rm b}^2 U \, + \, \frac{0.56\, u_{\rm b}^3}{1 + 2.7\, \hat{U}} \right) \\ &+ \frac{c_{\rm D}}{g(s-1)} \left(\frac{\epsilon_{\rm s}}{w_{\rm s}}\right)^2 \left(U^5 \, + \, (4.89 - 2.43\psi) u_{\rm b}^2 U^3 \right. \\ &\left. + (1.14 - 0.452\psi) u_{\rm b}^3 U^2 \, + \, (1.91 - \psi) u_{\rm b}^4 U \, + \, 1.13 u_{\rm b}^5 \right) \;\; . \end{aligned} \tag{2.54}$$

Notice that equation 2.53 is valid in the case that all the terms of the cross-shore transport are included, i.e. if the undertow and if the effect of wave skewness are considered. If we neglect the cross-shore transport, we assume that the instantaneous downslope gravitational transport is:

$$\vec{q_{\rm g}} = -\gamma_{\rm g}\, \vec{\nabla} h \;\; , \tag{2.55}$$

where h is the bed level deviation from the initial bathymetry.

2.5.6.4 Wave contribution

Following Plant *et al.* (2001) and extracting the contribution of cross correlations between sediment and wave motion, we assume:

$$\vec{q_{\rm w}} = \gamma_{\rm N} \left(\frac{H_{\rm rms}}{D y_{\rm c}} \right)^p \;\; \frac{\vec{k}}{k} \;\; , \tag{2.56}$$

where γ_N describes the stirring of sediment by the waves (volume per length and time units). The parameters p and y_c are related to the parameterization of the relative importance of undertow and cross correlation terms. Their meaning is given in Plant *et al.* (2001) and Ribas *et al.* (2000). We can take $p \simeq 1$ and $y_c \sim 0.25 - 0.75$.

According to Plant *et al.* (2001), the stirring computed by using bedload transport alone is given by:

$$\gamma_N = c_D \, \epsilon_b \, \frac{s-1}{s^2} \, \frac{\gamma_g \sqrt{2g}}{32} \, (\frac{H_{rms}}{\sqrt{D}})^3 \quad . \tag{2.57}$$

Since Plant *et al.* (2001) use sediment mass the transformation to sediment volume has been made.

2.5.7 Total load sediment transport

An alternative to describe the sediment transport is a general total load formula characterized by the mean sediment flux:

$$\vec{q} = \alpha(\vec{v} - \gamma \, u_b \, \vec{\nabla} h) \quad , \tag{2.58}$$

where α is called the stirring factor, and γ, the bedslope coefficient. This equation is based on the Soulsby and Van Rijn formula (Soulsby, 1997). Since it depends on the mean current $\vec{v}$ and on the bed perturbation h, the onshore transport driven by wave nonlinearity and undertow is excluded. In fact, this onshore transport is assumed to be in balance with the gravitational downslope transport which take into account the total beach slope ($\vec{\nabla} z_b$).

We consider two different stirring factors:

- a cross-shore uniform or constant wave stirring (CWS formula),
- a function based on the Soulsby and Van Rijn formula (Soulsby, 1997) (SVR formula).

The bedslope coefficient γ is a critical parameter in our model which will differ depending on the stirring function used. There is a large uncertainty on its value and this is why a sensitivity study will be done. Nevertheless, a default value must be found for each stirring function by analogy with previous modelling studies. Assuming that the velocities are of order 1 m s^{-1}, the original γ advised by Soulsby (1997) was 1.6. Regarding the Bailard's transport formula (Bailard, 1981), the order of magnitude of γ was 1.5 for the suspended load transport and 0.2 for the bedload transport. For the reference cases, γ has been fixed to 1.5 with the SVR stirring and to 0.5 with the constant stirring.

2.5.7.1 Constant Wave Stirring (CWS) formula

The value chosen for the constant wave stirring is:

$$\alpha = 0.001 \text{ m} \ . \tag{2.59}$$

This value has been found by analogy with the Bailard formula and the SVR formula (appendix F).

The main motivation for using the CWS transport is that it has been used in a number of existing stability studies (Hino, 1974; Falqués *et al.*, 2000; Ribas *et al.*, 2003). As it is argued in Falqués *et al.* (2000), a constant stirring may be associated with the situation where the infra-gravity wave energy is important. This can be seen from the Bailard formula (Bailard, 1981) by considering (i) a wave-dominated beach, i.e. a beach where the orbital velocity of waves is stronger than the current (Ribas *et al.*, 2003) and (ii) a significant low frequency wave energy (Falqués *et al.*, 2000) whose shoreward increasing orbital velocity compensates the decrease induced by the breaking of high frequency waves.

The default value of γ, in the CWS transport formula has been fixed to $\gamma = 0.5$ (appendix F).

2.5.7.2 Soulsby Van Rijn (SVR) formula

The stirring factor corresponding to the SVR transport reads

$$\begin{aligned} \alpha \quad &= A_{\mathrm{S}} \left[\left(|\vec{v}|^2 + \frac{0.018}{c_{\mathrm{D}}} {u_{\mathrm{b}}}^2 \right)^{1/2} - u_{\mathrm{crit}} \right]^{2.4} \\ &\text{if} \left(|\vec{v}|^2 + \frac{0.018}{c_{\mathrm{D}}} {u_{\mathrm{b}}}^2 \right)^{1/2} > u_{\mathrm{crit}} \\ &= 0 \quad \text{otherwise} \ , \end{aligned} \tag{2.60}$$

where the constant $A_{\mathrm{S}} = A_{\mathrm{SS}} + A_{\mathrm{SB}}$ depends essentially on sediment characteristics and water depth and where A_{SS} represents the suspended load transport and A_{SB} the bedload transport (Soulsby, 1997):

$$\begin{aligned} A_{\mathrm{SS}} \quad &= \quad \frac{0.012 d_{50} D_*^{-0.6}}{\left[(s-1) g d_{50}\right]^{1.2}} \ , \\ A_{\mathrm{SB}} \quad &= \quad \frac{0.005 h \left(d_{50}/D\right)^{1.2}}{\left[(s-1) g d_{50}\right]^{1.2}} \ , \end{aligned} \tag{2.61}$$

where d_{50} is the median grain size (default value: $d_{50} = 0.25$ mm), s is the relative density of sediment (default value: $s = 2.65$), and D_* is the dimensionless grain size:

$$D_* = \left[\frac{g(s-1)}{\kappa_{\mathrm{b}}^2} \right]^{1/3} d_{50} \ , \tag{2.62}$$

and κ_b is the kinematic viscosity of water (default value: $\kappa_b = 1.3\,10^{-6}\ \mathrm{m^2\,s^{-2}}$).

$$c_D = \left[\frac{0.40}{\ln(D/z_0) - 1}\right]^2 \quad , \tag{2.63}$$

where z_0 is a roughness length, here, due to the grain size or bed ripples (default value: $z_0 = 0.006$ m). Typical values of c_D found in Damgaard *et al.* (2002) are $0.006 \leq c_D \leq 0.01$. Here, the morphodynamical drag coefficient c_D is chosen different from the hydrodynamical one c_d, whereas in the Bailard formula of section 2.5.6, the same value has been considered. Further research are needed in this subject, but Soulsby (1997) suggests that these two coefficients may differ.

The threshold current velocity for sediment transport u_{crit} depends on sediment properties and depth (Soulsby, 1997):

$$u_{crit} = \Lambda \log_{10} \frac{h}{d_{50}} \quad , \tag{2.64}$$

where,

$$\Lambda = \begin{cases} 0.19\,(d_{50})^{0.1} & \text{for} \quad 0.0001\ \mathrm{m} \leq d_{50} \leq 0.0005\ \mathrm{m} \\ 8.5\,(d_{50})^{0.6} & \text{for} \quad 0.0005\ \mathrm{m} \leq d_{50} \leq 0.002\ \mathrm{m} \end{cases} \quad . \tag{2.65}$$

The difference between our SVR sediment transport formula and the original one (Soulsby, 1997) concerns the downslope term where $|v|$ has been substituted by u_b. The motivation is the following. Actually, both $|v|$ and u_b contribute to stir the sediment and u_b is typically larger than $|v|$. Furthermore, for normal wave incidence the current vanishes in the basic state so that small topographic departures from equilibrium would not cause downslope transport which is unrealistic. The default value of γ, in the SVR transport formula has been fixed to $\gamma = 1.5$ (appendix F).

2.5.8 Including/excluding the cross-shore processes

As it has been suggested in section 2.5.4, three dimensional cross-shore processes have been parameterized in the model, by considering first the undertow (in the bed shear stress and sediment transport parameterizations) and second the wave skewness (in the sediment transport parameterization). Because all the sediment transport formulations described here can not describe these three dimensional effects, or because we want to focus on particular processes, the model allows to connect/disconnect the three dimensional effects. While in the hydrodynamical mode they only affect the bed shear stress vector 2.44, in the morphodynamical mode they affect more processes. Particularly, we need to be careful with the coherence of the model structure.

The two sensitive points are:

- the way to describe the near bed mean current,

  - $(\vec{U})$ dependence, by including the undertow, i.e., by using the vector $\vec{U}$ defined in equation 2.41,
  - $(\vec{v})$ dependence, by excluding the undertow, i.e., by approximating: $\vec{U} = \vec{v}$,

- the way to describe the slope of the bed in the sediment transport formulation,
  - (z_b) dependence, by considering the total topography $(\vec{\nabla} z_\mathrm{b})$,
  - (h) dependence, by considering the perturbed topography $(\vec{\nabla} h)$.

For the Bailard sediment transport described in section 2.5.6, to include the three dimensional effects, we use the following structure:

$$\begin{aligned} &\vec{\tau_\mathrm{b}}(\vec{U}) \ , \\ &\vec{q}(\vec{U}, z_\mathrm{b}) = \vec{q_\mathrm{bl}}(\vec{U}) + \vec{q_\mathrm{sl}}(\vec{U}) + \vec{q_\mathrm{g}}(\vec{U}, z_\mathrm{b}) + \vec{q_\mathrm{w}}(\vec{U}) \end{aligned} \tag{2.66}$$

while to exclude them we use:

$$\begin{aligned} &\vec{\tau_\mathrm{b}}(\vec{v}) \ , \\ &\vec{q}(\vec{v}, h) = \vec{q_\mathrm{bl}}(\vec{v}) + \vec{q_\mathrm{sl}}(\vec{v}) + \vec{q_\mathrm{g}}(\vec{v}, h) \ . \end{aligned} \tag{2.67}$$

The total load sediment transport described in section 2.5.7, does not describe the three dimensional effects, thus, we can only use:

$$\begin{aligned} &\vec{\tau_\mathrm{b}}(\vec{v}) \ , \\ &\vec{q}(\vec{v}, h) \ . \end{aligned} \tag{2.68}$$

In the case that the cross-shore transport is excluded, i.e., the model is governed by equations 2.67 or 2.68, the onshore transport driven by wave nonlinearity and undertow is assumed to be in balance with the gravitational downslope transport. Thus, if the initial topography is alongshore uniform, characterized by the cross-shore profile: $z_\mathrm{b}^0(x_1)$, this profile is supposed to be an equilibrium profile. When this equilibrium is broken by growing features, it is assumed that the downslope gravitational transport will only cause a diffusive sediment transport proportional to the gradient of the bed level deviation from equilibrium, h. This simplification is motivated by the interest in the growth of alongshore non-uniformities rather than cross-shore migration of bars and has been commonly adopted in all the modelling studies on rhythmic topography (Deigaard *et al.*, 1999; Caballeria *et al.*, 2002; Damgaard *et al.*, 2002; Ribas *et al.*, 2003). It is physically based on the fact that the transport driven by the longshore current and rip currents is typically quite stronger than the transport directly driven by the waves (at least for well developed rips).

2.6 Numerical method

The finite-difference numerical scheme to solve the governing equations presented in section 2.3 is given in this section.

2.6.1 Computational domain

The time step is denoted by Δt. The time index k satisfies: $k \in [0, N_t]$, where N_t is the final time index. The time is given by:

$$t(k) = t_0 + k\,\Delta t \quad , \quad k = 0 : N_t \ , \tag{2.69}$$

where t_0 is the initial time.

As shows figure 2.4, the uniform grid spacing is defined by the couple $(\Delta x, \Delta y)$:

$$\begin{aligned} \Delta x &= \frac{L_x}{N_x - 1} \ , \\ \Delta y &= \frac{L_y}{N_y} \ , \end{aligned} \tag{2.70}$$

where N_x and $N_y + 2$ are the number of points of the computational domain in the cross-shore and longshore direction, respectively. The couple of space indexes (i, j) satisfies: $(i, j) \in [1, N_x] \times [0, N_y + 1]$.

A staggered grid is considered which consists in defining the scalar discretized variables and the two component of the vector discretized variables at three different positions (figure 2.4):

- the scalar discretized variables such as (D, E, Φ or z_b) are defined at the centre of the cell, i.e. at the position:

$$\begin{aligned} x(i) &= \left(i - \frac{1}{2}\right) \Delta x \quad , \quad i = 1 : N_x \ , \\ y(j) &= \left(j - \frac{1}{2}\right) \Delta y \quad , \quad j = 0 : N_y + 1 \ . \end{aligned} \tag{2.71}$$

- the x-component of the vector discretized variables (u or q_x) is defined at the u-node position:

$$\begin{aligned} x_u(i) &= (i - 1)\,\Delta x \quad , \quad i = 1 : N_x \ , \\ y(j) &= \left(j - \frac{1}{2}\right) \Delta y \quad , \quad j = 0 : N_y + 1 \ , \end{aligned} \tag{2.72}$$

- the y-component of the vector discretized variables (v or q_y) is defined at the v-node position:

$$\begin{aligned} x(i) &= \left(i - \frac{1}{2}\right)\Delta x \quad , \quad i = 1 : N_x \ , \\ y_v(j) &= (j-1)\,\Delta y \quad , \quad j = 0 : N_y + 1 \ . \end{aligned} \tag{2.73}$$

Thus, if we denote f a discretized variable, we introduce the notation $f^k_{i,j}$ which depends on the kind of f. Whatever the kind of f, we can approximate its value at the previous (forward) half space step in each direction. To this end, we introduce the notations $f^k_{i+1/2,j}$, $f^k_{i-1/2,j}$ $f^k_{i,j+1/2}$ and $f^k_{i,j-1/2}$ defined as:

$$\begin{aligned} f^k_{i\pm1/2,j} &= \frac{f^k_{i,j} + f^k_{i\pm1,j}}{2} \ , \\ f^k_{i,j\pm1/2} &= \frac{f^k_{i,j} + f^k_{i,j\pm1}}{2} \ . \end{aligned} \tag{2.74}$$

- If f is a scalar discretized variable (D, E, Φ or z_b), it is defined at the central node:

$$f^k_{i,j} = f(x(i), y(j), t(k)) \ . \tag{2.75}$$

In some cases, we need to compute f at the u-node and v-node positions which are called f_u and f_v, respectively:

$$\begin{aligned} {f_u}^k_{i,j} &= f^k_{i-1/2,j} = \frac{f^k_{i,j} + f^k_{i-1,j}}{2} \ , \\ {f_v}^k_{i,j} &= f^k_{i,j-1/2} = \frac{f^k_{i,j} + f^k_{i,j-1}}{2} \ . \end{aligned} \tag{2.76}$$

- If f is the x-component of the vector discretized variables (u or q_x), it is defined at the u-node:

$$f^k_{i,j} = f(x_u(i), y(j), t(k)) \ . \tag{2.77}$$

f at the v-node is computed as:

$${f_v}^k_{i,j} = f^k_{i+1/2,j-1/2} = \frac{f^k_{i,j} + f^k_{i+1,j} + f^k_{i+1,j-1} + f^k_{i,j-1}}{4} \ . \tag{2.78}$$

We can also approximate f at the central node:

$${f_c}^k_{i,j} = f^k_{i+1/2,j} = \frac{f^k_{i+1,j} + f^k_{i,j}}{2} \ . \tag{2.79}$$

- If f is the y-component of the vector discretized variables (v or q_y), it is defined at the v-node:

$$f^k_{i,j} = f(x(i), y_v(j), t(k)) \ . \tag{2.80}$$

f at the u-node is computed as:

$$f_{u\,i,j}^{\;k} = f_{i-1/2,j+1/2}^{k} = \frac{f_{i,j}^{k} + f_{i-1,j}^{k} + f_{i-1,j+1}^{k} + f_{i,j+1}^{k}}{4} \ , \tag{2.81}$$

and f at the central node is:

$$f_{c\,i,j}^{\;k} = f_{i,j+1/2}^{k} = \frac{f_{i,j+1}^{k} + f_{i,j}^{k}}{2} \ . \tag{2.82}$$

As said in section 2.2.1, the beach system is defined by $0 \leq x \leq L_x$ and $0 \leq y \leq L_y$. It is delimited in figure 2.4 by the four brackets. The boundary conditions must be applied at the boundaries of this system, even if the computational domain for each kind of variables is different.

2.6.2 Time-dependent equations

The time-dependent governing equations, i.e. equations: 2.9, $2.10_{i=1,2}$, 2.11, 2.14 and 2.22, have been discretized with the same method. They can be formulated as:

$$\frac{\partial f}{\partial t} = \Phi_f \ , \tag{2.83}$$

where f corresponds to any of the unknowns: D, u, v, E, Φ or z_b. Φ_f is the corresponding flux, which includes all the term of the equation of f except the term of the temporal derivative. The discretization is given in the particular case $f = D$. Equation 2.83 gives:

$$\frac{\partial D}{\partial t} = \Phi_D \ , \tag{2.84}$$

and the corresponding flux is:

$$\Phi_D = -\left(\frac{\partial}{\partial x}(D\,u) + \frac{\partial}{\partial y}(D\,v)\right) \ , \tag{2.85}$$

2.6.2.1 Temporal derivative

For the temporal derivative, the explicit Adams-Bashforth second order scheme is adopted. Thus, the discretized equation 2.83 becomes:

$$\frac{f_{i,j}^{k} - f_{i,j}^{k-1}}{\Delta t} = \frac{3}{2}\Phi_{f\,i,j}^{\;k-1} - \frac{1}{2}\Phi_{f\,i,j}^{\;k-2} \ , \tag{2.86}$$

This is valid for $k \in [2, N_t]$. The value of variables for $k = 1$ is obtained by using the Euler first order scheme. The value of variables for $k = 0$, i.e. at time t_0 is an input of the model.

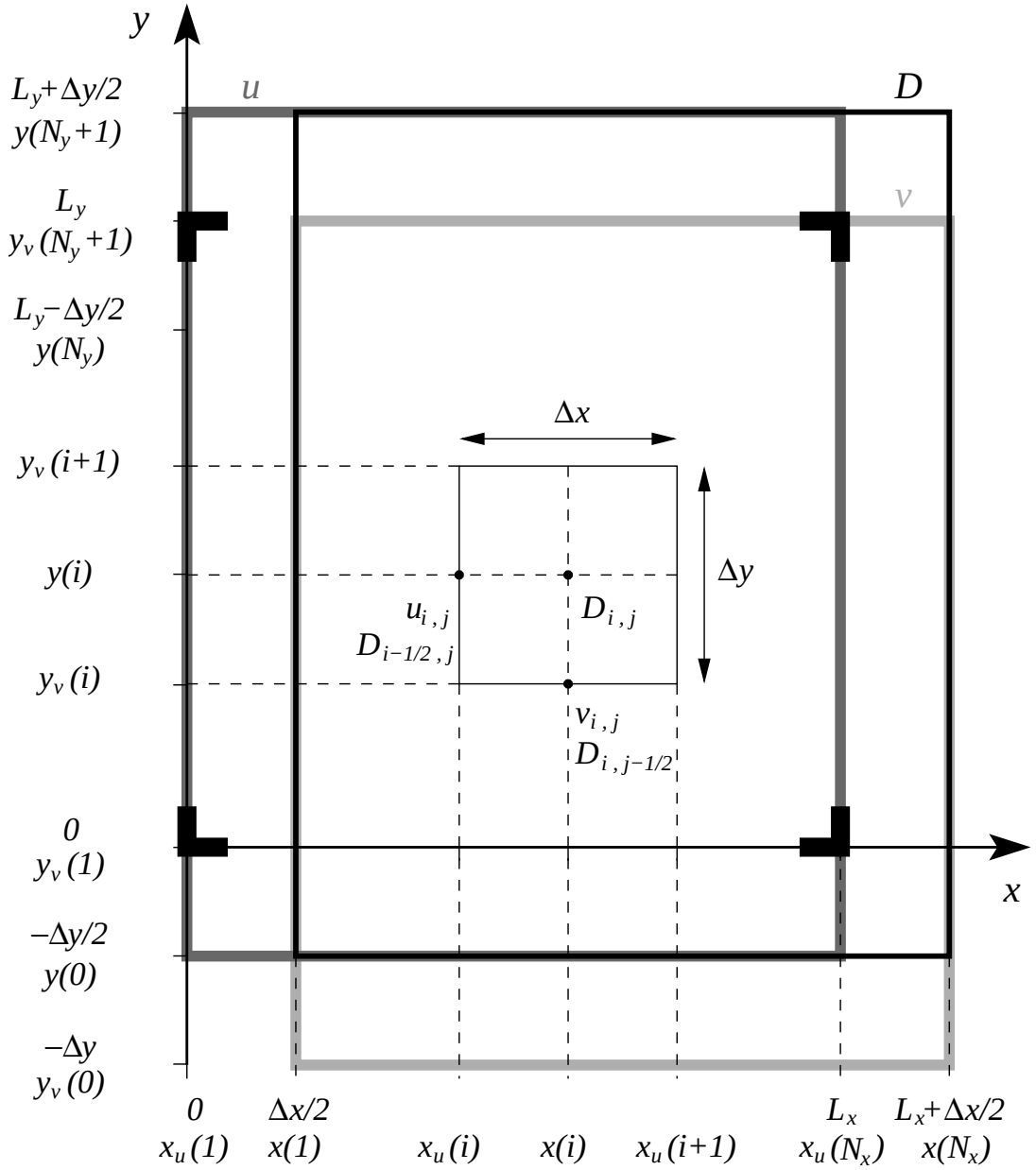

Figure 2.4: Computational domain. The four brackets delimit the beach system, defined by $0 \leq x \leq L_x$ and $0 \leq y \leq L_y$. The black square represents the total domain for the variables of the kind of D, i.e., for the scalar variables. The dark grey square represents the total domain for the variables of the kind of u, i.e., for cross-shore components of the vector variables. The light grey square represents the total domain for the variables of the kind of v, i.e., for longshore components of the vector variables.

2.6.2.2 Spacial derivatives

The discretization of the function Φ_f is done by using the central second order approximation for the spacial derivatives.

In the case $f = D$, ${\Phi_f}^k_{i,j}$ becomes (omitting the sub-index k):

$$\Phi_{D\,i,j} = \frac{1}{\Delta x}\left[-\left(D_{u\,i+1,j}u_{i+1,j} - D_{u\,i,j}u_{i,j}\right) - q_{xy}\,\left(D_{v\,i,j+1}v_{i,j+1} - D_{v\,i,j}v_{i,j}\right)\right] \ , \quad (2.87)$$

where q_{xy} is the rate between the spatial increments:

$$q_{xy} = \frac{\Delta x}{\Delta y} \ . \quad (2.88)$$

$D_{u\,i,j}$ and $D_{v\,i,j}$ are defined following equation 2.76.

2.6.2.3 CFL conditions

According to Caballeria (2000), the explicit Adams-Bashforth scheme for the temporal derivative required two generic stability conditions (Courant-Friedrichs-Levy conditions, or CFL conditions) on the time increment Δt, due to the parabolic and hyperbolic characters of the system of equations. The most restrictive is the numerical stability condition caused by the hyperbolic nature and stands:

$$\Delta t \leq t_{\mathrm{CFL}} \ , \quad (2.89)$$

where:

$$t_{\mathrm{CFL}} = c_1\ \min\{\Delta x, \Delta y\}\,/\sqrt{g\,D_{\max}} \ . \quad (2.90)$$

The constant c_1 is determined empirically and is found to be about 0.1 (Caballeria, 2000).

2.6.3 Snell law

2.6.3.1 Local Snell law

By using the local Snell law (equation 2.16), the wave angle $\theta(x(i), y(j))$ is given by (Caballeria, 2000):

$$\theta_{i,j} = \theta^*_{i,j} + {\theta_{u}}^n_{i,j} \ , \quad (2.91)$$

where ${\theta_{u}}^n_{i,j}$ is the angle between the normal to the local depth contour and the x-axis evaluated at the u-node, and the local incidence angle $\theta^*_{i,j}$ is given by the relation:

$$k_{i,j}\sin\theta^*_{i,j} = k_{i+1,j}\sin\theta^*_{i+1,j} \ , \quad (2.92)$$

where $\theta^*_{i+1,j}$ is given by:

$$\theta^*_{i+1,j} = \theta_{i+1,j} - {\theta_{u}}^n_{i+1,j} \ . \quad (2.93)$$

2.6.3.2 Global Snell law

By using the global Snell law (equation 2.15), $\theta_{i,j}$ is deduced from its previous step $\theta_{i+1,j}$, by solving the equation:

$$k_{i,j} \sin\theta_{i,j} = k_{i+1,j} \sin\theta_{i+1,j} \ . \tag{2.94}$$

2.6.4 Dispersion relation

From the dispersion relation (equation 2.12), we deduce $k(x(i), y(j))$:

$${\sigma_{i,j}}^2 = g\, k_{i,j}\, \tanh(k_{i,j}\, D_{i,j}) \ , \tag{2.95}$$

2.6.5 Mild slope equation

The discretization of the complete parabolic mild slope equation may be found in Kirby *et al.* (2002). It is based on the Crank-Nicolson technique. Here, we give an example applied to equation 2.17. Omitting the bar on A, this equation may be written as:

$$\frac{\partial A}{\partial x} = -\alpha_{\mathrm{rd}}\, A \ , \tag{2.96}$$

where $\alpha_{\mathrm{rd}} = \varepsilon / 2\, c_{\mathrm{g}}\, E$.

Thus, the discretized equation, by using the Crank-Nicolson technique, gives :

$$\frac{A_{I+1} - A_I}{\Delta x} = -0.5\, (\alpha_{\mathrm{rd}\, I+1} A_{I+1} + \alpha_{\mathrm{rd}\, I} A_I) \ , \tag{2.97}$$

i.e.,

$$(\frac{1}{\Delta x} + 0.5\, \alpha_{\mathrm{rd}\, I+1})\, A_{I+1} = (\frac{1}{\Delta x} - 0.5\, \alpha_{\mathrm{rd}_i})\, A_I \ . \tag{2.98}$$

I is the cross-shore space index used in REF/DIF 1. As the x-axis has an apposite orientation in REF/DIF 1 and in MORFO55, we have the relation $i = N_x + 1 - I$. Then, the solution for the step $I + 1$ is deduced from the step I by solving a linear system. Notice that a special treatment for $\alpha_{\mathrm{rd}\, I+1}$ is needed because it depends on A_{I+1} which is the unknown. This treatment is described in appendix D, particularly, the original method used in REF/DIF 1 (Kirby *et al.*, 2002) seems to present problems when the grid spacing is large ($\Delta x > 1$ m).

2.6.6 Boundary conditions in difference form

2.6.7 Shore boundary

At $x = 0$, the non-flux conditions from equation 2.23 and 2.24 are discretized as:

$$u_{1,j} = 0 \ , \tag{2.99}$$

and,

$$q_{x\,1,j} = 0 \ . \tag{2.100}$$

The non-slip condition (equation 2.25) $v(0, y, t) = 0$ is written as $v_{1/2,j} = 0$. By using a linear extrapolation, we obtain:

$$v_{1,j} = \frac{1}{3} v_{2,j} \ . \tag{2.101}$$

The other variables: $D_{1,j}$, $E_{1,j}$, $\Phi_{1,j}$ and $z_{\mathrm{b}1,j}$ do not need special treatment at the shore boundary, so as their respective discretized equation 2.86 is used.

2.6.8 Off-shore boundary

Due to the staggered grid, the imposed variables are defined at $x = L_x + \Delta x$ in place of at $x = L_x$, thus:

$$H_{\mathrm{rms}\,N_x,j} = H^0_{\mathrm{rms}} \ , \tag{2.102}$$

and,

$$\theta_{N_x,j} = \theta^0 \ . \tag{2.103}$$

From the boundary condition introduced in section 2.26, we find:

$$u_{N_x,j} = \frac{\kappa}{\kappa + 1} u_{Nx-1,j} \ , \tag{2.104}$$

$$v_{N_x,j} = \frac{\kappa - 1/2}{\kappa + 1/2} v_{Nx-1,j} \ , \tag{2.105}$$

where κ is defined as (Caballeria, 2000):

$$\kappa = \frac{\kappa_x}{\Delta x} - \frac{1}{2} = \frac{\kappa_y}{\Delta x} \ . \tag{2.106}$$

For $\kappa = 0$, the boundary conditions lead to: $u_{N_x,j} = 0$ and $v_{N_x-1/2,j} = 0$, i.e. $\vec{v}(L_x, y, t) = \vec{0}$. This physically means that a solid wall is placed at $x = L_x$. For increasing values of κ, the boundary conditions become more permeable. For large values

of κ, an open boundary is obtained. Note that equation 2.106 implies a larger decay for u than for v.

The variables $D_{N_x,j}$ and $z_{\mathrm{b}\,N_x,j}$ are obtained by linear approximation of the kind:

$$f_{N_x,j} = 2\, f_{N_x-1,j} - f_{N_x-2,j} \quad . \tag{2.107}$$

The phase $\Phi_{N_x,j}$ is obtained as:

$$\Phi_{N_x,1} = 0 \quad , \tag{2.108}$$

$$\Phi_{N_x,j} = \Phi_{N_x,j-1} + k_{N_x,1}\, \sin\theta^0\, \Delta y \quad , \tag{2.109}$$

2.6.9 Lateral boundaries

The periodic lateral boundary conditions for the variable f referring to D, u, v, H_{rms} or z_{b}, and for its first y-derivatives (section 2.4.3) imply:

$$f_{i,0} = f_{i,N_y} \quad , \tag{2.110}$$

$$f_{i,1} = f_{i,N_y+1} \quad . \tag{2.111}$$

The periodic lateral boundary conditions applied to k_y and to its first y-derivative is used to compute $\Phi_{i,0}$:

$$\Phi_{N_x,0} = -k_{N_x,1}\, \sin\theta^0 \quad , \tag{2.112}$$

$$\Phi_{i,0} = \Phi_{i+1,0} + \Phi_{i,N_y} - \Phi_{i+1,N_y} \quad , \tag{2.113}$$

and Φ_{i,N_y+1}:

$$\Phi_{N_x,N_y+1} = \Phi_{N_x,N_y} + k_{N_x,1}\, \sin\theta^0\, \Delta y \quad , \tag{2.114}$$

$$\Phi_{i,N_y+1} = \Phi_{i+1,N_y+1} + \Phi_{i,1} - \Phi_{i+1,1} \quad . \tag{2.115}$$

2.7 MORFO55 options and limitations

The main improvements from MORFO50 concern the wave transformation equations and the sediment transport formulation. The original formulations have been kept but they have not been used in the present thesis. In this section, the main model options are listed. They concern the wave transformation and the sediment transport.

2.7.1 Wave transformation

As figure 2.3 indicates, three options are described in the thesis. Here, we also present the original option (W0).

- (W0)

  The original wave transformation (Caballeria *et al.*, 2002) was obtained by: (i) a simple formulation for the wave height transformation and (ii) the Snell law and the dispersion relation for the wave vector. This wave transformation method is similar to the option (W2) of the present model, but the time-dependent energy equation is not used. The crude assumption of regular waves, i.e., of a single breaking point is made. The wave-current interaction is not taken into account. These two assumptions are relaxed in the new formulations. The description of the wave energy transformation was made by making the hypothesis that the wave height is (1) proportional to the water depth in the saturated surf zone shoreward the breaking point and (2) constant seaward the breaking point.

- (W1)

  The wave transformation is described by the time-dependent wave energy and Eikonal equations (equations 2.11 and 2.14, respectively). Its implementation is not yet reliable as numerical problems occur when the grid spacing becomes too small. In particular, the basic state (equilibrium hydrodynamical state) is only reached for big grid spacing.

- (W2)

  The wave transformation is governed by (i) the time-dependent wave energy equation and (ii) the (local (a) or global (b)) Snell law and the dispersion relation. This option is the most stable, particularly when considering the global Snell law (W2b), the local Snell law (W2a) imposing a critical wave incidence angle. The shortcoming of the global Snell law is that it does not take into account the refraction by the perturbed topography.

- (W3)

  The wave transformation is governed by the parabolic mild slope equation from the REF/DIF 1 model. This equation has the advantage of taking into account the wave refraction and the wave diffraction (that can not be described in the other cases). The disadvantage is that it is not time-dependent and an intermediate time step is needed: this equation is run every 100 s (in the default case). Moreover, some numerical oscillations are observed.

In order to make long term morphodynamical simulations, for numerical stability reasons, the option (W2b) is chosen by default. A comparison of the formulations (W2a), (W2b), and (W2c), is shown in appendix E, in the hydrodynamical case of waves propagating over a shoal. This example shows that wave refraction may affect the current circulation, whereas the wave diffraction seems to not have an essential importance. This test case suggests that wave refraction may change the morphodynamical results.

2.7.2 Sediment transport formulation

Two kinds of sediment transport formulations are presently used in the MORFO55 model: a formula based on the Bailard sediment transport (Bailard, 1981) which may take into account the cross-shore processes (option (S1)), and a simple formula based on the Soulsby and Van Rijn study (Soulsby, 1997), (option (S2)). The original (MORFO50) formulation (Caballeria *et al.*, 2002) is presented as the option (S0).

- (S0)

  The original (MORFO50) formulation (Caballeria *et al.*, 2002) is based on the Bailard transport formula in the weak current hypothesis (appendices A and C). It does not take into account the cross-shore processes and its general formulation is simple and is close to the formulation presented in case (S2).

- (S1)

  The complete Bailard transport formula (Bailard, 1981) has been adapted in the MORFO55 model (section 2.5.6). The three-dimensional cross-shore processes, i.e. the undertow and the wave skewness have been parameterized (case (S1a)). In this case, the sediment transport due to the wave skewness comes from the Plant formula (Plant *et al.*, 2001). In case (S1b), we suppose that these cross-shore processes are in equilibrium. As chapter 3 shows, the use of this sediment transport formulation, particularly in case (S1a), lead to numerical instabilities. Two reasons may explain this shortcoming: first, the effect of diffusivity in the bedslope contribution could be underestimated, second, the discretization method applied to the sediment conservation equation could be inadequate, a more sophisticated numerical scheme such as a non-oscillatory scheme could be necessary (Saint-Cast, 2002; Marieu *et al.*, 2006).

- (S2)

  The total load sediment transport formula based on the Soulsby and Van Rijn study (Soulsby, 1997) is described by the sediment flux equation 2.58. The cross-shore processes of (S1a) are not taken into account. The advantage of this formulation are (i) it allows for long term simulations (ii) its simple form allows us to easily understand the physical mechanisms. The wave stirring α may be chosen as a function based on Soulsby (1997) (option (S2a), or SVR), or a constant (option (S2b), or CWS). The second one would represent stronger conditions than the first one, supposing that infragravity waves have more importance.

The analogy between (S1) and (S2) has been detailed in appendix F. The option (S1) is probably the most realistic, some tests have been made in chapter 3, but only in the (S1a) case. In the further chapters, the option (S2) is preferred for the reasons (i) and (ii) given before.

Chapter 3

Longitudinally non-uniform beaches

3.1 Introduction

One of the goals of numerical modelling in the nearshore zone is the study of the behaviour of particular beaches in order to predict how they will change and how the shoreline will be affected. In particular, most beach changes are due to wave action. The numerical modelling allows us to simulate any wave conditions and allows us to anticipate possible damage caused by waves.

In order to preserve the shoreline, a lot of coastal engineering projects are dedicated to the building of artificial structures, basically to stop the wave breaking near the shoreline. By using these kinds of structures, some engineering studies propose to be able to lead to an auto-regeneration of beaches. Nevertheless, these methods are not infallible and in most cases, unexpected changes are produced, sometimes in the place where structures have been build, and sometimes in different places. In fact, the safest way to preserve and regenerate beaches would probably be the sediment import. But this technique is far from being fully controlled, particularly two fundamental questions remain on the agenda:

- where the imported sediment should be taken from ?
- where should it be put ?

The main difficulty is that each beach system is unique, thus, there are no trivial answers. Because of the ecological damages they can engender and because of their costs, all coastal projects should be preceded by meticulous numerical morphodynamical simulations.

Until now no morphodynamical model is fully reliable, that is why a lot of modelling improvements are necessary. Because of the infinite complexity of beach dynamics, it is impossible to take into account all the processes. In this sense, MORFO55 has been developed: in order to take into account most of processes but with the priority of keeping understanding the mechanisms behind. In particular, new processes have been included from the previous model MORFO50 (chapter 2), and other processes are planned to be studied in the next version of the model. Nevertheless we have felt that it is sometimes better to go back to a simpler version, by thinking about sensible hypothesis, not to loose the main interest of our research: to understand the mechanisms. The first version of the model (MORFO50) was made to study the stability of longitudinally uniform beaches. Even if this is also the main objective of MORFO55, this new model is also applied to the study of real beaches, in a more general context. Thus, we do not pretend to use a fully reliable model to foresee the evolution of complex beaches. We present how such a stability model can be adapted to engineering studies through some examples of applications of longitudinally non-uniform beaches.

In this chapter, we present three kinds of engineering problems. The objective is not to supply an engineering solution to these problems, but it is to test the model in the case of longitudinally non-uniform beaches. Specifically, the main goals are:

- to adapt such a stability model to a complex/non-uniform beach,
- to test different model formulations,
- to analyse the hydrodynamics on the fixed topography,
- to look at the engendered sediment transport and the evolution of the bed,
- to know if the model predicts that the initial beach system is in equilibrium,
- to know if the model predicts another equilibrium beach state.

The first part of this chapter is dedicated to the morphodynamical study of a particular beach: the Barrosa beach, Cadiz, Spain. In section 3.2 we will analyse the morphodynamical behaviour of the entire beach. The main interest lies in adapting the MORFO55 model to a real case. We will take into account all the available data such as topography, wave conditions and water level. In section 3.3 we will focus on ephemeral rhythmic features that have seen to be a characteristic of the Barrosa beach: the gully systems, through a highly idealised case study (Dodd *et al.*, 2007). In the second part of this chapter (section 3.4), we will bring up the engineering problem of sediment import by modelling the morphodynamical evolution of a submerged shoal test case (Garnier *et al.*, 2004).

3.2 The Barrosa beach (Cadiz, Spain)*

3.2.1 Introduction

One emphasis of the HUMOR project has been to investigate demanding beach change problems. In particular, a part of the project dealt with the concrete case of the Barrosa beach near Cadiz in the south of Spain (figure 3.1). This is a mesotidal sandy beach, where the tidal range varies from 1 to 3 metres. It has the characteristic to be almost rectilinear and large in the longshore direction (figure 3.2). It is located on the Atlantic coast and the incoming swell may be considered as moderate, mostly obliquely incoming.

The Barrosa beach is an appropriate application case because of its rectilinearity and its longshore length. Indeed, the rectilinear computational domain with periodic lateral boundary conditions used by MORFO55 is well adapted. Nevertheless, a work on adapting the field data, both for the initial topography and for the hydrodynamical conditions, has been necessary.

The goals of this project are:

- to apply the model to a concrete beach study,
- to run the hydrodynamical model, disconnecting the sediment transport, in order to understand the main hydrodynamical patterns,
- to understand the morphological response.

The next part of this section will be dedicated to explain the model adaptations to this real case, then the model results will be presented.

3.2.2 Modelling

3.2.2.1 Topographic input

The topographic data consist in level lines in the North-South coordinate system. Figure 3.3, shows the topography measured during June 2001, the north direction is given by the decreasing longitude axis and the west direction is given by the increasing latitude axis. As the input topography of MORFO55 must be interpolated on a rectilinear grid, the initial topographic data of figure 3.3 has been rotated by 5 ° in order to have the straightest-possible coastline (figure 3.4). The coastline has been chosen as the level line of 1 m. It corresponds to the mean tide level measured during the year 2001. Then, the

*This work is taken from an oral presentation made during the Final Workshop of the HUMOR project: Garnier, R., Ribas, F., Falqués, A., Calvete, D. & Caballeria, M. 2004 MORFO55 applications to the Single Cell.

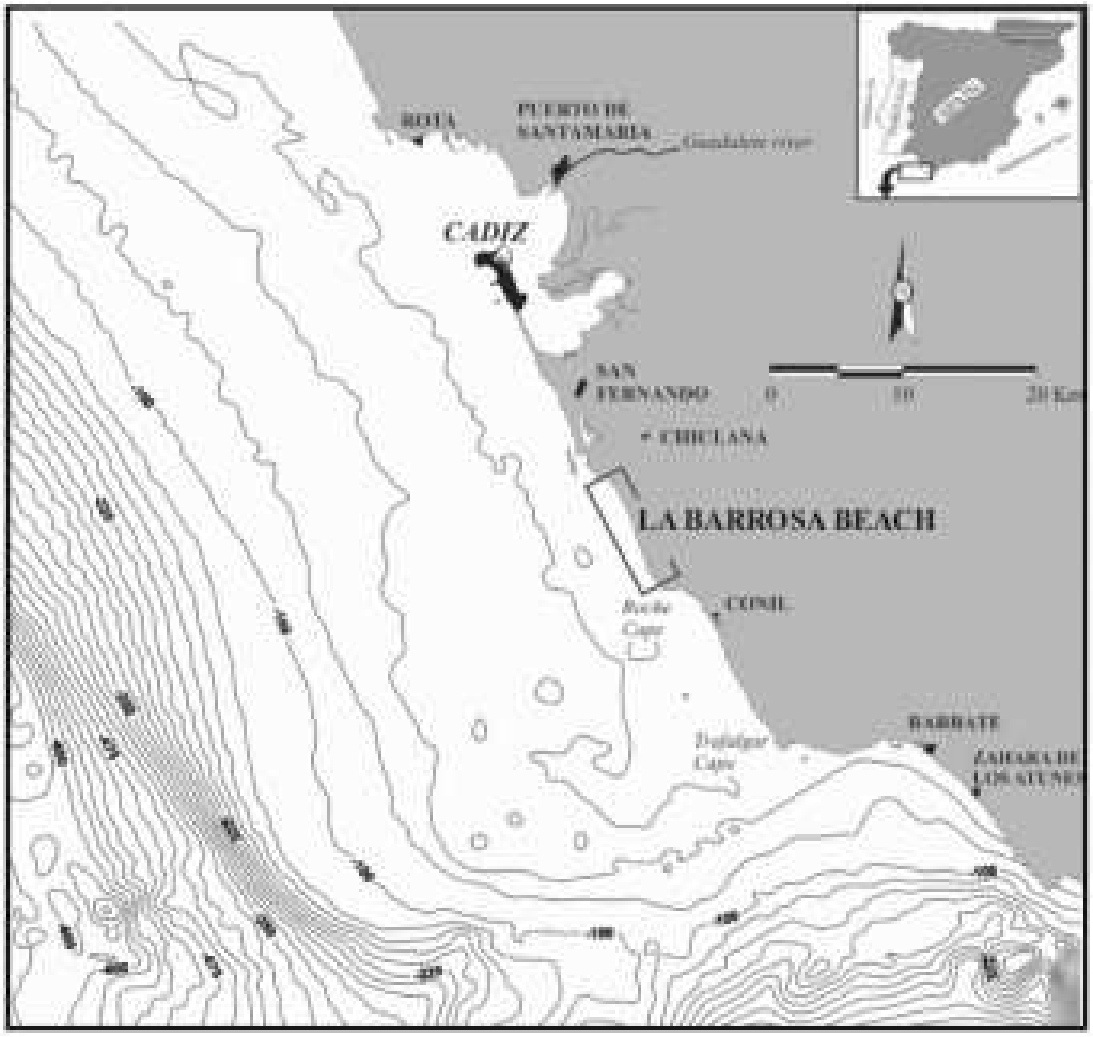

Figure 3.1: The Barrosa beach. Location.

Figure 3.2: The Barrosa beach. A Photo.

topography has been cut in order to apply periodic boundary conditions (grey window in figure 3.4). Finally the topography presented in figure 3.5 is included in MORFO55. The grey window of figure 3.4 is represented by the darkest lines. Some points have been added in order to preserve the boundary conditions: uniformity in the coastline and in the off-shore boundary and periodicity in the lateral boundary. The first step of MORFO55 consists in interpolating this topography, giving the initial bathymetry of figure 3.6

This beach is non-longitudinally uniform, particularly due to a 200 m width terrace like (TE1) centred at the point ($x = 200$ m, $y = 500$ m). Attached to it, a 100 m width trough (TR1) is centred at the point ($x = 300$ m, $y = 600$ m).

3.2.2.2 Wave conditions

The most representative wave conditions of the year 2001 are shown in table 3.1. These values correspond to the wave conditions (wave height and wave angle) at the off-boundary of MORFO55. As the wave data were measured far off shore ($x = 2000$ m), previous calculus have been made by using the MORFO60 model run on a mean topographic profile in order to have the wave conditions at the off-shore boundary of the computational domain.

Among these six cases, we have selected the strongest conditions. To this end, we introduce three dimensionless numbers:

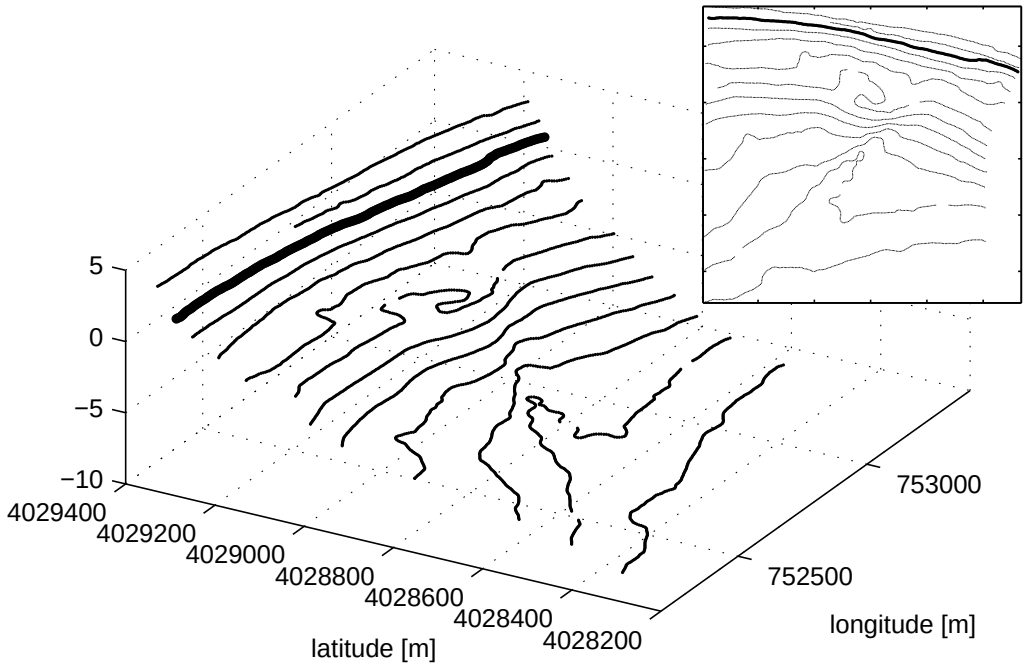

Figure 3.3: The Barrosa beach. Initial bathymetry. 3D view and plane view. The big line corresponds to the level line of the mean tide level.

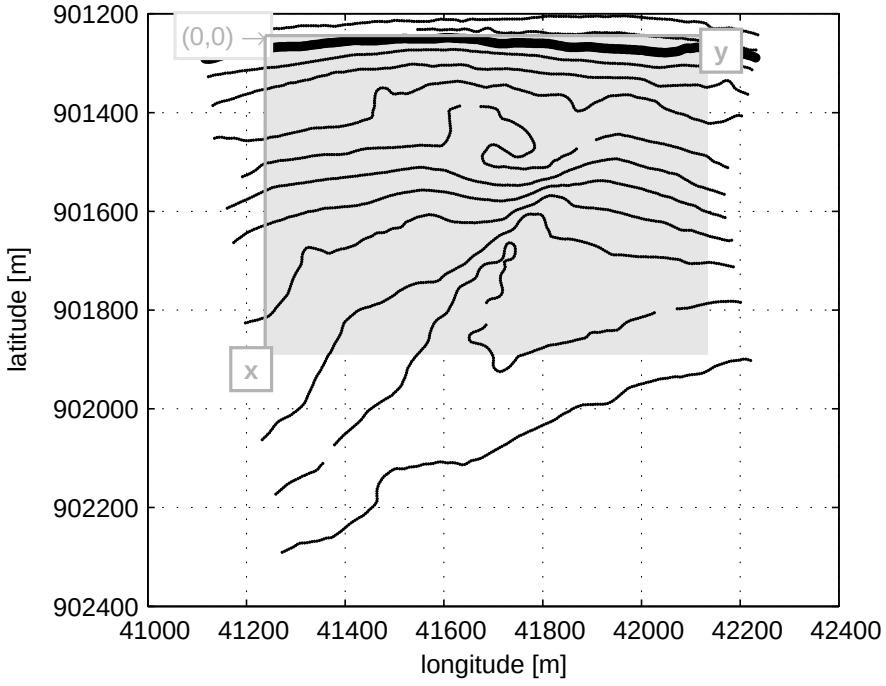

Figure 3.4: The Barrosa beach. Rotated Initial bathymetry.

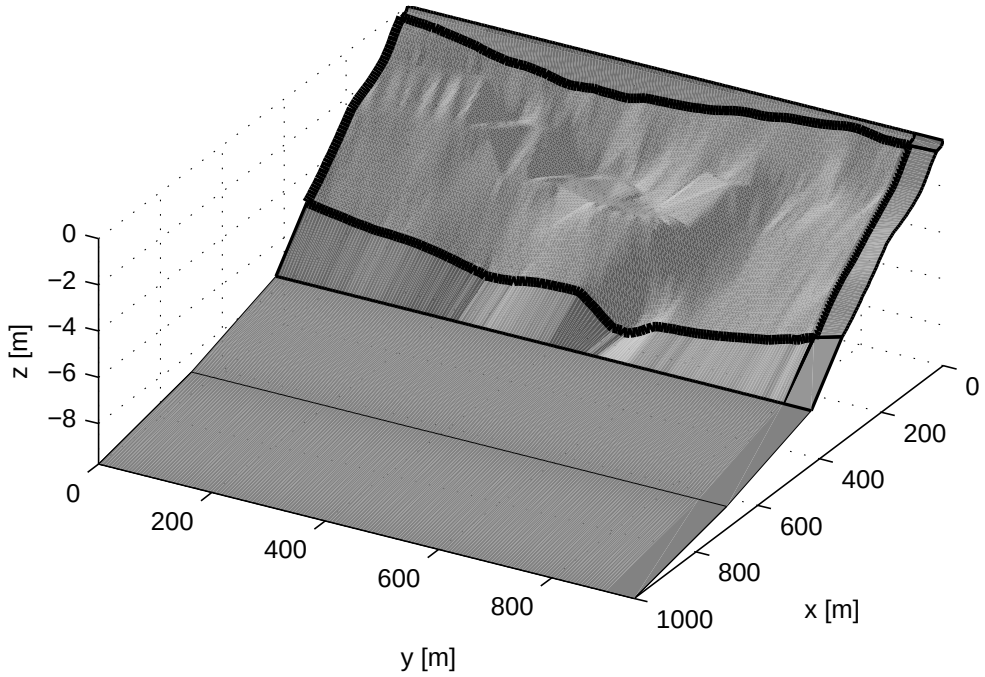

Figure 3.5: The Barrosa beach. Modified bathymetry before interpolation (model input).

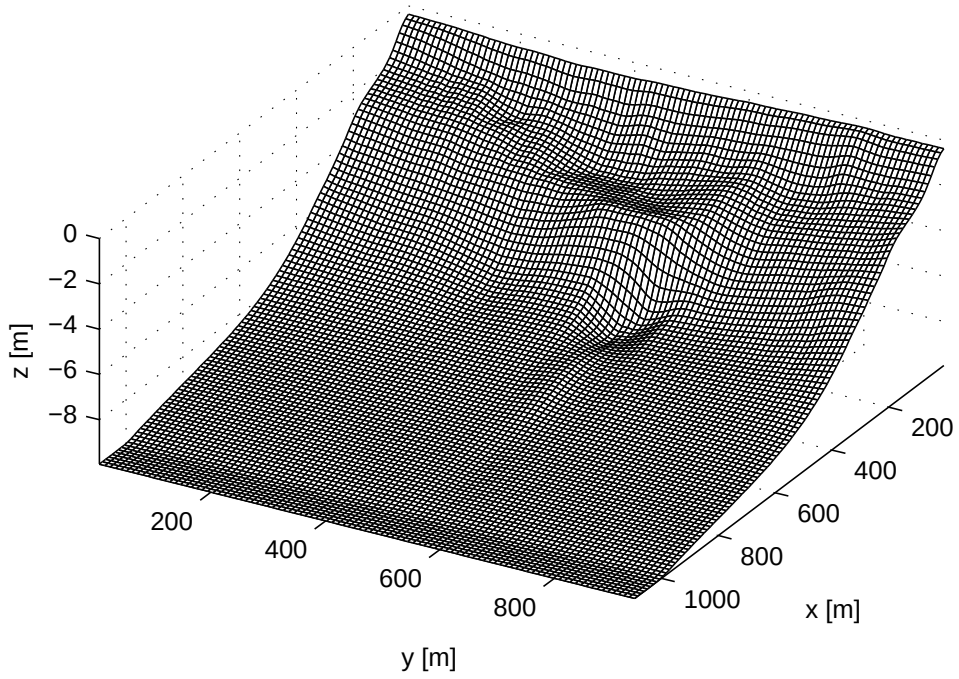

Figure 3.6: The Barrosa beach. Interpolated initial bathymetry.

case	$H^0_{\rm rms}$ [m]	θ^0 [deg]	T [s]	Ω	$\Gamma_{\rm c}$	S [10^{-3}]	$c_{\rm d}$
1	0.92	20.0	9	2.03	59	1.16	0.1
2	1.05	19.2	12	1.72	64	0.74	0.01
3	1.50	20.0	10	3.00	77	1.53	0.01
4	1.60	18.6	12	2.67	79	1.13	0.01
5	1.72	18.6	16	2.16	82	0.69	0.01
6	3.00	15.3	18	3.33	108	0.94	0.035

Table 3.1: The Barrosa beach. Wave conditions

1) the dimensionless fall velocity Ω, defined as (Short, 1999) :

$$\Omega = \frac{H^0_{\rm rms}}{w_{\rm s} T}\,, \tag{3.1}$$

which characterizes three beach types: the reflective beach ($\Omega < 1$), the intermediate beach ($1 < \Omega < 6$) and the dissipative beaches ($\Omega > 6$),

2) the nondimensional morphological diffusivity $\Gamma_{\rm c}$, defined as (Caballeria *et al.*, 2002) :

$$\Gamma_{\rm c} = \frac{\sqrt{g H^0_{\rm rms}}}{w_{\rm s}}\,, \tag{3.2}$$

3) the wave steepness S defined as:

$$S = \frac{H^0_{\rm rms}}{\lambda} \sim \frac{H^0_{\rm rms}}{g T^2}\,. \tag{3.3}$$

Whereas the parameters Ω and $\Gamma_{\rm c}$ measure the tendency of the beach to be dissipative, the parameter S measures the wave nonlinearity. All of these measure the tendency of the beach to have the most morphological changes. Table 3.1 shows that both Ω and $\Gamma_{\rm c}$ are the biggest in case 6 whereas the wave steepness is the biggest in case 3. Therefore, experiments have been done for these two cases. These cases simulate oblique waves but the corresponding normal wave incidence cases has been checked too.

3.2.2.3 Parameterization

The computational domain has been fixed to 1100 m cross-shore and 945 m longshore. The mesh spacing is 10×10 m^2. The time step used is $\Delta t = 0.05$ s for the hydrodynamics. For the morphodynamics it is $\Delta t_{\rm m} = 0.5$ s since an acceleration factor of 10 is used

(factor in front of $\vec{q}$ in equation 2.22). The drag coefficient c_{d} for the bottom friction has been analytically fixed and depends on the wave conditions (c.f. table 3.1). In order to have the most realistic result, the Bailard formulation has been chosen to describe the sediment transport. For numerical reasons the sediment transport is only driven by the depth averaged current, the undertow and wave asymmetry effects being neglected. For the non-specified parameterizations, we have respected the default values of chapter 2.

3.2.3 Results

3.2.3.1 Hydrodynamics

The MORFO55 model is first run disconnecting the bed evolution equation. Results after one hour of hydrodynamical evolution are presented. Figures 3.7 and 3.8 show the wave height and the wave vectors in the cases 3 and 6, respectively. For waves of 1.5 m, the trough TR1 does not seem to affect the wave propagation whereas for waves of 3 m it slows down the wave breaking. On the contrary, the terrace forces the waves to break in the two cases.

In the same way, looking at the mean sea level (figures 3.9 and 3.10), there is more set up over the terrace TE1 itself than at its left and right sides, and there is less set up over the troughs TR1 than over its two sides. This has a direct influence on the current circulation.

Nevertheless, due to the complexity of the Barrosa beach, because of the complex shape of the terrace TE1 and the trough TR1 and because of other shoals, troughs and bars, the wave height and the sea level contours are difficult to meticulously analyse. This also happens for the current circulation: in the case of normal wave incidence, numerous cells appear (figures 3.11 and 3.12). The simplest case is probably the second one (waves of 3 m) with three predominant cells.

In the case of oblique wave incidence, the circulation cells disappear due to the strong ambient longshore current (figures 3.13 and 3.14). The maximum magnitude of the current is about 1 $\mathrm{m\,s^{-1}}$ and it is mainly longshore. Nevertheless the current is deflected and tends to follow the bathymetric contours. It is more observable in figures 3.13 where the width of the ambient longshore current is smaller because of smaller waves.

3.2.3.2 Morphodynamics

The complexity of the hydrodynamical patterns detailed in the last section is seen in the bed evolution. The following results are obtained by coupling the bed evolution equation once the hydrodynamics were stabilised. In fact the results presented in the last section correspond to the initial state of the morphological evolution. The model crashes very quickly because of the morphodynamical diffusivity which seems to not be

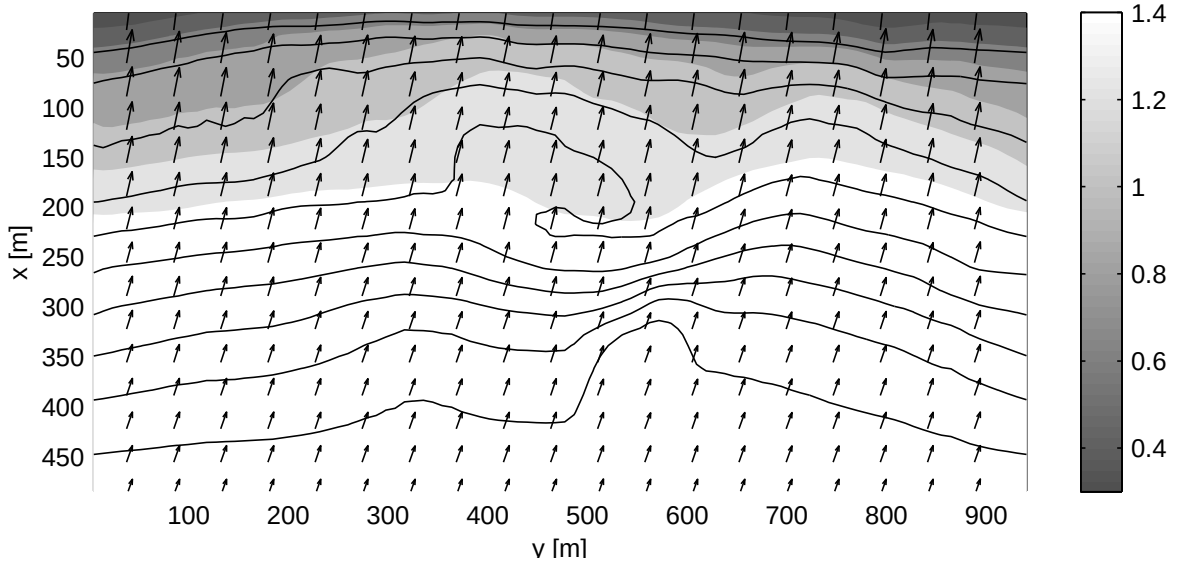

Figure 3.7: The Barrosa beach. Hydrodynamics. Oblique wave incidence. $H^0_{\mathrm{rms}} = 1.5$ m at the seaward boundary. Wave height H_{rms} in metres (contour plot) and wave vectors.

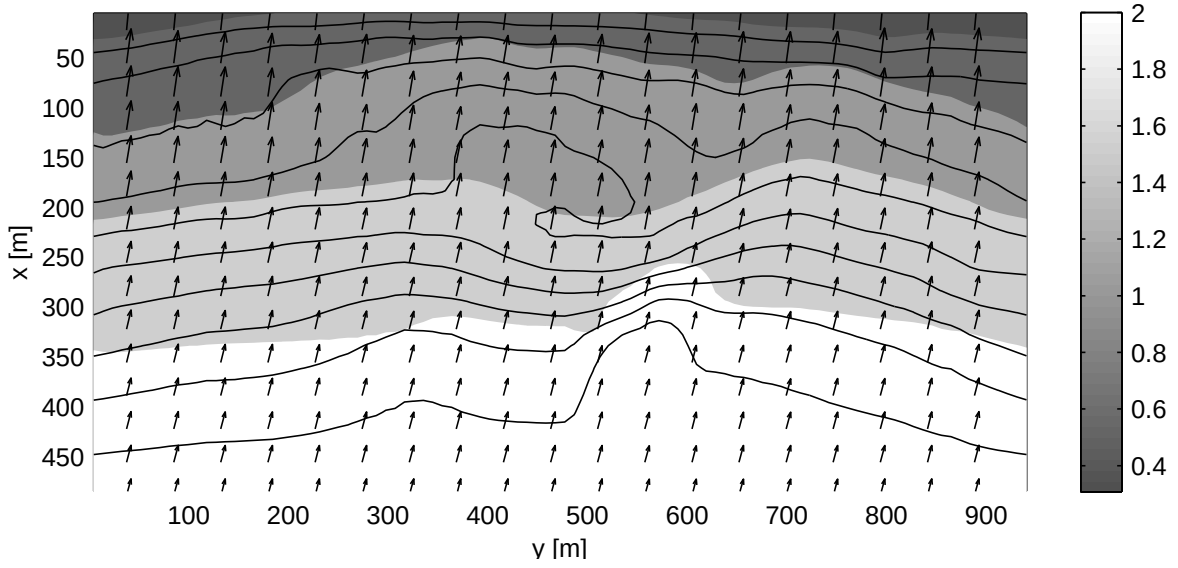

Figure 3.8: The Barrosa beach. Hydrodynamics. Oblique wave incidence. $H^0_{\mathrm{rms}} = 3$ m at the seaward boundary. Wave height H_{rms} in metres (contour plot) and wave vectors.

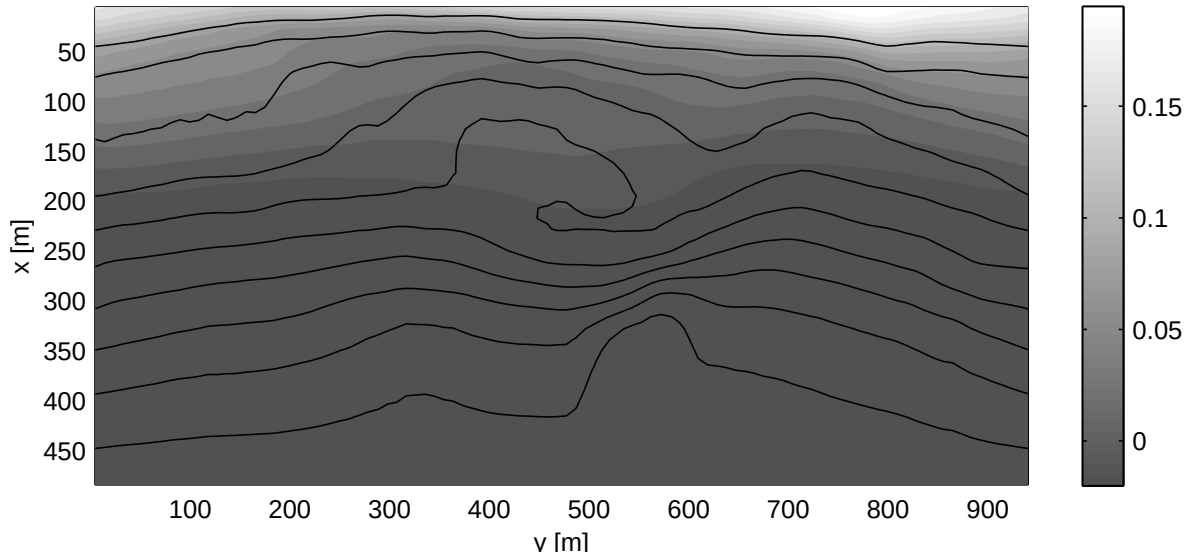

Figure 3.9: The Barrosa beach. Hydrodynamics. Oblique wave incidence. $H^0_{\mathrm{rms}} = 1.5$ m at the seaward boundary. Mean sea level z_{s} in metres (contour plot).

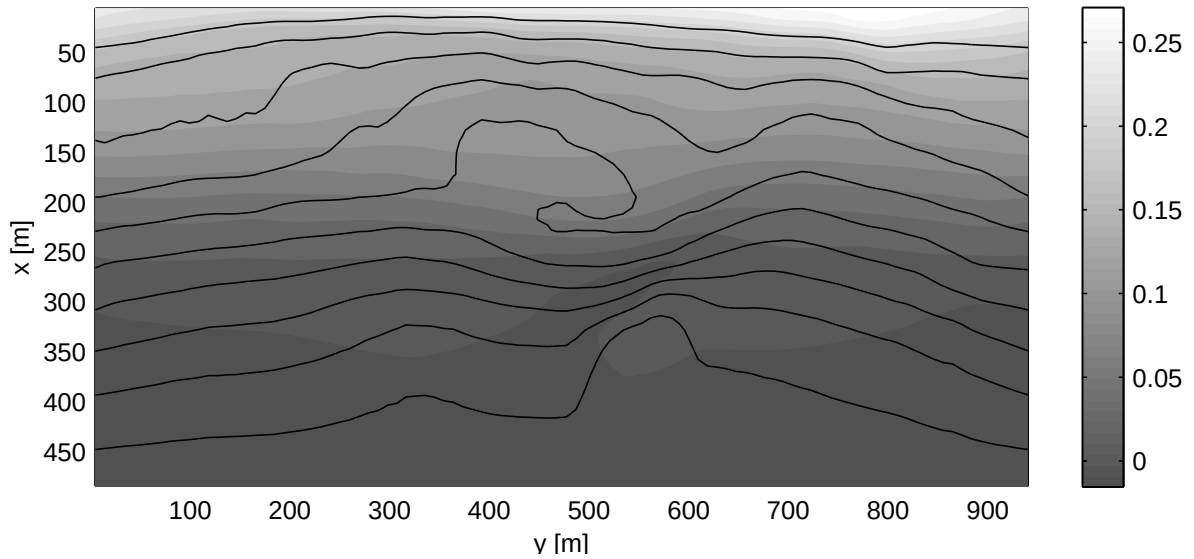

Figure 3.10: The Barrosa beach. Hydrodynamics. Oblique wave incidence. $H^0_{\mathrm{rms}} = 3$ m at the seaward boundary. Mean sea level z_{s} in metres (contour plot).

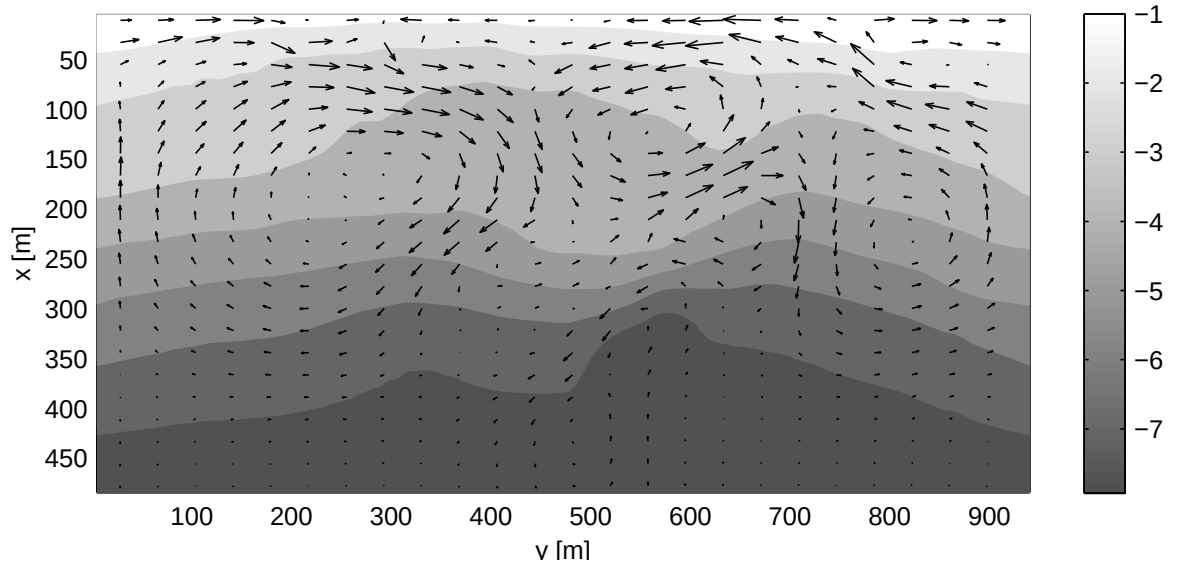

Figure 3.11: The Barrosa beach. Hydrodynamics. Normal wave incidence. $H^0_{\mathrm{rms}} = 1.5$ m at the seaward boundary. Bathymetry z_{b} in metres (contour plot) and current vectors. Maximum current magnitude: 0.5 $\mathrm{m\,s^{-1}}$.

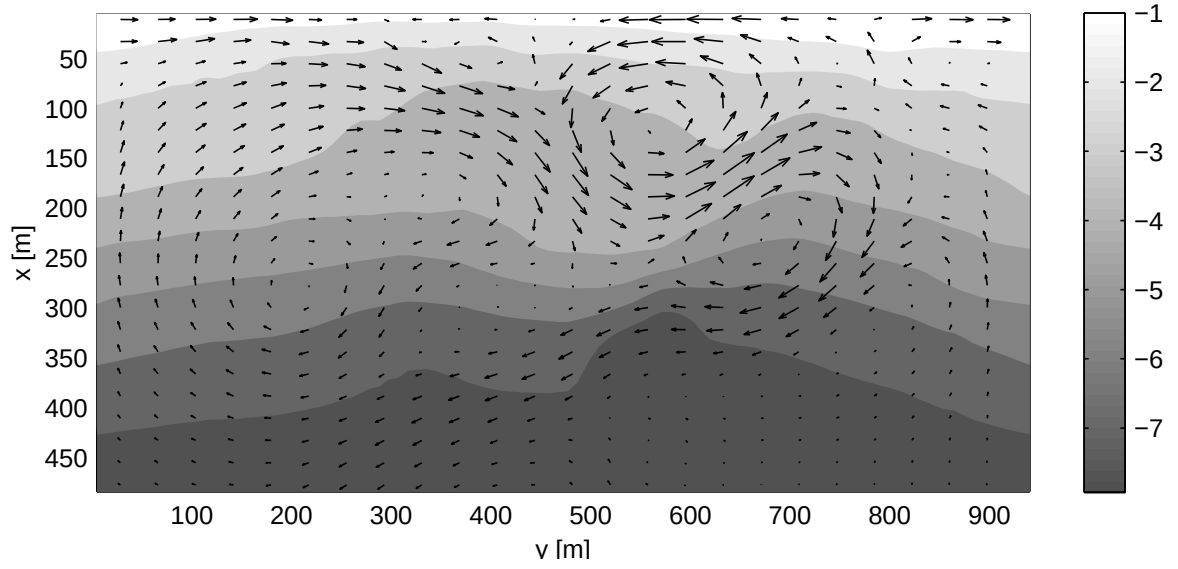

Figure 3.12: The Barrosa beach. Hydrodynamics. Normal wave incidence. $H^0_{\mathrm{rms}} = 3$ m at the seaward boundary. Bathymetry z_{b} in metres (contour plot) and current vectors. Maximum current magnitude: 1.1 $\mathrm{m\,s^{-1}}$.

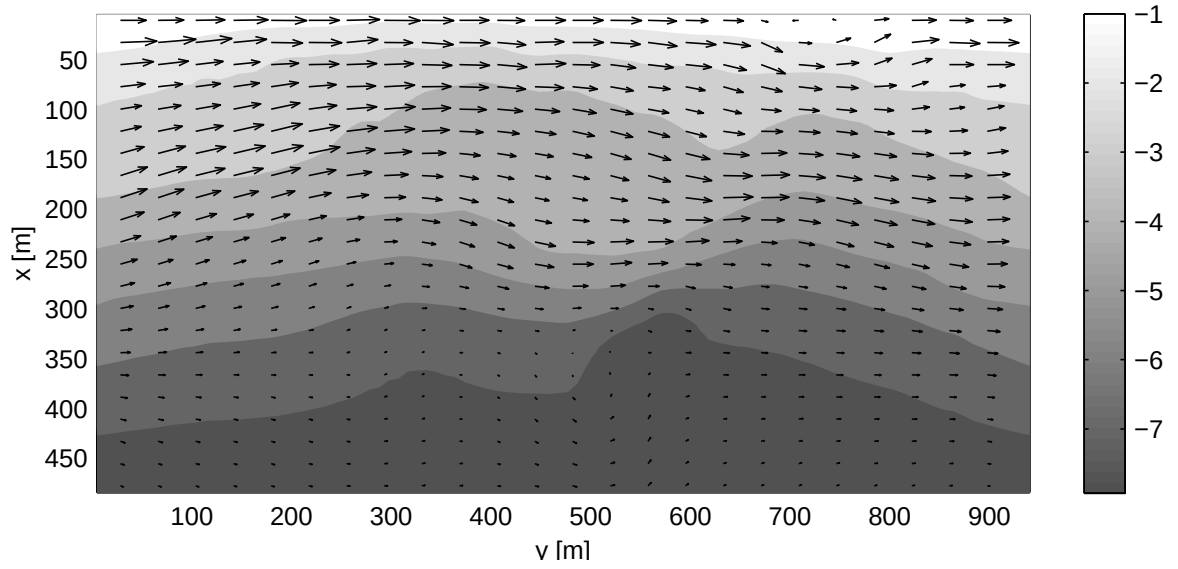

Figure 3.13: The Barrosa beach. Hydrodynamics. Oblique wave incidence. $H^0_{\mathrm{rms}} = 1.5$ m at the seaward boundary. Bathymetry z_{b} in metres (contour plot) and current vectors. Maximum current magnitude: 0.6 $\mathrm{m\,s^{-1}}$.

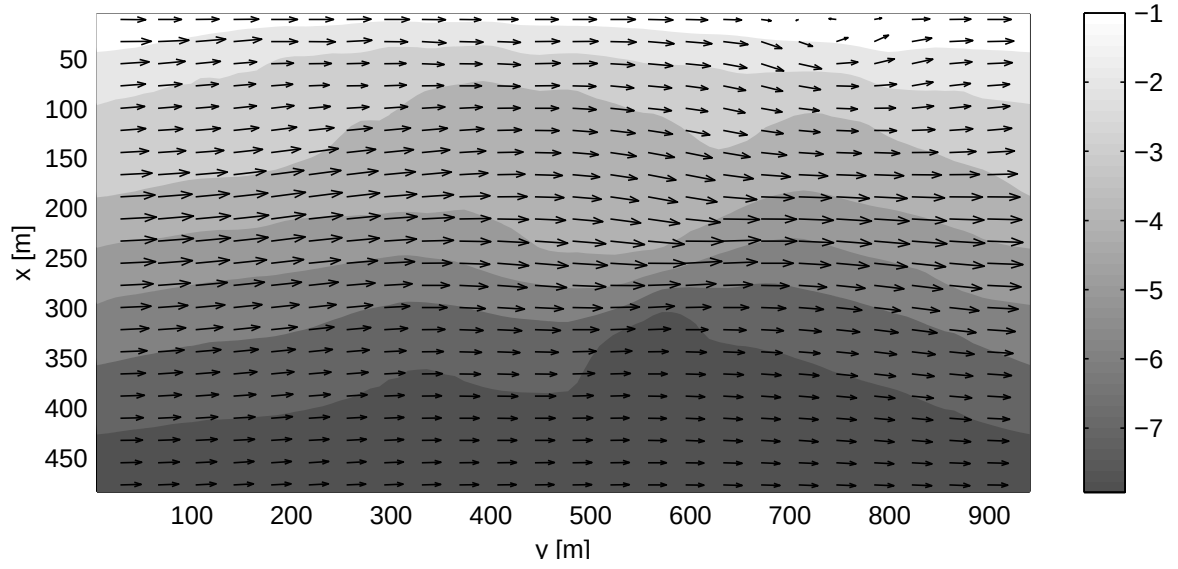

Figure 3.14: The Barrosa beach. Hydrodynamics. Oblique wave incidence. $H^0_{\mathrm{rms}} = 3$ m at the seaward boundary. Bathymetry z_{b} in metres (contour plot) and current vectors. Maximum current magnitude: 1.1 $\mathrm{m\,s^{-1}}$.

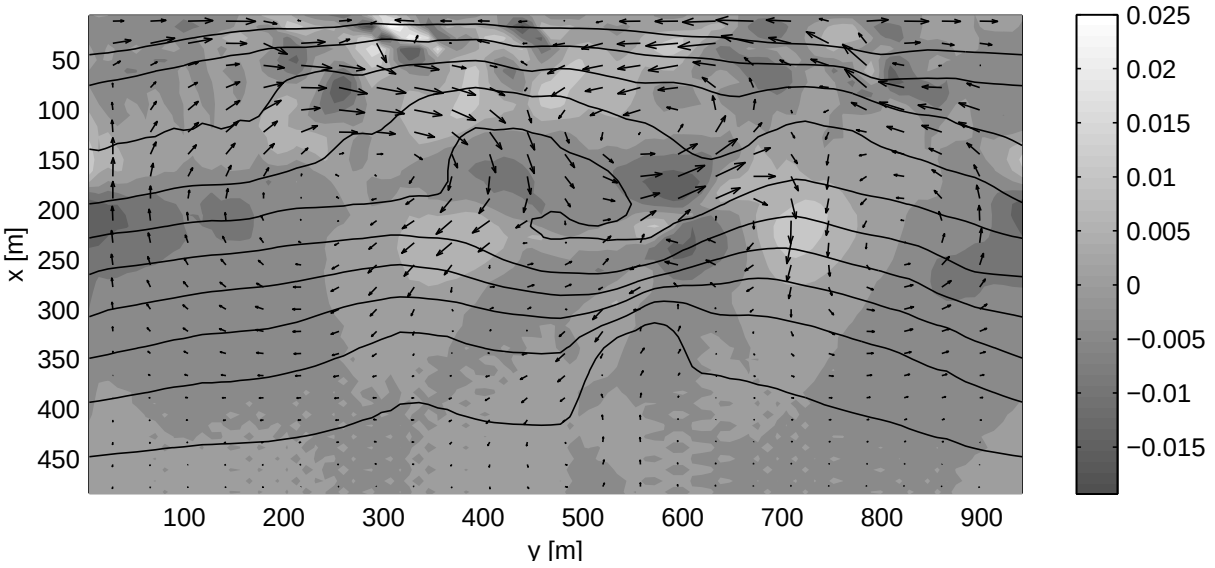

Figure 3.15: The Barrosa beach. Morphodynamics, hour 2.5. Normal wave incidence. $H^0_{\text{rms}} = 1.5$ m at the seaward boundary. Bottom perturbation h in metres (contour plot) and current vectors. Maximum current magnitude: $0.5\,\text{m}\,\text{s}^{-1}$.

properly formulated in the sediment flux formula (section 2.5.6).

In the case of normal wave incidence, the model crashes after 2.5 hours for 1.5 m waves whereas, for 3 m waves, it crashes after 8 hours (figure 3.15 and 3.16). More wave dissipation occurs for bigger waves: this seems to have a damping effect which slows down the growth of small scale instabilities. In both cases, the morphological patterns are similar, we will focus mainly on the 3 m wave case because it allows more evolution of the bed: the difference between the initial and the final topographic level is up to 20 cm for 3 m waves. Looking at the top view of the bottom perturbation (figure 3.16) and the 3D view of the total bathymetry (figure 3.17), three kind of patterns emerge. (1) Some topographic instabilities emerge near the coastline at $y = 350$ m. As the longshore section shows, in the first plot of figure 3.18, these instabilities could be bars but their wave length is very close to the grid size. Thus, they could be numerical instabilities. (2) A transverse bar, which is attached to the coastline, emerges at $y = 600$ m with a characteristic width of 150 m. It is somewhat down current oriented because of the current direction form right to left at this point. Its cross-shore span is about 100 m. (3) Finally, the terrace tends to be damped, as shown in the last plot of figure 3.18.

In the case of oblique wave incidence, the strong longshore current plays a diffuse role so as to allow the evolution to persist for 5 hours in the case of 1.5 m wave height and 25 hours in the case of 3 m wave height (figures 3.19 and 3.20). In the latter case the bottom level varies by up to 40 cm. As in the normal wave incidence case , three different discernible behaviours appear at similar positions (figures 3.19 and 3.20): (1) A down current bar system (three bars) emerges at $y = 400$ m near the coastline. Their wave length is about 80 m as the first plot of figure 3.22 shows. (2) The transverse bar somewhat up current for normal waves is now down current. In its trough, numerical instabilities develop. (3) The terrace tends to be damped and the trough tends to fill.

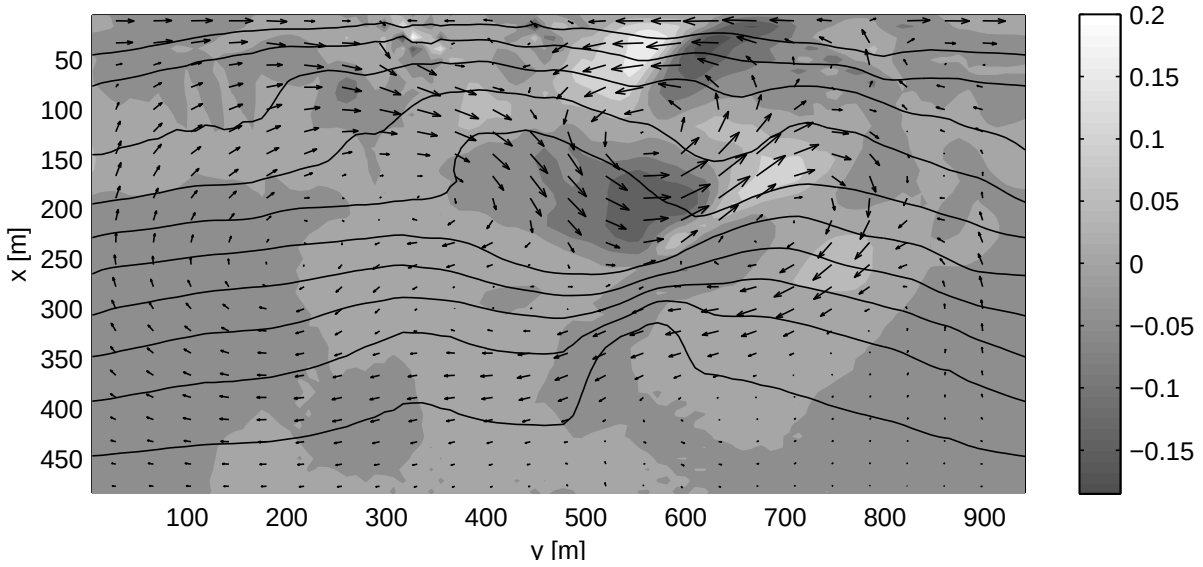

Figure 3.16: The Barrosa beach. Morphodynamics, hour 8. Normal wave incidence. $H^0_{\rm rms} = 3$ m at the seaward boundary. Bottom perturbation h in metres (contour plot) and current vectors. Maximum current magnitude: 1.1 m s^{-1}.

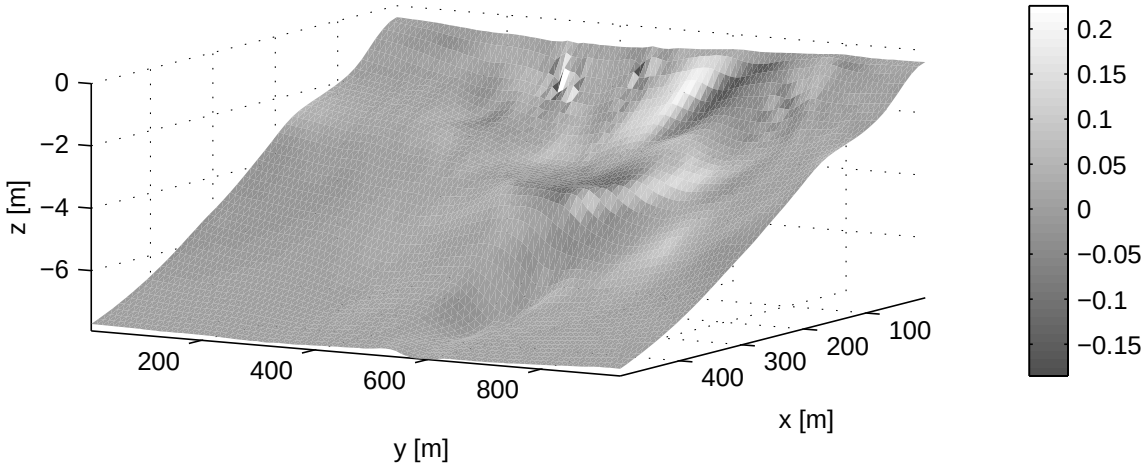

Figure 3.17: The Barrosa beach. Morphodynamics, hour 8. Normal wave incidence. $H^0_{\rm rms} = 3$ m at the seaward boundary. Total bathymetry and bottom perturbation h in metres (colours).

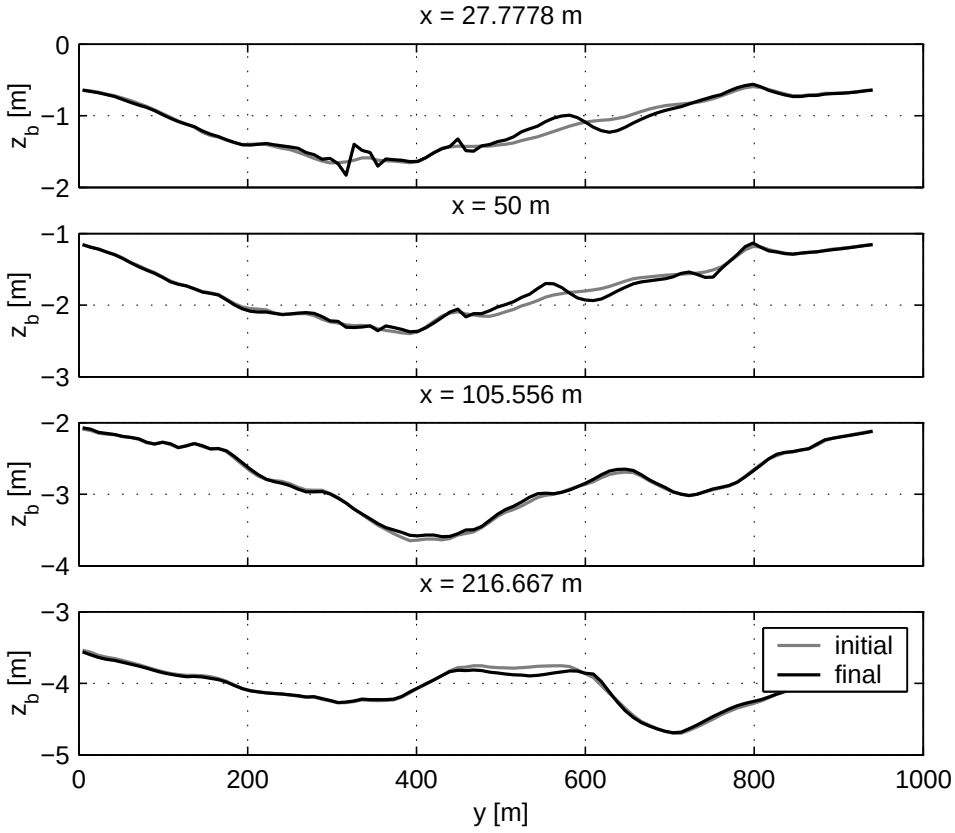

Figure 3.18: The Barrosa beach. Morphodynamics, hour 8. Normal wave incidence. $H^0_{\rm rms} = 3$ m at the seaward boundary. Cross-shore sections of the bathymetry.

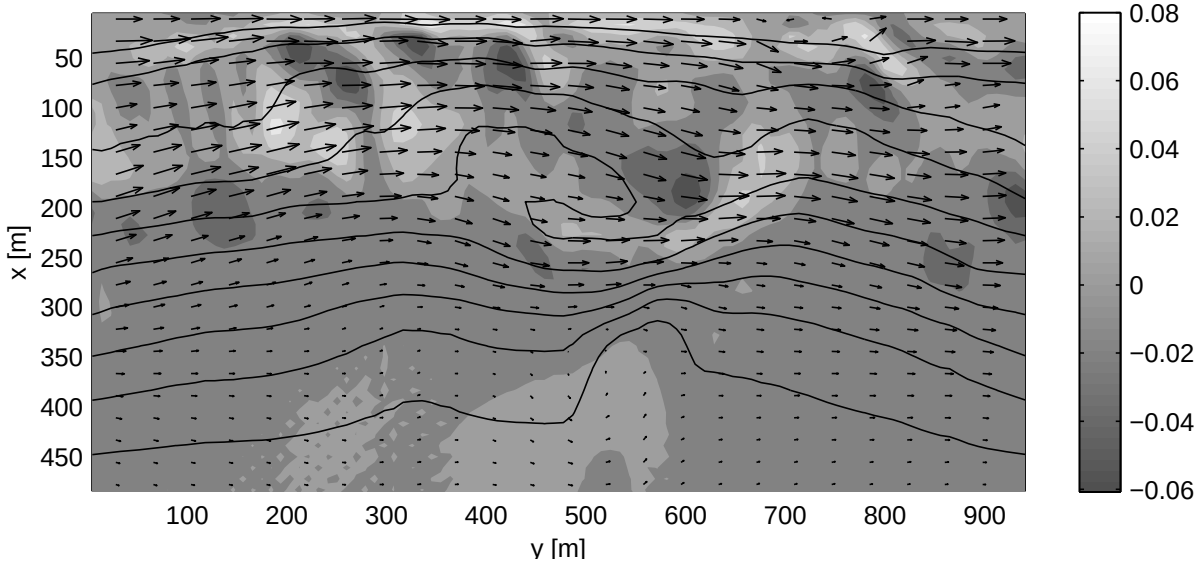

Figure 3.19: The Barrosa beach. Morphodynamics, hour 5. Oblique wave incidence. $H^0_{\rm rms} = 1.5$ m at the seaward boundary. Bottom perturbation h in metres (contour plot) and current vectors. Maximum current magnitude: 0.6 $\mathrm{m\,s^{-1}}$.

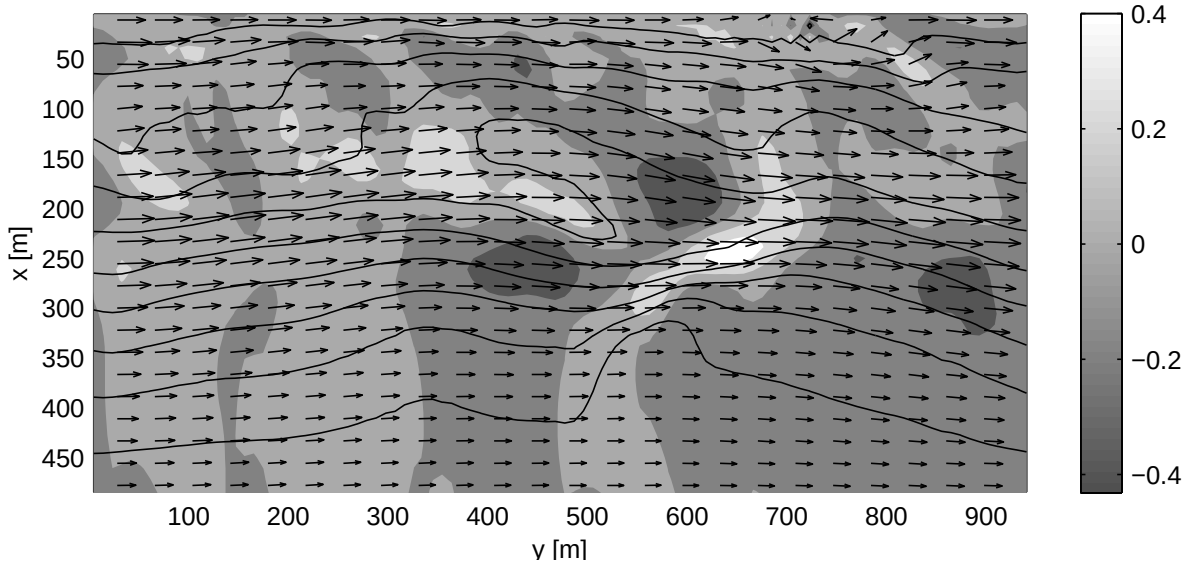

Figure 3.20: The Barrosa beach. Morphodynamics, hour 25. Oblique wave incidence. $H^0_{\rm rms} = 3$ m at the seaward boundary. Bottom perturbation h in metres (contour plot) and current vectors. Maximum current magnitude: 1.3 $\mathrm{m\,s^{-1}}$.

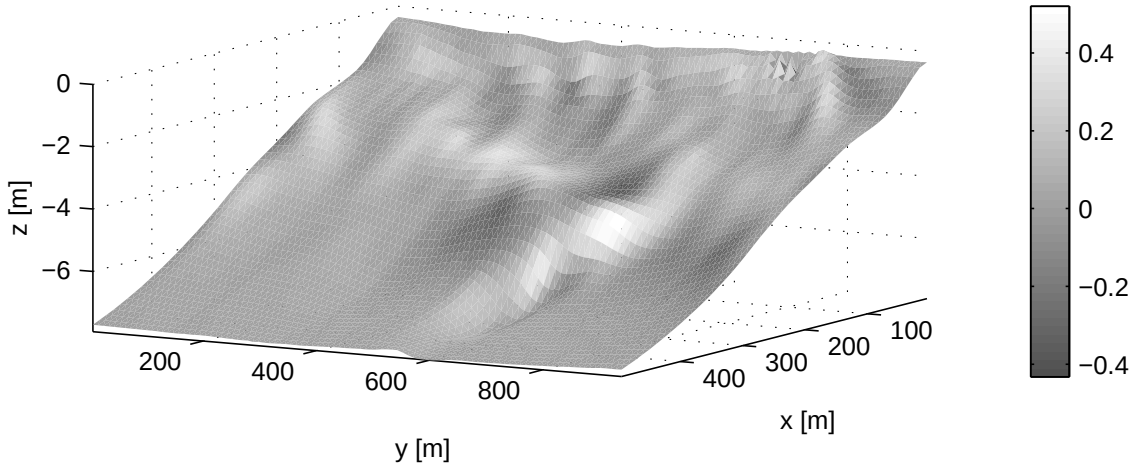

Figure 3.21: The Barrosa beach. Morphodynamics, hour 8. Oblique wave incidence. $H^0_{\rm rms} = 3$ m at the seaward boundary. Total bathymetry and bottom perturbation h in metres (colours).

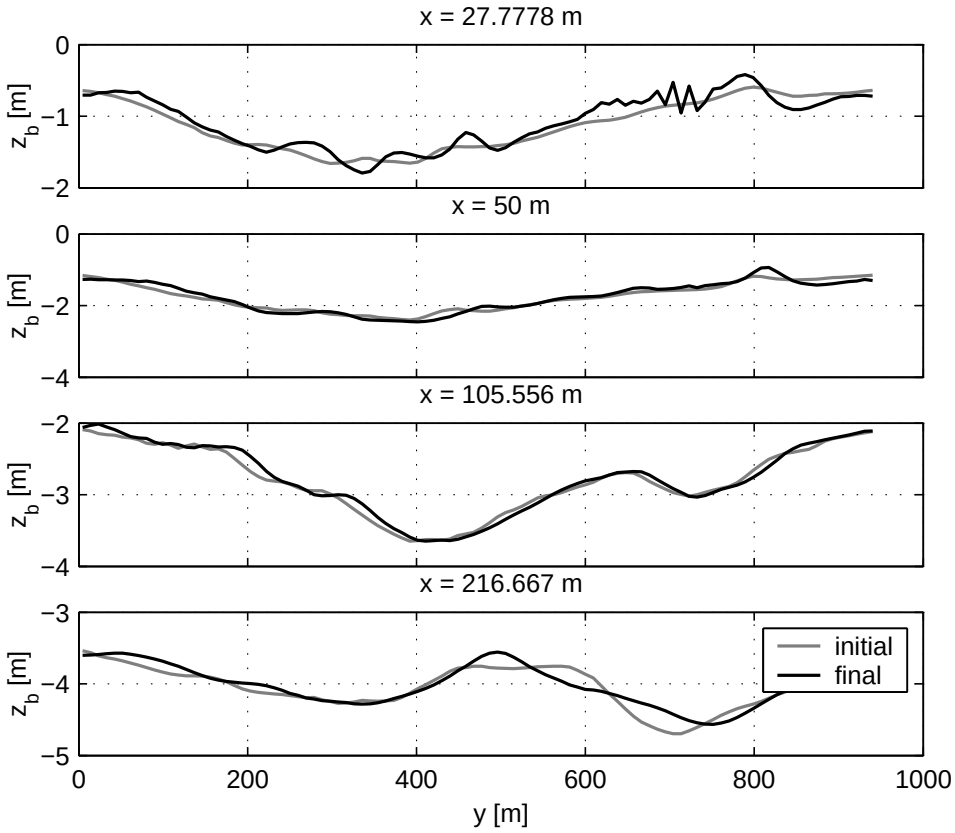

Figure 3.22: The Barrosa beach. Morphodynamics, hour 25. Oblique wave incidence. $H^0_{\mathrm{rms}} = 3$ m at the seaward boundary. Cross-shore sections of the bathymetry.

3.2.4 Conclusion

A detailed analysis of the morphological study of the Barrosa beach has been presented. The model inputs come from data from the year 2001. Particularly, the first part of this work has been to adapt the field data to the MORFO55. Firstly, the topographic data, from the month of June 2001 have been transformed in order to respect the rectangular grid and the periodic boundary conditions. The hypothesis made during the topographic transformation seem reasonable because of the shape of the Barrosa beach. Secondly, the wave input has been given through data from the year 2001 at 2000 m off-shore. It has been transformed by up to 500 m by the mean of the MORFO60 model. Among the most recurrent conditions, we have selected the most energetic ones according to distinct criteria. Two cases of oblique waves have been chosen, they have been previously done for normal wave incidence.

By fixing the topography, a complex hydrodynamical equilibrium state is reached in each case, but by coupling the bed evolution equation, the model crashes after some time, probably due to the complex sediment transport formulation of Bailard (1981) (see chapter 2). We obtain the longest and biggest evolution in the case of high waves and oblique waves. Indeed, a strong wave breaking or a strong ambient longshore current plays a diffusive role so that the small scale instabilities are damped. Some interesting features have been observed close to the shore as the formation of oblique/transverse bars with the wave length of 80 m up to 150 m. We also observed the deformation of the terrace which tends to be damped.

Because of a lack of field data, neither the hydrodynamical state nor the morphological predictions have been validated. The three dimensional cross-shore processes such as undertow and wave asymmetry have been neglected, this would have probably caused discrepancies with observations. Furthermore, the off-shore sea level has been considered as fixed (from month-averaged values) whereas the tidal range in the Barrosa beach is about 2 m. The predicted morphology close to the shoreline could therefore be affected by the tide. Thus, the present model is maybe not the most realistic tool to predict accurate beach evolution, however, these experiments suggest its ability to describe rhythmic alongshore morphological instabilities.

3.3 Gully systems*

3.3.1 Introduction

Gullies are ephemeral streams that collect rain water excess generated over a catchment area. Gullies can be defined as open erosion channels at least 30 cm deep, which conduct ephemeral run-off and are frequently characterized by steep sidewalls. Gully heads are located along the cliff edge at similar length intervals, if the upstream conditions are uniform. One such site where these gully systems can be found is the Barrosa beach (see section 3.2, figure 3.1). At the Barrosa gullies occur at fairly regular intervals along the shore. The beach at the Barrosa also exhibits some quasi-rhythmic undulations alongshore. It has been speculated that there is a correspondence between the two, although this has yet to be established. Where beach undulations and gullies are in phase, then, at high tide and during storm conditions, where the water level reaches the cliff toe, the gully effectively extends a distance offshore. Although there is no direct evidence of sediment being supplied to the nearshore waters at the Barrosa by the gullies the existence of the beach undulations may imply a direct run-off onto the beach, and therefore a certain amount of sediment being supplied to the swash/surf zone at these locations.

Notice that no comparison between the gully systems and the study of the entire beach described in section 3.2 has been made because of the lack of data. Indeed, the existing 3D data used in section 3.2 do not allow to track down the gully system, because, (1) they are not extended enough to the shore, particularly they do not show the cliff, so the correlation beach channel with gully is difficult, (2) we dispose of only a few measurements which maybe do not correspond to the ephemeral presence of gullies.

The morphological behaviour of the surf zone extension of a highly idealised gully is first studied. The gully characteristics are taken from Dodd *et al.* (2007) and are based on observations at the Barrosa beach. Particularly some crescentic rhythmic patterns develop. This is a preliminary result of generation of instabilities. They are excited because of the longshore non-uniformity of the gully. These kind of instabilities will be described and understood in the next chapters. The last part of the gully study is dedicated to the morphological response of the beach after an import of sand supposed to have been deposited during a run-off event.

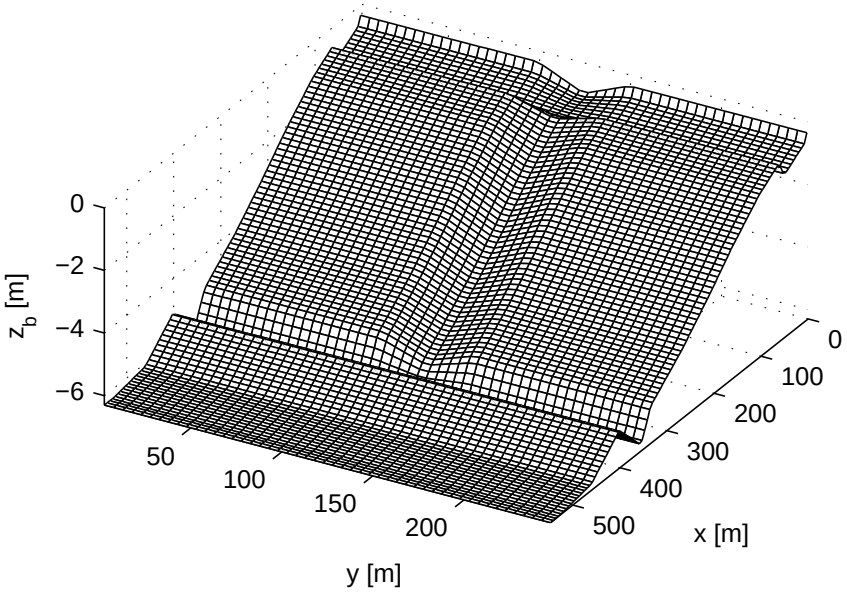

Figure 3.23: Gully systems. Initial bathymetry. The shoreline is at $x = 0$ m.

3.3.2 Modelling

The finite difference non-linear shallow water solver MORFO55 has been used to describe the long term morphological behaviour of the gully-beach-surf zone system. The initial topography is shown in Figure 3.23. The computational domain is 550 m cross-shore and 250 m longshore, with a grid spacing of 5×5 m^2. The time step used is 0.025 s for the hydrodynamics and 4 s for the morphodynamics. The default formulation and parameterization described in chapter 2 has been used. In particular, the Bailard formulation has not been selected. For numerical reasons, we preferred the Soulsby and Van Rijn formula.

Four wave conditions are considered: i) incident wave height of 0.9 m and period of 9 s for normal incidence; ii) a corresponding case for oblique wave incidence. These are denoted cases (a) and (c) respectively, and correspond to a calm swell. iii) and iv): 1.5 m wave height and 6 s period wave for normal and oblique incidence, corresponding to bigger, shorter waves (cases (b) and (d)). The heights and periods chosen here reflect average rather than storm related conditions, because we consider now morphodynamical evolution for all seas. Note that for oblique incidence, the angle at the off-shore boundary is $\theta = 17^{\circ}$ to the offshore normal. Note that all incident (offshore boundary) wave parameters are set by first selecting the four typical off-shore wave conditions from data from 2001, and then computing the corresponding wave conditions at $x = 550$ m using the (basic state part of the) linear model MORFO60 (see Calvete *et al.*, 2005), with

*This study has been made through the HUMOR European project for the Work Package 2. It is a part of the paper Dodd *et al.* (2007): Dodd, N., Stoker, A. M., Garnier, R., Vittori, G., De Los Santos, F., Brocchini, M., Soldini, L. & Losada, M. A. 2007 Use of numerical models to study land-based sedimentation and subsequent nearshore morphological evolution. *Coastal Eng.*. Submitted.

which we have driven the present simulations.

In the following the final state for each wave condition is described, then an analysis of the formation and evolution of bed-forms is presented for case (d), and finally the effect of a deposition of 700 m^3 of sediment from a storm is analysed for cases (b) and (d).

3.3.3 Results

3.3.3.1 Final states

For normal wave incidence, the final state is attained after 120 days; for oblique wave incidence this happens after 400 days. Most of changes appear after only about 10 days. Wave height and period have no influence on the general behaviour of the beach, steeper waves (1.5 m, 6 s) only implying higher and larger bedforms.

Figure 3.24 shows the final topography for each case. Two kinds of behaviour are observed. (1) For normal incidence and calm conditions (a), opposing behaviours can be seen in the cross-shore, shoreward of 100 m ($0 < x < 100$ m) and seaward of 100 m. In the nearshore part there is erosion in the gully channel and accretion on the sides of the gully, with the maximum erosion on the first longshore bar (at $x = 50$ m) and a maximum accretion just before the bar ($x < 50$ m). In the seaward part, there is an opposite effect. The velocity is more intense in the channel, where the current is onshore shoreward of the bar and offshore in lee of it, with a maximum intensity where there is deposition, between $x = 150$ m and $x = 250$ m. For (b) (steeper waves) all the same trends are observed, but the picture is purely depositional. It is not clear whether this depositional picture is physical; it may be due to the lack of cross-shore sediment transport processes in the model. (2) For oblique incidence ((c) and (d)), the maximum erosion and accretion is on the longshore bar ($x \approx 50$ m). The general behaviour is, however, different: there is accretion on the left side (up-current) of the gully and erosion in the channel, the gully becoming more down-current oriented. The longshore current is very low shoreward of the bar and strong seaward of it ($x > 50$ m). There is an onshore deflection in the deposition zone and an offshore deflection in the channel. Looking at the longitudinally averaged cross-shore profiles (Figure 3.25), the influence of the longshore bar at $x = 50$ m seems also important, and apparently provides a limit for the zone with the most accretion (shoreward of the bar) for normal incidence; for oblique incidence there is a general deposition zone on the bar and an erosion zone just shoreward. This figure also reveals a general accretion at the shore in all the cases, although in predictions at the shore the lack of a swash zone in the model must be borne in mind.

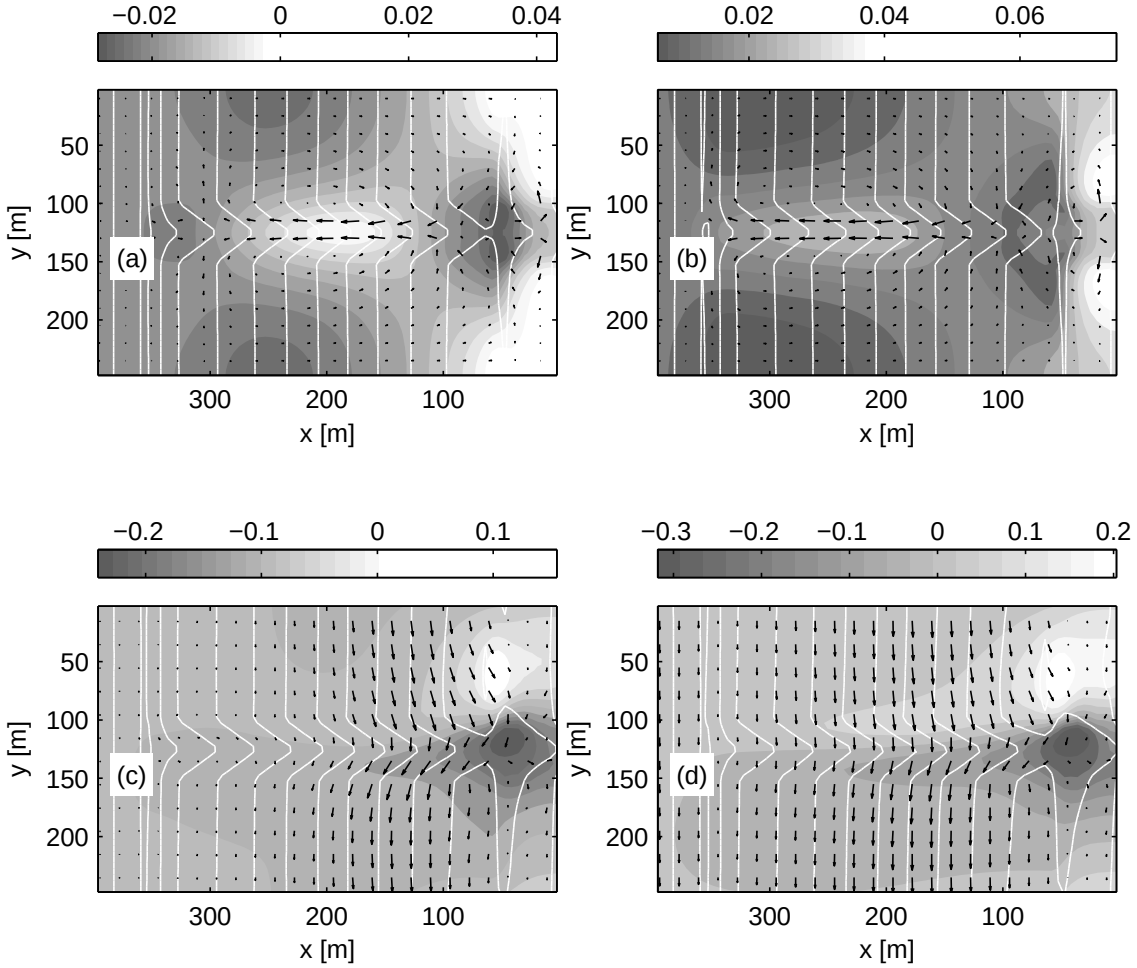

Figure 3.24: Gully systems. Final states for normal wave incidence ((a),(b)) and oblique wave incidence ((c),(d)). 0.9 m and 9 s waves ((a),(c)) or 1.5 m and 6 s waves ((b),(d)). The colormap represents h (in metres): the bottom perturbation with respect to the initial topography (shoals are white and troughs are shaded). White lines are the total topography contours. Arrows are the total current vectors. Maximum current magnitude: (a) $0.3\,\mathrm{m\,s^{-1}}$, (b) $0.3\,\mathrm{m\,s^{-1}}$, (c) $0.4\,\mathrm{m\,s^{-1}}$, (d) $0.5\,\mathrm{m\,s^{-1}}$.

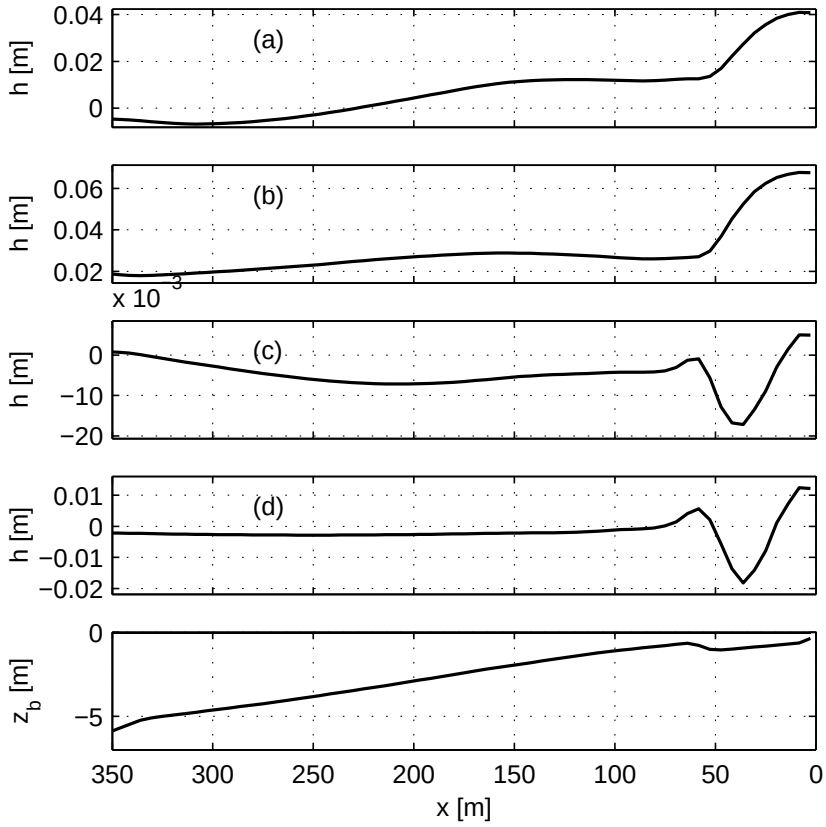

Figure 3.25: Gully systems. Longitudinally average cross-shore profiles of the bottom perturbation (h) in the cases (a),(b),(c) and(d) and of the total topography (z_b).

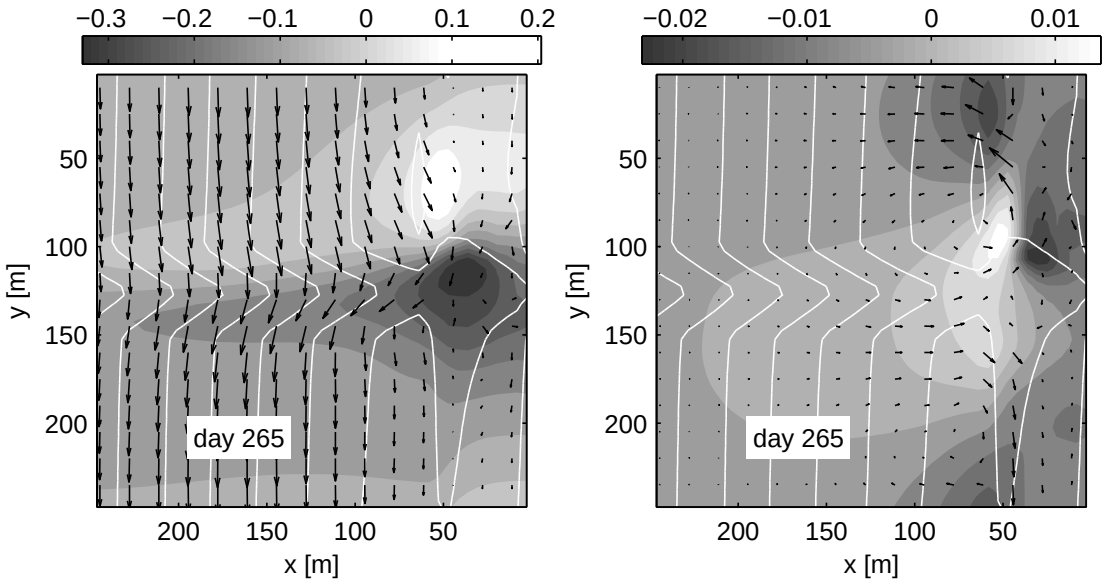

Figure 3.26: Gully systems. Left: Bottom perturbation h (in metres) at day 265 in the case (d). Right: Final topography subtracted with the total topography (in metres) at day 265.

3.3.3.2 Development of crescentic patterns

It is interesting to note that this longshore bar seems to be the reason for the development of crescentic patterns. The beach system has been excited by the alongshore non-uniformity of the gully and crescentic instabilities have been generated. Even though crescentic patterns are small in comparison with the bed-forms described above, they can be observed by subtracting the topography at the final state (when crescentic patterns have totally disappeared) with the topography at previous states. Figure 3.26 shows the total (left) and the subtracted (right) topography at day 265 in the case (d). The total and the subtracted current vectors, respectively, are also plotted. The total bed-forms have an amplitude of the order of 30 cm whereas the amplitude of crescentic bars are 2 cm. Note that the subtracted vectors are reminiscent of those seen in previous studies with the onshore flow over the shoal and the offshore flow in the troughs (see eg. Falqués *et al.*, 2000; Damgaard *et al.*, 2002). The crescentic spacing is 250 m and therefore coincides with the longshore size of the computational domain in this case. However, it is independent of the size: simulations in a bigger domain reveal an unchanged spacing. Figure 3.27 shows the subtracted topography and current vectors during 15 days of beach evolution: these crescentic bars migrate with the period of 30 days, giving the migration velocity of 8 m day^{-1}.

3.3.3.3 Sediment deposition due to run-off

A quantity of sand of about 700 m^3, supposed to have been deposited during a run-off event, is now added to the initial bathymetry, within the gully and touching the shore.

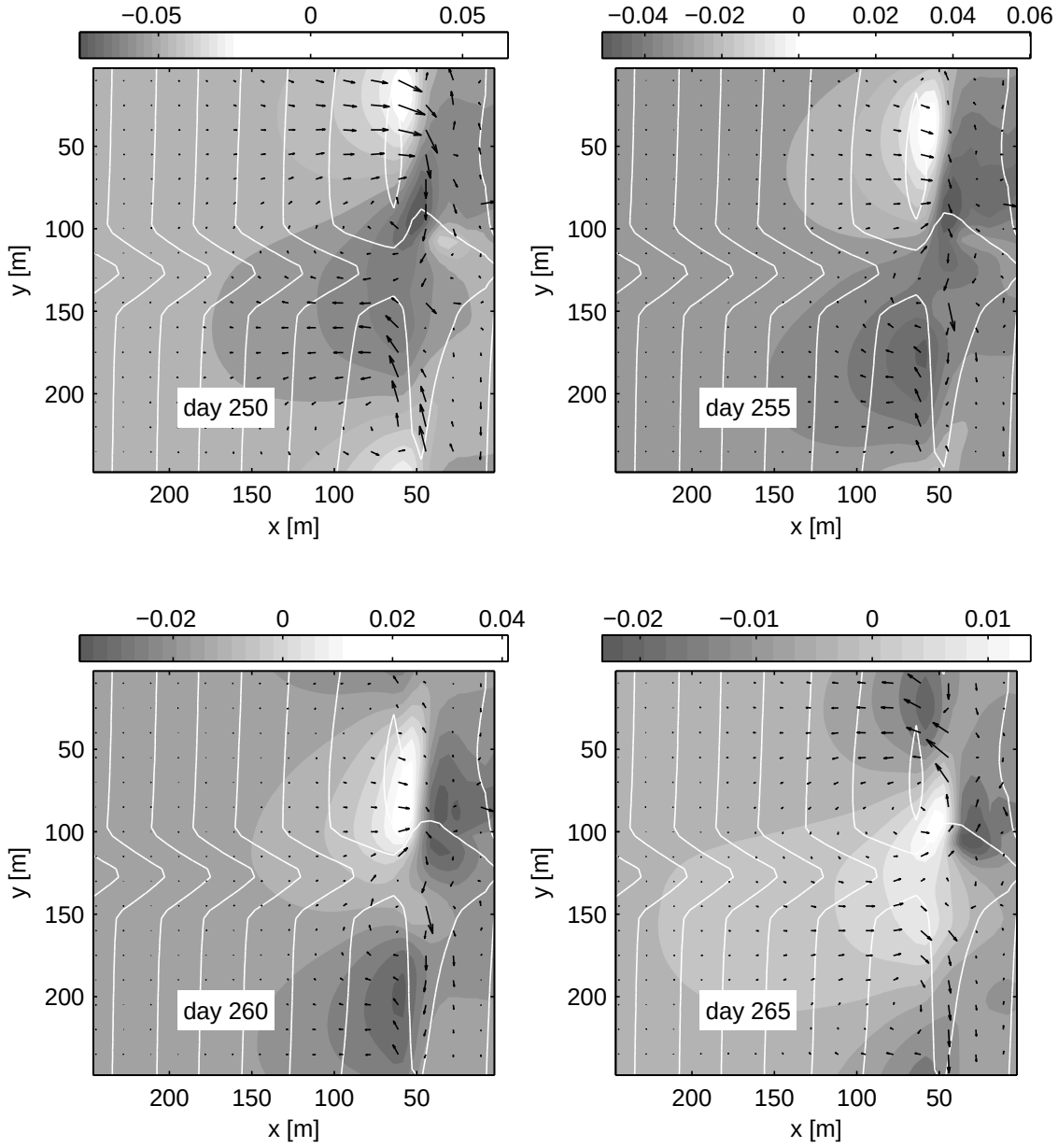

Figure 3.27: Gully systems. Migration of crescentic patterns during half a period. Bottom perturbation h (in metres)

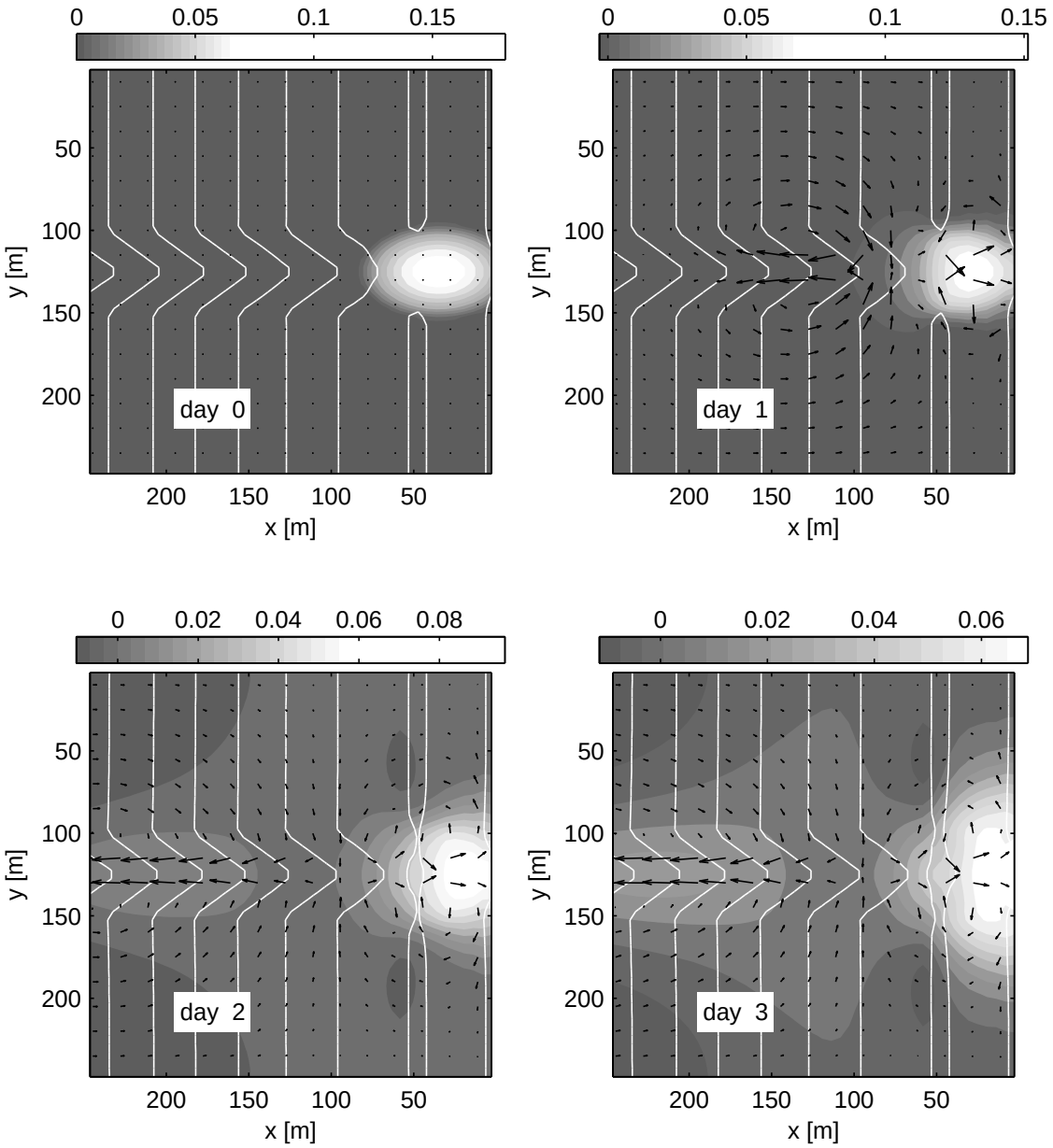

Figure 3.28: Gully systems. Initial evolution of the bottom perturbation h (in metres) including the sediment import during 4 days. Case (b).

The morphodynamical behaviour is studied in the case of storm waves (height 1.5 m and period 6 s), for both normal (b) and oblique (d) wave incidence. In both cases, the model predicts that this additional sediment has not effect on the final state. Figure 3.28 shows the initial diffusion of the shoal over 4 days. It starts from a maximum height of 20 cm and diminishes to 10 cm by day 4. The shoal diffuses primarily alongshore. At day 120. the average of the cross-shore profile reveals that the additional sediment has no effect; see figure 3.29 where dashed lines and straight lines correspond, respectively, to the case without and with the added sediment. Similarly, with oblique incident waves, the added sediment diffuses away very quickly (figure 3.30). Note that at day 2, it aligns with the crescentic bar, which begins to migrate. This, however, will have no effect on the final

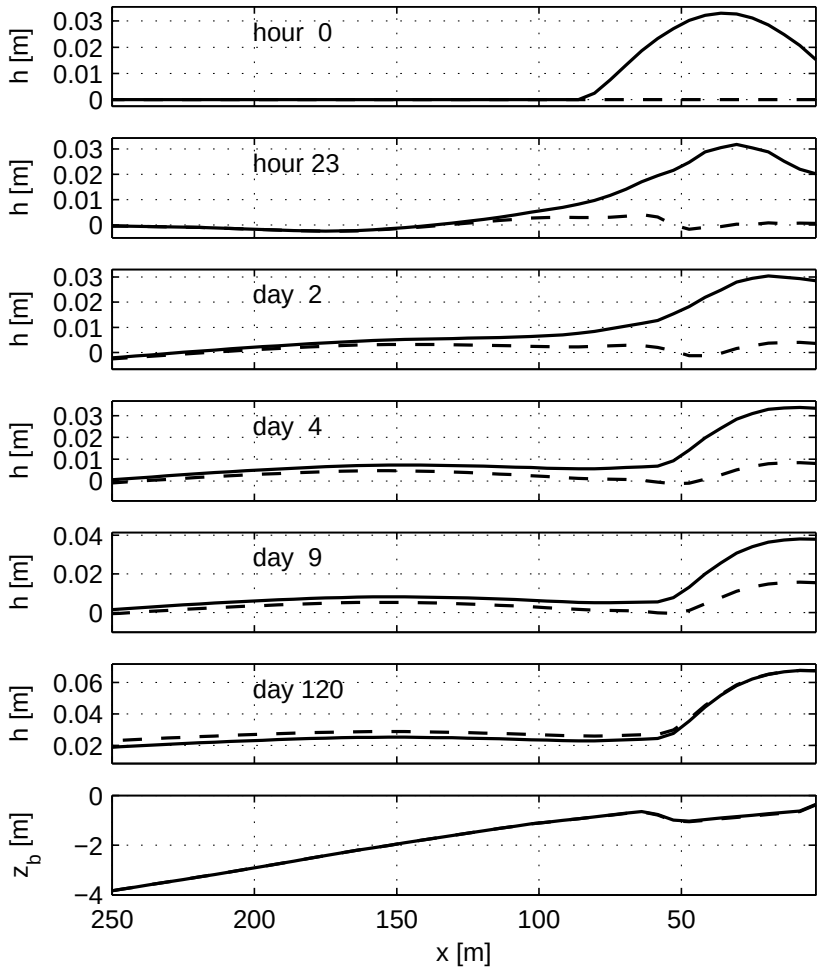

Figure 3.29: Gully systems. Longitudinally average cross-shore profiles of the bottom perturbation (h) including, or not, the sediment import (straight lines, or dashed lines, respectively) until the final state and of the initial total topography (z_b). Case (b).

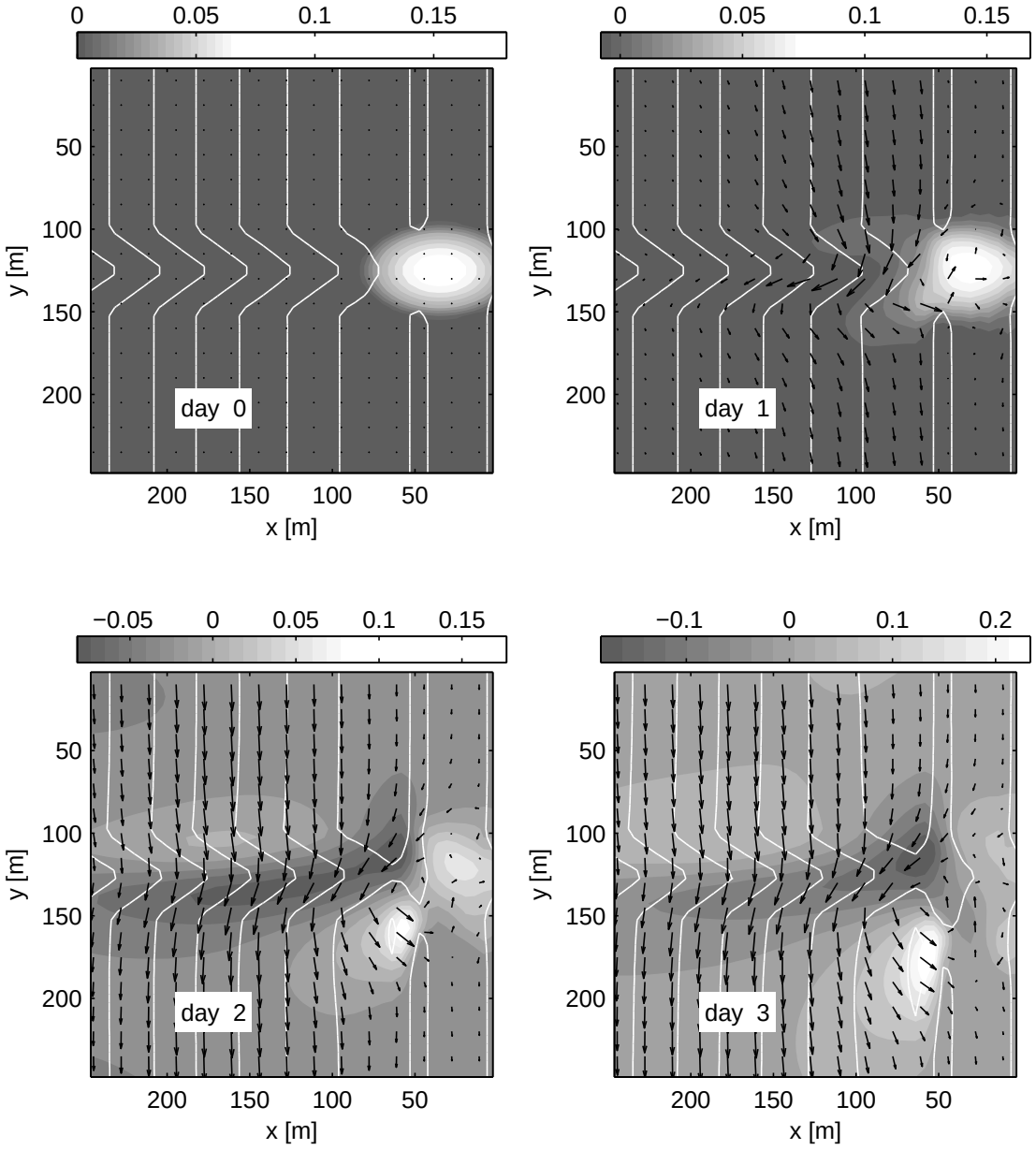

Figure 3.30: Gully systems. Initial evolution of the bottom perturbation h (in metres) including the sediment import during 4 days. Case (d).

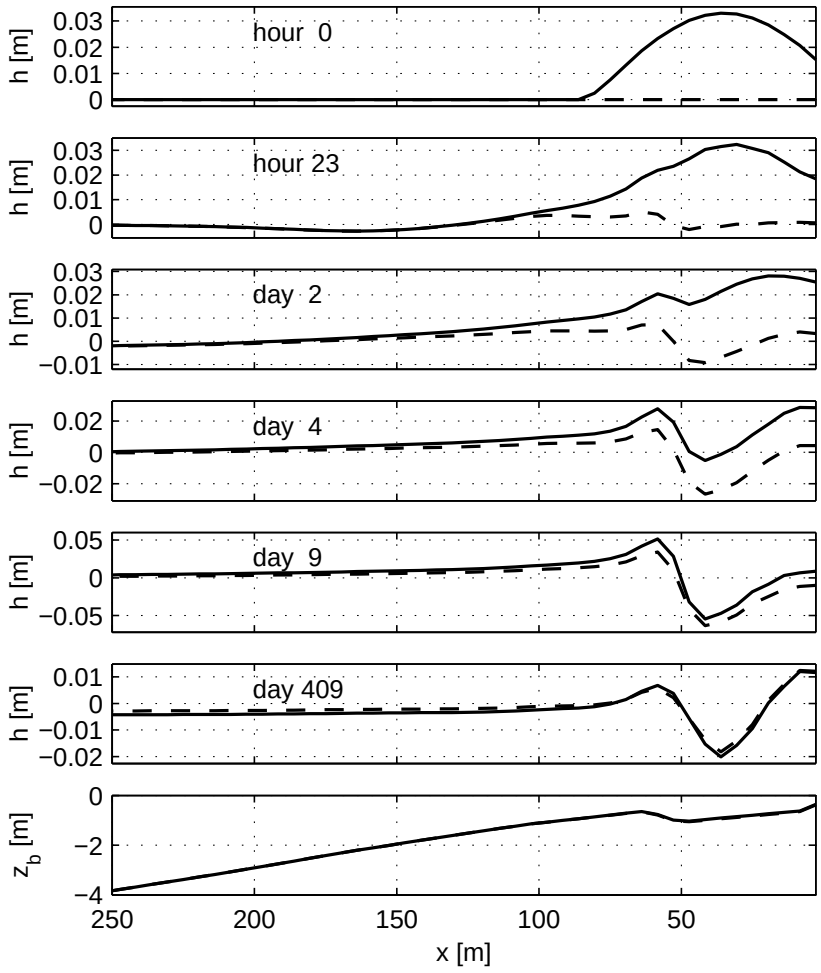

Figure 3.31: Gully systems. Longitudinally average cross-shore profiles of the bottom perturbation (h) including, or not, the sediment import (straight lines, or dashed lines, respectively) until the final state and of the initial total topography (z_b). Case (d).

states, and, even from day 9, the total topography (figure 3.31).

3.3.4 Conclusion

The long-term morphological behaviour of a gully system has been investigated. The Bailard formula (see chapter 2) used in the section 3.2 has been substituted by the Soulsby and Van Rijn formula (see chapter 2) in order to allow for a longer evolution. Indeed, whereas the model crashed after few hours of evolution by using the Bailard formula, a final equilibrium state is reached by using the Soulsby and Van Rijn formula. Two distinct behaviours are observed: (1) in the case of normal wave incidence, the inner part of the gully channel tends to become deeper whereas the opposite effect appear in the outer part of the gully channel ; (2) in the case of oblique wave incidence, the gully takes an oblique down current orientation. The global morphological impact of such a system is weak as we only observe a deformation of the initial gully. Moreover the maximum observed perturbation with respect to the initial state is only 30 cm, difference in bed level. Simulations of a sand import from a extreme run-off event (700 m^3) also show that the gully systems are not very affected as the imported amount of sand quickly laterally diffuses. A caveat that must be added is the lack of cross-shore transport. Indeed, additional sediment at the shoreline is likely to be taken offshore by the undertow thus contributing to a bar.

An interesting modelling finding has been the observation of development of crescentic features. Indeed, first because of the presence of a cross-shore irregularity on the initial topography which has the same effect as a longshore bar, and because of the alongshore non-uniformity due to the channel, instabilities have grown by the self-organization mechanism which will be describe in chapter 5.

3.4 Artificial shoal*

3.4.1 Introduction

A shoal in front of a sandy coastline disturbs the wave distribution in the surf zone and the wave set-up. In case of shore-normal wave incidence, a circulation is created and in case of oblique incidence, the longshore current is disturbed. All these effects influence the sediment transport and produce patterns of erosion/deposition. When these patterns reinforce the shoal itself, this can be the cause of the formation of complex alongshore non-uniform topography. More importantly, artificial shoals have been used for beach protection and beach nourishment (Kroon *et al.*, 1994; DHI, 2004). The perturbed hydrodynamics and how the bathymetry evolves becomes therefore crucial in order to assess the efficiency of the nourishment.

A suitable tool in order to investigate the evolution of the artificial shoal are the large 2DH morphodynamical models (MIKE21-CAMS, or Delft3D (Klein, 2006)). However, given the complexity of such models, a more idealised model like MORFO55 is worth using as a complementary tool. It is suitable to analyse the main processes under a good control and without unnecessary complications.

Here we apply the MORFO55 model to look at the effect of a shoal in front of the coast on the waves and the currents. The short term morphological evolution is also investigated.

3.4.2 Modelling

We have considered a stretch of rectilinear coastline of 300 m. The model domain is a rectangle of 400 m cross-shore 300 m longshore and (figure 3.32, left). The mesh spacing is $\Delta x = 5$ m, $\Delta y = 4$ m. The time step used is 0.01 s for the hydrodynamics and has been accelerated by a factor 10 for the morphodynamics. A bar-shaped shoal has been superimposed on the alongshore uniform topography (figure 3.32, right) at a water depth of 3 m. The shoal has a maximum relief of 0.5 m and its alongshore length is about 100 m. The waves are of $H^0_{\rm rms} = 1$ and 1.5 m and $T = 8$ and 12 s. The wave angle is 0 and 17 °.

The default formulation/parameterization described in chapter 2 has been used except for the sediment transport where the Bailard formulation is chosen, neglecting the undertow and wave asymmetry effects for numerical reasons. The wave refraction by the

*This study has been made through the HUMOR European project (Human Interaction with Large Scale Coastal Morphological Evolution). It has been published in a technical report Garnier *et al.* (2004): Garnier, R., Falqués, A. & Caballeria, M. 2004 Analysis of the evolution of the shoreline in case of an artificial shoal/pool. *Tech. Rep.*. HUMOR project, Grup de Morfodinàmica de Costes, Appl. Physics Dept., Univ. Politècnica de Catalunya, Barcelona, Spain, work package 4, Coupling between nearshore bedforms and shoreline evolution in unbounded coasts. Task M4.3.3.

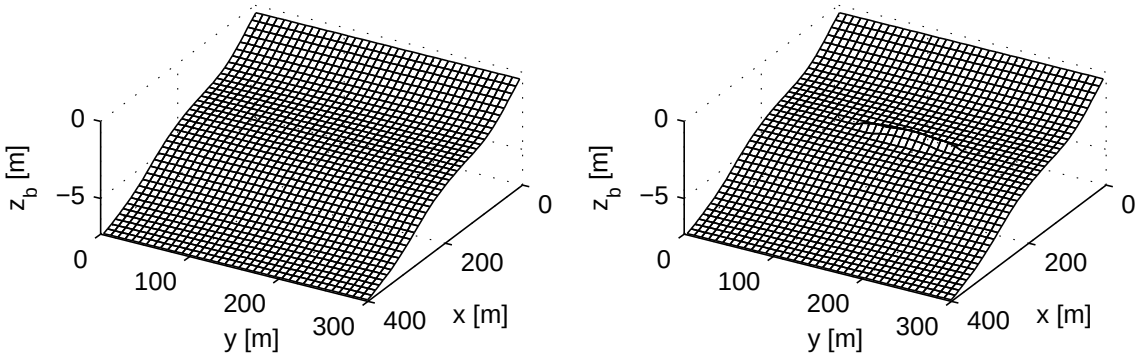

Figure 3.32: Artificial shoal. Left: ambient bathymetry without the shoal. Right: Initial bathymetry with the shoal.

runs	H^0_{rms} [m]	T [s]	θ^0 [deg]	bathymetry
1	1	8	17 and 0	with shoal
2	1.5	12	17 and 0	with shoal
3	1	8	17 and 0	with shoal
4	1.5	12	17 and 0	with shoal
4_0	1.5	12	17 and 0	without shoal

Table 3.2: Artificial shoal. Set up of the numerical experiments

shoal and by the developing topography is not accounted for.

3.4.3 Results

Here we will focus mainly on runs 4 and 4_0. Results in cases 1, 2 and 3 are qualitatively similar to 4. We will first focus on the steady hydrodynamics and then we will show the bathymetric evolution during 8.5 hours.

3.4.3.1 Hydrodynamics

Figure 3.33 shows the flow arrows for test 4 in case of normal incidence. The most striking feature is a couple of vortices at the edges of the shoal. The intensity of the flow in these vortices is not symmetric in the cross-shore direction, the strongest currents occurring shoreward of the shoal. There is onshore current over the shoal, and return flow at the sides. Interestingly, two secondary vortices which are opposite to the main ones appear shoreward of them. The details of the hydrodynamics are shown in figure 3.34. The reduction in wave height shoreward of the shoal can be seen. Also, the quadruplet of vortices becomes nicely apparent.

The cross-shore profile of wave height is shown in figure 3.35. It can be seen that the

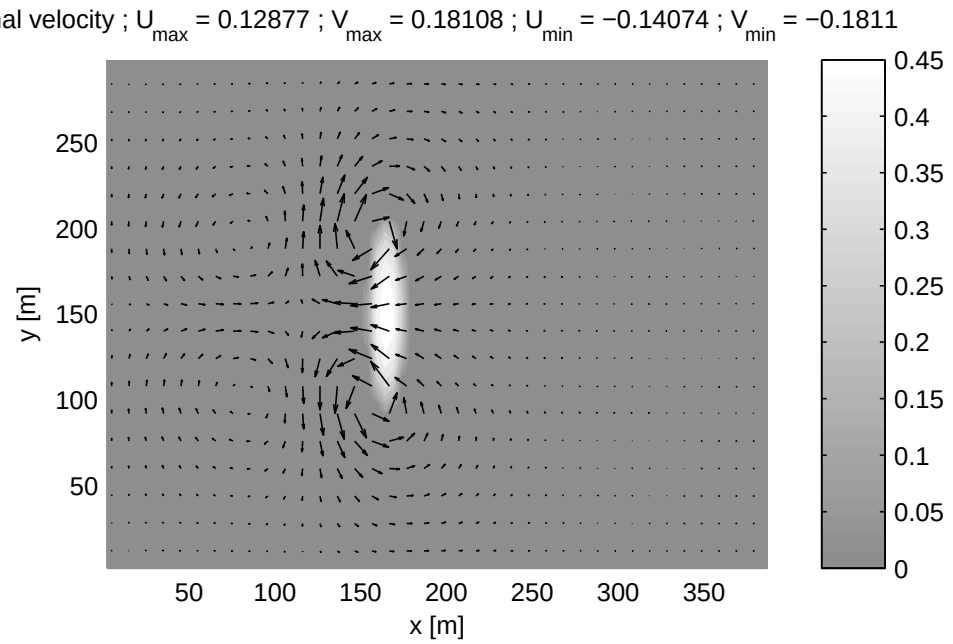

Figure 3.33: Artificial shoal. Flow pattern for test 4, in case of shore-normal wave incidence. The coastline is the y axis, on the left. The cross-shore direction is the x axis. The waves come from the right. The colormap represents h (in metres): the bottom perturbation with respect to the equilibrium topography (without shoal). Arrows are the total current vectors. Maximum cross-shore velocity: 0.14 $\mathrm{m\,s^{-1}}$, maximum longshore velocity: 0.18 $\mathrm{m\,s^{-1}}$.

waves of 1 m start to break about the cross-shore position of the shoal while the waves of 1.5 m already are breaking offshore of this position. The shoaling becomes also apparent, specially in case of $T = 12$ s. The most steep waves (test 3) do not almost shoal. The shoal produces a reduction in wave height, specially for the higher waves and an increase in shoaling specially for the longest waves (test 2).

The current in case of oblique wave incidence ($\theta = 17\,^{\circ}$) is shown in figure 3.36. This plot does not show too much since the maximum longshore current is 0.48 $\mathrm{m\,s^{-1}}$ while the maximum cross-shore deflection is only 0.06 $\mathrm{m\,s^{-1}}$. The waves shadow produced by the shoal can be appreciated in figure 3.37. A very interesting feature is an offshore veering of the current at the up-wave edge of the shoal and an onshore veering at the lee. Again, the opposite effect (but weaker) can be found shoreward on the shoal. It is also noticeable how the longshore current intensifies on top of the shoal and slightly onshore of the lee of it. Intriguingly, there is also an intensification of the longshore current shoreward of the shoal, very close to the coast. In contrast, just shoreward of the shoal the current slow down. Figure 3.38 also shows the behaviour of the longshore current just described.

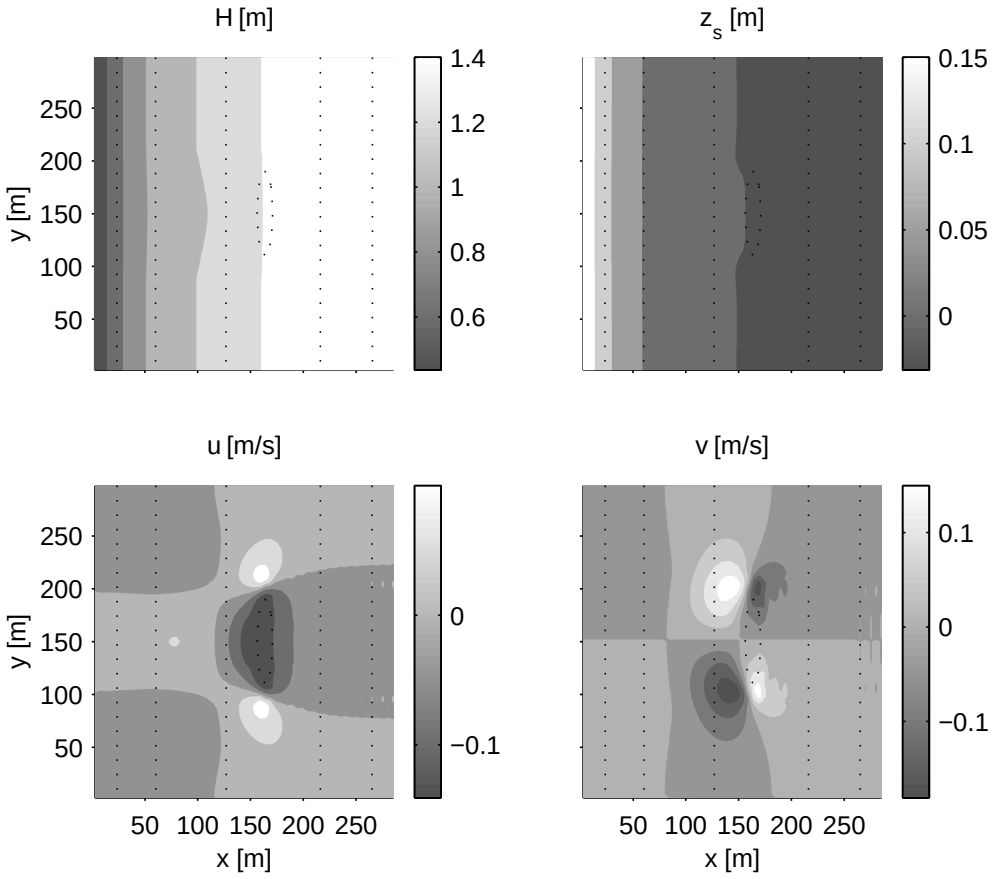

Figure 3.34: Artificial shoal. Details of the hydrodynamics for run 4, normal wave incidence. The colours represent: the wave height H_{rms} (top left), the free surface elevation z_{s} (top right), the cross-shore u and the longshore v current components (bottom, left and right, respectively).

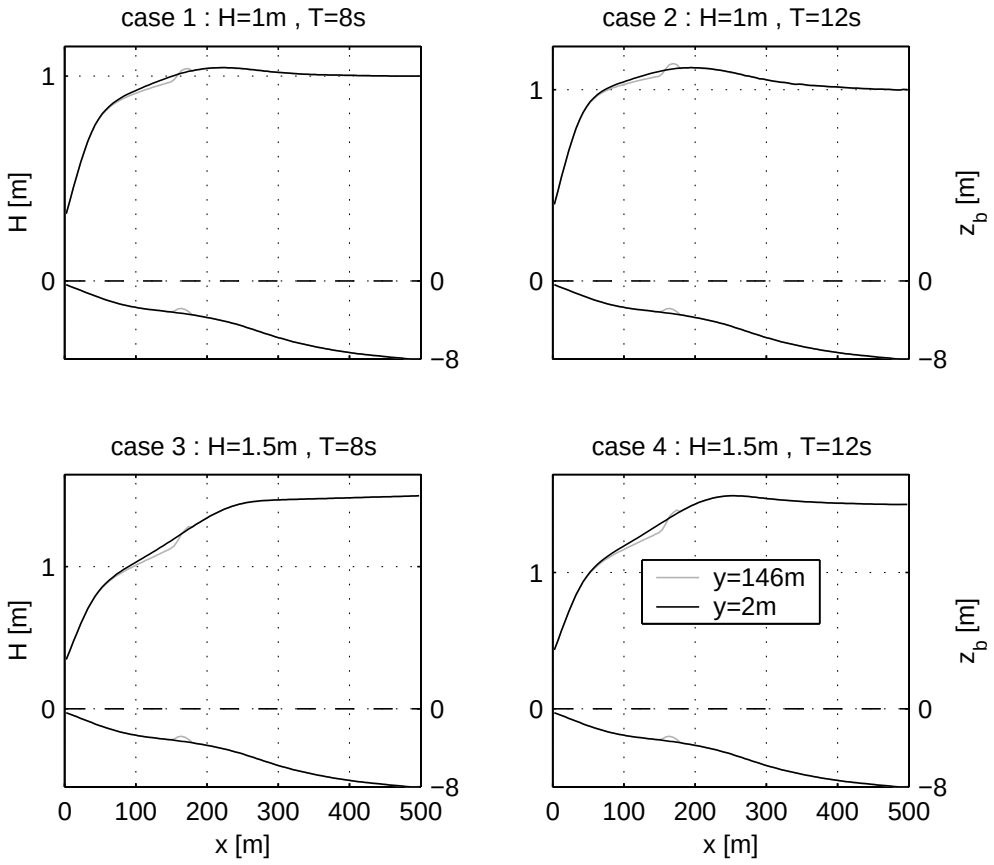

Figure 3.35: Artificial shoal. Cross-shore profile of wave height for run 1 (top left), run 2 (top right), run 3 (bottom left) and run 4 (bottom right). Grey line: cross-shore section crossing the shoal, black line: lateral cross-shore section far from the shoal.

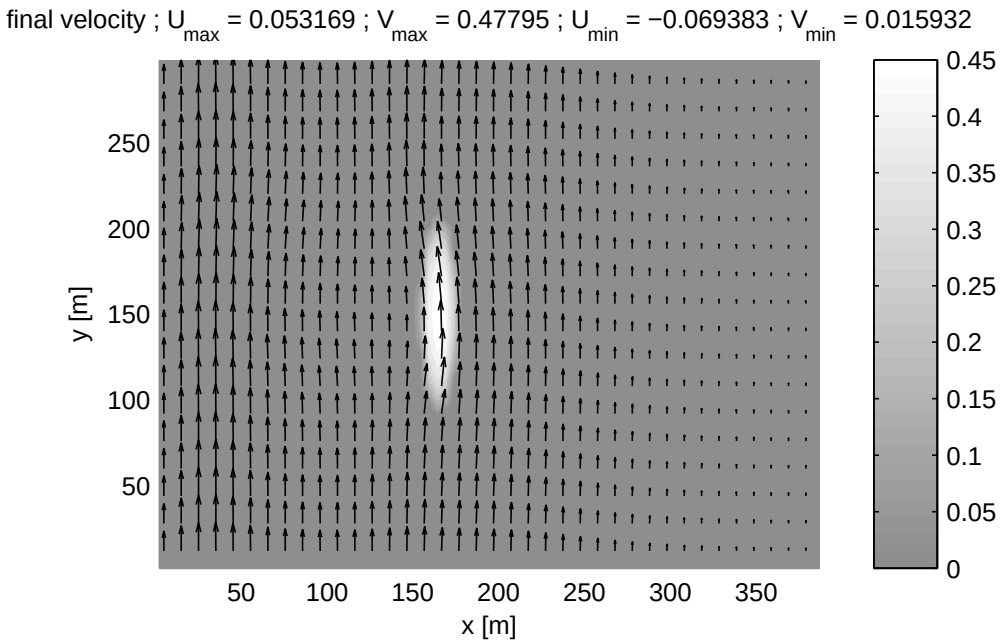

Figure 3.36: Artificial shoal. Flow pattern for run 4 in case of oblique wave incidence (from bottom right corner). The colormap represents h (in metres).

3.4.3.2 Morphodynamics

The topographic evolution after 8.5 hours of wave action is presented in figure 3.39. After this time, the model crashes. Again, we focus in test 4 which is qualitatively representative of runs 1, 2 and 3. In case of shore-normal wave incidence, figures 3.39 and 3.40 show this evolution. The most clear effect is a shoreward migration of the shoal and a slight decay at the side parts. Besides, figure 3.39 shows that the sides of the shoal tend to bend slightly offshore, with a subtle suggestion of a crescentic-bar shape. This is more prominent at the left side, viewing from the coast. Probably due to small numerical irregularities that amplify during the simulation, the evolution is not exactly symmetrical with respect to the centre cross-shore section, $y = 150$ m. The maximum bed rising is about 0.19 m and the maximum bed fall is about 0.12 m. In the present version of the MORFO55 the coastline is fixed, so that its possible evolution can only be inferred a posteriori and we will do it in the Discussion section.

The topographic evolution for test 4 and oblique wave incidence is shown in figures 3.41 and 3.42. Now, the shoal tends to migrate mainly down-current, but slightly onshore too. The onshore migration is more prominent at the down-current part so that the shoal would tend to trend obliquely to the coast like up-current shore oblique bars (Ribas *et al.*, 2003). This is seen both in figures 3.41 and 3.42 ($y = 190$ m section). The maximum bed rising is about 0.2 m and the maximum bed fall about 0.15 m. It is also seen that a subtle alongshore uniform shore-parallel bar is formed close to the coast. This is a slow process, the bar growing only about 0.03 m within the 8.5 hours. Figure 3.43 for test 4_0 (i.e., without the shoal) shows that its formation its not triggered by the shoal. This figure also displays that even in case where the shoal is not present, there are gradients in cross-shore transport driving small changes in the beach profile. This cross-shore transport is due to

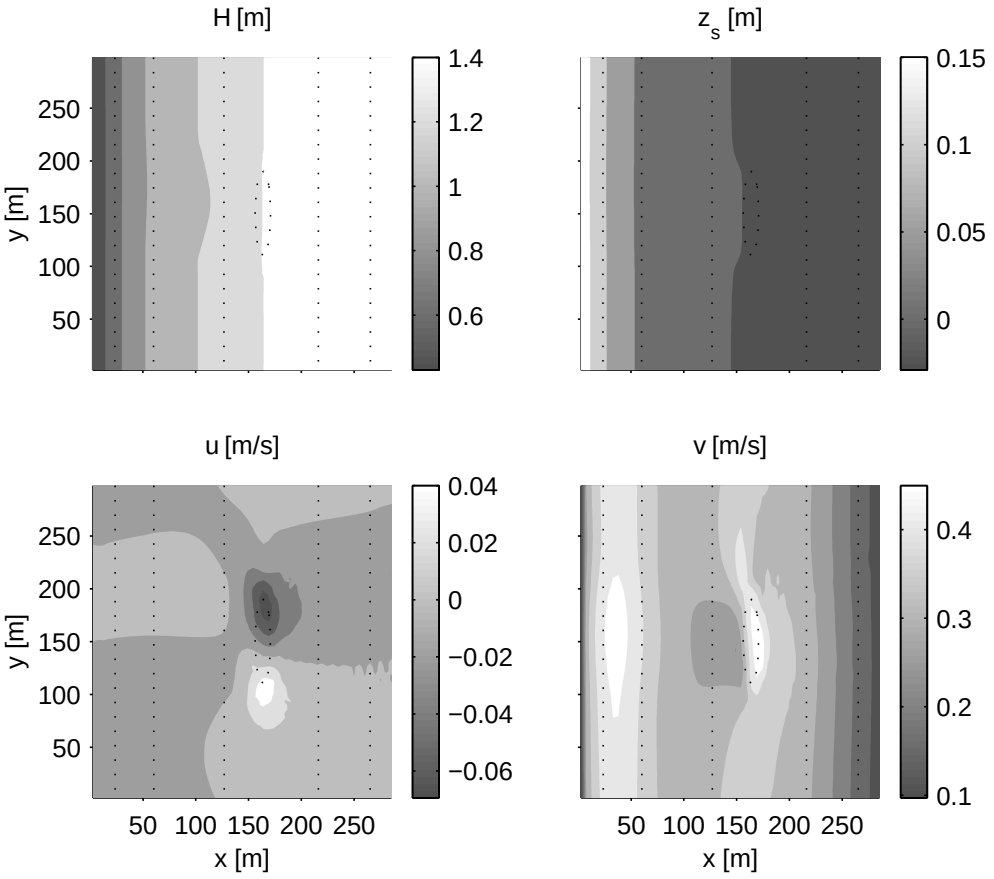

Figure 3.37: Artificial shoal. Details of the hydrodynamics for run 4, oblique wave incidence. The colours represent: the wave height H_{rms} (top left), the free surface elevation z_{s} (top right), cross-shore u and longshore v current components (bottom, left and right, respectively).

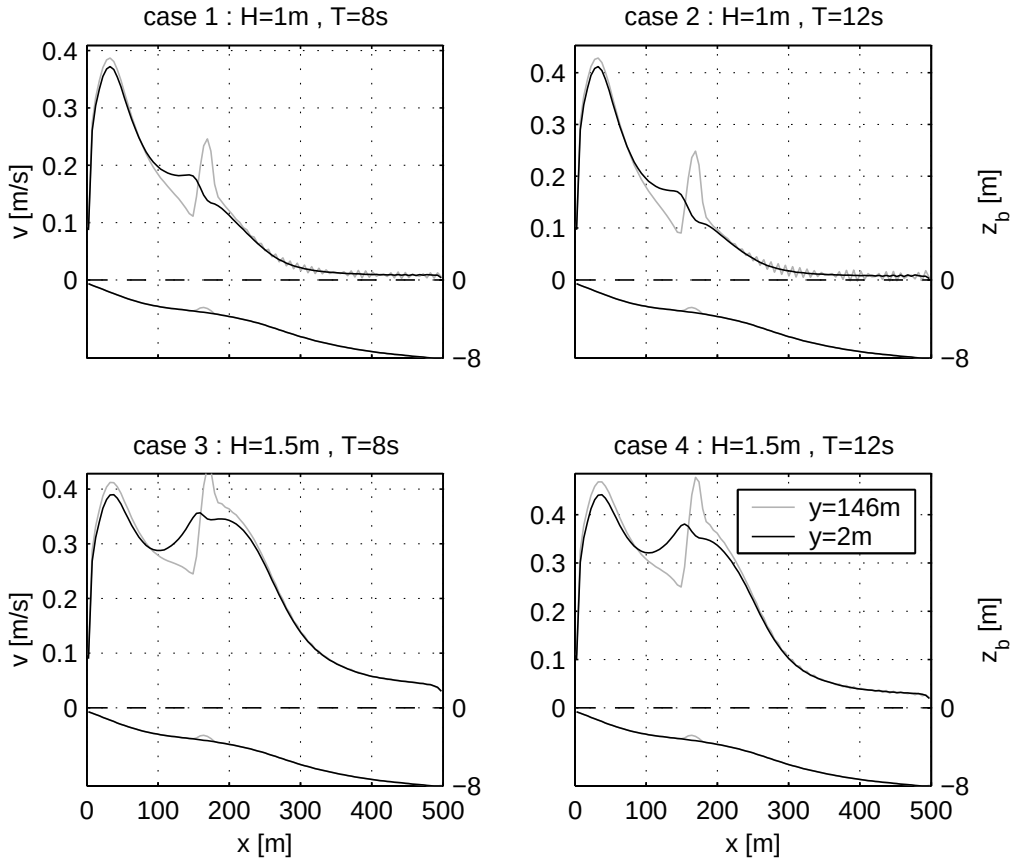

Figure 3.38: Artificial shoal. Cross-shore profile of longshore current for run 1 (top left), run 2 (top right), run 3 (bottom left) and run 4 (bottom right). Grey line: cross-shore section crossing the shoal, black line: lateral cross-shore section far from the shoal.

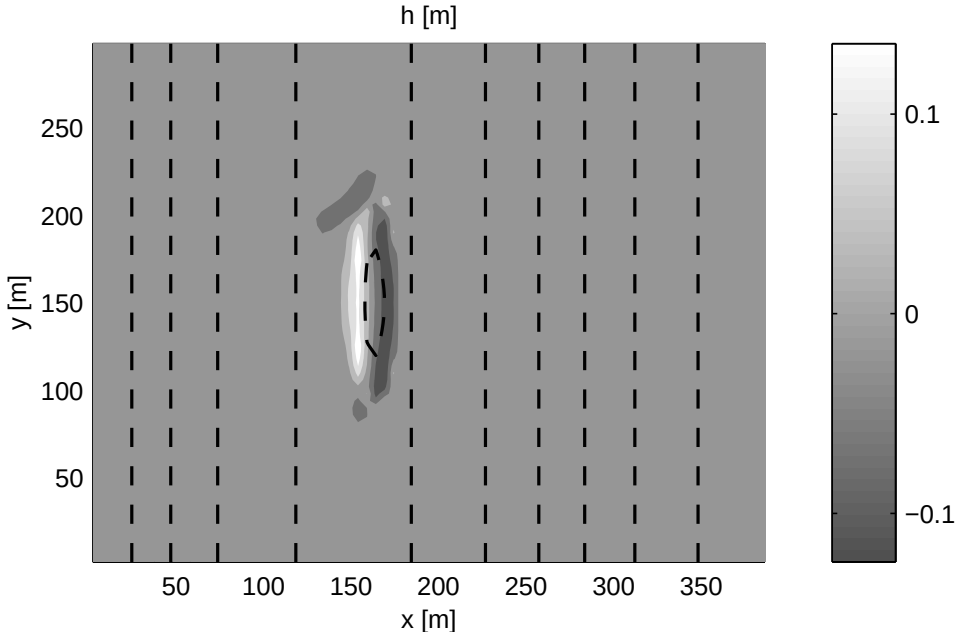

Figure 3.39: Artificial shoal. Topographic perturbation with respect to the initial bathymetry (in metres) for test 4, after 8.5 hours of normal wave incidence.

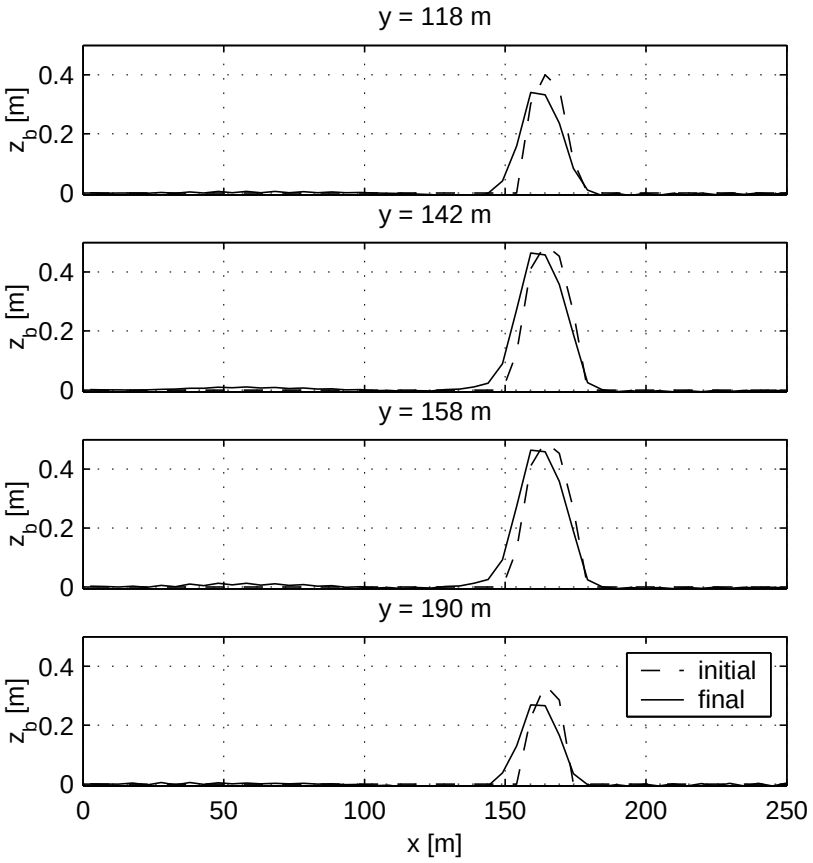

Figure 3.40: Artificial shoal. Topographic perturbation with respect to the ambient topography without the shoal. Various cross-shore sections of the shoal showing its initial shape and its final shape are presented. Test 4, normal wave incidence.

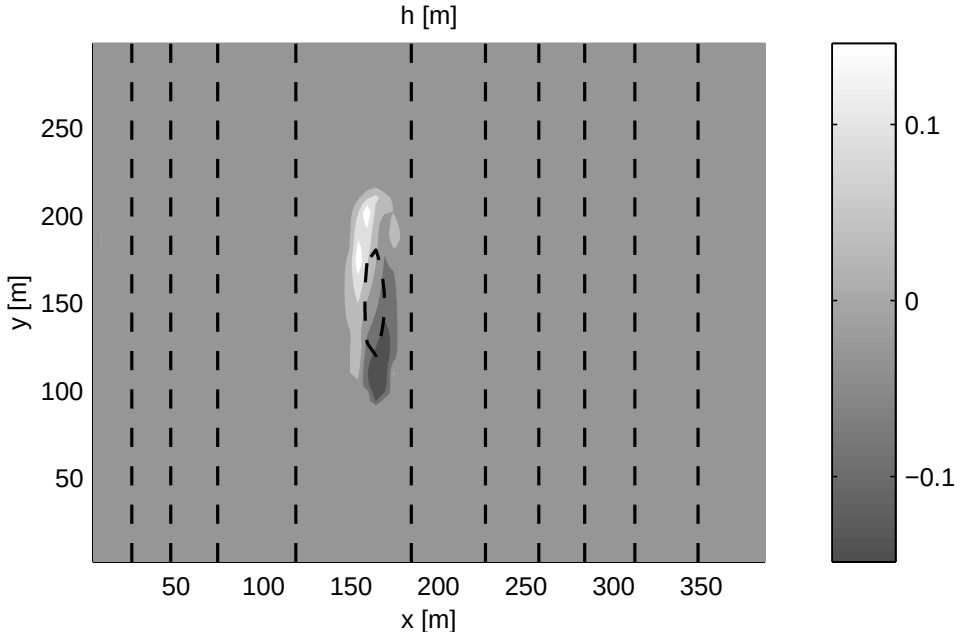

Figure 3.41: Artificial shoal. Topographic perturbation with respect to the initial bathymetry (in metres) for test 4, after 8.5 hours of oblique wave incidence.

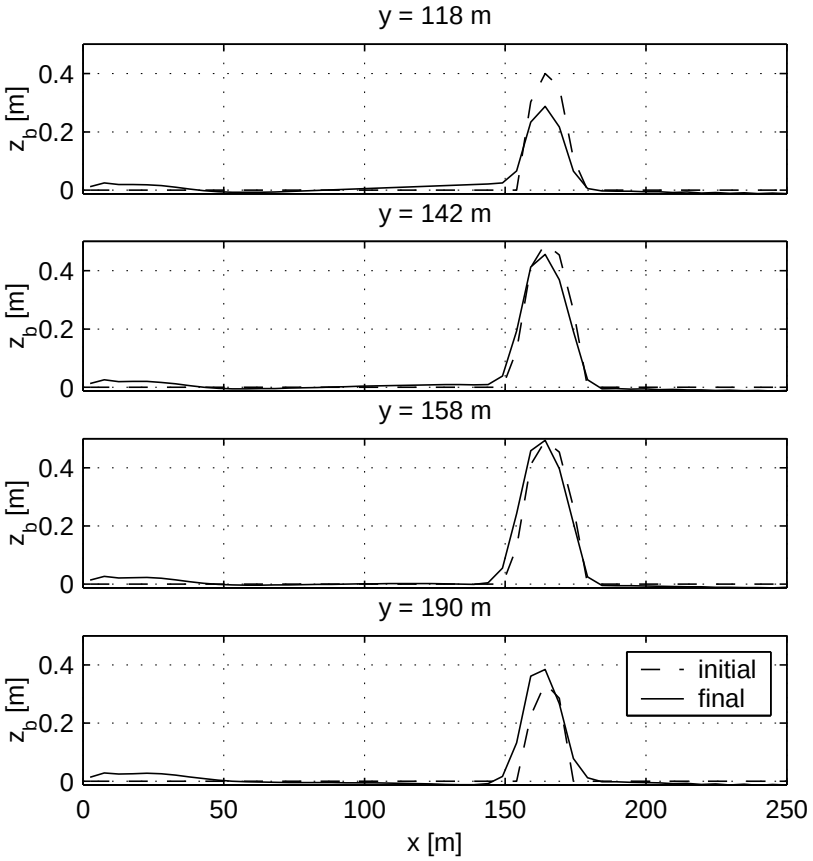

Figure 3.42: Artificial shoal. Topographic perturbation with respect to the ambient topography without the shoal. Various cross-shore sections of the shoal showing its initial shape and its final shape are presented. Test 4, oblique wave incidence.

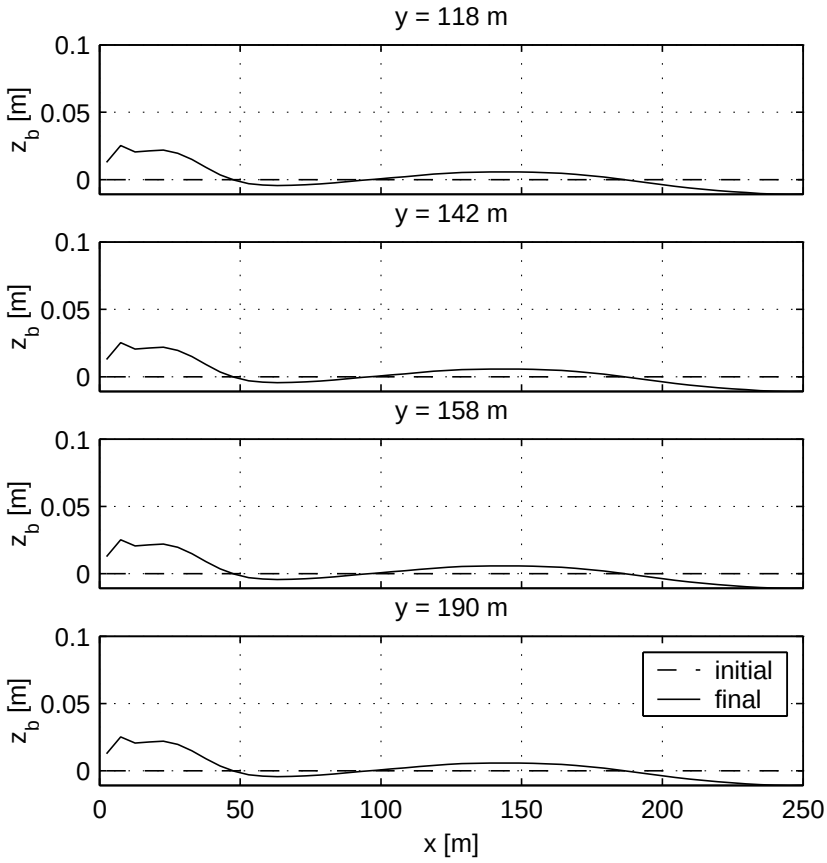

Figure 3.43: Artificial shoal. Bottom perturbation at four different cross-shore sections in case where the shoal is absent (test 4_0) for oblique wave incidence.

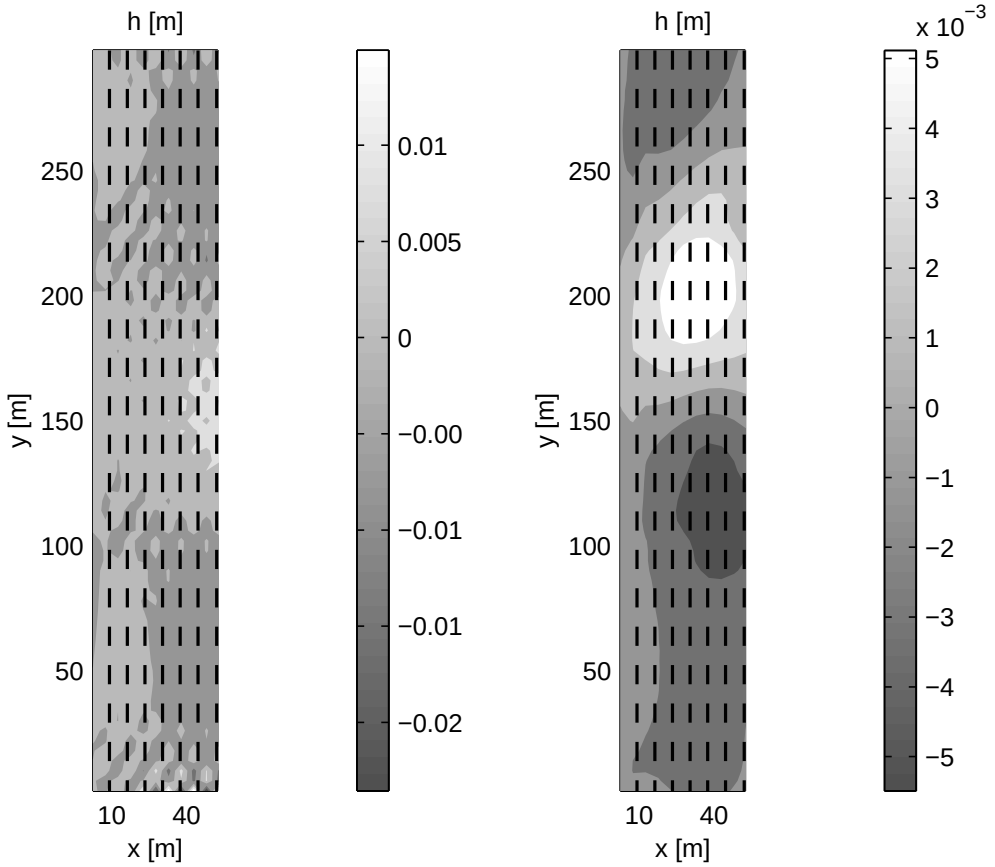

Figure 3.44: Artificial shoal. Bottom perturbation with respect to the initial bathymetry (in metres) in the inner surf zone for test 4. Left: normal wave incidence. Right: oblique wave incidence. The variations corresponding to the shore-parallel bar have been removed.

the combined effect of the longshore current and the waves along with the non-linearity of sediment transport described by the Bailard formulation (Falqués *et al.*, 2004).

3.4.4 Discussion

The model hydrodynamics is qualitatively as expected and also the magnitudes of the currents and wave set-up are in agreement which what is commonly observed. Some streaking features are found. This comprises the presence of two strong vortices at the edges of the shoal in case of normal wave incidence, and two opposite weaker vortices shoreward of them. In case of oblique wave incidence, the longshore current intensifies over the shoal and weakens shoreward of it. Intriguingly, the longshore current intensifies next to the coast in the area onshore of the shoal too. In case of normal wave incidence, the shoal tends to migrate onshore. Also some diffusion is observed and a slight tendency of the edges for lagging behind the onshore translation of the central part suggesting a subtle crescentic-bar reshaping. In case of oblique wave incidence, the shoal moves down-current and, to a minor extend, onshore. Actually, the onshore migration is only clear at the lee edge, so that the shoal tends to trend obliquely to the coast as an up-current

oriented bar. For oblique wave incidence, the combined effect of waves and longshore current causes some cross-shore sediment transport and this creates some changes in the cross-shore beach profile tending to form a shore-parallel bar close to the coastline. This phenomenon is independent of the presence of the shoal.

As a moving coastline is not implemented in MORFO55, the effect of the shoal on the coastline can only be inferred indirectly. In figures 3.39 and 3.41, the bottom evolution at the shoal and next to it are much stronger than the bottom evolution close to the coast and overwhelms it. To show the morphodynamical tendency next to the coast, figure 3.44 has been added where only the inner surf zone ($0 < x < 50$ m) is displayed. Figure 3.44 (left) shows that for normal wave incidence there is a tendency for deposition at the shadow from the shoal, thereby a tombolo would tend to form. For oblique wave incidence the bed changes related to the formation of the longshore bar have been removed since they are not related to the presence of the shoal. According to figure 3.44 (right) there would be accretion at the coast somewhat down-drift of the shoal ($y \simeq 200$ m) and erosion at the rest of the stretch of coast, specially down-drift of the position of maximum accretion ($y \simeq 270$ m). The changes in the 8.5 hour period of simulation are however rather weak, with $\Delta z_{\mathrm{b}} \sim 0.5$ cm . In account of a mean beach slope of about 0.016, this could mean a displacement of the coastline of the order of 30 cm. Although the model capabilities are still very limited with respect to prediction of coastline changes, the present runs show a good overall performance and are encouraging.

3.5 Conclusion

Three kinds of engineering problems have been tackled: first the global study of a particular beach, second the study of a particular existing feature, and third the study of a possible import of sand in order to preserve the coastline. Through the second study, another sand import test is involved, in the case of sand imported from the cliff by a run off event. A pleasant result has been that the undesirable imported sand (from the run off event) has been rapidly diffused whereas the built shoal has globally conserved its size and position.

The goal was not to concretely apply our morphodynamical results to a precise building project but was to test the model and to show that the MORFO55 model may be valid and useful in particular cases of longitudinally non-uniform beaches. Particularly due to the periodic lateral boundary conditions and due to the uniformity of the coastline boundary, the domain of validity of the model seems limited. Nevertheless, in the three cases, these main assumptions seem sensible, because of the general structure of the Barrosa beach, because of the rhythmicity of the gully systems, or because of the large domain used in the shoal experiment.

Even if the final objective of our modelling studies is to simulate the morphodynamical behaviour of the beaches, the model has first been run by disconnecting the sediment transport. In all the cases, an equilibrium hydrodynamical state has been reached. The hydrodynamical study seems essential before the morphodynamical one, indeed, it is useful to control the model parameters such as the grid spacing, the time step, and the size of the domain. Moreover, hydrodynamical data are more easily and frequently taken and are more reliable than the bed evolution data, thus, a first model calibration must be done.

By connecting the sediment transport, the evolution of the bed has been predicted. In none of the cases, the initial beach has never been found in equilibrium. Depending on the sediment transport formulation a new equilibrium has been reached or not. The same model formulation has been used in the three experiments except for the sediment transport formulation. The dilemma between performing the most realistic experiment and preserving the simplicity of the model has been considered. The Bailard formulation is seen as more complete and therefore more realistic than the Soulsby and Van Rijn (SVR) formulation but is less numerically robust. This could be due to the underestimation of the morphological diffusivity due to the bedslope contribution, or due to an inadequate numerical scheme used for the sediment conservation equation. Moreover the cross-shore effect of wave asymmetry and undertow has been disconnected from the Bailard formulation in order to simulate a few hours of evolution. For longer simulations, a numerical diffusivity would have been necessary. The SVR sediment transport has two advantages: firstly, it allows morphological evolution of the time scale from day to years, particularly, equilibrium morphological states of the beach may be reached, secondly, due to its simpler formulation, the physical mechanisms behind the formation/evolution of rhythmic features and the equilibrium states of the beaches are more easily understood. Thus, SVR type (shortened) formulations will be preferred for the rest of the thesis.

Chapter 4

Planar beach instabilities*

4.1 Introduction

In this chapter we study the morphodynamical instabilities of the simplest alongshore uniform beach case: a planar beach. Numerous types of instabilities may emerge in the surf zone of planar beaches. For instance, on fixed topography, hydrodynamical instabilities may appear, as appendix G shows, where a nonlinear evolution of shear waves is presented. The study of these kinds of instabilities is not the main objective of this thesis which is dedicated to morphological changes. In particular, the morphology of the beach could respond to these hydrodynamical instabilities. Nevertheless, in order to lead to the formation of shear waves, the frictional parameter and the turbulence parameter had to be fixed much smaller than the ones used in the default model parameterization. More generally, all the morphological instabilities presented in this thesis are purely morphodynamical: we have verified that the hydrodynamical beach system is stable if we consider a fixed bed. Numerous modelling studies deal with morphodynamical instabilities on planar beaches (Hino, 1974; Christensen *et al.*, 1994; Falqués *et al.*, 2000; Ribas *et al.*, 2003; Caballeria *et al.*, 2002; Fachin & Sancho, 2004*b*; Klein, 2006). They show that transverse bars and oblique bars may appear by self-organization of the coupling between topography, waves and currents. Specifically, the linear stability analysis of Ribas *et al.* (2003) demonstrates that the type of the sediment transport and of the incident waves condition the emergence, the shape and the orientation of the bars. All of these previous studies, being linear or nonlinear, only describe the formation of the bars. Here, we extend them to the nonlinear regime. Two types of sediment transport will be considered in the cases of normal waves and oblique waves.

*Most results are taken from Garnier *et al.* (2006*b*): Garnier, R., Calvete, D., Falqués, A. & Caballeria, M. 2006*b* Generation and nonlinear evolution of shore-oblique/transverse sand bars. *J. Fluid Mech.* **567**, 327–360. Some results have been presented in Garnier *et al.* (2005*a*) (section 4.6.1 and 4.6.2), Garnier *et al.* (2005*b*) (section 4.6.2 and 4.6.3) and Garnier (2005) (section 4.6.4.3)

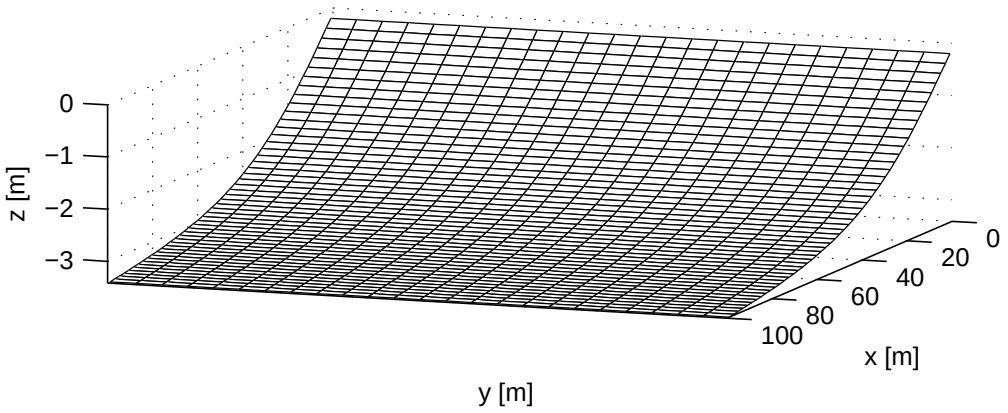

Figure 4.1: Planar beach. Initial beach profile. The shoreline is at $x = 0$.

4.2 Initial beach profile

For the reference case, the alongshore uniform equilibrium beach profile is taken from Yu & Slinn (2003), but the shore parallel bar has been excluded. It is defined as:

$$z_{\mathrm{b}}^{0}(x) = -a_0 - a_1 \left(1 - \frac{\beta_2}{\beta_1}\right) \tanh\left(\frac{\beta_1\, x}{a_1}\right) - \beta_2\, x \ . \tag{4.1}$$

The motivation for excluding the longshore bar is twofold: i) oblique/transverse bars are sometimes observed without the presence of bars and ii) even in the case of a barred beach, the dynamics of bars observed at the inner surf zone close to the coastline are believed to be independent of the outer (alongshore uniform) shore-parallel bar. This is suggested by the linear stability analysis of Calvete *et al.* (2005) where, in this barred beach, transverse bars at the shore grow from a linear mode which fits with the initial state of our transverse bars evolution described later. Furthermore, previous modelling shows that oblique/transverse bars form in areas where there is significant wave breaking. Thus, this would occur next to the shore with the incident waves no matter whether there would have been a reduction of wave height on the bar or not.

To avoid the complications of swash zone dynamics which are expected to have little influence on surf zone dynamics, the shoreline is assumed to consist of a vertical wall at $x = 0$ with a small still-water depth, a_0, and to be fixed in time. Although this assumption filters out the dynamics of the formation of megacusps, the tendency for the formation of megacusps in nature could still be inferred from model results if there is sediment accumulation/erosion at the (fixed) coastline. The value of a_0 has been chosen between 0.10 m to 0.25 m, depending on the amplitude of the bathymetric patterns that will develop close to the shoreline. The other parameter is fixed to $a_1 = 2.97$ m and the shoreline and offshore slopes are $\beta_1 = 0.075$ and $\beta_2 = 0.0064$. These parameters come from an approximation of the beach profile measured at Duck, North Carolina (Yu & Slinn, 2003). Figure 4.1 shows the three-dimensional view of this default bathymetry, in the case of the wall height of: $a_0 = 0.10$ m. The seaward boundary is at $x = L_x = 100$ m. No ticks have been plotted on the y-axes because the longshore size of the domain may differ depending on the experiment.

case	L_x [m]	L_y [m]	Δx [m]	Δy [m]	a_0 [m]	t_{CFL} [s]	Δt [s]	Δt_{m} [s]	t_{CPU} [hrs]
SVR	100	300	1.0	1.0	0.25	0.018	0.01	1.51	4.0
CWS	100	800	2.0	4.0	0.10	0.036	0.01	1.51	1.0

Table 4.1: Planar beach. Fixed input parameters for each sediment transport formula.

case	H^0_{rms} [m]			θ^0 [deg]			T [s]		
	def	min	max	def	min	max	def	min	max
SVR-i	1.0	0.5	1.25	0	-	-	6	6	12
SVR-ii	1.0	0.5	1.25	25	5	45	6	6	12
CWS	1.0	0.5	1.25	25	5	45	6	6	12

case	γ		
	def	min	max
SVR-i	1.5	1.4	2.5
SVR-ii	1.5	1.5	1.8
CWS	0.5	0.3	0.9

Table 4.2: Planar beach. Variable input parameters for each experiment. Default (def), minimum (min) and maximum (max) values.

4.3 Experiments and default parameters

The experiments have been done by using two different sediment transport formulae. The SVR transport in the case of normal wave incidence (SVR-i), oblique wave incidence (SVR-ii) and the CWS transport only in the case of oblique waves (CWS) will be presented, the case of normal wave incidence appearing to be stable in agreement with Falqués *et al.* (2000). All the experiments have been compared with a reference or default case which is studied in detail here.

The fixed input parameters arbitrarily set for each sediment transport formula are shown in table 4.1. L_x is the same for all experiments in order to keep the same equilibrium cross-shore profile independently of the sediment transport used, whereas L_y is chosen to be about 10 times the final spacing of bars for the reference cases. As the longshore length of the integration domain artificially imposes a final spacing of bars as a divisor of L_y, the relative error of this final spacing will be of about 10 %. Δx depends on the cross-shore span of the bars, a bar must be described by more than 15 points in the off-shore direction and Δy must be sufficiently small to avoid numerical oscillations. The height of the artificial wall at the coastline depends on the distance from the coastline to the top of the bars. The morphodynamical processes have been artificially accelerated by a factor 150 for computational convenience (Caballeria, 2000, see), giving the morphodynamical time step as: $\Delta t_{\mathrm{m}} = 150\,\Delta t$. This acceleration factor has been empirically determined on small computational domains obtaining the same results by

using it or not. Finally, t_{CPU} is defined as the CPU time corresponding to 1 day of beach evolution using a Pentium IV, 2.8 GHz.

In order to excite the system and develop the instabilities, the longshore uniformity has been broken off by adding a smoothed random function to the initial bathymetry. In order to check that the final state does not depend on the particular choice of the initial conditions, a 'Dirac-function like' initial perturbation has been considered as well. Similarly, several domain lengths have also been tested. Although the particular intermediate states may differ from test to test, the final state and the growth rate of the instabilities were the same.

Each reference case is characterized by a wave forcing at the offshore boundary (H^0_{rms}, θ^0, T) and by the bedslope parameter (γ). The influence of these parameters will also be investigated. The default value of these variables and the minimum (maximum) value studied are shown in table 4.2.

4.4 Basic state

Figure 4.2 shows some characteristic values of the system at the basic state. This is the equilibrium state reached by the system if there are no alongshore irregularities, the morphodynamics remaining steady. In the next sections, when morphodynamical instabilities develop, the new equilibrium state eventually reached by the system is called the saturated state. The model is run on the concave up beach (cf. equation 4.1) without any initial perturbation. At the offshore boundary, waves are assumed to approach from an angle with the shore-normal, $\theta^0 = 25\,^{\circ}$. The wave height is forced to increase from $H^0_{\mathrm{rms}} = 0$ to 1 m within a time period of 5 min. This gradual switching on of the wave height avoids strong transient oscillations from the hydrodynamic equations. After about 50 min the system became steady, the maximum longshore current being $v_{\max} = 0.8\,\mathrm{m\,s^{-1}}$ at $x = 11$ m. It is worth noting that in other related studies (e.g. Fachin & Sancho, 2004*a*) the instability of the equilibrium state develops just from the unavoidable random numerical inaccuracies without any initial perturbation. In contrast, this is not the case with the present MORFO55 model (also with MORFO50 Caballeria *et al.*, 2002). Without superposing initial disturbances to the equilibrium, the initial topographic system state remains constant during all the simulation with the present model. Most probably, this is due to a higher numerical stability of the integration method. A representative value of the characteristic width of the surf zone is the distance from shore to the point of maximum breaking dissipation (ε_{b}) which for this simulation turns out to be $x_{\mathrm{b}} = 11$ m. This 'maximum breaking' point is represented by the vertical dashed line.

According to previous studies where the sediment flux is described as a stirring factor multiplied by the current, the morphodynamical behaviour is mainly governed by the 'potential stirring', i.e. the stirring factor divided by water depth (Falqués *et al.*, 2000; Coco *et al.*, 2002; Ribas *et al.*, 2003). Figure 4.3 shows that (i) for the SVR transport, in each case, the stirring factor and the potential stirring increase seaward at the inner

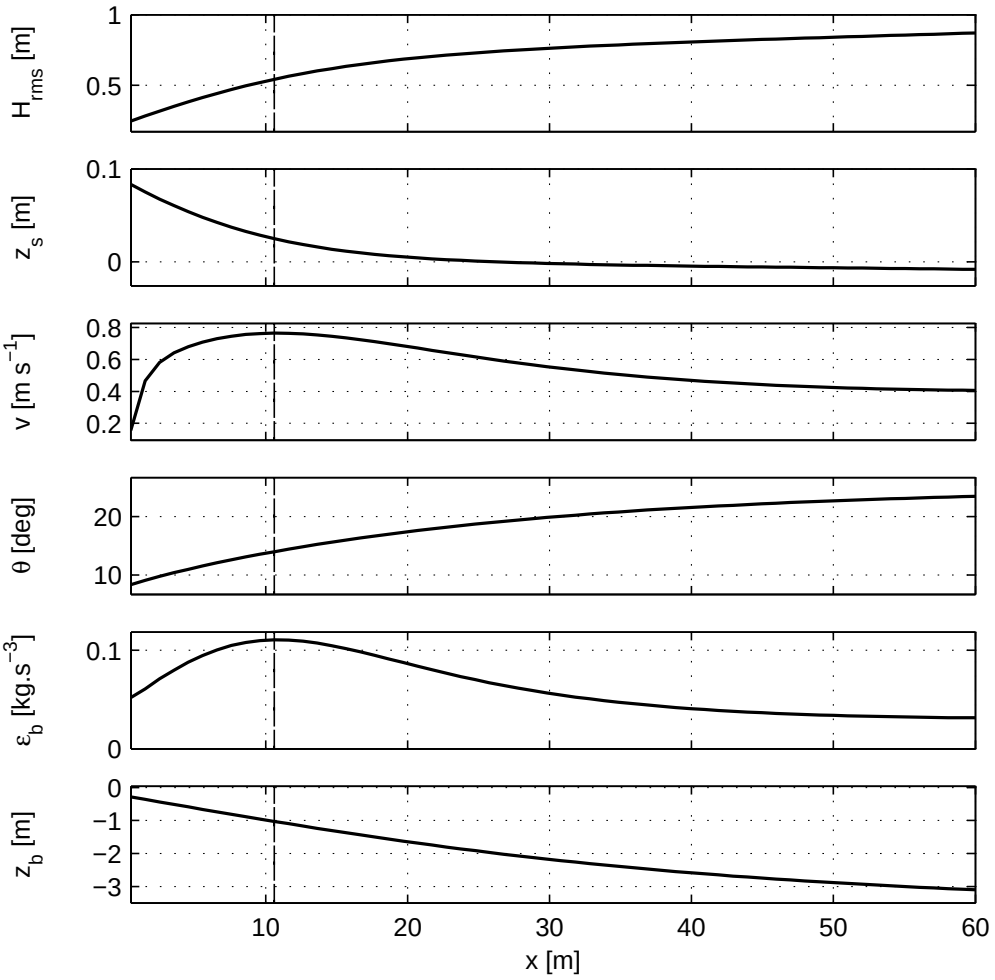

Figure 4.2: Planar beach. Incident waves: $H^0_{\mathrm{rms}} = 1.0$ m, $T = 6$ s, $\theta^0 = 25\,^\circ$. Equilibrium profiles of the basic state in the case of oblique wave incidence. From top to bottom: wave height (H_{rms}), mean sea level (z_{s}), longshore velocity (v), wave angle (θ), dissipation rate (ε_{b}) and bottom level (z_{b}). Shoreline at $x = 0$.

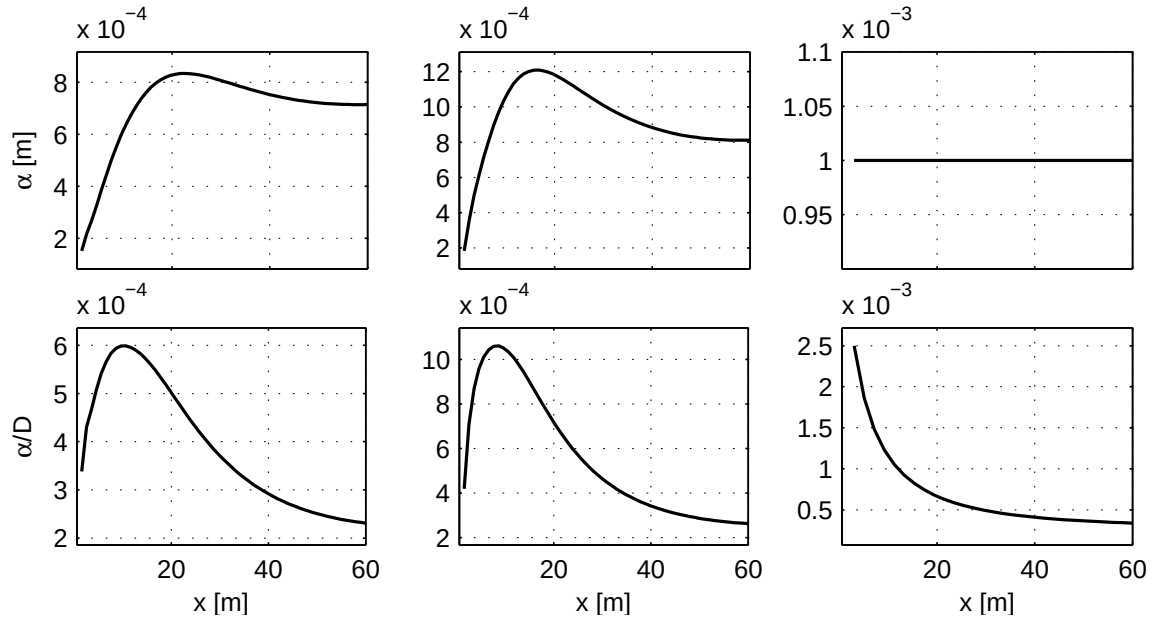

Figure 4.3: Planar beach. Incident waves: $H^0_{\rm rms} = 1.0$ m, $T = 6$ s. Stirring factor α (up) and potential stirring α/D (down) at the equilibrium state for three cases (from left to right): (i) SVR transport, $\theta^0 = 0\,^{\rm o}$, (ii) SVR transport, $\theta^0 = 25\,^{\rm o}$, (iii) CWS transport, $\theta^0 = 25\,^{\rm o}$.

surf zone and decrease seaward beyond a certain point and (ii) for the CWS transport, the stirring factor has been chosen approximately as the maximum of the SVR stirring and gives a seaward decreasing potential stirring.

4.5 How to characterize the bars?

As in nature, the bars generated by a nonlinear model starting with random initial conditions may have a relatively irregular shape whose quantitative characterization is not straightforward.

To this end, six time-dependent quantities have been used:

(1) The amplitude $A_{\rm m}$ (m) is defined as $A_{\rm m} = 0.5\,(h_{\rm max} - h_{\rm min})$, where $h_{\rm max}$ ($h_{\rm min}$) is the maximum (minimum) value of h throughout the model domain.

(2) The angle $\beta_{\rm m}$ (deg) (≥ 0) is the mean of the angle formed by crests and troughs with the x-axis. It may be either 'up' or 'down' according to whether bars are up-current or down-current and it is zero for transverse bars.

(3) The longshore mean spacing $\lambda_{\rm mean}$ (m) is the average spacing between two crests of bars which is obtained by counting the number of bar crests in a longshore section along the domain.

(4) The longshore dominant spacing λ_{m} (m) is the dominant wave length of bars according to Fourier analysis. To this end, we use the discrete Fourier transform of the bed level at the longshore section $x = 10$ m:

$$\mathcal{H}(k_l) = \sum_{j=1}^{N_y} h(10, y_j) \exp\left(-i\frac{2\pi}{N_y}(j-1)(l-1)\right), \quad k_l = \frac{2\pi(l-1)}{L_y}, \quad l = 1 : N_y, \tag{4.2}$$

where $\mathcal{H}(k_l)$ is the Fourier coefficient corresponding to the wavenumber of the topographic signal k_l and $y_j = j\Delta y$. The normalised modulus of the Fourier coefficients is defined as $|\mathcal{H}|_n(k_l) = |\mathcal{H}(k_l)|/\max_{k_l}|\mathcal{H}(k_l)|$. The wavenumber for which $|\mathcal{H}(k_l)|$ is maximum defines the dominant mode and is called k_{m}. Finally, the variables with the subscript m correspond to the dominant mode and the variables with the subscript l correspond to any mode with the wavenumber k_l, for example $\lambda_{\mathrm{m}} = \lambda_{l=m} = 2\pi/k_{\mathrm{m}}$.

(5) The cross-shore span S_{m} (m) is the mean horizontal cross-shore approximate span of bar crests and bar troughs.

(6) The total approximate span or length L_{m} (m) is given by $S_{\mathrm{m}}/\cos\beta_{\mathrm{m}}$.

Furthermore, the temporal behaviour of bars will be characterized by three quantities.

(1) The period T_{m} (day) is the time that the bars spend in travelling across one dominant spacing.

(2) The growth rate σ_{m} (day^{-1}) is obtained plotting the time evolution of $|\mathcal{H}(k_l)|$. At the initial stages of the simulation, the perturbations are expected to grow exponentially in time, consistent with the linear stability theory. This means that for each wavenumber k_l, $\mathcal{H}(k_l, t) \approx \mathcal{H}(k_l, 0)\exp\sigma_l t$. Thus, by taking the logarithm of the modulus, its real growth rate, $\mathrm{Re}(\sigma_l)$, can be isolated from: $\ln|\mathcal{H}(k_l, t)| \approx \mathrm{Re}(\sigma_l)t + \ln|\mathcal{H}(k_l, 0)|$. Therefore, the initial growth of $\ln|\mathcal{H}(k_l, t)|$ for each wavenumber k_l should be a straight line with a slope $\mathrm{Re}(\sigma_l)$. For the dominant mode, we define $\sigma_{\mathrm{m}} = \mathrm{Re}(\sigma_{l=m})$.

(3) The migration velocity c_{m} (m day^{-1}) is calculated as $\lambda_{\mathrm{m}}/T_{\mathrm{m}}$.

4.6 Oblique/transverse bars

4.6.1 Transverse bars (SVR-i)

Figure 4.4 shows four steps of the evolution of the topography during 8 days. The domain has been reduced for the visualisation: (0 m $< x <$ 30 m and 50 m $< y <$ 150 m). At day 1, the initial random perturbations seem erased and the total depth seems

case	mode	A_m [m]	β_m [deg]	λ_mean [m]	λ_m [m]	S_m [m]	L_m [m]
SVR-i	1	0.13	0	30	30	11	11
SVR-ii		0.37	51	30	30	19	30
CWS	1	0.28	34	50	50	30	36
	2	0.26	49	73	73	40	61

case	mode	T_m [day]	σ_m [day^{-1}]	c_m [m day^{-1}]
SVR-i	1	-	2.1	0
SVR-ii		0.18	1.6	167
CWS	1	0.7	1.25	71
	2	1.7	0.7	43

Table 4.3: Planar beach. Characteristics of the dominant modes for the default case.

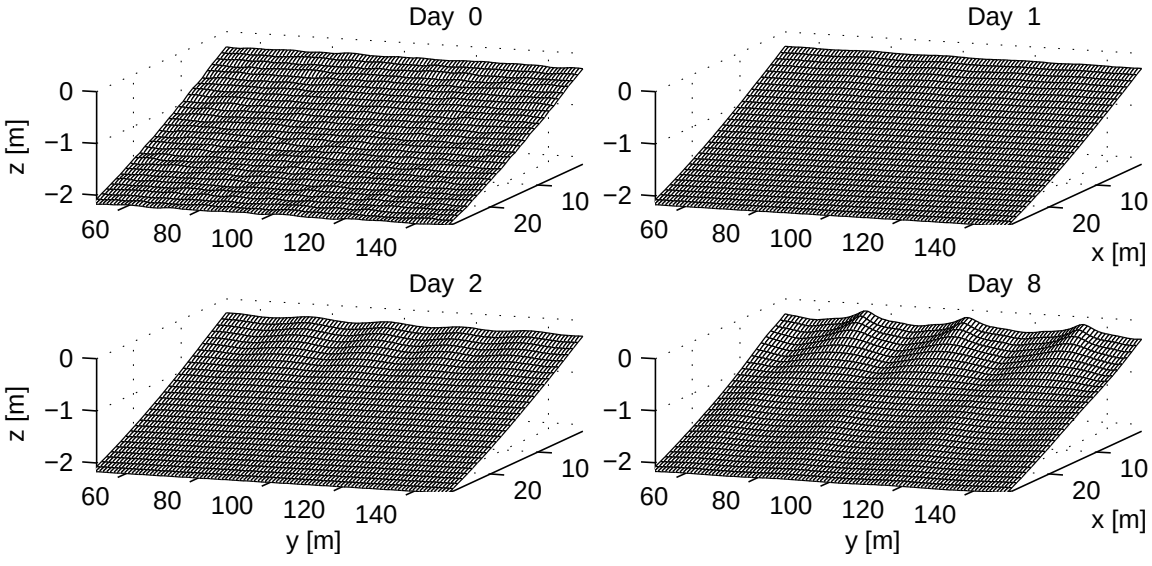

Figure 4.4: Planar beach, transverse bars. SVR-i default case (SVR transport, $\theta^0 = 0\,^\circ$). Zoom of the total bathymetry during the formation, development and growth saturation of shore-transverse bars.

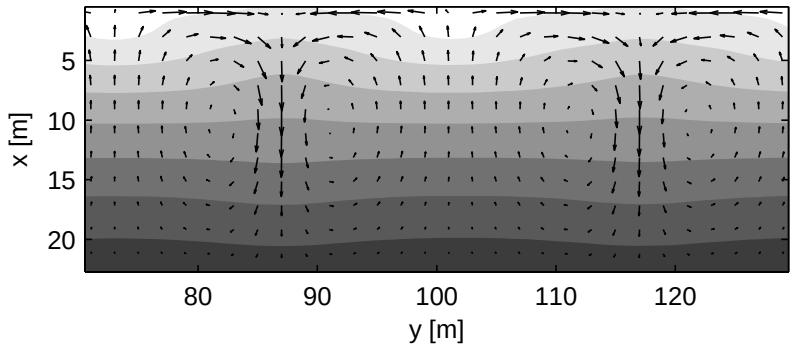

Figure 4.5: Planar beach, transverse bars. SVR-i default case (SVR transport, $\theta^0 = 0\,^\circ$). Final state (day 8). Bathymetric contours (z_b) and circulation ($\vec{v}$) over transverse bars. The shallowest areas are white and the deepest areas are shaded. Maximum current magnitude: $0.4\,\mathrm{m\,s^{-1}}$.

longitudinally uniform. At day 2, regular and gentle transverse bars with an amplitude up to 5 cm appear with a spacing of $\lambda_\mathrm{mean} = 20$ m. They will grow and merge together until the system reaches its final state at day 8. The final characteristics of these bars are given in table 4.3: the bar amplitude is $A_\mathrm{m} = 0.13$ m, the mean spacing is $\lambda_\mathrm{mean} = 30$ m and the cross-shore span is the size of the surf zone, $S_\mathrm{m} = x_\mathrm{b} = 11$ m.

Figure 4.5 is a top view of the final bathymetry and circulation. The latter consists of a very clear rip-current system, the current going offshore at the troughs and onshore over the shoals. It is also apparent that, as is observed in nature, the seaward flowing current is narrow, jet-like and stronger than the shoreward flow which is wider and weaker. The maximum seaward current is $|u| = 0.38\,\mathrm{m\,s^{-1}}$ and the maximum feeder current (longshore current) is $|v| = 0.37\,\mathrm{m\,s^{-1}}$.

A more precise description of the dynamics of these bars may be obtained by looking at the time evolution curves. The crests and the troughs of the bars can be seen in figure 4.6(a). As described in figure 4.4, bars are very subtle until day 2. Between days 2 and 4, the merging of some of the bars can be seen. At day 6, the state of the bars seems very close to the final state at day 8. It is also clear that crests and troughs remain parallel to the time axis, showing the non-migration of the bars. Merging of bars (and also splitting) is shown in figure 4.6(b) where the different steps presented in figure 4.6(a) are recovered. It can be seen that the number of bars in the domain systematically decreases from day 1 until the final state where $\lambda_\mathrm{mean} = 30$ m. Figure 4.6 (c) shows that at the beginning of the simulation, the spectral energy is randomly distributed among the different wavenumbers consistently with the randomness of the initial perturbation, and after day 1, one wavenumber becomes clearly dominant. It is important to notice the difference between the mean spacing (figure 4.6b) and the dominant spacing (figure 4.6d). Indeed, as seen in this plot, the time when λ_m grows does not necessarily correspond to the merging of bars, i.e., the time when λ_mean is increasing. At the final steady state, however, both wavelengths coincide, $\lambda_\mathrm{m} = \lambda_\mathrm{mean} = 30$ m. This plot indicates that at day 1 the finally dominant wavelength is already dominant. The final spacing actually corresponds to an instability mode which appears very soon in the evolution, but other modes are also present during all the simulation. The nonlinear competition between all these modes accounts for $\lambda_\mathrm{m} \neq \lambda_\mathrm{mean}$, but the other modes never dominate upon the

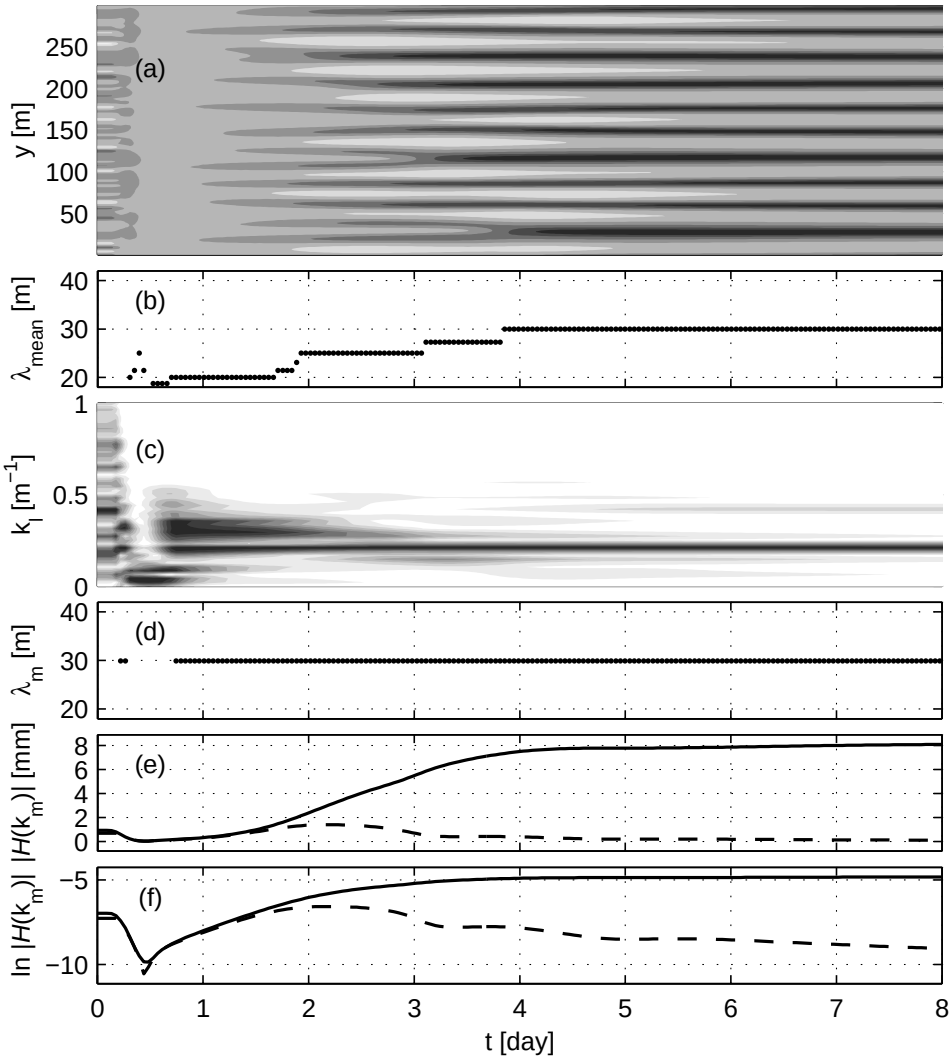

Figure 4.6: Planar beach, transverse bars. SVR-i default case (SVR transport, $\theta^0 = 0\,^\circ$). Time series of (a) the bed level along the longshore section at $x = 10$ m ($h(y,t)$), crests are white and troughs are black, (b) the mean spacing of the bars ($\lambda_{\mathrm{mean}}(t)$), (c) the normalised modulus of the Fourier coefficient of the topographic signal ($|\mathcal{H}|_n(k_l,t)$), (d) the resulting predominant spacing of bars ($\lambda_{\mathrm{m}}(t)$), (e) the two predominant most energetic (non-normalised) Fourier coefficients of the topographic signal ($|\mathcal{H}|(k_l,t)$), corresponding to: $\lambda_{\mathrm{m}} = 2\pi/k_{\mathrm{m}} = 20$ m (dashed line), $\lambda_{\mathrm{m}} = 30$ m (thick line), and (f) their logarithmic value ($\ln|\mathcal{H}(k_{\mathrm{m}},t)|$).

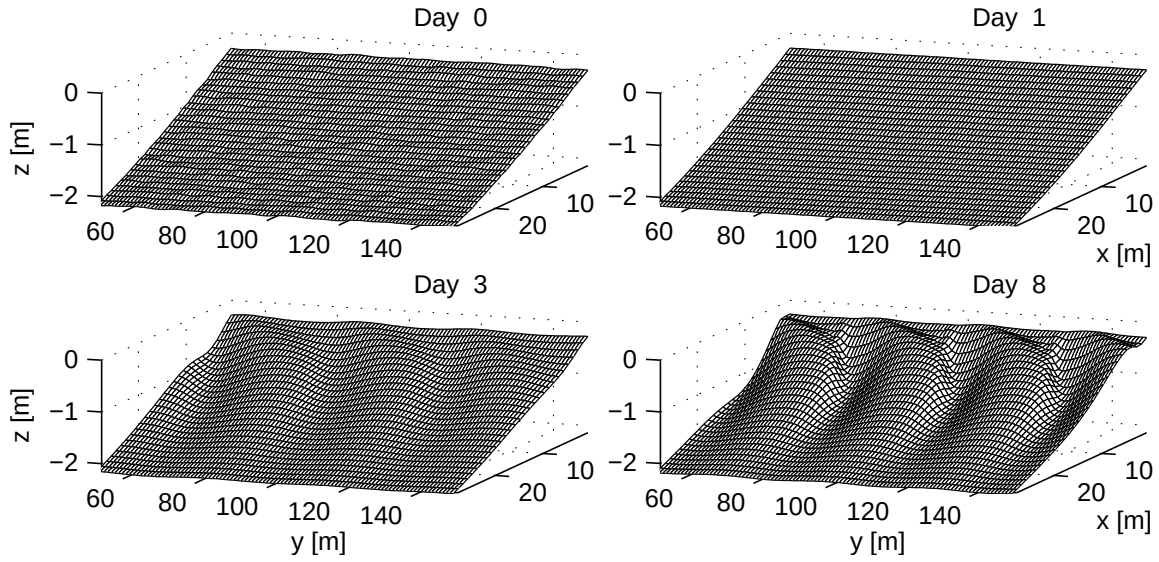

Figure 4.7: Planar beach, down-current oriented oblique bars. SVR-ii default case (SVR transport, $\theta^0 = 25\,^\circ$). Zoom of the total bathymetry during the formation, development and growth saturation of oblique down-current oriented bars.

finally dominant mode. Figure 4.6 (*e*) shows the time evolution of the two largest Fourier coefficients $|\mathcal{H}(k_l, t)|$: the dominant one during all the evolution and the second one at the initial stage. The slope of the linear part of each curve of figure 4.6 (*f*) gives a very similar growth rate for the two modes: $\sigma_\mathrm{m} = 2.3$ day^{-1}.

4.6.2 Oblique down-current oriented bars (SVR-ii)

As shown in figure 4.7, bars trending obliquely to the coast with a down-current orientation appear in this case. They have reached the middle of the growth at day 3 and the final saturated state is obtained at day 8 when the amplitude of the bars is $A_\mathrm{m} = 0.37$ m (table 4.3). At this state, they have adopted a backward curved shape in plan view with the seaward tip of the bar becoming perpendicular to the coast rather than oblique.

A meandering of the longshore current is observed as a result of the bars (figure 4.8), the current being deflected onshore over the crests and offshore over the troughs. This meandering is consistent with previous studies (Ribas *et al.*, 2003) and has been called 'current refraction'. The deflection is relatively weak, the cross-shore flow component being smaller than the longshore component (up to $|u| \simeq 0.3\,\mathrm{m\,s^{-1}}$ in comparison with $|v| \simeq 0.9\,\mathrm{m\,s^{-1}}$). The most significant deflection occurs close to the shoreline, especially at the troughs.

The formation of bars is clearly visible in figure 4.9(*a*) between days 2 and 4. The down-current migration of the bars is easily seen through the slope of the dark and white strips. In the final saturated state, bars move about 300 m within 1.8 days so

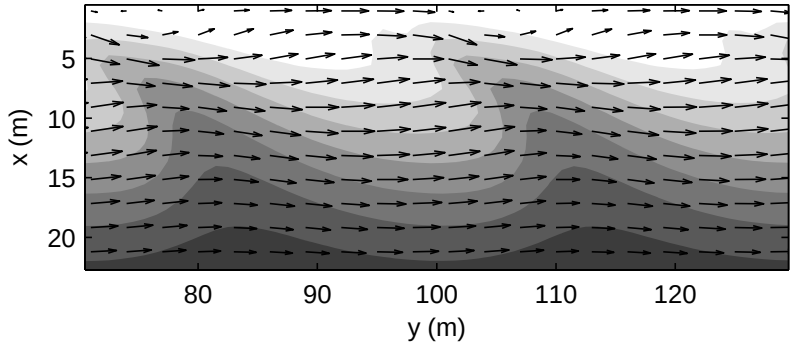

Figure 4.8: Planar beach, down-current oriented oblique bars. SVR-ii default case (SVR transport, $\theta^0 = 25\,^\circ$). Final state (day 14). Bathymetric contours (z_b) and circulation ($\vec{v}$) over down-current oriented bars. The shallowest areas are white and the deepest areas are shaded. Maximum current magnitude: $0.9\,\mathrm{m\,s^{-1}}$.

that the migration celerity is about $c_\mathrm{m} = 167$ m day^{-1}. The mean wavelength λ_mean remains constant to 30 m from day 3 (figure 4.9*b*), indicating that there is no clear merging/splitting after the waves have reached their final amplitude, in contrast with the case of transverse bars. Figure 4.9 (*c*) shows the initial uniformly distributed spectral energy and the process of energy concentration at wavelengths of 20 m and larger during the first three days. For example, a mode with $\lambda_\mathrm{m} = 25$ m emerges from this process and becomes dominant at day 1. At the same time, the finally dominant mode, $\lambda = 30$ m, is already present and competes with that one. This competition can be clearly seen in the plot of $\ln|\mathcal{H}(k_l, t)|$ shown in figure 4.9(*f*). This 30 m mode becomes dominant over the 25 m mode just after day 1 and competes with other modes. At day 3, it remains dominant until the end of the simulation. This plot allows us to estimate the growth rate of the finally dominant mode as $\sigma_\mathrm{m} \simeq 1.6$ day^{-1}. Figure 4.9(*g*) is in fact a transect of figure 4.9(*a*). The period T_m of sand waves can be easily extracted from it. The final period, reached after day 5, is $T_\mathrm{m} = 0.18$ day. The migration velocity may also be calculated as $c_\mathrm{m} = \lambda_\mathrm{m}/T_\mathrm{m}$ and the values are consistent with figure 4.9(*a*).

4.6.3 Oblique up-current oriented bars (CWS)

Figure 4.10 displays the evolution of the topography during the first 140 days. Only a partial view of the domain is shown in the y-direction (200 m $< y <$ 400 m). The time leading to the final saturated state seems very long, but at day 7, the bars have already grown and have reached their final amplitude. At this time, they start to merge together so that their wavelength grows up to 73 m, and at day 35 the bar system is very close to the final one at day 140.

Figure 4.11 shows the final morphology and hydrodynamics of this up-current bar system. As for the down-current bars, the longshore flow component ($|v| \simeq 0.8\,\mathrm{m\,s^{-1}}$) is considerably larger than the cross-shore component (up to $|u| \simeq 0.2\,\mathrm{m\,s^{-1}}$). The corresponding meandering is opposed to that in the case of down-current bars: the longshore current is deflected seaward over the crests and shoreward at the troughs.

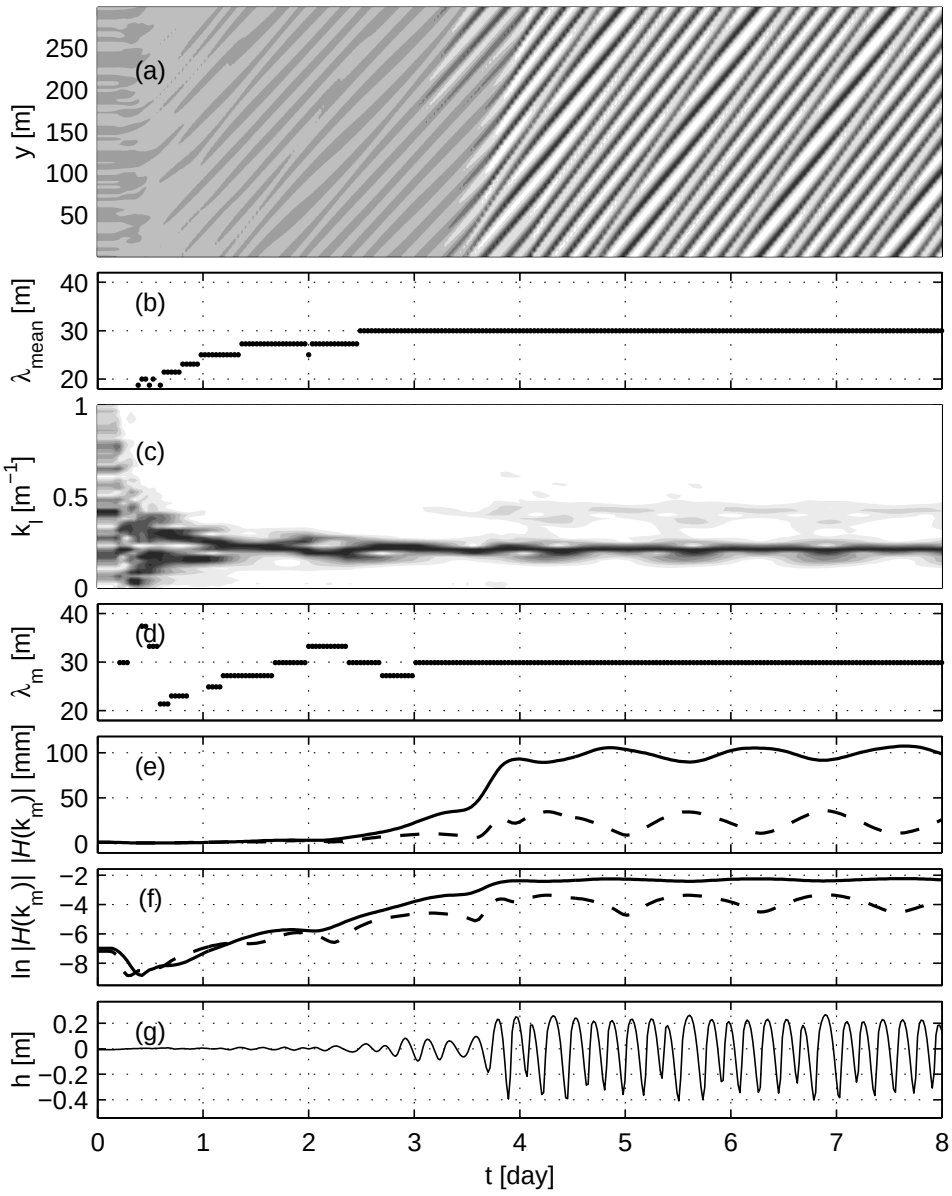

Figure 4.9: Planar beach, down-current oriented oblique bars. SVR-ii default case (SVR transport, $\theta^0 = 25\,^\circ$). The graph description is the same as figure 4.6 with (g) the time evolution of the bottom perturbation at one point: ($x = 10$ m, $y = 22.5$ m). For (e) and (f), $\lambda_\mathrm{m} = 2\pi/k_\mathrm{m} = 25$ m (dashed line), $\lambda_\mathrm{m} = 30$ m (thick line).

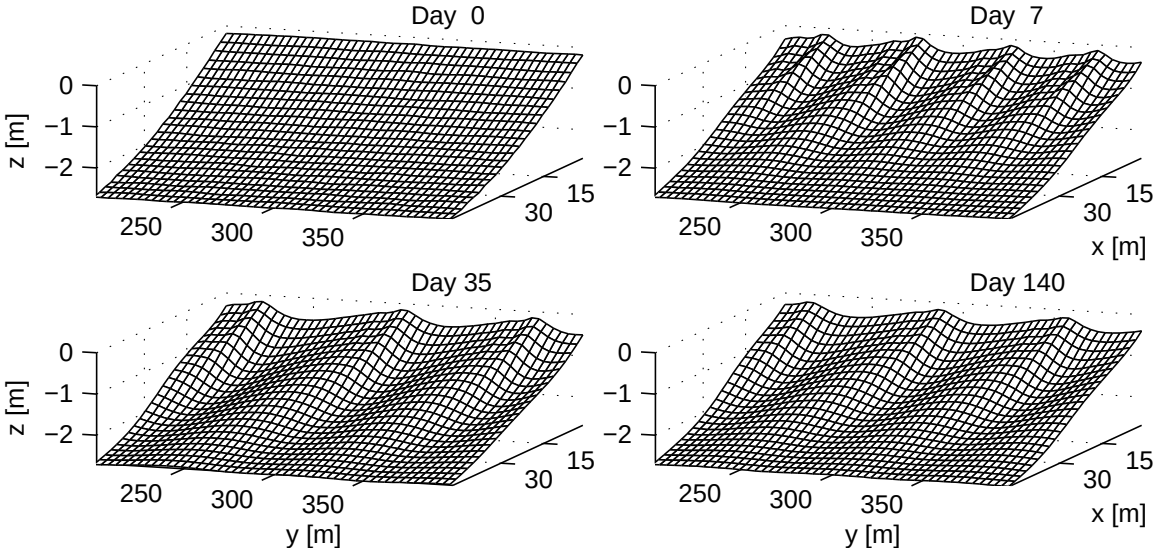

Figure 4.10: Planar beach, up-current oriented oblique bars. CWS default case (CWS transport, $\theta^0 = 25\,^{\circ}$). Zoom of the total bathymetry during the formation, development and growth saturation of oblique up-current oriented bars.

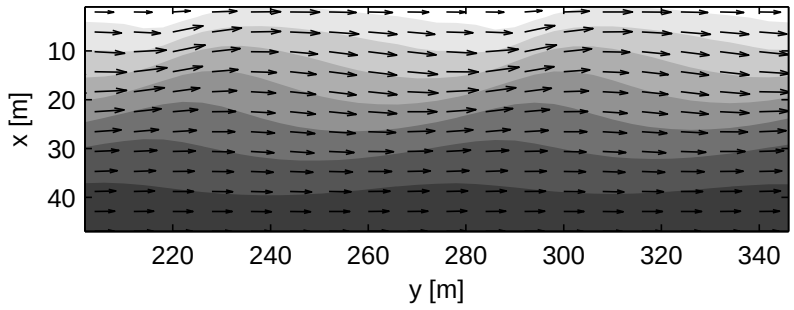

Figure 4.11: Planar beach, up-current oriented oblique bars. CWS default case (CWS transport, $\theta^0 = 25\,^{\circ}$). Final state (day 85). Bathymetric contours (z_b) and circulation ($\vec{v}$) over up-current oriented bars. The shallowest areas are white and the deepest areas are shaded. Maximum current magnitude: $0.8\,\mathrm{m\,s^{-1}}$.

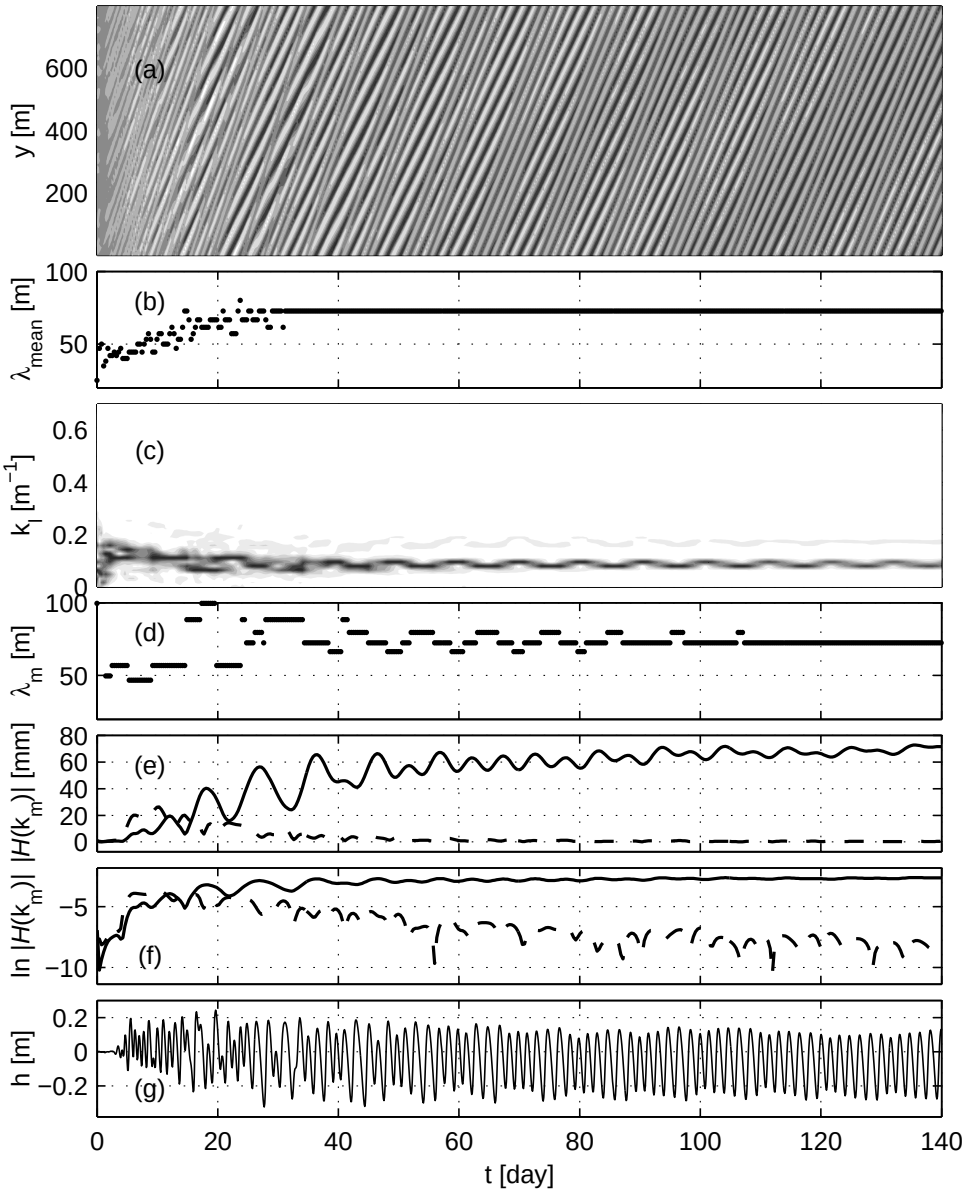

Figure 4.12: Planar beach, up-current oriented oblique bars. CWS default case (CWS transport, $\theta^0 = 25\,^\circ$). The graph description is the same as figure 4.9 but for (e) and (f), $\lambda_\mathrm{m} = 2\pi/k_\mathrm{m} =$ 50 m (dashed line), $\lambda_\mathrm{m} = 72$ m (thick line).

Again, this 'current refraction' is consistent with previous linear stability analysis (Ribas *et al.*, 2003). In this case (constant wave stirring), it is similar to that of storm currents over shoreface-connected ridges on the inner continental shelf (Trowbridge, 1995; Calvete *et al.*, 2001) which occurs at a larger length scale.

The steps observed in figure 4.10 are clearly recovered in figure 4.12(a). In particular, like the transverse bars and unlike the down-current oriented bars, these are visible on the total topography before having reached their final length. Complex dynamics in which the mean spacing λ_mean (figure 4.12b) oscillates around 50 m occur because of splitting and merging of bars during the first 10 days. Merging eventually dominates so that the mean spacing increases up to about $\lambda_\mathrm{mean} = 72$ m at day 35 and does

case	mode	H^0_{rms} ↗			θ^0 ↗				T ↗		
		A_{m}	λ_{m}	σ_{m}	λ_{m}	T_{m}	σ_{m}	c_{m}	A_{m}	T_{m}	c_{m}
SVR-i SVR-ii	1	↗	↗	↗	↗	↘	↗	↗	↘	↘	↗
CWS	1										
	2		↗↘		↘						

case	mode	γ ↗				
		A_{m}	λ_{m}	T_{m}	σ_{m}	c_{m}
SVR-i SVR-ii	1	↘	↗	↗	↘	↘
CWS	1					
	2		↘			

Table 4.4: Planar beach. Main influence of the variable input parameters (H^0_{rms}, θ^0, T and γ) on the characteristics of the dominant modes. The symbol ↗ (↘) means that the corresponding characteristic increases (decreases) when the input parameter increases.

not change anymore. Two states are observed (1) corresponding to the wavelength of about $\lambda_{\mathrm{mean}} = 50$ m (from day 5 to day 10) and (2) the final state (at day 140, but very close to day 35). In contrast with the transverse bar case, state (1) corresponds to a predominant mode different to the final one (figure 4.12*c, d*). In this default case, we will assume the bar system has reached state (1) at day 7. We will denote the corresponding predominant modes for states (1) and (2) by the subscripts $m1$ and $m2$, respectively (table 4.3). The oscillating Fourier coefficients of these two modes which are the most energetic are displayed in figure 4.12(*e, f*) and show how a final equilibrium is hardly reached by the system. Because of these oscillations, the computed growth rates of these modes are just crude approximations.

4.6.4 Parametric trends

4.6.4.1 Incident waves

The influence of changing H^0_{rms} between 0.5 and 1.25 m has been investigated in all the cases (see table 4.4). For waves smaller than 0.5 m the morphological system is stable so that bars do not grow. For waves bigger than 1.25 m, an extension of the cross-shore length of the domain is necessary. The dependence of bar formation on the wave height agrees with previous linear studies (Ribas, 2004). Indeed, an increase of wave height implies larger wavelengths (both λ_{m} and λ_{mean}) and a larger cross-shore span in direct relationship with a larger width of the surf-zone. It also implies larger bars in amplitude, but the shape (including the bar angle β_{m}) remains the same. The growth rate of the dominant mode also rises with rising wave height. In the case of oblique wave incidence, the period of bars keeps almost the same value, so the migration

celerity decreases with an increasing wave height. For the two SVR cases, the most of dependence occurs between $H^0_{\rm rms} = 0.5$ and 1 m. This is also the case for the mode 1 of the CWS case (which is dominant before the merging of bars). In particular, $\lambda_{\rm m}$ and $S_{\rm m}$ increase by the factor 1.6 while $H^0_{\rm rms}$ doubles. Nevertheless, in the CWS case, the growth of wave height stimulates nonlinearities, so the merging of bars is much stronger for waves of 1.25 m than for waves of 1 m and this leads to bar spacing of $\lambda_{m2} = 130$ m at the final state. In contrast, for waves of 0.5 m where bars do not merge, only mode 1 is present with a spacing of $\lambda_{m1} = 40$ m.

The wave angle is also a critical parameter for the formation of oblique bars (SVR-ii and CWS cases). Small wave incidence angles ($\theta^0 < 25\,^{\rm o}$) at the off-shore boundary have first been studied. By using the SVR transport, some cases lead to stability, but there is no clear threshold angle for the formation of down-current oriented bars. Where using the CWS transport, the threshold angle over which up-current oriented bars appear is about $\theta^0 = 20\,^{\rm o}$. Final amplitude is only 6 cm and only mode 1 is present. For larger wave incidence angles ($25\,^{\rm o} \leq \theta^0 \leq 45\,^{\rm o}$) (table 4.4), both for the SVR case and for CWS case (modes 1 and 2), the amplitude and the cross-shore span of the bar is not affected by the variation of the wave angle and the behaviour of the bars reveals some common tendencies: the increase of the wave angle implies the increase of $\sigma_{\rm m}$, the decrease of $T_{\rm m}$ and the increase of $c_{\rm m}$. Nevertheless, while $\beta_{\rm m}$ and $\lambda_{\rm m}$ decrease in the SVR case, they have an opposite behaviour in the CWS case for the two modes. In all cases, variation of bar characteristics does not exceed 40 % whereas the wave angle increases 80 %.

The increase of wave period from 6 to 12 s has a minor effect on the shape of the bars, although the final amplitude of the bars tends to reduce, and, in the case of oblique wave incidence, the bar period decreases a little which implies an increase of the migration celerity (table 4.4).

4.6.4.2 Bedslope parameter γ

For each case, the effect of the bedslope parameter γ has been investigated as indicated in table 4.3. For this range of γ, the results are summarised in table 4.4. For smaller values of γ, the bars grow too much and their tops tend to emerge from the water. The values of γ leading to numerically stable computations are characterized by a ratio of maximum bar amplitude to total mean water depth, $h/(D+h)$, not larger than about 0.6 during the simulation. In other words, if this ratio exceeds 0.6 at some location at some time, the numerical model crashes. On the other hand, for larger values of γ, patterns do not appear since an increase of bedslope transport coefficient causes an increase in morphodynamical diffusivity producing a damping of the patterns. For the same reason, the linear stability theory would suggest than an increase of bedslope transport coefficient would cause an increase of the spacing and a decrease of growth rate and, thereby, a decrease of the final amplitude (weakly nonlinear stability analysis, Knaapen 2001). This behaviour is observed in the SVR cases, where $\lambda_{\rm m}$ grows by 30 % and $\sigma_{\rm m}$ decreases by 70 % between the two critical values of γ, whereas the amplitude decreases down to 3 cm.

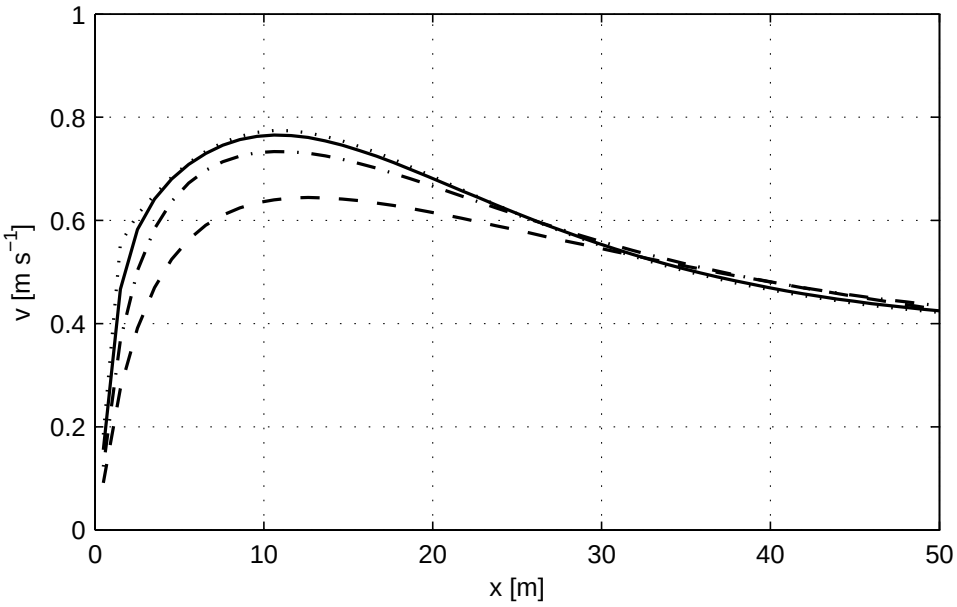

Figure 4.13: Planar beach. Variation of the turbulent parameter. SVR transport. Incident waves: $H^0_{\rm rms} = 1.0$ m, $T = 6$ s, $\theta^0 = 25\,^{\circ}$. Longshore velocity v at the basic state in the case of oblique wave incidence. Bottom axis: cross-shore distance. The coastline is at $x = 0$ m. $\cdots\cdots$, M=0.05; ——, M=1; —·—, M=5; – – – – –, M=20.

For the CWS case, the dynamics are more complicated. Indeed, mode 1 follows the same trends as described above and agrees with linear theory. Likewise, the amplitude and the growth rate of mode 2 also decrease with increasing γ. However, the final spacing λ_{m2} increases when γ decreases. This is probably because a very low γ leads to a strongly nonlinear regime where many wavelengths are allowed to interact, with the result that the dominant wavelength is a low subharmonic of the linearly dominant one. These increasing λ_{m1} and decreasing λ_{m2} with increasing γ lead to a particular case for $\gamma = 0.9$ where there is only one mode and bars do not merge.

More generally, the span of transverse bars remains the width of the surf-zone. For oblique bars, their angle is not affected, but their span grows when bars become larger. The migration velocity of oblique bars is also directly linked with the spacing: $c_{\rm m}$ decreases when $\lambda_{\rm m}$ increases, implying an even stronger reduction of $T_{\rm m}$.

4.6.4.3 Turbulent mixing

The effect of the wave-driven turbulence parameterization has been investigated in Garnier (2005). As in many numerical models, the default value of the turbulence parameter M, is $M = 1$ (equation 2.40). Nevertheless, there is a large degree of uncertainty in this value; experiments showing that computed values of $\nu_{\rm t}$ may are one order of magnitude larger than the measurements (Rodriguez *et al.*, 1999). Here, we extend the previous linear study Ribas (2000) in our nonlinear experiments. The influence of M varying between 0.05 and 20 is investigated.

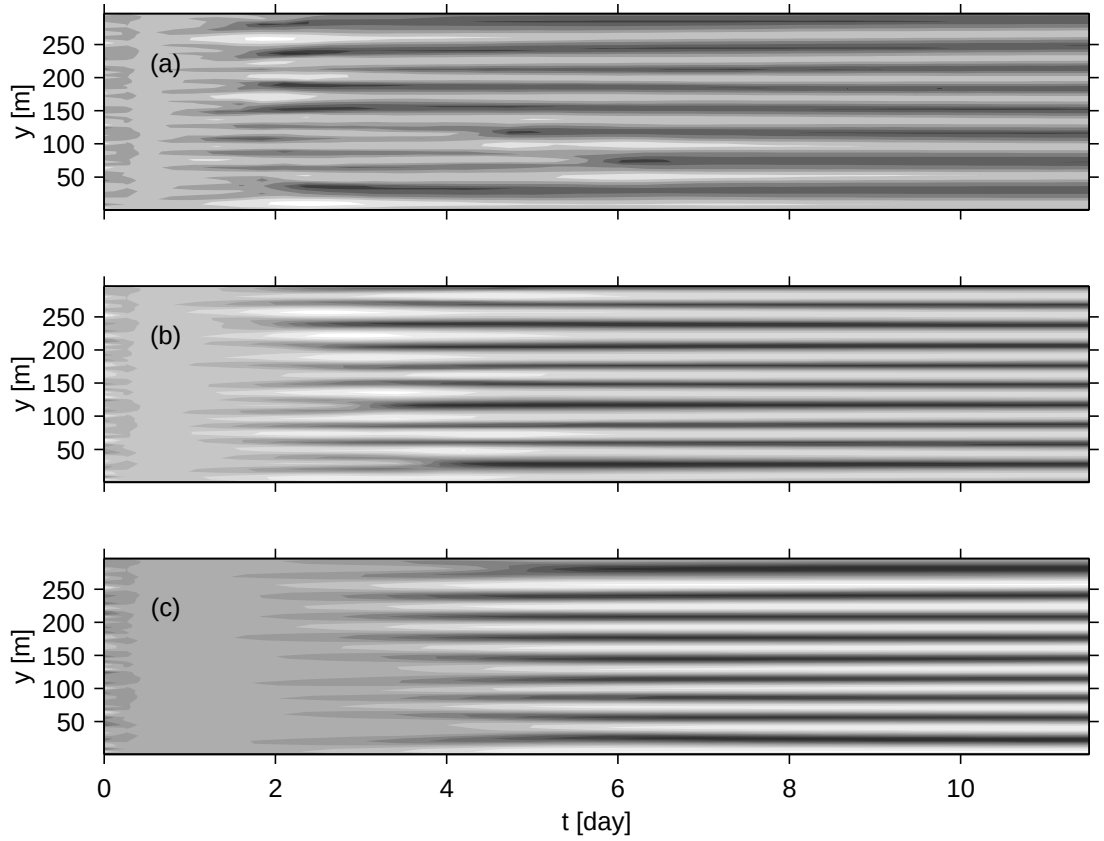

Figure 4.14: Planar beach, transverse bars. Variation of the turbulent parameter. SVR transport. Incident waves: $H^0_{\mathrm{rms}} = 1.0$ m, $T = 6$ s, $\theta^0 = 0\,^\circ$. Time series of the bed level along the longshore section at $x = 10$ m ($h(y,t)$), crests are white and troughs are black. (a) $M = 0.1$, (b) $M = 1$ and (c) $M = 2$.

For the basic state, i.e. the equilibrium state reached when there are not any alongshore irregularities on the bathymetry at the initial state, the initial topographic system remaining stable, a variation of the turbulence parameter only affects the hydrodynamics in case (SVR-ii), having a diffusive effect on the longshore current (figure 4.13). The effect of the variation of this parameter is weak because irregular waves are taken into account contrarily to Ribas (2000) which used the approximation of Longuet-Higgins (Longuet-Higgins, 1970) for regular waves. The decrease of M by the factor 20 does not affect the cross-shore profile of the longshore velocity whereas this profile is damped for an increase of M by the same factor, the relative maximum velocity decreasing by 10 %.

In the case of growing instabilities, the variation of the turbulence parameter M affects much more the behaviour of the bars. The ranging of M which allows the growth and the saturation of the bars is: $0.1 < M < 5$, remembering that in this interval of M, the hydrodynamics of the basic state is not affected (figure 4.13). Below the threshold value of $M = 0.1$, the numerical model crashes before leading to the saturation of the instabilities, and above $M = 5$ the morphological system keeps it stable.

More precisely, in case (SVR-i), the ranging of M is $0.1 < M < 2$ (figure 4.14). As the linear theory (Ribas, 2000) suggests, the diffusive effect of M affects the growth

rate of the dominant mode. The increase of M by factor 20 implies a divided-by-2 growth rate. The linear theory also suggests the increase of the initial wave spacing of bars. This is observed here, but the extension to the finite-amplitude regime shows a distinct behaviour. Indeed, the increase of the diffusivity in the momentum conservation equations allows less nonlinear behaviours in the bars evolution: less merging is observed so that the wave spacing of the bars at the final state is not unavoidably bigger. For example if M increases from 1 to 2, both the initial and the final wave spacing increases but if M increases from 0.1 to 1, the final spacing decreases.

The same behaviour is observed in the oblique down-current oriented bars (Garnier, 2005). We also observe that the migration velocity decreases when M increases.

4.6.4.4 Initial perturbed topography

Experiments have been done changing (1) the longshore size of the domain and (2) the alongshore non-uniform perturbations of the initial bathymetry.

(1) It is clear that if the longshore size of the domain is too small, the instabilities can not develop, or develop with a wavelength imposed by the domain size. To be sure that the domain size does not impose an unrealistic bars wavelength, the experiments have been firstly made by using a large domain (in the y-direction) (figure 4.15). Then, a predominant bar spacing is determined. The default domain is chosen as ten times this wavelength. We have shown that, if the longshore size of the domain is sufficiently large, even if it is not a multiple of the wavelength of the bars, the results are very close.

(2) Both (i) the structure of the initial energy spectrum and (ii) the amplitude of the initial perturbations may have an influence on the transient and final states.

   (i) In the default case, we use random perturbations. The use of random perturbations in a finite-grid does not give a uniformly distributed spectral energy (see figure 4.6, at day 0), some predominant modes already being present. Nevertheless, due to the presence of a lot of modes, we can consider that all modes may appear by interaction between the initial ones. To be sure of our consideration, we have made the experiments by using a uniformly distributed spectral energy. This has been obtained by adding a Dirac function to the uniform bathymetry (see figure 4.15, at day 0). We have found that the transient states may be affected, but the final dominant mode is unchanged.

   In some particular cases, the final states may depend on the initial perturbation. For instance, if only a few modes are present at the initial time, the nonlinear interactions are therefore limited. Thus, a different final state may be reached because of the non-uniqueness of the solution of our nonlinear system.

   (ii) The amplitude of the perturbation influences the growth time, particularly, the bars appear more rapidly for larger perturbation amplitudes. Nevertheless,

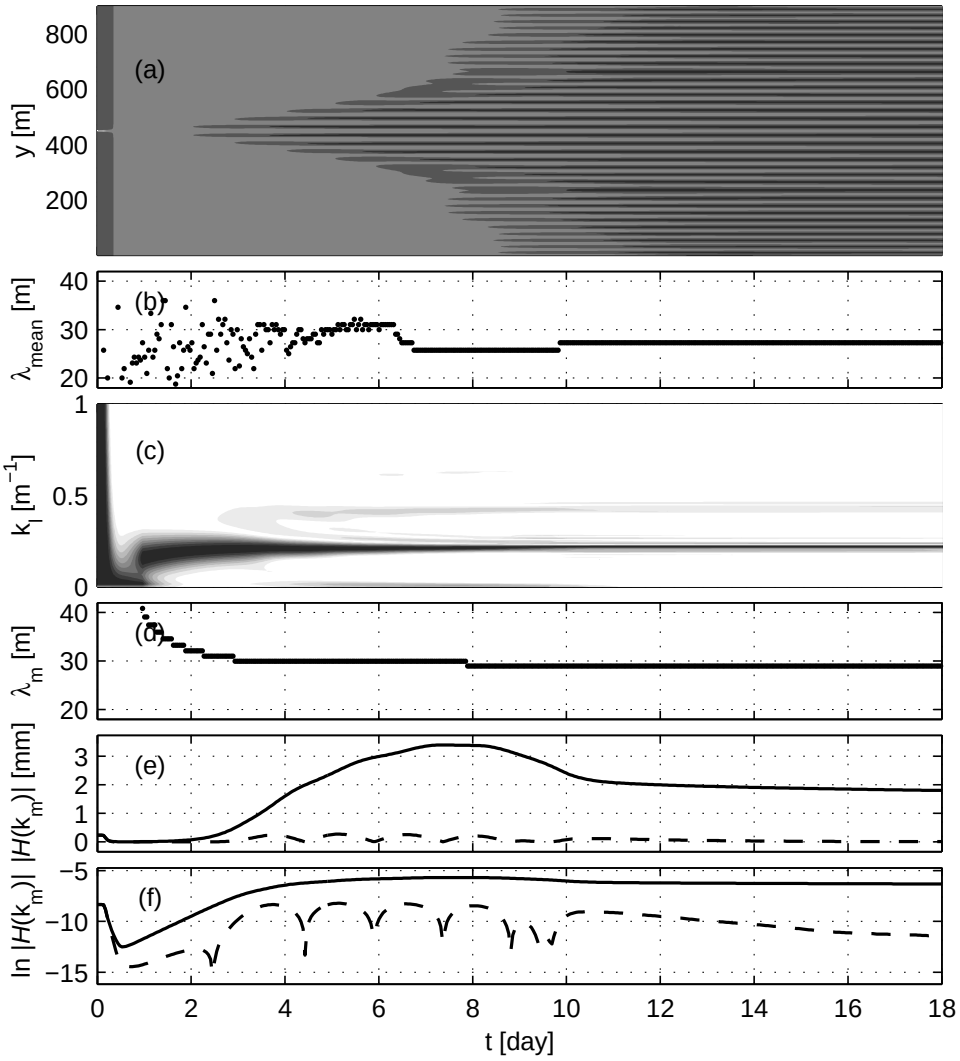

Figure 4.15: Planar beach, transverse bars. Different initial topography. SVR transport. Incident waves: $H^0_{\rm rms} = 1.0$ m, $T = 6$ s, $\theta^0 = 0\,^{\circ}$. The longshore size of the domain is extended by a factor 3. The initial perturbation is a Dirac function. The graph description is the same as figure 4.6.

the growth rate (or the e-folding time) of the dominant mode and the final state are not affected.

4.7 Conclusion

The previous results on the modelling of the formation of surf zone transverse/oblique bars (Ribas *et al.*, 2003; Caballeria *et al.*, 2002) have been recovered. The linear modelling of Ribas *et al.* (2003) predicts the formation of transverse bars, oblique down-current oriented bars and oblique up-current oriented bars in the same conditions as we observe here. Only the transverse bar systems were predicted by the nonlinear modelling of

Caballeria *et al.* (2002).Our bars have a smaller cross-shore extension. Moreover, each bar (trough) is extended in outer zone by a small trough (bar) giving a kind of crescentic pattern attached to the shoreline.

The main improvement achieved by this study has been the extension of the previous results to the finite-amplitude dynamics. Indeed, all the previous nonlinear studies are limited to the description of the initial steps of the evolution of rhythmic bars. Here, we have shown that the growth of rhythmic bars can saturate by surf zone processes. Moreover, equilibrium states of rhythmic instabilities have been reached. These states have been attained for highly idealised conditions with, most specifically, steady wave conditions. For normal waves, an equilibrium state of transverse bars may be reached after few days of morphological evolution. For oblique waves, oblique bars develop and saturate but are still in motion since they migrate with the longshore current. We qualify their final state as a dynamical equilibrium state. The saturation mechanism will be analysed in chapter 6.

Before reaching the final state, a complex dynamics occur owing to interactions between bars. In particular, merging and splitting of bars occurs, in general merging eventually dominates so that the final spacing of bars is often larger than the initial. The shape of bars also evolves from the initial state where their longshore profiles are sinusoidal to the final state where they have strong asymmetric properties. This asymmetry is represented by the corresponding rip current circulation: jet-like offshore oriented at the troughs, wide and weak onshore oriented at the bars. These nonlinear behaviours (merging/splitting of bars, asymmetry of both bars and currents) are often observed in nature.

Chapter 5

Barred beach instabilities*

5.1 Introduction

The nonlinear stability analysis of alongshore uniform barred beaches is studied. Numerous numerical studies describe the emergence of crescentic bars by self-organization of the coupling between topography, waves and currents. All these studies are limited to the formation of these rhythmic features, by using the linear stability analysis (Deigaard *et al.*, 1999; Klein *et al.*, 2002; Ribas *et al.*, 2003; Calvete *et al.*, 2005), or by using a nonlinear model (Caballeria *et al.*, 2002; Damgaard *et al.*, 2002; Castelle, 2004; Reniers *et al.*, 2004). Ridge and runnel systems also appear in many barred beaches (Castelle, 2004; Lafon *et al.*, 2002, 2004, 2005), but their numerical modelling is still unexplored. Conceptual models based on field observations show that ridges and runnels emerge by the deformation of the alongshore intertidal bar intercepted by crescentic bars (Castelle, 2004; De Melo Apoluceno, 2002), thus, these systems would appear as a further state of the evolution of crescentic bars. This suggests that the emergence of these systems cannot be described with a linear analysis and that an extension of the previous modelling studies on formation of rhythmic systems to the finite amplitude evolution is needed.

Firstly, simulations on the single barred beach presented in Yu & Slinn (2003) are made (section 5.2). This bathymetry is used by the linear stability analysis Calvete *et al.* (2005) on crescentic bar systems. We present its extension to the nonlinear regime for both normal and oblique wave incidence (sections 5.3 and 5.4, respectively). For oblique waves, a part of the results have been presented in Garnier *et al.* (2006*c*). The methodology to describe theses morphodynamical instabilities is similar to the one used in

*The general results of this chapter have been presented in Garnier *et al.* (2006*c*): Garnier, R., Calvete, D., Falqués, A. & Caballeria, M. 2006*c* Modelling ridge and runnel system development from an intertidal shore parallel bar. In *30th International Conference on Coastal Engineering*.ASCE, San Diego, USA. The application to the French Atlantic coast (section 5.5) has been presented in Garnier *et al.* (2006*a*).

chapter 4, but slightly simplified. Particularly, the parametric trends are not given as the same general trends are recovered. This first part consists in a theoretical study mainly motivated by the previous modelling studies which deals with this idealised bathymetry (Yu & Slinn, 2003; Calvete *et al.*, 2005; Garnier *et al.*, 2006*b*). However, this initial bathymetry is representative of many observed systems. In particular, the longshore bar is relatively close to the shore, so that it reminds us the intertidal zone of some beaches, for instance, of the French Atlantic beaches. The second part of this chapter (section 5.5) is dedicated to a more particular study by considering a characteristic bathymetry of the Truc Vert beach, France, from Castelle (2004). We focus our interest on the subtidal zone, particularly on the larger scale crescentic patterns emerging on the subtidal longshore bar. These simulations are taken from Garnier *et al.* (2006*a*).

5.2 Initial conditions and basic state

5.2.1 Initial topography

For the reference case, the alongshore uniform equilibrium profile is taken from Yu & Slinn (2003). In contrary to chapter 4, the longshore parallel bar is kept. The initial beach profile is defined as:

$$z_{\mathrm{b}}^{0}(x) = -a_0 - a_1\left(1-\frac{\beta_2}{\beta_1}\right)\tanh\left(\frac{\beta_1\,x}{a_1}\right) - \beta_2\,x + a_2\exp\left[-5\left(\frac{x-x_{\mathrm{c}}}{x_{\mathrm{c}}}\right)^2\right] \quad , \qquad (5.1)$$

where x_{c} is the bar location (default case: $x_{\mathrm{c}} = 80$ m and a_2 is the bar amplitude (default case: $a_2 = 1.5$ m). The height of the artificial wall is $a_0 = 25$ cm. The other parameters are defined in section 4.2. Figure 5.1 shows the three-dimensional view of this default bathymetry until the offshore boundary located at $x = L_x = 250$ m. The same profile has been used in the linear stability analysis of Calvete *et al.* (2005) which provides a useful tool for validating our initial results. This idealised profile is based on averages of the Duck beach, North Carolina, USA; nevertheless it is representative of many other beaches. In particular, it reminds us the intertidal zone of the French Atlantic coast which is known for its persistent crescentic bar and ridge and runnel systems.

5.2.2 Experiments and default parameters

Experiments have been done on the domain defined by: $0 \leq x \leq L_x = 250$ m and $0 \leq y \leq L_y = 2000$ m. The grid spacing is given by $(\Delta x, \Delta y) = (5, 10)$ m^2. The hydrodynamical time step is $\Delta t = 0.05$ s. The morphodynamical time step has been accelerated by the factor 150 and is $\Delta t_{\mathrm{m}} = 150\,\Delta t = 7.5$ s. Results are given up to 200 days of morphological evolution. The model formulation is the same as in the planar beach study (chapter 4), for the SVR case (Soulsby Van Rijn sediment transport, section 2.5.7.2). The default parameterization (described in chapter 2 and used in chapter 4) is used except for two parameter values. Firstly, the wave breaker index γ_{b} from

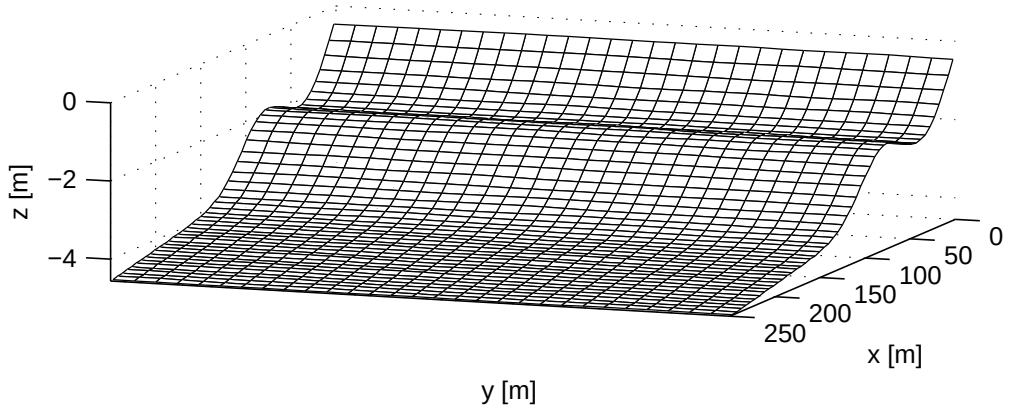

Figure 5.1: Barred beach. Initial beach profile. The shoreline is at $x = 0$.

equation 2.38 has been fixed to $\gamma_b = 0.6$ (default value: $\gamma_b = 0.42$). Indeed, by using the smaller value, waves start to dissipate very far off-shore and it seems unrealistic. The default parameterization has been validated relatively close to the beach (Thornton & Guza, 1983). We decided to use a bigger value as cross-shore extension of the computational domain is large ($L_x = 250$ m). Secondly, the downslope coefficient γ also takes a distinct value. It has been fixed to $\gamma = 5$ (default value: $\gamma = 1.5$). The default value has not been validated by data comparison and the down-slope sediment transport is not yet very well known. This parameter has been chosen in order to perform the saturation of the growth. By using the default value, the top of the bars tends to grow up to the mean sea surface. This causes overflow. The use of this new value provides the formation of transverse/oblique bar systems.

Two reference cases are described. (1) For normal wave incidence (section 5.3). (2) For oblique wave incidence (section 5.4), the wave angle is: $\theta^0 = 6\,^\circ$ at the seaward boundary. While in planar beaches (chapter 4) a large wave incidence angle ($\theta^0 \geq 20\,^\circ$) has been considered because it is more favourable of the development of instabilities (oblique up-current bars, in particular), it seems that barred beaches are more unstable in the cases of small wave incidence angle (Castelle, 2004).

5.2.3 Basic state

The cross-shore profiles of some variables at the basic state are shown in figure 5.2, in the oblique wave incidence case. Because of the presence of the longshore bar, some differences appear from the basic state of planar beach (figure 4.2). Indeed, whilst the transformation of the variables is similar in the inner surf zone ($x \leq 25$ m), a strong wave breaking occurs on the longshore bar and a second velocity peak appears at the top of the bar ($x = 80$ m). The stirring factor and the potential stirring curves (figure 5.3) also present a second peak at this cross-shore position.

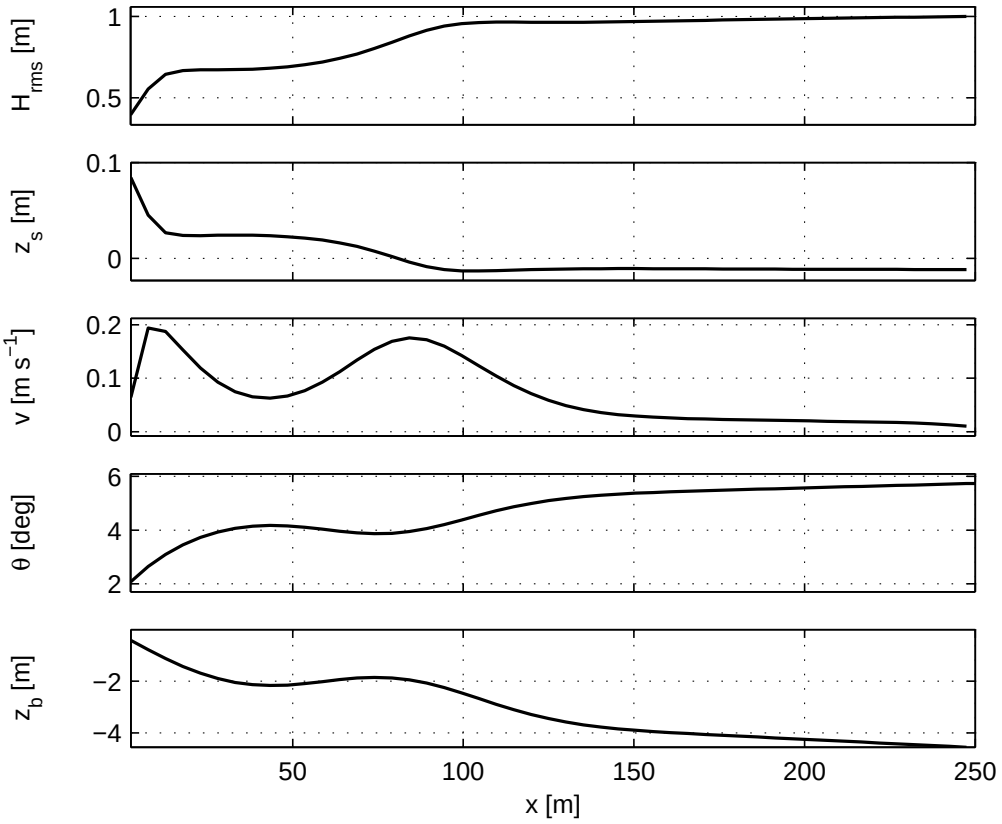

Figure 5.2: Barred beach. $H^0_{\rm rms} = 1.0$ m, $T = 6$ s, $\theta^0 = 5\ ^o$. Equilibrium profiles of the basic state in the case of oblique wave incidence. From top to bottom: wave height ($H_{\rm rms}$), mean sea level ($z_{\rm s}$), longshore velocity (v), wave angle (θ) and bottom level ($z_{\rm b}$). Shoreline at $x = 0$.

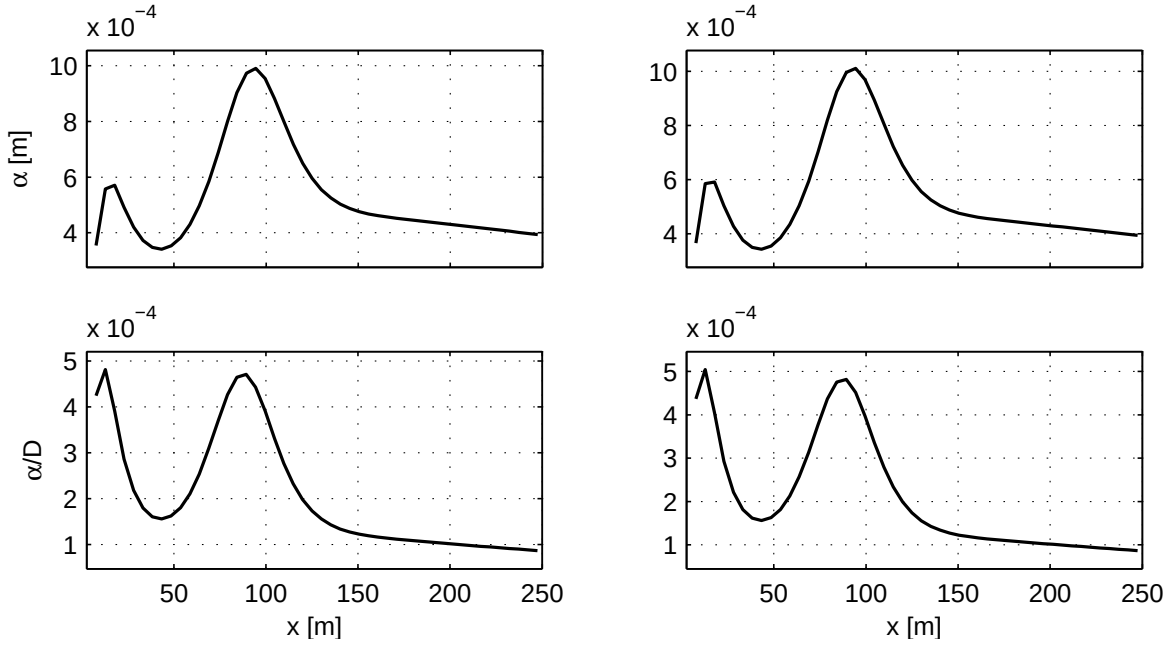

Figure 5.3: Barred beach. $H^0_{\rm rms} = 1.0$ m, $T = 6$ s. Stirring factor α (up) and potential stirring α/D (down) at the equilibrium state for the two cases (from left to right): i) $\theta^0 = 0\ ^o$, ii) $\theta^0 = 6\ ^o$.

5.3 Crescentic bars

For normal wave incidence, as predicted by previous modelling studies, crescentic patterns appear from a deformation of the longshore bar. From the initial time up to day 177, figures 5.4 and 5.5 show four snapshots of the bed level (z_b) and of the bottom perturbation (h), respectively. At day 0, the random perturbation is displayed. A series of bumps (troughs) appear on the shoreward part of the longshore bar with a sinusoidal shape (day 13) and extend seaward with less developed troughs (bump). At day 27, these crescentic bars have reached a maximum amplitude ($A_m = 0.49$ m) and are slightly damped until day 177 ($A_m = 0.45$ m). At this time, we consider that the bars have reached an equilibrium state. Their shape differs from the initial state (day 13) as they present asymmetry: in the shoreward part of the longshore bar, shoals have a larger longshore span than troughs. They extend onshore causing the undulation of the shoreline. Moreover, the general extension of the crescentic bars is larger. Figure 5.6 shows the current circulation on the total topography. The maximum current magnitude is 0.3 m s^{-1}. A clear rip-current system appears, jet-like offshore oriented in the sections defined by the troughs of the shoreward part of the longshore bar, and wider over the bars.

The time series presented in figure 5.7 give the predominant spacing of the bars. From the formation of the bars to the final state, it is $\lambda_m = 200$ m. With the same method as the one used in chapter 4, for each mode, the growth rate σ_m or its inverse, the e-folding time τ_m may be computed. In this case, we find a unique mode ($\lambda_m = 200$ m). The e-folding time is $\tau_m = 2.5$ day. Notice that this time is different from the growth time which is about 20 days. This time seems unrealistically large because it depends on the initial conditions, particularly on the amplitude of the initial perturbation. As the amplitude of the initial perturbations is only 2 cm, the growth time is large. When the model starts from higher perturbations, e.g. from bigger ripples or from a previous step of crescentic bars, the growth time is smaller. The e-folding time is a more reliable variable as it does not depend on the initial perturbations.

5.4 Ridges and runnels

For oblique wave incidence, crescentic patterns appear later with an oblique orientation (figures 5.8 and 5.9). On the shoreward part of the longshore bar, the patterns take a down-current orientation whereas on the seaward part, they take an up-current orientation. At day 27, we notice a slight undulation of the coastline which is much more significant at day 177. At this state, the shape of the bars is definitive but they are still migrating. We qualify this state as a dynamical equilibrium state. A kind of large oblique bar system is obtained, the troughs are deeper on the coastline, and the bars are higher at $x = 50$ m. The characteristic amplitude of the bars is $A_m = 0.68$ m. Figure 5.10 shows the current circulation. The ambient longshore current is deflected showing a rip-current system. Even if the model does not represent the tidal variation of sea level, it seems that the longshore bar on the initial bathymetry has similar char-

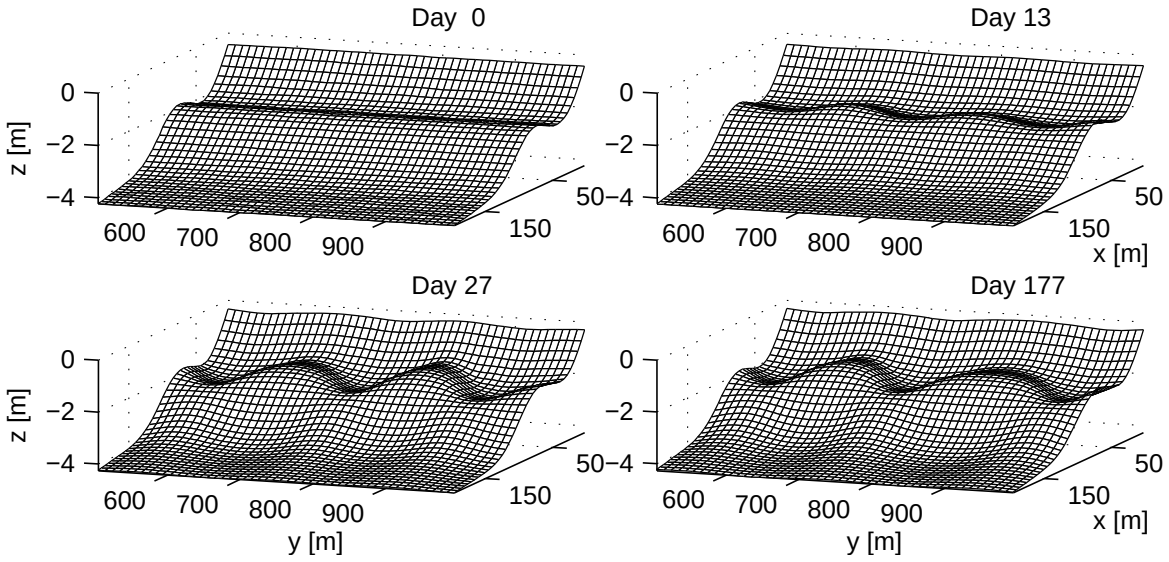

Figure 5.4: Barred beach. $H^0_{\rm rms} = 1.0$ m, $T = 6$ s, $\theta^0 = 0^o$. Zoom of the total bathymetry during the formation, development and growth saturation of crescentic bar systems.

acteristics than the intertidal bar on the French Atlantic coast, for mean tide level. The modelled rhythmic features remind us the ridge and runnel systems observed in nature. The model results are in agreement with the conceptual models Castelle (2004); De Melo Apoluceno (2002), the formation and the evolution of ridge and runnel systems being described through the following steps: (1) crescentic structure appears on the intertidal bar, (2) the crescentic bar sticks to the coast, (3) the ridge and runnel systems appear and migrate with the ambient longshore current.

Figure 5.11 shows a complex time evolution of the morphodynamical system. The initial mode seems to dominate until day 75, characterized by a predominant wave length of $\lambda_{\rm m} = 200$ m. Then, strong nonlinear behaviours of merging and splitting in bars appear. The predominant wave length oscillates between $250\,{\rm m} \leq \lambda_{\rm m} \leq 300\,{\rm m}$. In contrast to the previous results, the predominant wave length does not stabilise and seems to evolve periodically (with a period of about 50 days). We do not assume that this is a general result characteristic to the ridge and runnel evolutions. It is more a particular result that has been obtained in particular conditions. This illustrates the capability of the model to simulate strong nonlinear behaviours, and that an equilibrium state with a unique mode is not inevitably reached. The upper plot of figure 5.11 allows to compute the migration velocity of the bars which is about: $c_{\rm m} \sim 20\,{\rm m\,day^{-1}}$. This speed is larger than the observed one ($c_{\rm m} \sim 5\,{\rm m\,day^{-1}}$, Lafon *et al.* (2004)). This is probably because of the model simplifications, particularly: (1) the intense and constant wave conditions imposed by the model, (2) in nature, due to the tidal variation in sea level, ridge and runnel systems are dry for a significant time.

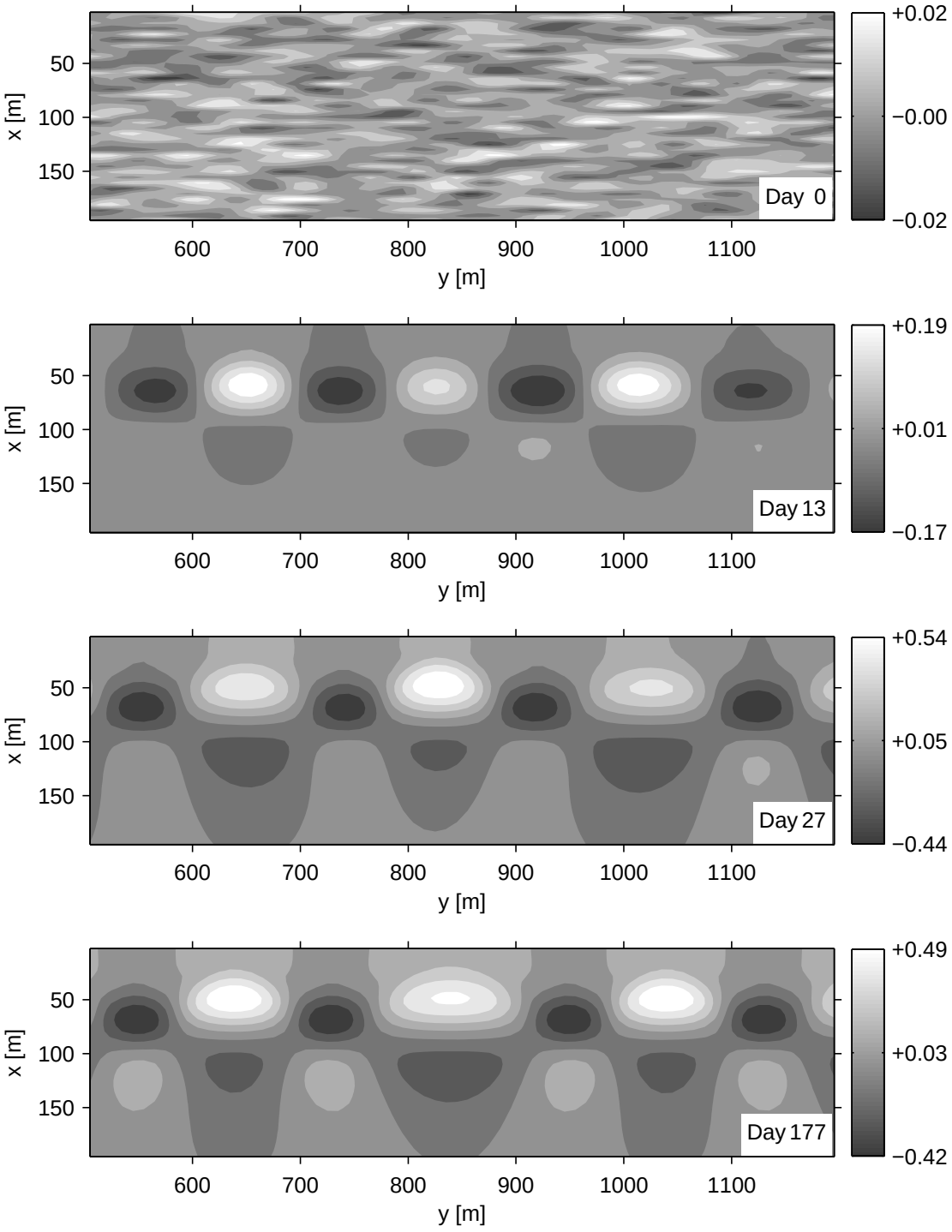

Figure 5.5: Barred beach. $H^0_{\mathrm{rms}} = 1.0$ m, $T = 6$ s, $\theta^0 = 0^o$. Snapshots of the bottom perturbation h.

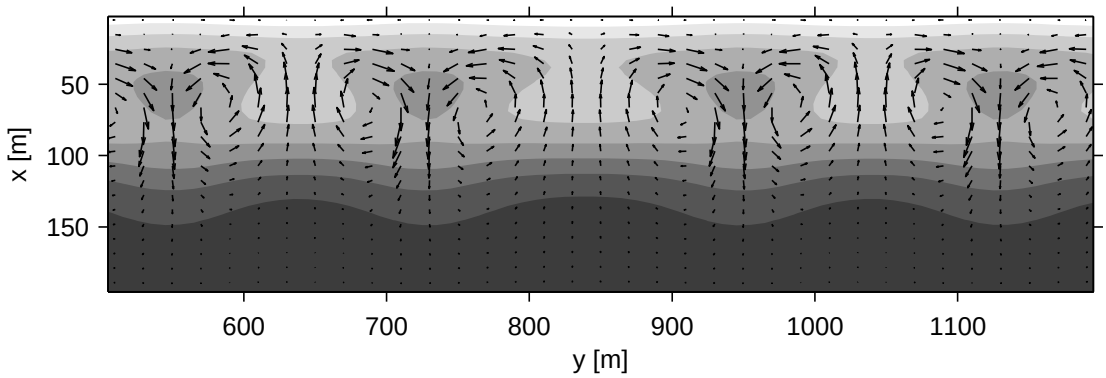

Figure 5.6: Barred beach. $H^0_{\mathrm{rms}} = 1.0$ m, $T = 6$ s, $\theta^0 = 0^o$. Final state (day 177). Bathymetric contours (z_{b}) and circulation ($\vec{v}$) over crescentic bar systems. The shallowest areas are white and the deepest areas are shaded. Zoom of the total bathymetry during the formation, development and growth saturation of ridge and runnel systems. Maximum current magnitude: 0.3 $\mathrm{m\,s^{-1}}$.

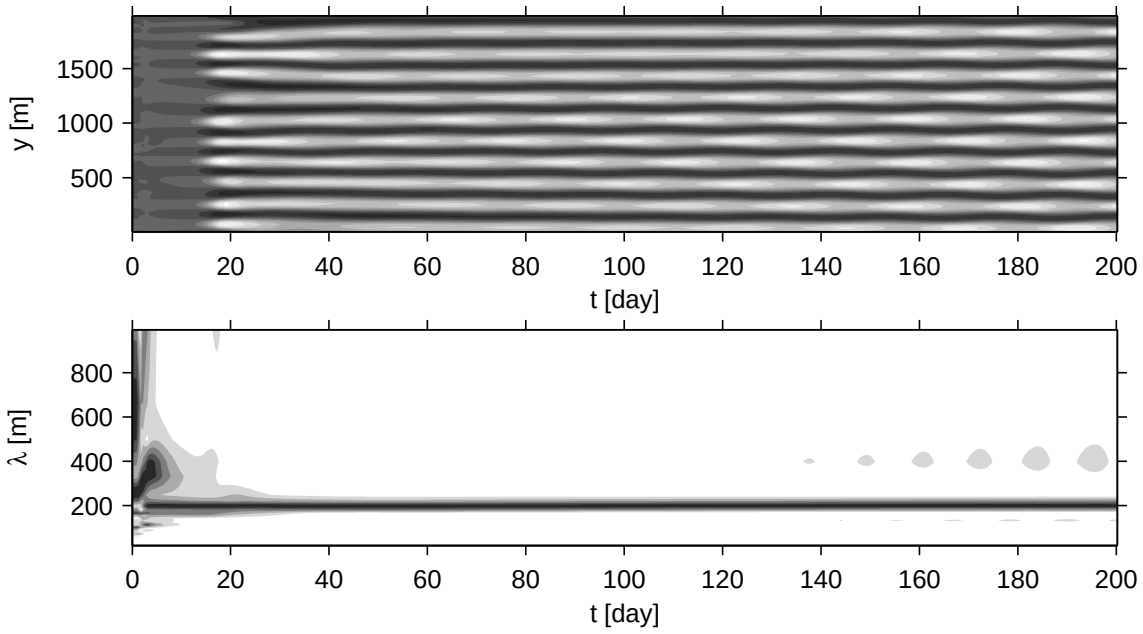

Figure 5.7: Barred beach. $H^0_{\mathrm{rms}} = 1.0$ m, $T = 6$ s, $\theta^0 = 0^o$. Time series of: Up, the bed level along the longshore section at $x = 80$ m ($h(y,t)$), crests are white and troughs are black, Down, the resulting predominant spacing of bars ($\lambda_{\mathrm{m}}(t)$) obtained by Fourier analysis.

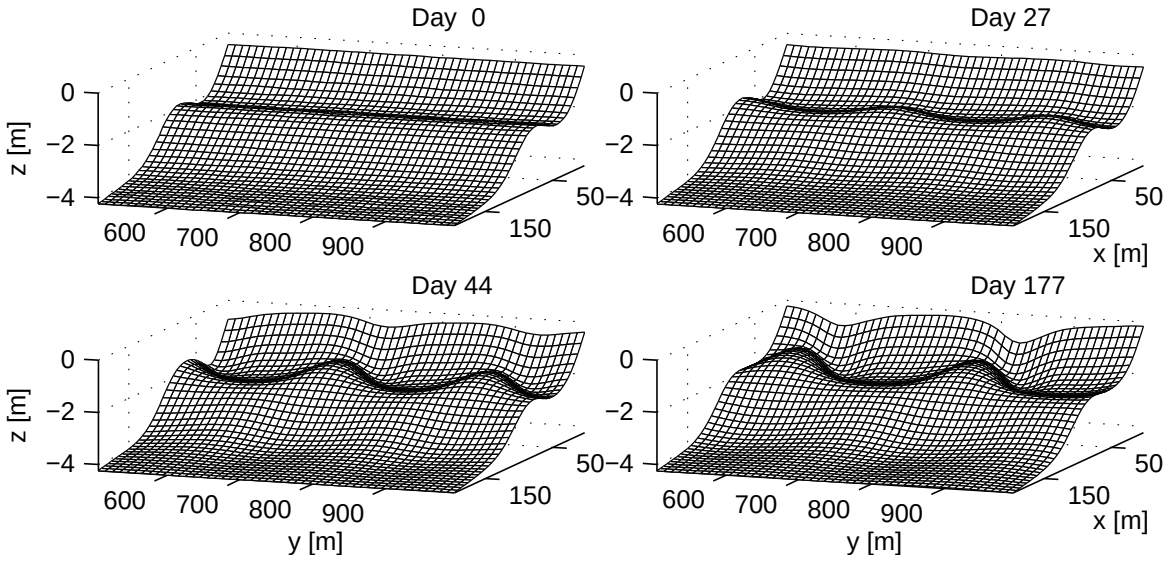

Figure 5.8: Barred beach. $H^0_{\rm rms} = 1.0$ m, $T = 6$ s, $\theta^0 = 6^o$. Zoom of the total bathymetry during the formation, development and growth saturation of ridge and runnel systems.

5.5 French subtidal crescentic bars*

5.5.1 Introduction

More than one longshore sand bar may be found in nature. For instance, the French Atlantic sandy coast is usually characterized by its double barred beach profile (Castelle, 2004; Lafon *et al.*, 2004, 2005). This coast may be classified as a mesotidal to macrotidal environment; in general the tidal range varies from 3 m to 4 m. In the intertidal zone, the inner (intertidal) bar displays crescentic bar systems or ridge and runnel systems. In the first part of this chapter, we have studied the case of a single 2 m depth bar beach. This could represent the intertidal zone of French beaches for a particular tide level: when the sea level has increased by about 2 m from the low tide. In the subtidal zone, the outer (subtidal) bar displays larger scale crescentic bar systems. The depth at the top of the longshore bar is about 6 m (at mid tide) so that the crescentic bars are immerged all the time. Thus, the mechanisms of the generation and evolution of these subtidal rhythmic features are only governed by surf zone processes. This was not so clear concerning the emergence of tidal patterns because swash zone processes may play an important role. The present model should therefore be more suitable for describing subtidal beach instabilities.

In general, the characteristic wave length of crescentic bars depends on the position of the longshore bar (Damgaard *et al.*, 2002), this explains that subtidal crescentic systems have larger spacing than intertidal systems. Nevertheless, the former are characterized

*This section has been presented in Garnier *et al.* (2006*a*): Garnier, R., Bonneton, P., Falqués, A. & Calvete, D. 2006*a* Modélisation de la formation et de l´évolution non linéaires des barres en croissant de la côte aquitaine. In *IX* emes *Journées Nationales Génie Côtier - Génie Civil*. Brest, France.

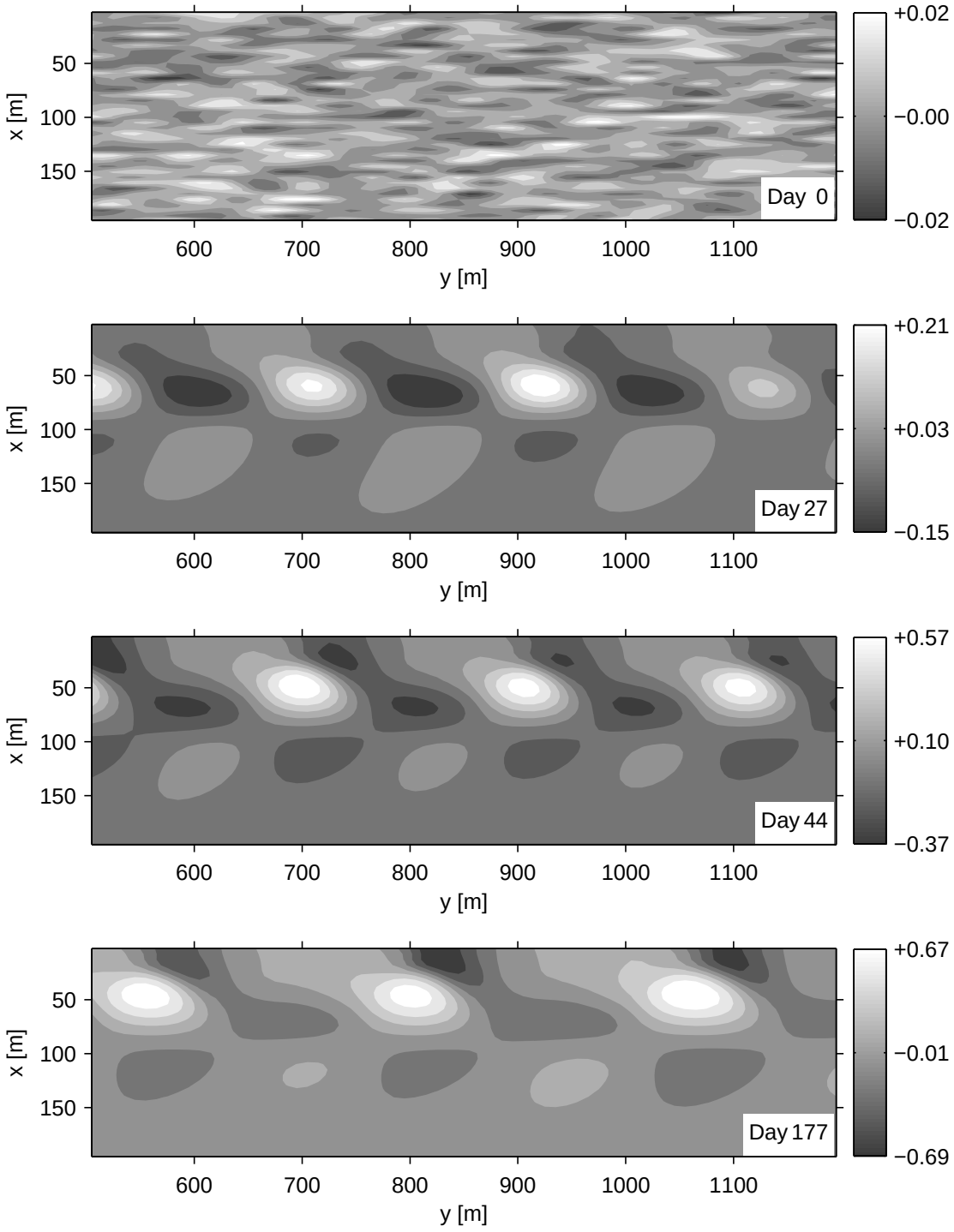

Figure 5.9: Barred beach. $H^0_{\rm rms} = 1.0$ m, $T = 6$ s, $\theta^0 = 6^o$. Snapshots of the bottom perturbation h.

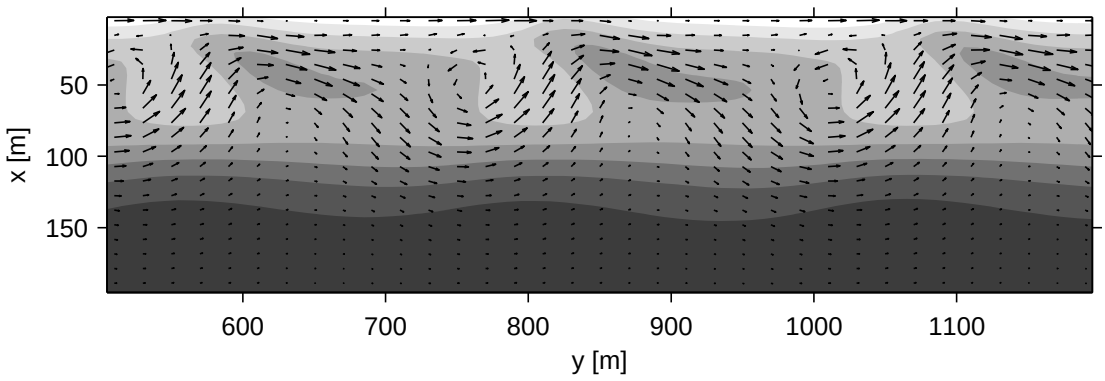

Figure 5.10: Barred beach. $H^0_{\mathrm{rms}} = 1.0$ m, $T = 6$ s, $\theta^0 = 6^o$. Final state (day 177). Bathymetric contours (z_{b}) and circulation ($\vec{v}$) over ridge and runnel systems. The shallowest areas are white and the deepest areas are shaded. Zoom of the total bathymetry during the formation, development and growth saturation of ridge and runnel systems. Maximum current magnitude: $0.4\ \mathrm{m\,s^{-1}}$.

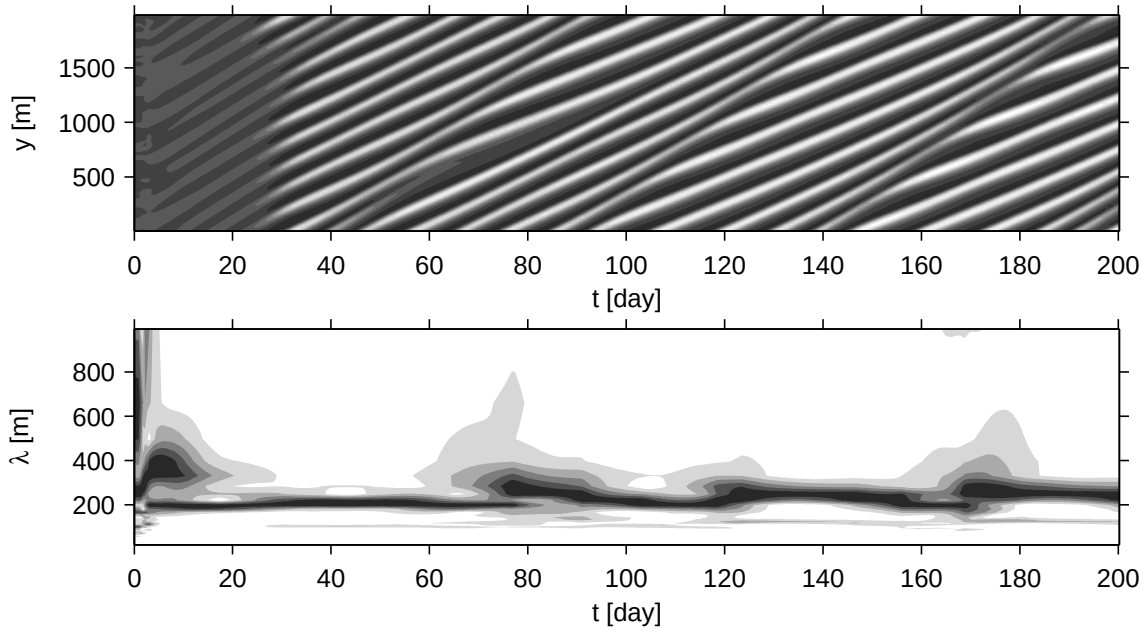

Figure 5.11: Barred beach. $H^0_{\mathrm{rms}} = 1.0$ m, $T = 6$ s, $\theta^0 = 6^o$. Time series of: Up, the bed level along the longshore section at $x = 80$ m ($h(y,t)$), crests are white and troughs are black, Down, the resulting predominant spacing of bars ($\lambda_{\mathrm{m}}(t)$) obtained by Fourier analysis.

by a wave length ranging between 300 m and 1500 m whereas the position of the subtidal bar is almost constant. This suggests that the wave length of crescentic bars depends on other variables. This study allows us to gain insight on the wave length dependence, by looking at the finite amplitude dynamics.

5.5.2 Experiments

The initial equilibrium bathymetry is taken from Castelle (2004) and is based on a longitudinal average of bathymetric profiles of the Truc Vert beach at mean tide level. The size of the computational domain is defined by $0 \leq x \leq L_x = 1000$ m and $0 \leq y \leq L_y = 9000$ m. The morphodynamical time step is 18 s. The grid spacing is 25×25 m^2. Four wave conditions are considered: normal waves with a period of $T = 12$ s and a wave height (at the seaward boundary) of $H^0_{\text{rms}} = 1.5$ m (case (a)) and $H^0_{\text{rms}} = 1.8$ m (case (b)); corresponding cases for oblique wave incidence ($\theta^0 = 6\,^{\text{o}}$ at the seaward boundary) are denoted cases (c) and (d), respectively.

The model formulation is the same as in the previous sections (and as in chapter 4). The default parameterizations have been kept except for the bedslope coefficient which is fixed to: $\gamma = 2$. In this particular case ($\gamma = 2$), chapter 4 would suggest that oblique/transverse bars appear. Nevertheless, these instabilities with a wave length of $\lambda \sim 30$ m are filtered due to the large grid spacing ($\Delta x = \Delta y = 25$ m). The bathymetric profile is displayed in the bottom plot of figure 5.12. It shows the presence of two longshore bars: at $x = 200$ m and at $x = 550$ m. Crescentic patterns appear on the inner bar reminiscent of the instabilities of the previous sections. Here, probably because of an underestimated bedslope coefficient in this area, they do not attain saturation and an overflow of the model occurs. In order to study the long term behaviour of the subtidal crescentic bars, the sediment transport has been disconnected in the inner surf zone, for $x < 200$ m.

The basic state is shown in figure 5.12 for oblique waves. Notice that the wave transformation in the two cases is very similar between $0 \leq x \leq 200$ m because of the Thornton and Guza wave dissipation formula (Thornton & Guza, 1983). The intensity of the longshore current is larger for higher waves; in the outer zone $x \geq 200$ m, the maximum current magnitude is on the top of the bar: 0.06 m s^{-1} for waves of 1.5 m and 0.12 m s^{-1} for waves of 1.8 m.

5.5.3 Stationary wave conditions

Figure 5.13 shows a snapshot of a part of the topography until day 222 in case (a). At this time, the beach system has reached an equilibrium state: the wave length is 650 m and the height of the bar is 2.80 m. A top view of the topography is shown in 5.14. A rip current system is observed at the bar location (offshore (onshore) oriented current at the troughs (shoals) of the crescentic bars) and an opposite circulation appears in the inner zone. Figure 5.15(a) represents the time evolution of the longshore section

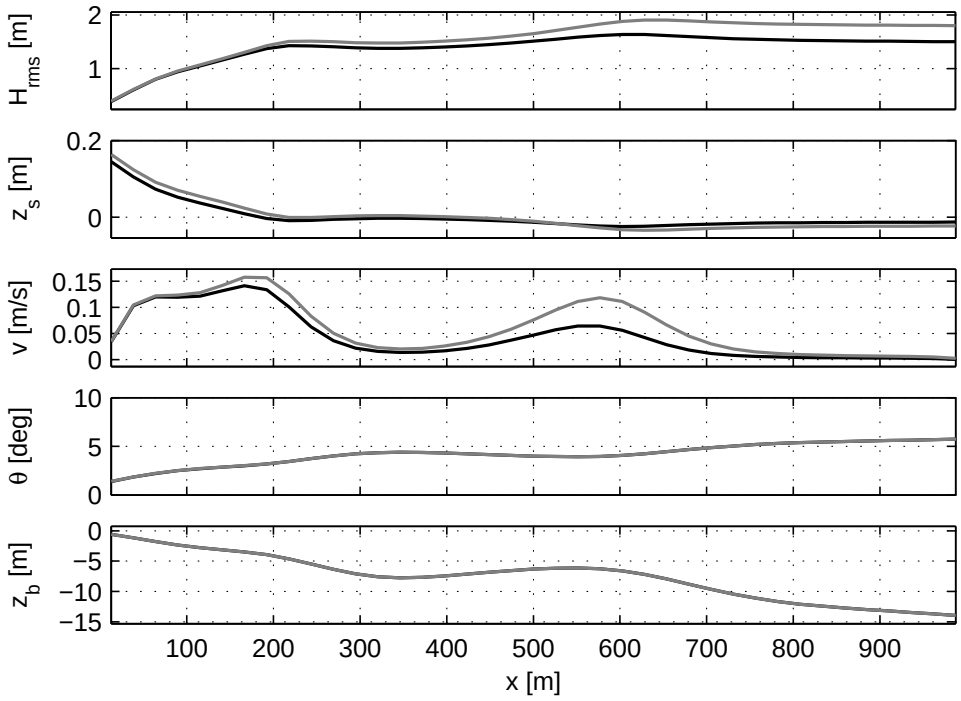

Figure 5.12: Truc Vert beach. Basic states. Black lines: case (c), oblique waves of 1.5 m. Grey lines: case (d), oblique waves of 1.8 m.

corresponding to the top of the bar. The rhythmic bars reach their maximum amplitude at about day 75, and then slightly decrease to reach an equilibrium state at day 200. For bigger waves (figure 5.15(b)), as the previous studies suggest (Damgaard *et al.*, 2002; Calvete *et al.*, 2005), the height and the growth rate of the bars are larger. The bars reach their maximum amplitude at about day 45. The e-folding time is $\tau_{\mathrm{m}} = 12$ day in case (a) and $\tau_{\mathrm{m}} = 5$ day in case (b). Nevertheless, contrarily to the previous studies, the final wave length at the final state is smaller (case (a): $\lambda_{\mathrm{m}} = 650$ m, case (b): $\lambda_{\mathrm{m}} = 550$ m). The variation of the wave height between (a) and (b) is slight, and we observe similar wave lengths at the initial state ($\lambda_{\mathrm{m}} = 500$ m). The predominant effect of this increase of wave height is probably bear in the Reynolds stresses which are more intense for bigger waves. For bigger waves, the diffusivity of the system is therefore larger so that the nonlinear interactions are reduced. This may explain the reason for a higher tendency of bars merging for smaller waves. For oblique waves, the growth rate is almost the same. Concerning the wave length, the effect of increasing wave height reduces the final wave length is observed too: at the initial state, the wave length is $\lambda_{\mathrm{m}} = 500$ m in both cases, at the final state it is $\lambda_{\mathrm{m}} = 750$ m in case (c) and $\lambda_{\mathrm{m}} = 700$ m in case (d). The bars migrate down-current with the migration velocity of $c_{\mathrm{m}} = 5\,\mathrm{m\,day^{-1}}$ in case (c) and $c_{\mathrm{m}} = 12\,\mathrm{m\,day^{-1}}$ in case (d).

5.5.4 Varying wave conditions

Incident waves of 1.8 m high have been imposed on the final state of case (a): case (a_2), and incident waves of 1.5 m high have been imposed on the final state of case (b):

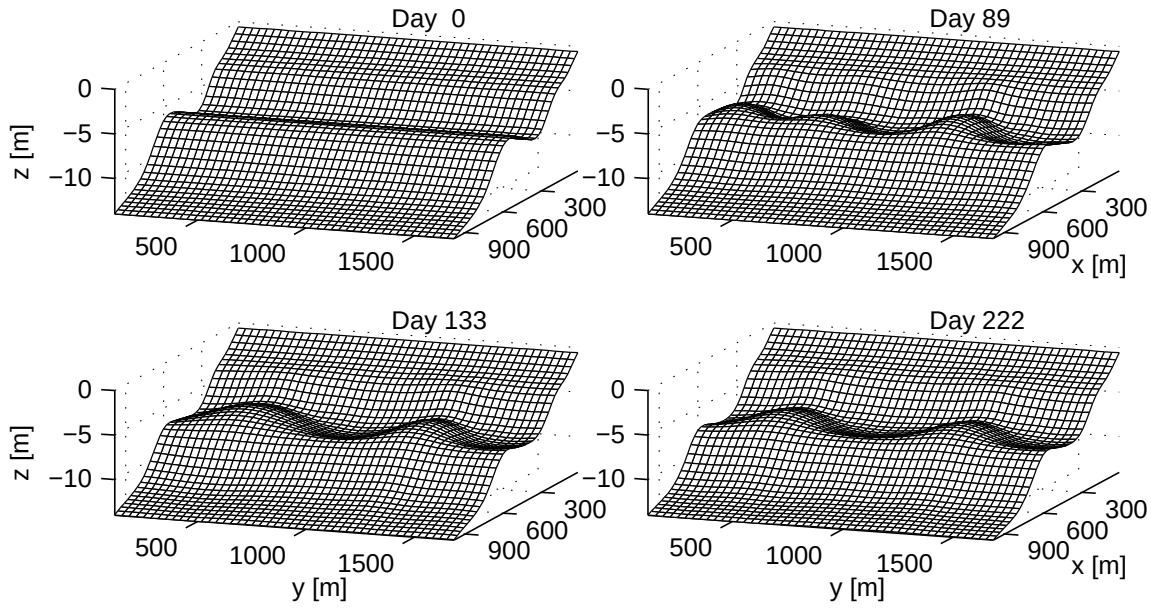

Figure 5.13: Truc Vert beach. Three dimensional view of the Truc Vert beach. Case (a): normal wave incidence, $H^0_{\rm rms} = 1.5$ m, $T = 12$ s.

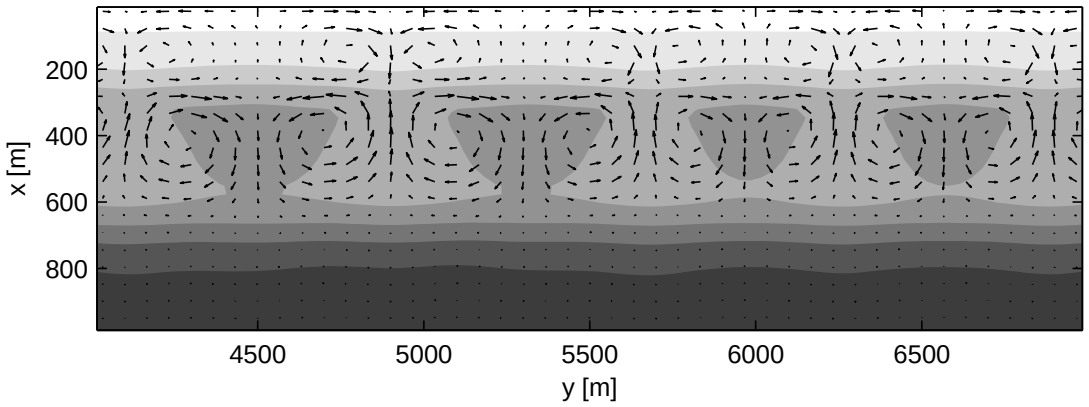

Figure 5.14: Truc Vert beach. Final state of the crescentic bar system (day 150) in case (a). Normal wave incidence, $H^0_{\rm rms} = 1.5$ m, $T = 12$ s. For the figure description, see figure 5.6. Maximum current magnitude: 0.16 m s^{-1}.

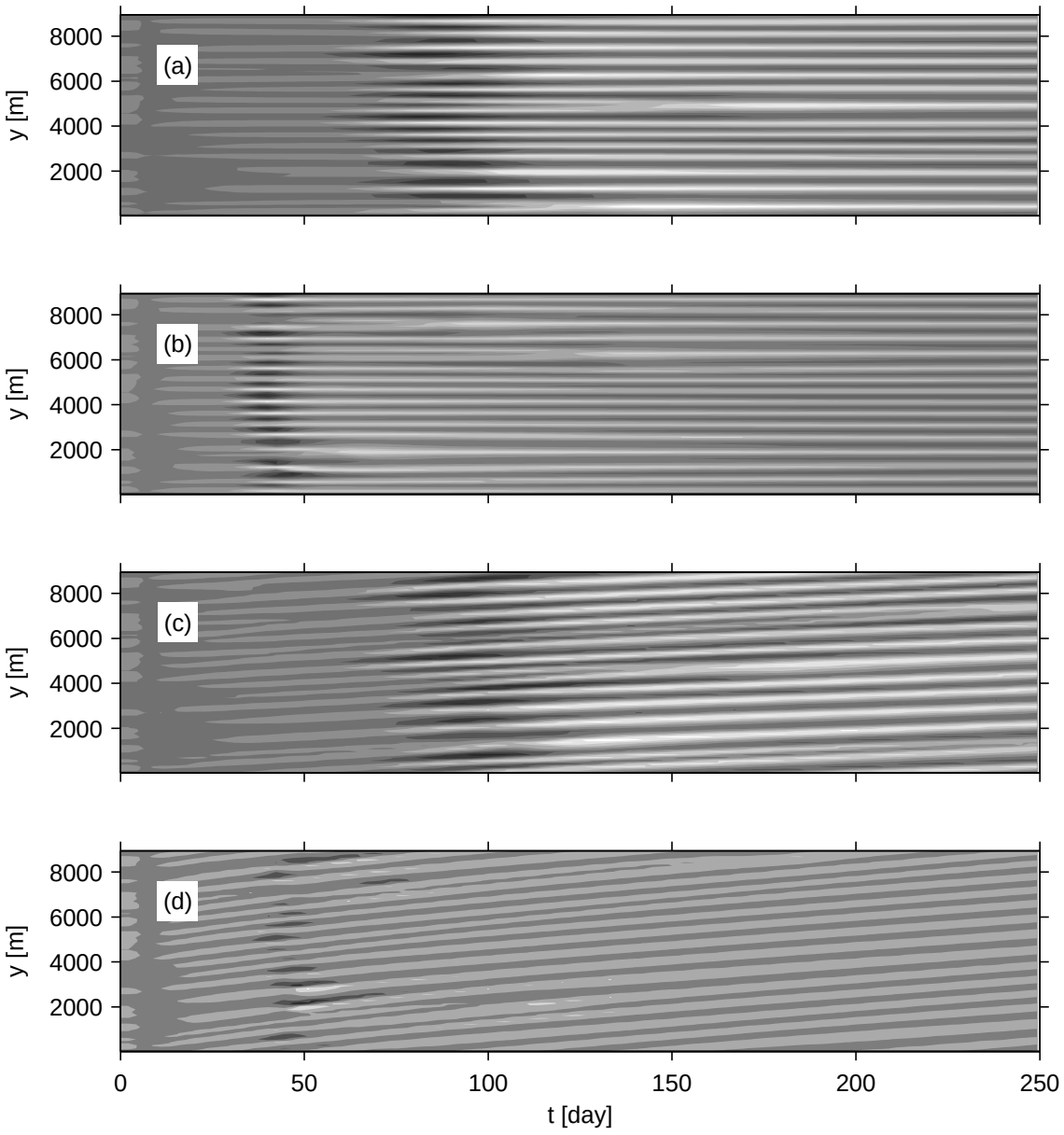

Figure 5.15: Truc Vert beach. Time series of the bed level along the longshore section at $x = 500$ m ($h(x = 500, y, t)$). The panels are labelled as their respective cases: (a): normal waves and $H^0_{\mathrm{rms}} = 1.5$ m, (b): normal waves and $H^0_{\mathrm{rms}} = 1.8$ m, (c): oblique waves and $H^0_{\mathrm{rms}} = 1.5$ m, (d): oblique waves and $H^0_{\mathrm{rms}} = 1.8$ m.

case (b_2). While the shape of the bars (asymmetry and height) is recovered, it does not therefore depend on the initial conditions, both in case (a_2) and in case (b_2), the initial wave length is kept, in particular no merging/splitting of bars is observed from the initial states of (a_2) and (b_2) (the results are not plotted). Thus, the final equilibrium state is not unique and depends on the initial conditions.

5.5.5 Conclusion

Equilibrium states of the subtidal crescentic bar systems of the Truc Vert beach have been found. We have shown that an increase of the incident wave height may imply a decrease of the final wave length of bars. This is not a general result but this suggests the importance of the nonlinear modelling in the prediction of the wave length of rhythmic features.

5.6 Conclusion

This chapter performs the first morphological study of the long-term evolution of crescentic systems. The previous results on the formation of crescentic bars have been recovered. Particularly, in sections 5.3 and 5.4, we have reproduced experiments of the linear stability analysis Calvete *et al.* (2005) and our initial results are in agreement. These results have been extended to the nonlinear regime showing, (1) an equilibrium state of crescentic bars may be reached, (2) the characteristic of the final dominant mode may differ from the initial mode, (3) the wave length does not inevitably stabilise and may remain oscillating, (4) ridge and runnel systems may appear as a subsequent mode of intertidal crescentic bars, for oblique wave incidence, (5) as say the observations, crescentic features developing on a inner longshore bar (sections 5.3 and 5.4), have different characteristics than the subtidal crescentic bars (section 5.5).

Chapter 6

Physical mechanisms of beach instabilities*

6.1 Introduction

The physical mechanisms behind the nonlinear evolution of the surf zone bars are presented. Firstly, an explanation for the growth of bars is given. It has been introduced in the previous studies Falqués *et al.* (1996, 2000); Caballeria *et al.* (2002); Ribas *et al.* (2003); Calvete *et al.* (2005) and has been extended in our results. The general method used is a local analysis since it involves the spatial distribution of the potential stirring. This traditional approach has the interest of being suitable for a comparison with field data; in particular, the potential stirring could be measured as it is a depth averaged concentration. However this technique does not allow understanding as to why the growth of bars saturates. For instance, for oblique waves, even at a saturated state, the bars are still in movement (they migrate), a local analysis of the potential stirring will still predict erosion and accretion. This precise case suggests the use of other techniques by integrating the processes of migration. We propose a second method given by a global analysis which involves the bar dynamics on the whole domain by introducing new space integrated variables as the mean production term and the mean damping term.

*This part is mainly taken from Garnier *et al.* (2006*b*): Garnier, R., Calvete, D., Falqués, A. & Caballeria, M. 2006*b* Generation and nonlinear evolution of shore-oblique/transverse sand bars. *J. Fluid Mech.* **567**, 327–360.

6.2 Local analysis of the growth

The first part of this section presents the general method used to understand the physical mechanisms behind the growth of surf zone bars. It has been introduced in the previous studies Falqués *et al.* (1996, 2000); Caballeria *et al.* (2002); Ribas *et al.* (2003); Calvete *et al.* (2005). Then, it is applied to each case of rhythmic features described in chapters 4 and 5.

6.2.1 General method

According to the present modelling, the formation of the bars is due to a feedback between the morphology and the water flow which is positive – and dominant – only for certain shapes of the bars. Obviously, this is an output of the coupling between morphology and water motion through the sediment transport and it is as a result of sediment, water, momentum, and energy conservation. However, the reasons why certain bar shapes grow and others do not, why it results in particular longshore spacing, migration celerity and final amplitude are not straightforward. Nevertheless, some further insight may be gained by looking at the spatial distribution of the potential stirring, α/D, as done in some previous studies (Falqués *et al.*, 2000; Coco *et al.*, 2002; Ribas *et al.*, 2003).

By using the sediment flux expression (equation F.1), the sediment conservation equation 2.22, reads

$$(1-p)\frac{\partial h}{\partial t} + \vec{\nabla}\cdot(\alpha\vec{v}) - \vec{\nabla}\cdot(\Gamma\vec{\nabla}h) = 0 \ , \tag{6.1}$$

where $\Gamma = \gamma\alpha u_\mathrm{b}$ and where $\partial z_\mathrm{b}/\partial t = \partial h/\partial t$ since z_b^0 is constant in time. Notice that the main difference with Caballeria *et al.* (2002) is that it is here assumed that, in general, $\alpha = \alpha(|\vec{v}|, u_\mathrm{b})$. Thus, if the sediment flux was for instance proportional to $|\vec{v}|^{m-1}\vec{v}$, the factor $|\vec{v}|^{m-1}$ would now be included in α in contrast with Caballeria *et al.* (2002). According to the water mass conservation (equation 2.9),

$$\vec{\nabla}\cdot(\alpha\vec{v}) = \vec{\nabla}\cdot\left(\frac{\alpha}{D}D\vec{v}\right) = D\vec{\nabla}\left(\frac{\alpha}{D}\right)\cdot\vec{v} - \frac{\alpha}{D}\frac{\partial D}{\partial t} \ . \tag{6.2}$$

By inserting equation 6.2 in equation 6.1,

$$(1-p)\frac{\partial h}{\partial t} + D\,\vec{v}\cdot\vec{\nabla}\Pi = \vec{\nabla}\cdot(\Gamma\vec{\nabla}h) + \Pi\frac{\partial D}{\partial t} \tag{6.3}$$

is obtained, where $\Pi = \alpha/D$ stands for the potential stirring. The last term in this equation can be neglected because of the following. Firstly, a reasonable upper bound for the stirring coefficient can be obtained from the SVR sediment transport in case of $|\vec{v}| \sim 1\,\mathrm{m\,s^{-1}}$ as $\alpha \lesssim 0.001$ m and, by assuming $D \gtrsim 0.1$ m, we can therefore assume $\Pi \lesssim 0.01$ (see also figure 4.3). Secondly, if the effects of infragravity waves on sediment transport are neglected, we can assume that the flow adjusts instantaneously to the slow bed changes (quasi-steady behaviour, see Caballeria *et al.* (2002)). In this situation,

$|\partial D/\partial t| = |\partial z_s/\partial t - \partial h/\partial t| \sim |\partial h/\partial t|$. Thus, the last term on the right-hand side in equation 6.3 is much smaller than the first one on the left-hand side and we can therefore use the following bottom evolution equation (BEE):

$$(1-p)\frac{\partial h}{\partial t} = \vec{\nabla}\cdot(\Gamma\vec{\nabla}h) - D\,\vec{v}\cdot\vec{\nabla}\Pi\,. \tag{6.4}$$

If the last term on the right-hand side is ignored, this is a diffusion equation for the bed perturbation, $h(x,y,t)$, and Γ is hence referred to as morphodynamical diffusivity. Thus, without the second term on the right-hand side, the bed perturbations would just diffuse away (and propagate owing to advection effects because of the gradient in Γ), but instabilities could not develop. If morphodynamical instabilities occur, they should be induced by the second term. The condition for instability is that this term be positive (causing $\partial h/\partial t > 0$) over the shoals ($h > 0$) and negative (causing $\partial h/\partial t < 0$) at the bed depressions ($h < 0$). This means that to have instability, the current must go against the gradients in potential stirring at the shoals and with the gradients in potential stirring at the troughs. Given a particular current ($\vec{v}$) and wave (u_b) distributions, BEE allows for predicting and understanding the morphodynamical effect of such a hydrodynamical pattern. In particular, once the hydrodynamical pattern caused by a given morphology is known, BEE is useful for elucidating whether the morphological pattern will grow or decay or migrate. Notice that the flow enters the BEE not only explicitly through $\vec{v}$, but also implicitly via the dependence of α and Γ upon $|\vec{v}|$ and u_b.

6.2.2 Transverse bars

Figure 6.1 (a) shows the circulation pattern together with the contour lines of the potential stirring at the initial development of transverse bars ($t = 3$ day). In the inner surf zone, the gradient in potential stirring is offshore directed so that, according to the BEE, sediment deposition should occur at the onshore flow regions while erosion should occur at the rip current locations. This is fully corroborated by the bottom panel (b) where the perturbation in bed level is plotted. Furthermore, this type of flow pattern with onshore current at the shoals and offshore flow at the troughs is the one driven by the increased wave breaking over the shoals in comparison with the troughs (Falqués *et al.*, 2000). The positive feedback is thus established leading to the formation of the bars. This is essentially similar to transverse bar formation in the earlier model of Caballeria *et al.* (2002).

The essentially new aspect in the present contribution is the saturation of the growth. Looking at the final state in figure 6.1(c, d), the gradient in potential stirring has now not only a cross-shore component, but also a longshore component. This is a consequence of the significant perturbations in water depth, D, but also of the sediment stirring by the currents, $\vec{v}$. Looking at the distribution of $D\vec{v}\cdot\vec{\nabla}\Pi$ on the bottom panel, it is seen that it still causes deposition over the shoals and erosion at the troughs. Thus, the saturation is reached not because the positive feedback between flow and morphology owing to the bedsurf coupling ceases, but because a balance between this effect and that from the downslope sediment transport is reached.

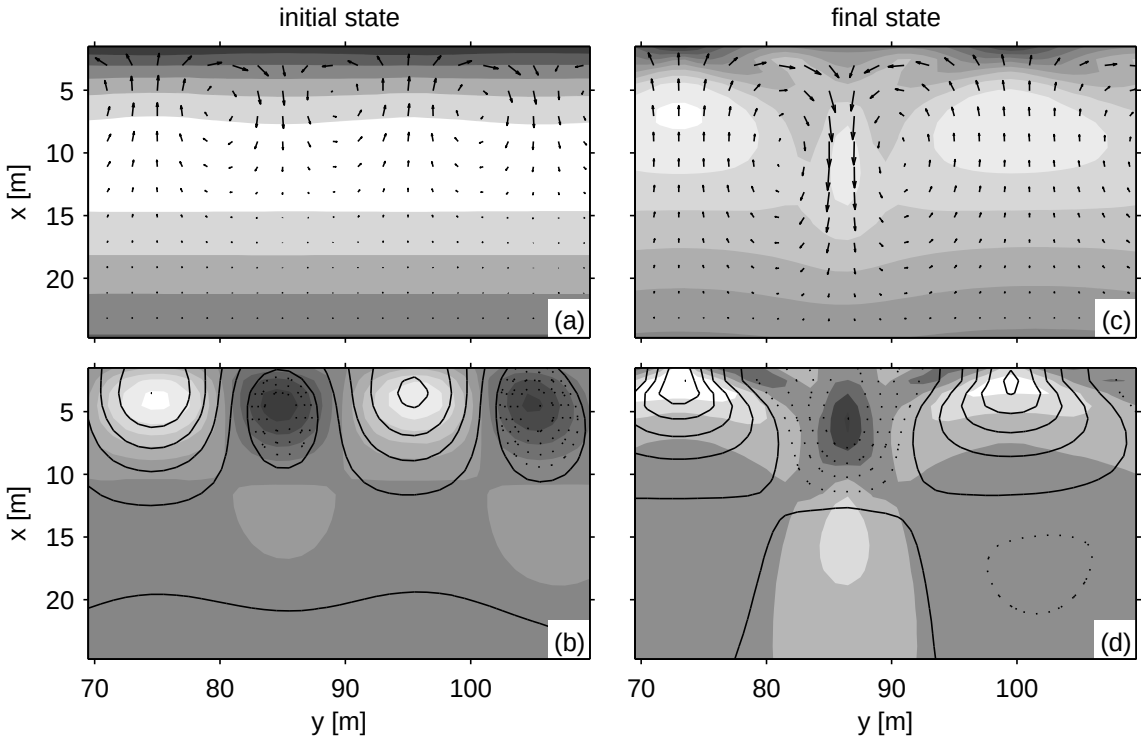

Figure 6.1: Planar beach, transverse bars. SVR-i default case (SVR transport, $\theta^0 = 0\,^\circ$). Left (a, b): initial state (day 3). Right (c, d): final state (day 12). Top (a, c): α/D (small values are shaded and large values are white) and current vectors. Bottom (b, d): $D\vec{v} \cdot \vec{\nabla}(\alpha/D)$ (negative values (accretion) are white and positive values (erosion) are shaded) and bottom perturbation (h) contours (crests are straight lines, troughs are dotted lines).

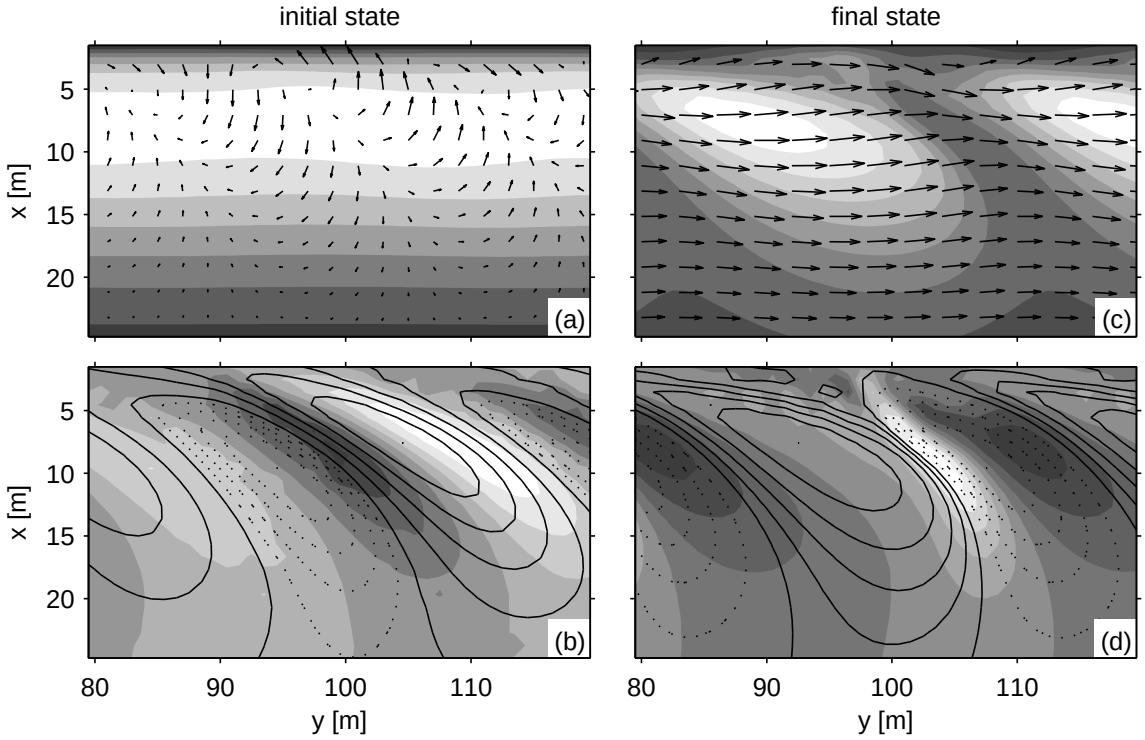

Figure 6.2: Planar beach, down-current oriented oblique bars. SVR-ii default case (SVR transport, $\theta^0 = 25\,^\circ$). Left (a, b): initial state (day 8). Right (c, d): final state (day 14). The graph description is the same as figure 6.1, but vectors in (a) show only the current perturbation.

6.2.3 Down-current oriented bars

Figure 6.2 (a) shows the contour lines of the potential stirring at the initial development of oblique bars ($t = 8$ day). The perturbation in the current, $(u, v - V(x))$, where $V(x)$ is the longshore current in the unperturbed state, is also shown. In figure 6.2(b), the bottom perturbation is displayed. In the unperturbed state the current runs alongshore and the gradient in Π is cross-shore directed. As a result, for small amplitude bars the approximation

$$D\,\vec{v}\cdot\vec{\nabla}\Pi \simeq D\,u\frac{\partial\Pi}{\partial x} + D\,V\frac{\partial\Pi}{\partial y} \tag{6.5}$$

holds to first order in the perturbations. As can be seen in figure 6.2(a), $\partial\Pi/\partial x > 0$ at the inner surf zone and there is onshore flow over the crests, $u < 0$. Therefore, the first term on the right-hand side of equation 6.5 is negative. Looking at the longshore gradient in potential stirring it turns out that $\partial\Pi/\partial y < 0$ somewhat down-current of the crests and $\partial\Pi/\partial y > 0$ somewhat down-current of the troughs. Although this is hard to see in figure 6.2(a) where the total stirring is shown it became apparent in plots where only the perturbation was displayed. Then, since $V > 0$, this means that the second term on the right-hand side is also negative at the crests and somewhat down-current of them. The result is that $-D\,\vec{v}\cdot\vec{\nabla}\Pi$ has its maximum (minimum) value somewhat down-current of the crests (somewhat down-current of the troughs) and, according to the BEE, this makes the bars grow and migrate down-current (figure 6.2b). The onshore veering of the current at the crests which is essential for bar growth is a consequence of

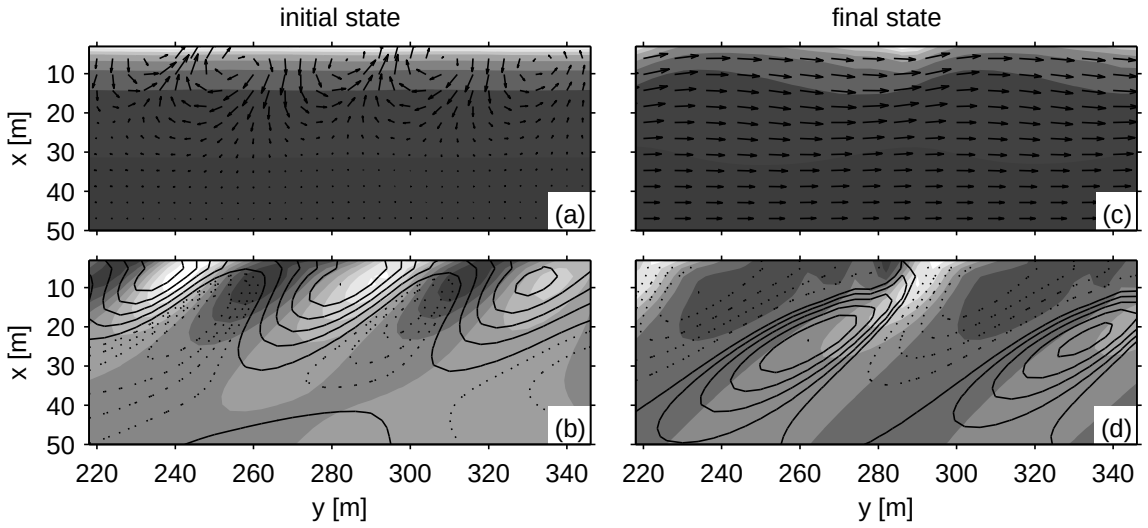

Figure 6.3: Planar beach, up-current oriented oblique bars. CWS default case (CWS transport, $\theta^0 = 25\,^\circ$). Left (a, b): initial state (day 5). Right (c, d): final state (day 85). The graph description is the same as figure 6.2.

both mass conservation and the increased breaking over the bars (Ribas *et al.*, 2003). In figure 6.2(c) the total current, $\vec{v}$, is shown instead of the perturbation. The maximum value of $-D\,\vec{v}\cdot\vec{\nabla}\Pi$ is located at the lee of the bar, indicating down-current migration without growth (figure 6.2(d). Nevertheless, this is hard to ascertain just looking at the figure and, moreover, the downslope transport has also some influence.

6.2.4 Up-current oriented bars

In general terms, the initial development of up-current oriented bars described in the present modelling is consistent with the linear stability predictions of Ribas *et al.* (2003). The use of the same sediment transport formulation and unbarred beach profile implies the same structure of the potential stirring, Π, i.e. seaward decreasing. Under such conditions, for zero or small wave incidence angle, the beach system is stable. For larger wave incidence angle, up-current oriented bars emerge with a shape which is very similar to the linear mode.

Similarly to the case of down-current oriented bars, the explanation for the initial formation of the bars can also be given in the present context on the basis of the approximation done in equation 6.5 which is now valid too. However, the gradient in potential stirring has now an opposite direction (shoreward) (figure 6.3a). Therefore, the formation of the bars also requires an opposite direction for the cross-shore flow component, seaward on the bars and shoreward on the troughs, which is met only for up-current oriented bars. Therefore, these are the emerging types of bar.

Although figure 6.3(b) indicates the growth and down-current migration of bars, looking at figure 6.3(a) it is difficult to see clearly the appropriate matching of the cross-

shore flow with the bar crests and troughs. Nevertheless, an analysis (not shown) of the effect of the two terms of the right-hand side of equation 6.5 reveals that $DV\partial\Pi/\partial y$ is the largest one, but only causes down-current migration. In contrast, $Du\partial\Pi/\partial x$ is smaller and produces growth of the bars along with a slight up-current migration.

The final state is displayed in figure 6.3(*c, d*). From the accretion/erosion pattern the down-current migration is clearly apparent. Yet, again, it is hard to see from it whether the saturation has been really achieved.

6.2.5 Crescentic bar systems

The mechanisms behind the emergence of transverse bar systems and crescentic bar systems are similar (figures 6.1 and 6.4, respectively). The transverse bars (troughs) appear in the inner surf zone corresponding to an increasing potential stirring ($\partial\Pi/\partial x < 0$, for $x \leq 10$ m, c.f. basic state profiles, figure 4.3); they outer extend by less pronounced troughs (bars), owing to a decreasing potential stirring ($\partial\Pi/\partial x > 0$, for $x \geq 10$ m). In the barred beach studies (chapter 5), we prevent the formation of these transverse bars of (i) a large bedslope coefficient ($\gamma = 5$), in the single barred beach study, or (ii) a large grid size, in the Truc Vert study. However, owing to the presence of the longshore bar, the potential stirring profile presents a second peak at $x \leq 80$ m (figure 5.3). Around this area, like the transverse bar systems, the bars (troughs) appear for increasing potential stirring, shoreward of the longshore bar (50 m $\leq x \leq$ 80 m) and slighter troughs (bars) appear in lee of it ($x \geq 80$ m). Thus, the main difference between crescentic and transverse bar systems concerns their length/time scale and their cross-shore location, these quantities being in relation.

6.2.6 Ridge and runnel systems

For oblique waves, the formation of oblique crescentic patterns could be explained by analogy with the down/up current oblique bars (sections 6.2.3 and 6.2.4). Indeed, for increasing potential stirring (shoreward of the longshore bar, $50 \leq x \leq 80$ m) down-current oriented bars and troughs appear whereas for decreasing potential stirring (in lee of the longshore bar, $x \geq 80$ m) up-current oriented features appear. Nevertheless, the approximation made in equation 6.5 is not valid here, because of the small wave incidence angle ($\theta^0 = 6\,^{\circ}$ at the offshore boundary). The magnitude of the ambient longshore current $V(x)$ is therefore smaller and the longshore current perturbation $v(x,y) - V(x)$ does not vanish (see panel (a) and (b) of figure 6.5) . Thus, the full BEE equation 6.4 must be considered, in particular, the term $D\,(v-V)\partial\Pi/\partial y$ can play a role for the initial evolution of these oblique crescentic patterns. Figure 6.5(c) shows the areas of deposition (white) somewhat down-current of the shoals and of erosion (shaded) somewhat down-current of the trough which suggest both growth and migration of the features. Moreover, as in the previous cases, the non-alongshore uniformity of the wave breaking will cause the positive feedback. Slight morphological changes seem to appear in the inner zone ($x \leq 50$ m). They form in the area around the first pick of the potential stirring profile

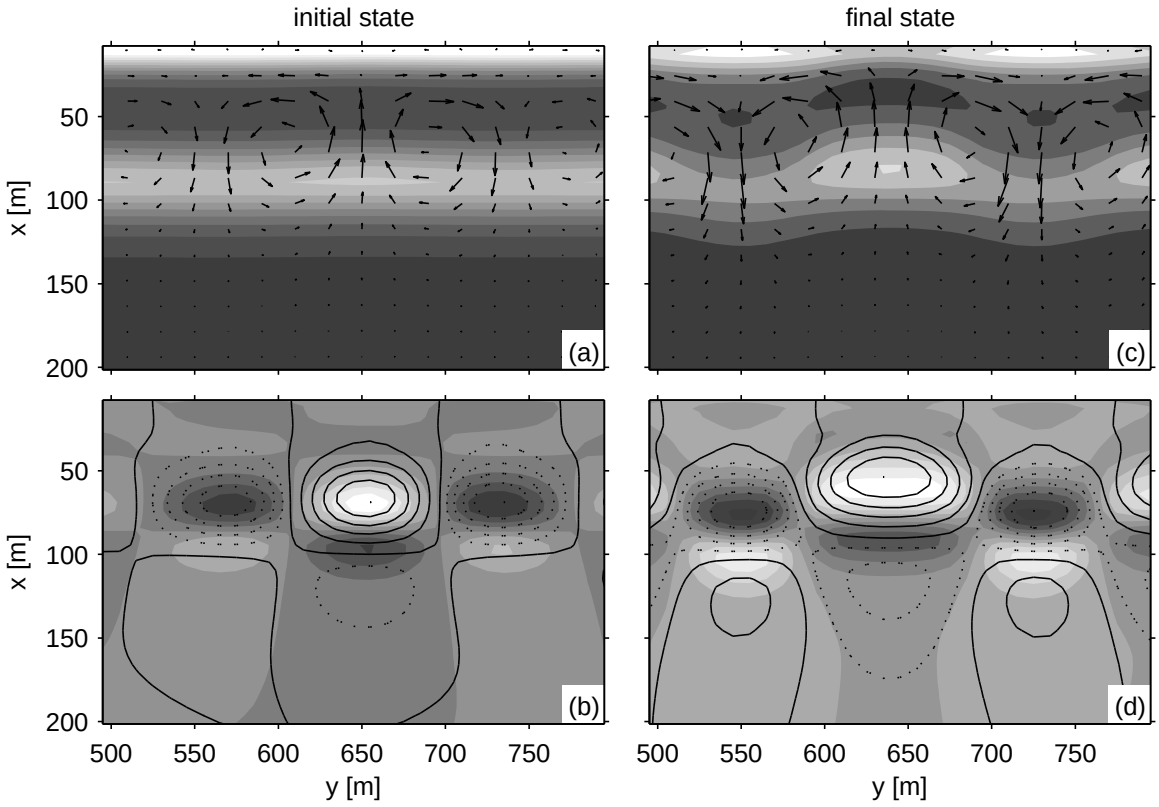

Figure 6.4: Barred beach, crescentic bar systems. SVR transport, $\theta^0 = 0^o$. Left (a, b): initial state (day 9). Right (c, d): final state (day 177). The graph description is the same as figure 6.1.

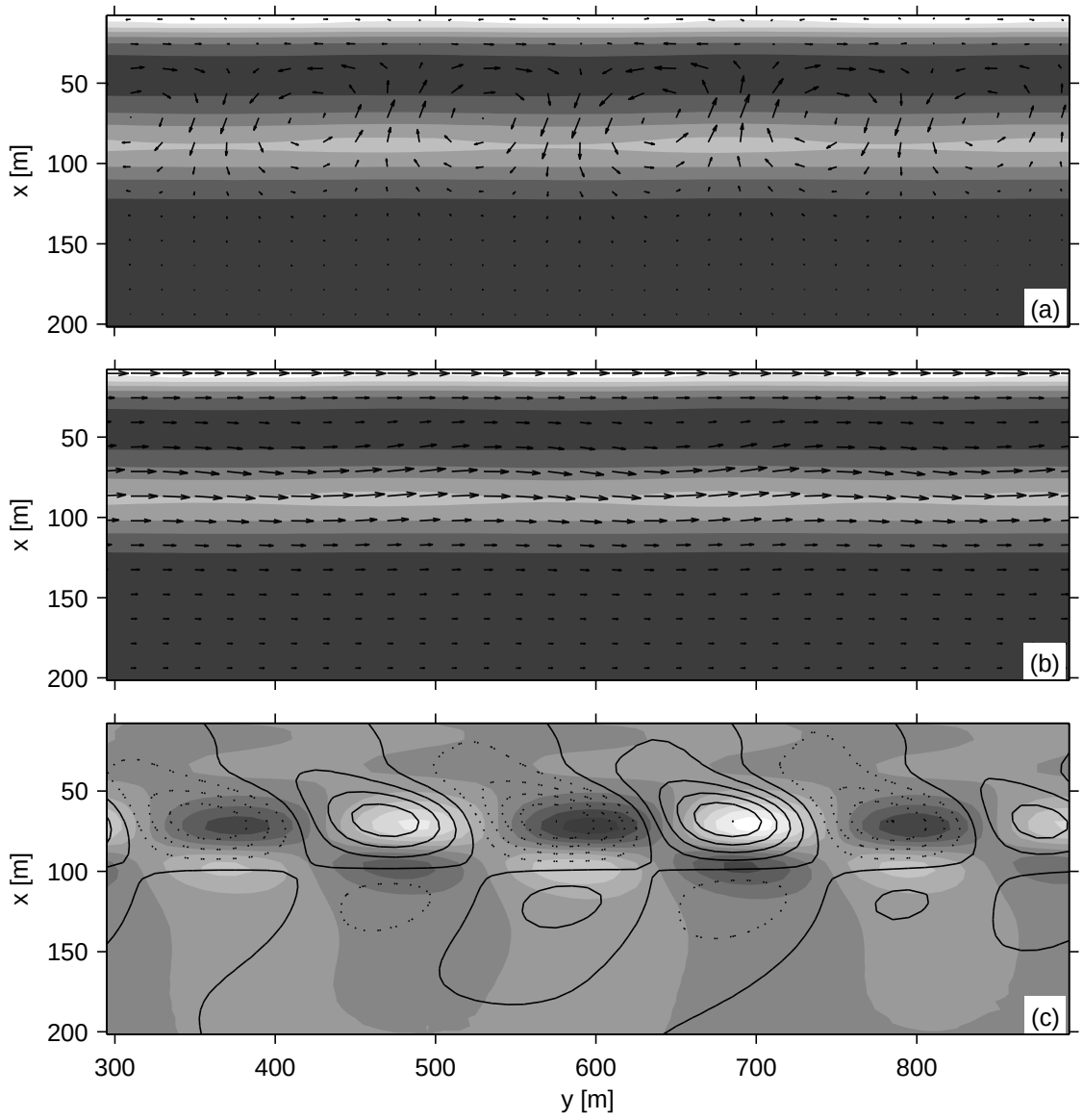

Figure 6.5: Barred beach, ridge and runnel systems. SVR transport, $\theta^0 = 6^o$. Day 18 (initial state). (a): α/D (small values are shaded and large values are white) and current perturbation vectors. (b): α/D (small values are shaded and large values are white) and current vectors. (c): $D\vec{v} \cdot \vec{\nabla}(\alpha/D)$ (negative values (accretion) are white and positive values (erosion) are shaded) and bottom perturbation (h) contours (crests are straight lines, troughs are dotted lines).

(figure 5.3) and they seem to be forced by the current resulting from the outer crescentic patterns.

These patterns seem to be at the origin of the formation of the ridge and runnel systems: they cause an undulation of the coastline, with pronounced troughs which connect to the deep troughs on the longshore bar, forming the runnels (figure 6.6). At day 177, the features have reached their final state and migrate in the direction of the ambient longshore current as figure 6.6(f) explains.

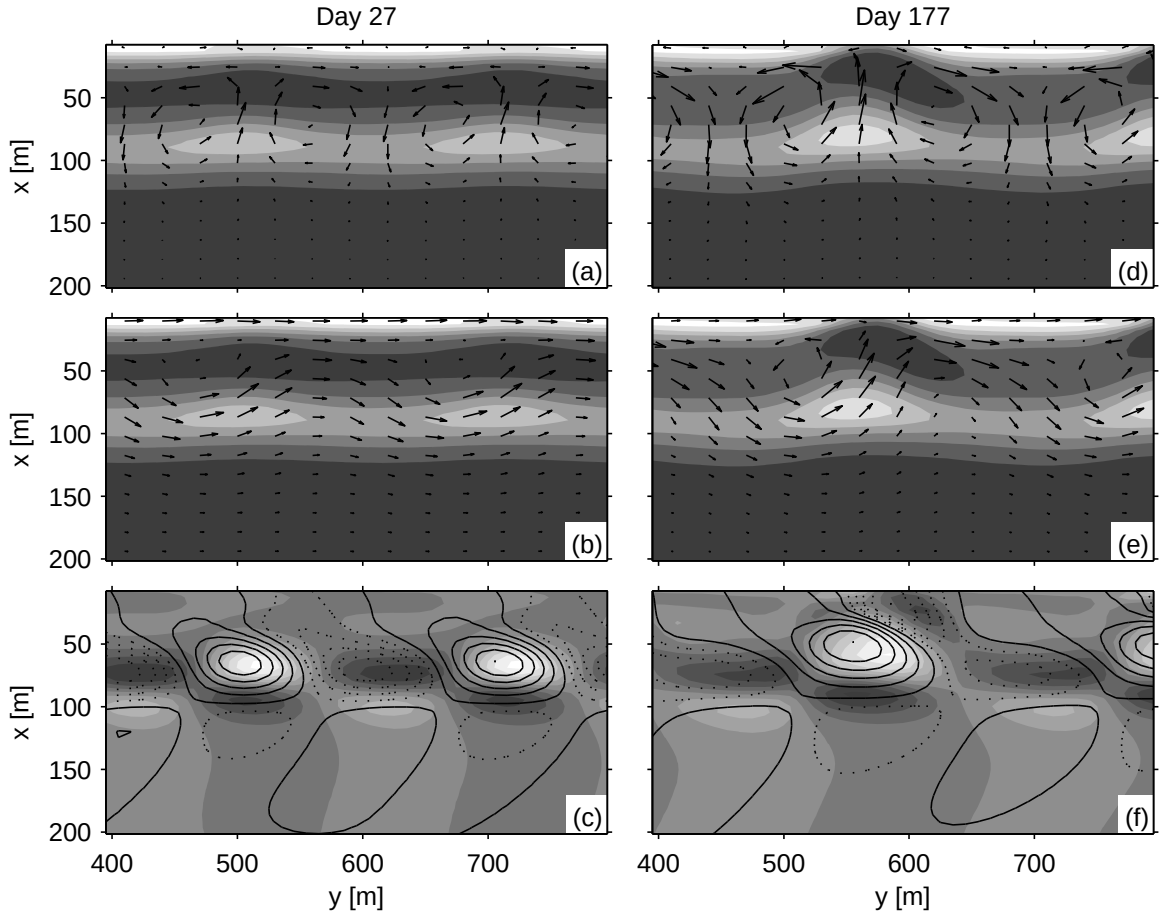

Figure 6.6: Barred beach, ridge and runnel systems. SVR transport, $\theta^0 = 6^o$. Left: day 27. Right: day 177 (final state). (a) and (d): α/D (small values are shaded and large values are white) and current perturbation vectors. (b) and (e): α/D (small values are shaded and large values are white) and current vectors. (c) and (f): $D\vec{v} \cdot \vec{\nabla}(\alpha/D)$ (negative values (accretion) are white and positive values (erosion) are shaded) and bottom perturbation (h) contours (crests are straight lines, troughs are dotted lines).

6.3 Global analysis of the saturation

The general method of a global analysis to understand the processes of the growth saturation presented in Garnier *et al.* (2006*b*) is explained first. Second, it is applied to the particular rhythmic features. Finally an analysis of the collapsing cases is given.

6.3.1 General method

Although previous morphodynamical modelling has occasionally predicted saturation of the growth of the emerging features, the analysis of the physical mechanisms leading to it was only based on indications given by local analysis at some particular locations (see, for instance, Calvete & de Swart (2003)) so that a thorough study was lacking. To this end, we develop here a method to analyse the saturation of the bars which is based on their dynamics on the whole domain. According to equation 6.1 or to the approximated BEE (equation 6.4), the tendency to the growth (or decay) of bars by the bedflow/bedsurf couplings can be measured by

$$\mathcal{P} = -\frac{1}{L_x L_y}\int_0^{L_y}\int_0^{L_x} h\vec{\nabla}\cdot(\alpha\vec{v})\,\mathrm{d}x\;\mathrm{d}y \simeq -\frac{1}{L_x L_y}\int_0^{L_y}\int_0^{L_x} hD\,\vec{v}\cdot\vec{\nabla}\Pi\,\mathrm{d}x\;\mathrm{d}y \quad ,$$

that will hereinafter be called 'production term'. Similarly, the 'damping term' due to the diffusive effect of downslope sediment transport is defined as

$$\Delta = \frac{1}{L_x L_y}\int_0^{L_y}\int_0^{L_x} h\vec{\nabla}\cdot(\Gamma\vec{\nabla}h)\,\mathrm{d}x\;\mathrm{d}y \quad .$$

which is typically negative. The precise meaning of both terms can be illustrated by considering the case of a topographic wave given by $h(x,y,t) = \varphi(t)f(x,y-c_m t)$, that is, a wave which propagates alongshore with celerity c_m, grows or decays according to $\varphi(t)$ but keeps a constant shape given by $f(x,y)$. It is assumed that f is L_y periodic with respect to y and that the topographic wave is confined within the longshore strip $0 < x < L_x$. Then, a measure of its amplitude is its $L2$-norm, defined as

$$\|h\| = \left(\frac{1}{L_x L_y}\int_0^{L_y}\int_0^{L_x} h^2\,\mathrm{d}x\;\mathrm{d}y\right)^{1/2} \quad . \tag{6.6}$$

Because of the L_y periodicity of f, the time derivative of $\|h\|^2$ is:

$$\frac{d}{dt}\|h\|^2 = \frac{2}{L_x L_y}\int_0^{L_y}\int_0^{L_x} h\frac{\partial h}{\partial t}\,\mathrm{d}x\;\mathrm{d}y = 2\,\frac{\varphi'}{\varphi}\|h\|^2.$$

According to the last equation, in the case of an exponential growth or decay, $\varphi(t) = \exp\sigma t$ with $\sigma \in \mathbb{R}$, the growth rate can be evaluated, independently of the migration, as:

$$\sigma = \frac{1}{L_x L_y\,\|h\|^2}\int_0^{L_y}\int_0^{L_x} h\frac{\partial h}{\partial t}\,\mathrm{d}x\;\mathrm{d}y \quad . \tag{6.7}$$

Now, by substituting $\partial h/\partial t$ using equation 6.1 or equation 6.4 in equation 6.7 it is found that the growth rate is directly related to the production and damping terms by

$$\sigma = \frac{1}{\|h\|^2}\left(\mathcal{P} + \Delta\right) \ . \tag{6.8}$$

Coming back to the general case of the solutions of our model equations, the instantaneous growth rate which is defined by equation 6.8 will decide the tendency to grow or to decay. Notice that for the initial formation of the bars, $\mathcal{P}$ will be larger than $-\Delta$ and they both will grow as $\|h\|^2$, since σ will be approximately constant according to linear stability theory. Once the bars reach a significant amplitude, these trends will no longer apply and saturation will occur when $\sigma = 0$, i.e. $\mathcal{P} = -\Delta$. Notice that this criterion is necessary but not sufficient, indeed, owing to the change of shape of the bars which may be the result of interactions of various modes, this criterion may be satisfied more than once during the evolution whilst the saturation is not reached. Thus, this prohibits a prediction of the moment of saturation.

6.3.2 Transverse bars

To find out why the balance between those two tendencies occurs, it is illustrative to analyse the trends in the production term, $\mathcal{P}$, and the damping term, Δ, when the bar amplitude measured by $\|h\|$ increases. Figure 6.7 (a) shows $\mathcal{P}^{1/2}$ and $(-\Delta)^{1/2}$ as a function of $\|h\|$. Both increase approximately linearly at the initial stages and $\mathcal{P}$ is larger than $-\Delta$ as the bars grow significantly. Nevertheless, the increase in $-\Delta$ with $\|h\|$ becomes larger than the increase in $\mathcal{P}$ so that both curves cross each other for $\|h\| = 0.018$ m. At this point, the bar growth stops and the final balance is reached. This behaviour is clearly seen plotting the difference between production and damping, $\mathcal{P}+\Delta$, as a function of bar amplitude, $\|h\|$ (figure 6.7 d). This difference is seen to increase from zero to a maximum at $\|h\| = 0.012$ m and then to decrease to $\|h\| = 0.018$ m where it vanishes. This maximum of $\mathcal{P} + \Delta$ characterized by a zero derivative is retrieved in figure 6.8(a) when the curve of $\mathrm{d}\mathcal{P}/\mathrm{d}\|h\|$ and $\mathrm{d}(-\Delta)/\mathrm{d}\|h\|$ cross each other. Even beyond this point, both $\mathcal{P}$ and $-\Delta$ keep on increasing their growth rate until the final equilibrium, although $-\Delta$ do it more vigorously.

6.3.3 Down-current bars

Comparison of figure 6.7 (b) with figure 6.7(a) shows three significant differences between down-current oriented bars and transverse bars. At the initial stage, the production and damping terms are closer for down-current bars (1). At the final stage, both terms moderate its growth and the instability source do it more drastically (2) and before reaching the final equilibrium the amplitude of bars decreases (3). Claim (1) is readily seen from the smaller initial slope of the $\mathcal{P} + \Delta$ curve in figure 6.7(e) in comparison to figure 6.7(d). The final loop in the $\mathcal{P} + \Delta$ curve in figure 6.7(e) corroborates claim (3).

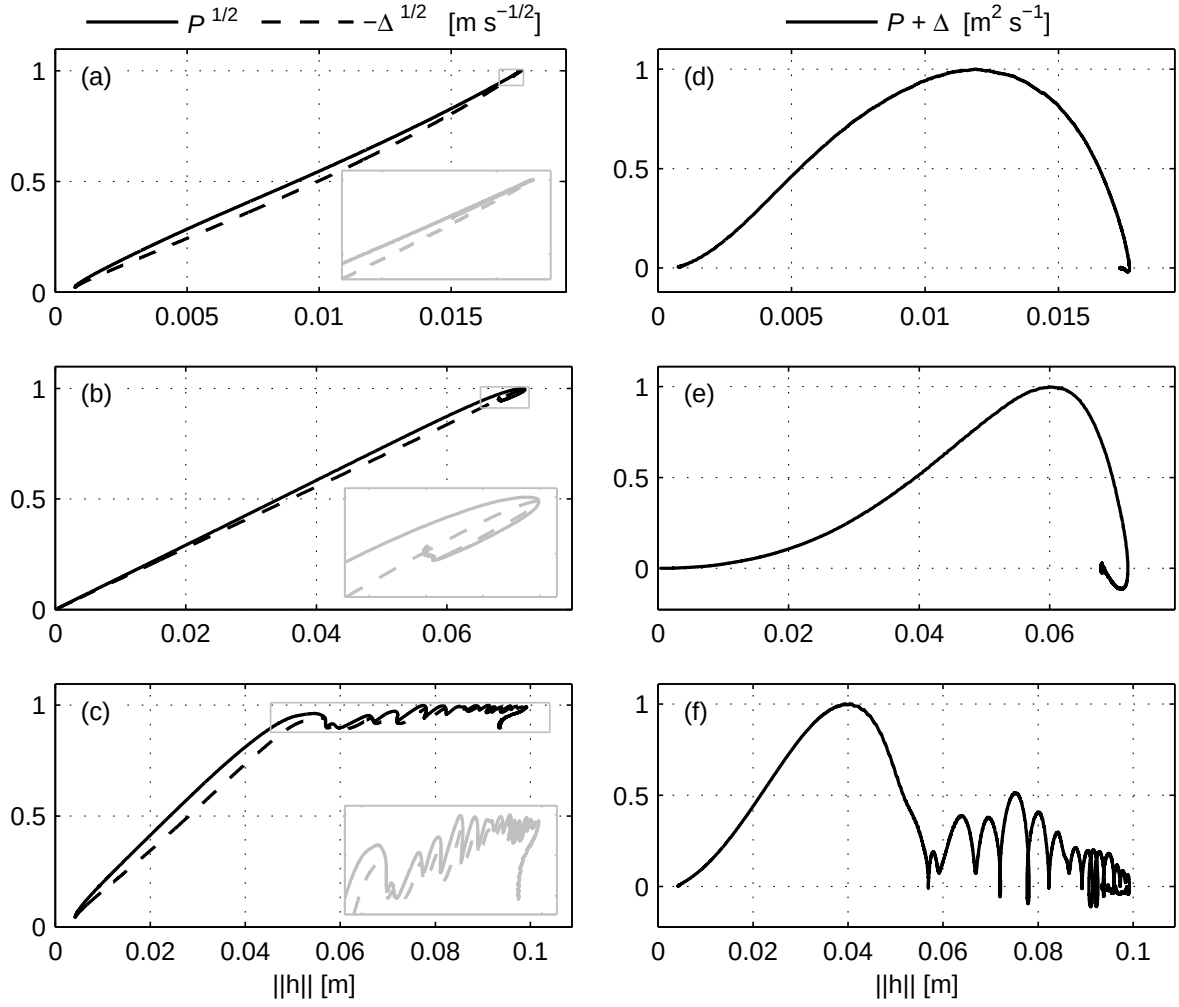

Figure 6.7: Planar beach, transverse/oblique bars. Left (a,b,c): Square root of the production and damping terms as a function of $\|h\|$. Right (d,e,f): Difference between production and damping, $(\mathcal{P} + \Delta)$ as a function of $\|h\|$. From top to bottom, (a,d):SVR-i default case (SVR transport, $\theta^0 = 0^o$), (b,e):SVR-ii default case (SVR transport, $\theta^0 = 25^o$), (c,f):CWS default case (CWS transport, $\theta^0 = 25^o$).

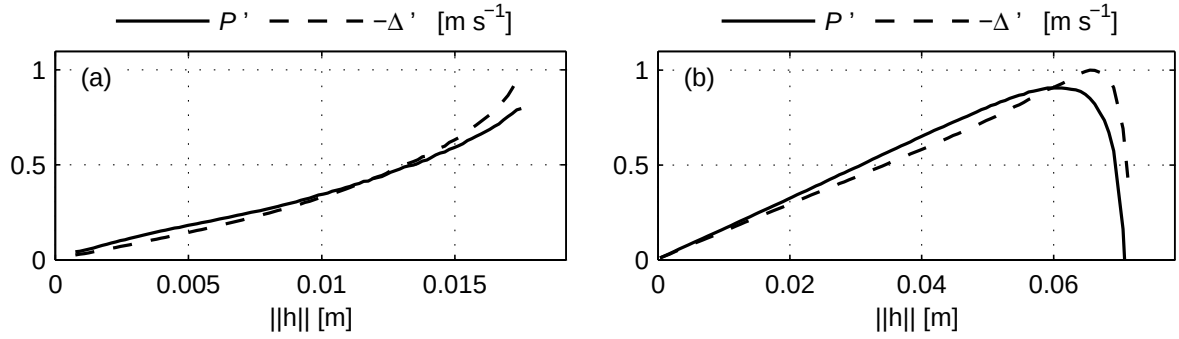

Figure 6.8: Planar beach, transverse/oblique bars. SVR transport. Derivatives of $d\mathcal{P}/d\|h\|$ and $-d\Delta/d\|h\|$ as a function of $\|h\|$. (a): SVR-i default case ($\theta^0 = 0^o$), (b): SVR-ii default case ($\theta^0 = 25^o$).

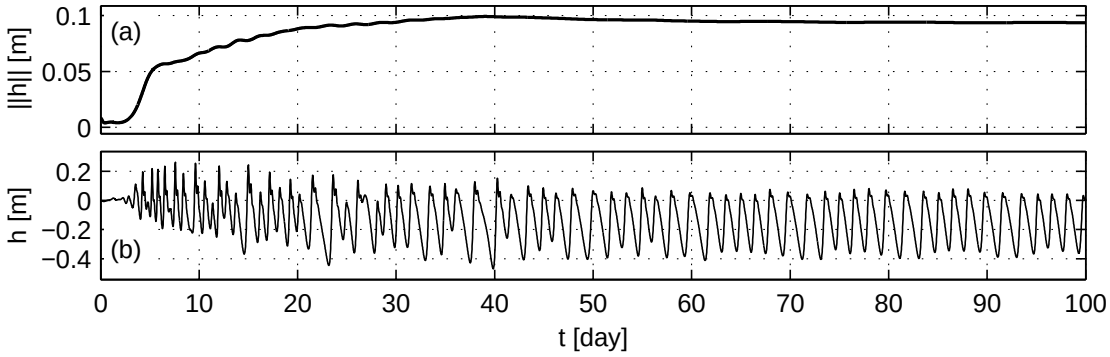

Figure 6.9: Planar beach, up-current oriented oblique bars. CWS default case (CWS transport, $\theta^0 = 25\,^\circ$). Time evolution of (a) $\|h\|$ and (b) $h(10, 22.5)$.

Claim (2) follows by comparing figure 6.7(b) with figure 6.7(a) but it becomes most apparent by looking at figure 6.8(b) where it is seen that $\mathrm{d}\mathcal{P}/\mathrm{d}\|h\|$ start to decrease earlier than $\mathrm{d}(-\Delta)/\mathrm{d}\|h\|$ and do it more strongly.

6.3.4 Up-current bars

As shown in figure 6.7(c, f) it is found that the behaviour of this kind of bar is more complicated than the others. This is because of the merging of individual bars occurring when bar amplitude is significant. It turns out that a first balance between production and damping appears when $\|h\| \approx 0.05$ m before day 7 (figures 6.9 and 6.7 c, f). This first saturation of the growth corresponds to the saturation of mode 1 described in section 4.6.3. Nevertheless, after day 7, $\|h\|$ resumes its growth and keeps on growing until nearly 0.1 m at day 40 (figure 6.9a). This increase in $\|h\|$ is not due to an increase of bar amplitude which remains nearly constant (figure 6.9 b) but to the increase of cross-shore span because of bar merging. Figure 6.7 (c, f) illustrates this strongly nonlinear behaviour with intriguing oscillations which begin with the first (unsteady) balance between production and damping and end up with the balance leading to the final saturated bars (mode 2 in section 4.6.3).

6.3.5 Crescentic bar systems

The saturation of the crescentic bar systems (and of ridge and runnel systems) is also explained by a balance between the production term $\mathcal{P}$ and the damping term Δ (figure 6.10). As for the oblique bars, a first balance between these two terms occurs, but the equilibrium is not reached at this time. New mechanisms appear. For normal waves, the $\mathcal{P} + \Delta$ curve (figure 6.10 c) reminds us the down-current bars case where a loop appears due to the decrease of $\|h\|$ (as suggested the time series in figure 5.7). The down-current bars leads to their equilibrium at a second balance of $\mathcal{P}$ and Δ. However, for crescentic bars, the $\mathcal{P} + \Delta$ curve seems to follow the horizontal axis until the loop closes. At the equilibrium state, $\|h\|$ takes the value it had at the first balance. For

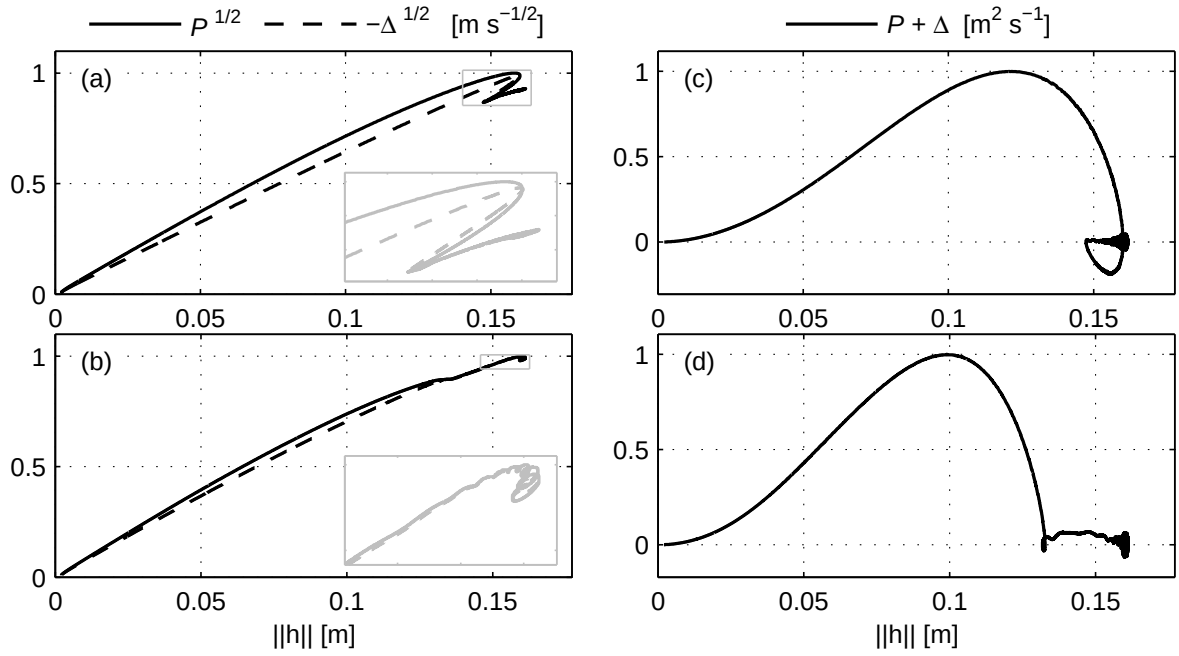

Figure 6.10: Barred beach. SVR transport. Left (a,b,c): Square root of the production and damping terms as a function of $\|h\|$. Right (d,e,f): Difference between production and damping, $(\mathcal{P}+\Delta)$ as a function of $\|h\|$. From top to bottom, (a,c): crescentic bar systems, $\theta^0 = 0^o$, (b,d): ridge and runnel systems, $\theta^0 = 6^o$.

oblique waves, the $\mathcal{P}+\Delta$ curve are more reminiscent of the up-current bars since $\|h\|$ resumes its growth after a first balance. This second saturation curve is probably due to the change in shape of the bars and could correspond to the formation of ridge and runnel systems from a (oblique) crescentic bar state.

6.3.6 Critical regime

The saturation of the growth and the equilibrium of rhythmic features are presented in some specific cases. However, as suggested the parametric trends for oblique/transverse bars (section 4.6.4), the saturation of the growth is not obtained every time, as for instance, for a small value of the bedslope coefficient γ. The reason for what the model turns out to collapse/break down has been clarified. Indeed, the domain of validity of the model is the surf zone, i.e. it is not valid when the bars emerge. More restrictively, when the height of bars becomes too big compared to the mean water depth, the overflow appears. We found a threshold value Γ_c of $h/(D+h) = h(x,y,t)/(D(x,y,t)+h(x,y,t))$ above it the model crashes, where h is the bed level deviation from the initial bathymetry and $D+h$ is the water depth at the basic state. As a result of all the computations, we found a threshold value of $\Gamma_c \simeq 0.6$. Figures 6.11 and 6.12 show the evidence of this threshold value for transverse bars and oblique up-current oriented bars. Notice that the default cases presented in the thesis are not in the critical regime ($\gamma = 1.5$ for the SVR transport corresponding to $\max_{x,y,t}\ h/(D+h) = 0.4$ and $\gamma = 0.5$ for the CWS transport corresponding to $\max_{x,y,t}\ h/(D+h) = 0.5$). This threshold value suits the assumption

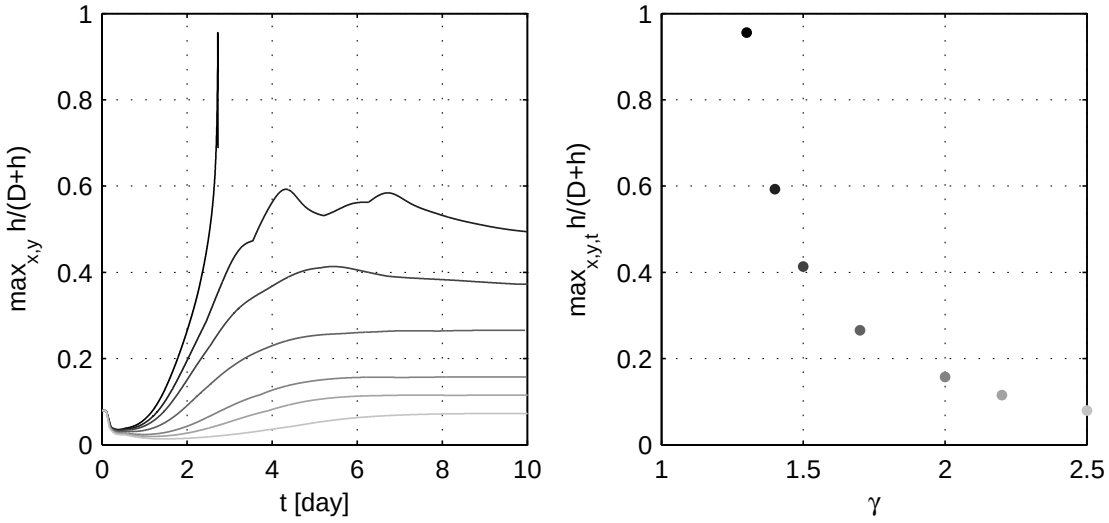

Figure 6.11: Planar beach, transverse bars. SVR-i cases (SVR transport, $\theta^0 = 0\,^\circ$). Left: time series of $\max_{x,y} h(x,y,t)/(D(x,y,t)+h(x,y,t))$. Right: $\max_{x,y,t} h(x,y,t)/(D(x,y,t)+h(x,y,t))$ as a function of γ.

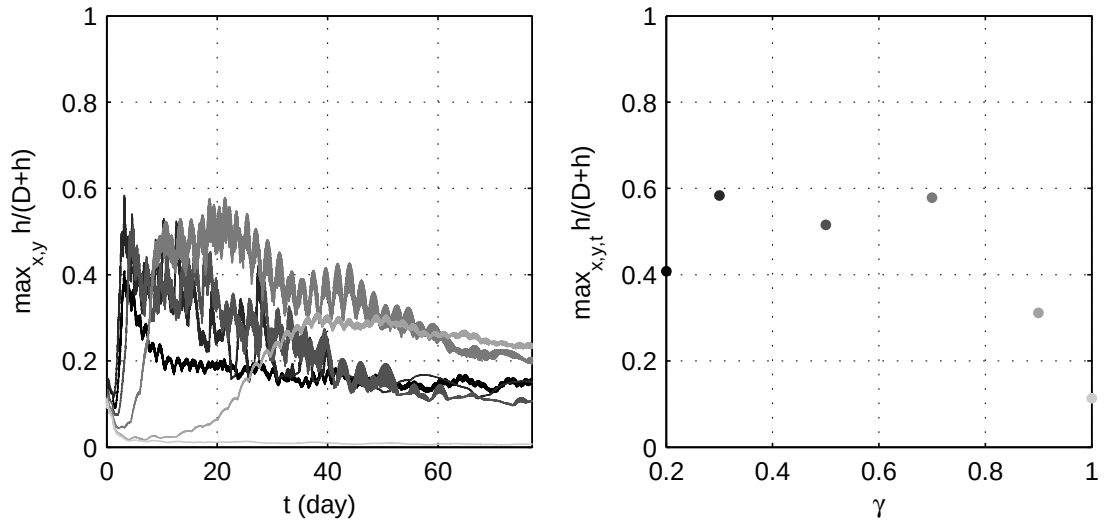

Figure 6.12: Planar beach, up-current oriented oblique bars. CWS cases (CWS transport, $\theta^0 = 25\,^\circ$). Left: time series of $\max_{x,y} h(x,y,t)/(D(x,y,t) + h(x,y,t))$. Right: $\max_{x,y,t} h(x,y,t)/(D(x,y,t) + h(x,y,t))$ as a function of γ.

of the model. For instance, the wave height is time averaged, thus, the wave troughs are not taken into account in the mean water depth. Therefore, the collapsing cases can be interpreted as going out of the domain study and the runs that do not break down may be considered as valid.

6.4 Conclusion

The physical mechanisms for the generation of rhythmic patterns described in the previous studies are valid in our case. For normal waves, the transverse and crescentic bar systems emerge with the same mechanisms: strong bars (troughs) appear for an off-shore increasing potential stirring and off-shore lengthen by slighter troughs (bars) for a decreasing potential stirring. The positive feedback is induced by bed-surf mechanisms which explain the onshore (off-shore) oriented current circulation at the strong bars (troughs). For oblique waves and increasing potential stirring, owing to the longshore current, the bars take an oblique orientation and they migrate down-current, both in planar beach (down-current oriented bars) and barred beach (ridge and runnel systems). For decreasing potential stirring, the positive feedback occurs for an opposite cross-shore flow component, i.e. offshore (on-shore) oriented at the bars (troughs). This only happens if the longshore current is sufficiently strong (high wave angle), in this case the bed-flow mechanisms (current refraction) dominate over the bed-surf mechanisms.

The essential new aspect of this study has been to understand why the growth of bars saturates and why the bars lead to an equilibrium state. The tendency of the growth and decay is measured by defining the production term and the damping term, respectively. Both increase approximately linearly at the initial stages, but the production is larger than the damping, this explains the growth of bars. Saturation occurs when these two terms balance. At this point, the equilibrium may be reached as in the transverse bars case, but this is not general. For each kind of features a different behaviour is observed and after a first balance, further balances usually occur before the eventual balance that characterize the equilibrium state.

Chapter 7

Discussion

7.1 Saturation of the growth

While the linear stability analysis shows the tendency of the morphodynamical system to produce bars, it does not actually prove that such bars should be observed in nature. It could very well be that in case of including the nonlinearities, the model prediction for bar amplitude would be exceedingly small. In such a case, the corresponding instability mechanism could not be considered as the origin of the observed bars. Thus, the present study can be considered as the first proof that shore-oblique bars can actually emerge by self-organization of the coupling between waves, currents and morphology via sediment transport. In the cases of transverse bars and crescentic bars, there was the earlier nonlinear stability analysis by Caballeria *et al.* (2002); Damgaard *et al.* (2002); Castelle (2004); Reniers *et al.* (2004), but those studies had the shortcoming that the models could not describe the saturation of the bar growth. This has now been overcome and finite-amplitude shore-transverse and oblique sand bars have been modelled for the first time.

The saturation is obtained as a balance between the down-slope sediment transport and the positive feedback between flow and morphology which is responsible of the initial formation of the bars. Both effects grow proportionally to bar amplitude at the initial stage, the instability term being somewhat stronger. The process by which equilibrium is eventually reached is complex and sometimes shows a number of oscillations which reveals that the criterion for the saturation is not sufficient; more exactly, saturation does not necessarily imply equilibrium. Essentially, two different scenarios are found for the saturation: (i) the damping term accelerates its growth so that it eventually balances the instability source or (ii) the instability source weakens so that it becomes balanced by the damping. This means that saturation occurs either because the finite-amplitude shape of the bars enhances downslope transport (i) or weakens the instability mechanism (ii). Notice that for some experiments, there are still interactions between several modes

even if the measure of the amplitude ($||h||$) is already stabilised and the criterion of the global saturation is verified. This state could be interpreted as a dynamical equilibrium state.

The final balance is very sensitive to the γ parameter of the down-slope transport. Typically, formation of finally equilibrated bars takes place only for a relatively narrow range of values. Values that are too large lead to stability of the alongshore uniform topography while values that are too small lead to overflow of the numerical model as the bars grow too much and their top tends to grow almost up to the mean sea surface. The saturation could occur in the latter case owing to processes related to very shallow water over the bars not described by the present model. The values of γ leading to numerically stable computations are characterized by a ratio of maximum bar amplitude to total mean water depth not larger than about 0.6. Even if the model does not resolve the individual waves, this ratio corresponds to the situation where the water depth at the troughs of the waves would be roughly zero. Thus, this numerical limitation does not pose any physical limitation on the model.

7.2 Characteristics of the bars

In line with previous linear stability analysis (Ribas *et al.*, 2003), the different types of bar emerging on a planar beach depend mainly on the cross-shore profile of the potential stirring, α/D, and on wave approach angle. In the case of an offshore decreasing potential stirring (CWS transport), for zero to moderate wave angle, the alongshore uniform morphology is stable. For quite oblique wave incidence (above $\theta^0 \approx 17^o$), up-current oriented bars emerge. The typical growth times are $2-4$ days. The amplitude ranges between 0.05 m and 0.5 m, increases with $H^0_{\rm rms}$ (between 0.5 and 1.25 m) and decreases with increasing bedslope transport coefficient, γ. The longshore spacing increases with wave angle and has a complex behaviour with γ, ranging between 60 to 130 m. For oblique wave incidence, the bars migrate down-current with celerity between 30 and 70 m day^{-1} that increases drastically with wave angle from 17^o to 35^o. The bar dynamics are coupled to a meandering of the longshore current with offshore flow over the bars and onshore flow at the troughs. The magnitude of the cross-shore component is about 0.3 m s^{-1} while the longshore component is about 0.9 m s^{-1} for waves of $H^0_{\rm rms} = 1$ m. The angle of the bars with the shore-normal ranges from $\beta_m = 42^o$ to 67^o.

In the case of an offshore increasing potential stirring across the inner surf zone up to a maximum and an offshore decreasing potential stirring beyond this point (SVR transport), transverse bars form in the case of normal wave incidence. The bars have amplitude between 0.08 and 0.19 m which increases with wave height. The longshore spacing is about 30 m, slightly increasing with $H^0_{\rm rms}$. The cross-shore length increases too with $H^0_{\rm rms}$ and ranges between 9 and 12 m. The existence of the bars is clearly linked to a horizontal circulation with jet-like rip currents in the troughs up to 0.52 m s^{-1}. A typical growth time is a couple of days. Their formation mechanism is similar to that described in Caballeria *et al.* (2002). Differences arise due only to a different description of hydrodynamics which consider irregular waves, but do not account for

wave refraction by the growing bars. Anyhow, the mean flow has the same structure, i.e. onshore (offshore) directed on the bars (at the troughs), and this is the essential characteristic that makes the bars grow.

With the same structure of the potential stirring that lead to the formation of transverse bars, but in the case of oblique wave incidence, down-current oriented bars emerge. The amplitude is about 0.30 m and the longshore spacing increases with wave height from 19 to 43 m. The angle of the bars with the shore-normal increases too from $\beta_m = 35^o$ to 60^o. The typical growth time is about 2 days. The bars migrate down-current at celerities which range between 100 and 260 m day^{-1} and increase with wave height, wave incidence angle and wave period. They are also linked to a meandering of the longshore current, this time with onshore flow over the bars and offshore flow at the troughs. The magnitude of the cross-shore flow component is about 0.3 m s^{-1} with a longshore component of 1 m s^{-1}.

The presence of a longshore bar affects the cross-shore profile of the potential stirring α/D by adding a peak. By using the SVR transport, crescentic bars appear around this cross-shore location. Their spacing depends on this position. In the case of normal wave incidence, they remind us the transverse bar systems obtained in planar beach but they have a larger scale and they are shifted off-shore. On the longshore bar located at $x = 80$ m, crescentic patterns appear with a wave length of 200 m and a final height of 1 m. The associated rip current systems have magnitudes up to 0.3 m s^{-1}. The typical growth time is about 20 days but we need to realise that the evolution of bars starts from a small initial perturbation. The e-folding time, independent of the size of the initial perturbation is 2.5 days. On the longshore bar at $x = 500$ m, larger crescentic patterns appear with a wave length of about 600 m, and a growth time of about 50 days (for waves of 1.8 m).

In the case of oblique wave incidence, on the longshore bar located at $x = 80$ m, oblique crescentic features emerge and evolve in ridge and runnel systems, characterized by deep channel with an height of 1.4 m. Their final wave length oscillates between 250 and 300 m, they migrate down-current at celerity of 20 m day^{-1}. They appear with a growth time of about 40 days (e-folding time of 5 days). Only the case of small wave incidence angle has been studied, so that the magnitude of the longshore current is small (0.2 m s^{-1}). The rip currents have a stronger intensity (0.4 m s^{-1}).

7.3 Initial characteristics versus finite-amplitude characteristics

An important limitation of the explanations of pattern formation by self-organization is that they are sometimes based on linear stability analysis. The question then arises as to whether the shape, length scale and migration celerities predicted by linear stability analysis actually applies to the finite-amplitude features which should be comparable to the corresponding patterns in nature. The present study sheds some light on this issue;

it turns out that the answer is sometimes 'yes' and sometimes 'no'. For instance, the longshore spacing of crescentic bars keeps unchanged during the evolution, for transverse bars, down-current oriented bars and ridge and runnel systems the final spacing is similar to the initial one, whereas it is significantly larger for up-current oriented bars, 72 m compared to 50 m for the default parameter set. Both for up-current and down-current oriented bars, the initial and final migration celerities are different. For up-current bars, the final celerity is smaller than the initial, 43 m day^{-1} compared to 71 m day^{-1}. In contrast, for down-current bars, it is the other way around, a final celerity of 167 m day^{-1} which is larger than the initial one, 150 m day^{-1} (for the default parameter set).

Regarding the shape, linear stability can only predict sinusoidal patterns where crests and troughs are symmetrical. Consistently, onshore and offshore flow with the same intensity is equally distributed along the coast. This is clearly not so for the finite amplitude features. For instance, transverse bars show an asymmetry of crests and troughs which is different close to the shoreline or far from it. Close to the shoreline the crests are narrow and the troughs wider while offshore the shoals are wider and the rip channels narrower. Very remarkable is the asymmetry between offshore flow (rip currents) and onshore flow. The former is strong and narrow whereas the latter is wider and weaker in accordance to common observations on rip-current systems (Short, 1999). This kind of asymmetric rip-currents is seen at crescentic bars too, where shoreward (in lee) of the longshore bar, bars (troughs) are weaker than troughs (bars).

In case of oblique wave incidence where the bars migrate down-current the longshore sections of the bars have the typical asymmetry, the lee being steeper than the stoss. In all the cases, this final asymmetric behaviour of the bars and of the current is crucial since we saw the final spatial structure of the topography and of the flow is responsible for the saturation of the growth. Indeed, in each case of non-saturation (when overflow occurs) we noticed the bars had kept its linear structure.

The overall shape in plan view of the transverse, up-current and crescentic bars do not differ much between the initial and the final stages. However, the initial shape of down-current bars turns out to be very linear while for large amplitude the down-current bars tend to curve backward with their offshore tip veering up-current. Moreover the ridge and runnel systems do not appear at the initial stage where oblique crescentic bars emerge around the longshore bar. It seems that ridges and runnels are due to strong nonlinear mechanisms, even if their spacing is similar to the spacing of the initial crescentic bars.

Thus, the final conclusion is that small amplitude analysis can reliably predict only the order of magnitude of the longshore spacing and migration celerity along with the overall shape but not the details of it.

7.4 Comparison with observations

Comparison of model results with experimental data can be done only in a very limited way. In particular, the model is at present very idealised and the main purpose was just to show that surf zone rhythmic bars of finite amplitude could emerge from morphodynamical instabilities of the surf zone and showed a realistic nonlinear dynamics.

7.4.1 Oblique/transverse bars

Although transverse/oblique bars are quite often observed in nature, field data sets on their generation involving morphological evolution along with hydrodynamics are scarce and incomplete. Thus, we firstly stick to an overall comparison between model results and observed bars by referring to the systematic summary of existing observations in Ribas *et al.* (2003). Nevertheless, a comparison between the model results and transverse/oblique bar systems observed in Trafalgar beach, Cadiz, Spain is under preparation. Shore-attached bars in nature can be either perpendicular or oblique to the coastline. According to Ribas *et al.* (2003), it seems that the most common orientation in the latter case is down-current but the up-current orientation can also exist as describes the recent studies Ribas *et al.* (2005); Ribas & Kroon (2006). In this respect the model is successful in describing the formation of the three types of bars. However, the conditions on the potential stirring necessary to produce the different types can not be checked through the field data description in the existing literature. It is nevertheless likely that the most common situation (for intermediate beach states where the infragravity wave energy is not dominant in the inner surf zone) is an offshore increasing stirring function through the inner surf zone for which the model predicts either transverse bars or down-current oriented bars according to wave angle. The shape of the bars in the model is overall representative of the ensemble of observed shapes for such bars. It is interesting that the model reproduces the observed asymmetry, the down-current flank being steeper than the up-current flank. The longshore spacing of shore-attached bar systems in the model ranges between 30 and 75 m, i.e., within the range of the observed spacing which is between 12 and 760 m (Ribas *et al.*, 2003). It seems that the spacing is correlated with the width of the surf zone and the large scatter in observed spacing is probably related to differences in surf zone width. Because of the use of Rayleigh distributed waves it is difficult to define the surf zone width in the model but we can define it as the distance from shore to the location of maximum wave dissipation which is about 15 m. Thus, the ratio spacing/surf zone width would be about $2 - 5$ which is comparable to the values reported in the literature. The typical growth times of a couple of days in the model are not in disagreement with the scarce data which point out to a formation time ranging between one and a few days.

The currents associated with the presence of the bars are also consistent with observations. In case of transverse bars, strong and narrow rip currents form in the troughs and wide and weaker onshore flow over the shoals. The onshore (offshore) veering of the longshore current over the bars (troughs) is also very typical of down-current oriented bars. Less well known is the observed flow pattern in the case of up-current oriented bars.

In this case, the meandering of the longshore current in the model can be compared to the observed one in case of storm-driven currents over the shoreface-connected ridges on the inner continental shelf and they show correspondence (Trowbridge, 1995).

As in nature, bars migrate down-current in the model. The computed celerities range between 30 and 70 m day^{-1} for up-current oriented bars and between 100 and 260 m day^{-1} for down-current oriented bars. In contrast, observed celerities reported in the literature range between a few meters up to 40 m day^{-1} (Ribas *et al.*, 2003; Lafon *et al.*, 2002) so that it seems that the model tends to over predict the migration speed. This however deserves further attention. First of all, the measured migration speeds are very often an average over several days, weeks or even months, during which the wave energy and direction may change substantially. Thus, the observed migration velocities are not representative of waves incoming all the time with a large angle with the shore-normal as in the model. For example, the measurements taken with a much higher frequency by Konicki & Holman (2000) gave celerities up to 40 m day^{-1}. A second aspect is that bar celerity depends largely on its size, both in the model and in nature (Falqués *et al.*, 1996), the larger the bars, the slower they move. The down-current bars in the model have a quite small spacing ($\sim$ 30 m, at the lower bound of the range of observed spacing) and this probably causes their large celerity. In contrast, the up-current bars which are larger have celerities that are roughly consistent with the ones observed by Konicki & Holman (2000).

7.4.2 Crescentic bars and ridge and runnel systems

Rhythmic features which appear in a barred beach have been the object of many systematic field studies. A review of existing observed crescentic bars is given in van Enckevort *et al.* (2004) and shows the strong variability firstly between different sites and secondly in a given site. The wave length of crescentic bar may range between 30 and 3000 m, and their migration velocity may be up to 180 m day^{-1}. Here we focus on a comparison with rhythmic features observed in the French Atlantic coast which is often characterized by its double barred beaches. Crescentic bar systems may develop from the two longshore bars, independently (Castelle, 2004; De Melo Apoluceno, 2002; Lafon *et al.*, 2002, 2004, 2005). In the subtidal zone their wave length ranges from 579 ± 200 m (variability is indicated by standard deviation) to 818 ± 214 m and their (down-current) migration celerity is about 1 m day^{-1}. In the intertidal zone they have smaller length scale and quicker migration: λ_{m} ranges from 370 ± 146 m to 462 ± 188 m and c_{m} is about $2.4 - 3.1$ m day^{-1} (Lafon *et al.*, 2004). These intertidal crescentic bars seem to be a preliminary state of the ridge and runnel systems from both our model results and the observations (De Melo Apoluceno, 2002; Castelle, 2004). The modelled features that develop from a shallow longshore bar are in general agreement with the observed intertidal features: the spacing of the bars being about 200−300 m, and the migration celerity being 20 m day^{-1}. This over-predicted speed is mainly due to a sustained model forcing with constant wave conditions while in reality, these intertidal features are discovered during part of the day and therefore, free of wave forcing. The modelled subtidal crescentic features match with the observation, regarding the wave spacing ($500 - 750$ m). The

migration velocity is again overestimated ($c_{\mathrm{m}} = 5 - 12\ \mathrm{m\,day^{-1}}$) because our modelling studies do not take into account the periods of very low wave energy and nearly normal wave incidence that happen in reality.

7.5 Model simplifications

The increased (decreased) wave breaking over the shoals (troughs) causes gradients in set-up and mean flows. When a longshore current is present, the alongshore non uniform topography also triggers gradients and meandering of the current. This is the main feedback mechanism of the morphology onto the hydrodynamics in the model. The morphodynamical loop is closed when a sediment transport parameterization is added to this framework. The two parameterizations used in the last chapters are suitable for the sediment transport driven by the longshore current and/or rip-current circulation and consistently disregard the weaker cross-shore transport due solely to the waves. Importantly, a preference for down-slope transport is included. These are the essential ingredients of the model that are shown to lead to the formation of self-organized shore-transverse or oblique bars of finite amplitude that compare reasonably well with observations.

Some aspects, however, deserve further attention. Wave refraction by the alongshore non uniform topography has been considered only in a simplified way. Although Caballeria *et al.* (2002) pointed out that it was essential for the onshore current over the crests of the transverse bars which in turn is essential for its growth, our computations have shown that this current may exist even without wave refraction. Apart from refraction, the essential difference between that model and the present one is that irregular waves are now considered. Therefore, the importance of wave refraction could likely be restricted to the case of regular waves. It is nevertheless advised for future research to include a description of wave refraction over the bars which is suitable for finite amplitude topographic features. This would allow for checking its influence which is however expected to be limited. This description should also include wave diffraction which has not been accounted for in the present model. While refraction tends to concentrate wave energy over the shoals, diffraction tends to diffuse it away. Thus, both effects are expected to oppose each other and their analysis is an interesting issue for future research.

Moreover, the down-slope sediment transport is not yet very well known and a rather crude description has been adopted here. The sensitivity of the model to the slope coefficient, γ, has however pointed out that down-slope transport may be crucial for the saturation of bar growth and for finite amplitude bar properties. Thus, more attention should be paid to the gravitational down-slope transport in the future.

Finally, the simple initial conditions used in our experiments are useful to understand the mechanisms behind the formation and the evolution of rhythmic features; however, they avoid a precise comparison with observations. For instance, the model over-predicts migration velocities for these possible reasons: (i) the stationary incident wave field does not represent periods of low wave energy and of changing wave incidence angle (ii)

the hypothesis of a fixed sea level does not take into account the periods of no waves (dry beach) which happens at low tide in the intertidal zone. Besides, the growth time predicted by the model seems large because of the unrealistically small perturbation added to the initial bathymetry while in nature higher ripples or bed forms are present.

Chapter 8

Conclusions

8.1 Overall conclusions

The nonlinear numerical model MORFO55 has first been applied to particular cases of the surf zone of longitudinally non uniform beaches (chapter 3). The domain of validity of the model is limited, particularly because of the periodic lateral boundary conditions and the rectilinear shore and off-shore boundaries. However, these examples show that the model seems to be valid in case of quasi rectilinear beaches (when the cross-shore variation of the coastline is small compared to the longshore size of the beach, e.g. the Barrosa beach). The model is also valid in test cases with an obstacle (e.g. shoal, gully...) which breaks the alongshore uniformity of the beach, if the longshore size of the domain is taken sufficiently large. Successful hydrodynamical tests have been performed and different sediment transport formulations have been used. In particular, the Soulsby and Van Rijn formula appears numerically more stable than the Bailard formula. The former formula allows performing longer time morphological evolution.

By using the Soulsby and Van Rijn formula in the following chapters, a long term stability analysis of longitudinally uniform beaches has been made for the first time with a 2DH model. Numerous numerical studies on the emergence of rhythmic features may be found by using either linear stability analysis or nonlinear models, but they are restricted to the initial states of the formation of such features. As demonstrated by previous studies, these features strongly depend on the wave conditions, on the sediment transport mode and on the cross-shore bathymetric profile of the beach. In particular these two latter dependencies may be combined into one: the potential stirring, defined as the sediment transport stirring factor divided by the depth. The shape of the cross-shore profile of the potential stirring at the basic state determines the types of instability susceptible to develop. Moreover, the emergence of instabilities will be possible if a positive feedback between flow and morphology is established.

For instance a decreasing off-shore potential stirring is favourable to the formation of up-current oriented oblique bars and the positive feedback occurs in case of high angle oblique waves (e.g. in case of: planar beach, constant stirring factor, incident wave angle $\geq 20\,^{\circ}$). On the other hand, if the potential stirring increases seaward and decreases beyond a certain point, a series of pronounced bars (troughs) tend to appear in the offshore directed gradient area and extend them by slight troughs (bars) in the location of the onshore directed gradient of potential stirring. Such a peak in the potential stirring appears in the inner surf zone and on the top of a longshore bar, especially in the case of the Soulsby and Van Rijn stirring factor. For normal waves, transverse bar systems develop in the inner surf zone (c.f. planar beach instabilities) and crescentic bar systems develop from the longshore bar. The positive feedback is launched by bed-surf mechanisms owing to an increasing (decreasing) set-up/breaking over the pronounced bars (troughs). For oblique waves, this latter mechanism occurs too, but the dominant longshore current will cause the (down-current) oblique orientation and migration of the bars (down-current bar systems on planar beaches and oblique crescentic bar systems or ridge and runnel systems on barred beaches).

The morphological diffusivity due to the downslope transport largely affects the emergence of beach instabilities. Although the conditions of emergence of instabilities are satisfied because of the shape of potential stirring profile and due to the incident wave conditions, a large bedslope coefficient may inhibit the formation of instabilities by causing too much diffusivity. For this reason, the oblique/transverse bar systems do not appear in our examples of barred beaches instabilities. A global analysis involving the bar dynamics on the whole domain by introducing the space integrated production and damping terms, shows that a necessary and sufficient condition for the emergence of instabilities is that the production term is higher than the damping term. Moreover, this method allows understanding the finite amplitude bar dynamics such as the processes of saturation of the growth of the bars. For each type of instabilities, equilibrium has been reached and it occurs when a balance between these two terms is stabilised.

8.2 Specific answers to the research questions

1. Is it possible to model finite amplitude (long term) evolution of morphodynamical instabilities?

The finite amplitude (long term) evolution of morphodynamical instabilities has been investigated with the model. The emergence of oblique/transverse bars (in case of planar beaches) and of crescentic patterns (in case of barred beaches) has been extended to the nonlinear regime. This has been possible because the model can predict the saturation of the growth. The saturation has been obtained as a balance between the down-slope sediment transport (damping term) and the positive feedback between flow and morphology which is responsible for the initial formation of the bars (instability term). Both effects grow proportionally to bar amplitude at the initial stage, the instability term being somewhat stronger. The saturation occurs because the finite amplitude shape of the bars either enhances downslope transport or weakens the instability mechanism.

2. Is there any physical reason which explains why previous nonlinear numerical models could not describe the finite amplitude (long term) evolution of morphodynamical instabilities?

Previous modelling studies did not describe the nonlinear regime. As it is not possible to give a general explanation, we refer to our own model. In this study, we have presented finite amplitude evolutions of beach instabilities, but also some cases that lead to an overflow of the numerical model. Precisely, these latter cases appear when the saturation is not reached and they may be physically explained. In these cases, the bars grow too much and their top tends to grow almost up to the mean sea surface. In nature, the saturation could occur in the latter case due to processes related to very shallow water over the bars not described by the present model. It seems that stable computations are characterized by a ratio of maximum bar amplitude to total mean water depth not larger than about 0.6. It is intriguing to realise that even if the model does not resolve the individual waves, this ratio corresponds to the situation where the water depth at the troughs of the waves would be roughly zero.

3. What are the gains that may be obtained by modelling finite amplitude (long term) evolution of morphodynamical instabilities?

The aim of this question is not to make a comparison with observing patterns in nature as much as it is the topic of the research question 6, but it is looking at the differences between the initial results that the linear theory would predict, and the longer term results. Finite amplitude modelling allows representing interesting nonlinear behaviour of rhythmic bars, showing that, in some cases, the linear (initial) mode may disappear. For instance, merging of bars is predicted and it results in the increase of the wave length during the evolution. The migration velocity may also differ from the initial state to the final state. Regarding the shape of bars, linear stability can only predict sinusoidal patterns where crests and troughs are symmetrical. Consistently, onshore and offshore flow with the same intensity is equally distributed along the coast. This is not the case for the finite amplitude features, that have shown interesting asymmetric patterns. First for the shape of bars, and second for the associated current circulation which is sometimes characterized by a jet-like offshore flow and a wider and weaker onshore flow. Finally, the linear solution seems not to predict the formation of ridge and runnel systems (see research question 5).

4. Does an equilibrium state with rhythmic bars exist?

In nature, an equilibrium state with rhythmic bars is never reached probably because of the complexity of the external forcing. Nevertheless, due to the simplification of the phenomena, particularly when considering stationary wave forcing, it seems that an equilibrium state may be predicted by a numerical model. For each kind of bars, an equilibrium state has been reached because of a saturation mechanism (see research question 1). This mechanism is complex and a balance between the damping and the instability terms does not necessarily imply that equilibrium is reached. Another necessary condition to reach equilibrium is that this balance must be stabilised, i.e. the global measure of bar amplitude must be stable. In the default case of transverse bar systems, at the final state, these condi-

tions are satisfied, and bars do not change in time. However, these conditions may be satisfied whereas bars are still evolving: i) in the crescentic bar case, the shape of the bars seems slightly oscillate periodically ii) in case of oblique wave incidence (oblique bars, ridge and runnel systems), the bars migrate. We qualify these states as dynamical equilibrium states.

5. Do the ridge and runnel systems appear by morphodynamical self-organization ?

As explained the conceptual models based on satellite imagery, the ridge and runnel system may emerge by the deformation of the alongshore intertidal bar intercepted by crescentic bars. The different steps of the formation and the evolution of these systems have been recovered with the model. This demonstrates that they may appear by morphodynamical self-organization. More precisely, they seem to emerge in two steps: first the intertidal bar would deform to let crescentic structures appear. Then, these structures would attach to the coast to form kinds of large scale oblique bars similar to the ridge and runnel systems.

6. How realistic are the model results on surf zone rhythmic bars?

Comparison of model results with experimental data are limited by the following: (i) numerous simplifications/parameterizations of real processes have been considered to obtain the model equations (ii) the initial conditions imposed are very idealised, particularly concerning the incident waves which are assumed to be stationary in most cases (iii) field data sets on the evolution of rhythmic bars involving morphological evolution along with hydrodynamics are scarce and incomplete. However the simulated bar properties are consistent with the observed features, in particular regarding the length scales, growth rates, shapes (asymmetry, orientation), amplitudes, and migration celerities. In addition, interesting strong nonlinear behaviours such as the merging/splitting of bars that can appear in nature are also represented by the model. In a particular study of crescentic bars on a real (averaged) bathymetry from the French Atlantic coast, the model overestimates the growth time and migration celerities. The former is due to the unrealistic smallness of the bottom perturbation, the latter is due to the unrealistic incident wave conditions which does not represent the periods of low wave energy and changing wave angle. Another particular study, in progress, is devoted to compare the model results with the transverse/oblique bar systems which appear in the planar beach of Trafalgar, Cadiz, Spain.

8.3 Further research

8.3.1 Interaction between features

Linear stability analysis (Calvete *et al.*, 2005) predicts the development of a crescentic shape on the bar and the formation of transverse bars as two separate modes. This finding could suggest that the formation of transverse bars is not altered by the longshore bar even if it becomes crescentic. In this thesis, we have described these two modes separately.

In planar beach, the transverse bar mode has been studied; the crescentic bar mode cannot appear (van Leeuwen *et al.*, 2006). In a barred beach, the former has been damped by using a high bedslope coefficient or large grid spacing, only the latter has been studied. However, crescentic bars might act on transverse bars simply because they may induce oscillations on the coastline. Therefore, some crucial questions remain open. Is the initial formation of one of the two rhythmic systems altered by the other one? Is there some finite amplitude interaction between them? Is there any equilibrium state composed by the superposition of the two modes? This is the object of the further work by Garnier *et al.* (2007).

8.3.2 Model improvement

The model formulation used to study the instabilities on longitudinally uniform beaches does not take into account all the processes described in chapter 2, thus, the nearest further research will be to include the new available processes, then to finalise/consider the implementation of others.

Concerning the wave transformation, effects of refraction/diffraction can be included by using the parabolic mild slope equation (REF/DIF, Kirby *et al.*, 2002). It has been successfully tested at the basic states, and will be applied to the planar/barred beach instabilities. Further numerical work is needed before the suitability of the wave phase Eikonal equation which will allow isolating the effect of refraction and diffraction, by comparison with the results obtained by using the present formulation and the mild slope equation, respectively.

Concerning the sediment transport formulation, the downslope sediment transport is not yet very well known and a rather crude description has been adopted here, in particular, the bedslope coefficient has changed among the experiments. However, the downslope transport seems crucial for the formation of bars, for the saturation of bar growth and for finite amplitude bar properties, further work is therefore needed. Moreover, the three dimensional cross-shore processes are not included in our stability studies. The first possibility to include them is to use the Bailard formula (chapter 2) which includes the undertow and the wave skewness in a parametric way. The second option is to adapt this formulation to the Soulsby and Van Rijn formula and a third is to implement a quasi three dimensional formulation, by considering a vertical (non averaged) distribution of the current. By using a more realistic sediment transport formulation, a more sophisticated numerical scheme such as a non-oscillatory scheme (Saint-Cast, 2002; Marieu *et al.*, 2006) could be necessary for the discretization of the sediment conservation equation.

The effect of rhythmic bars on the shape of the coastline will also be investigated by implementing a moving shoreline. In particular, it seems that transverse bars and crescentic systems have a direct effect on the coastline and can be at the origin of beach cusps/megacusps. A more realistic modelling of ridge and runnel systems should be possible, if in addition, the tidal variation in sea level is taken into account. By including

a moving shoreline, another perspective is to apply the model to the large scale beach instabilities of Falqués & Calvete (2005); Falqués (2006).

8.3.3 Comparison with observations

A more precise comparison with observations of rhythmic bar formation and evolution will be possible thanks to both the widespread and improvement of the remote sensing techniques such as ARGUS images. They are now available in many beaches where rhythmic bars appear and they allow to follow the morphological evolution. Moreover, recent advance of these techniques dedicates to find a correspondence with the hydrodynamics. The comparison of the model results with the oblique/transverse bars observed in Trafalgar beach, Cadiz, Spain (Ortega *et al.*, 2007) is in preparation. The formation/evolution of crescentic bars of Bogatell beach, Barcelona, Spain, is also on the agenda (Ribas *et al.*, 2007). These two sites have the particularity to be characterized by a small tidal range, thus, the present model seems well adapted. However, the implementation of the tidal variation in sea level seems essential before a more precise comparative study of rhythmic features of the French Atlantic coast, in particular to take into account the periods of emerged intertidal features. The numerous existing observation studies based on field measurement or satellite imagery and the 2007 campaign will constitute a very complete database on the formation and on the evolution of crescentic bar and ridge and runnel systems.

Appendix A

Auxiliary integrals

This analytical approximation of the auxiliary integrals is taken from Falqués *et al.* (2002). For the evaluation of bottom friction and sediment transport with Bailard (1981) parameterization, the integral:

$$\vec{I}_n = \frac{1}{T}\int_0^T \left(\int_0^\infty |\vec{U} + \vec{\tilde{u}_{\rm b}}|^n (\vec{U} + \vec{\tilde{u}_{\rm b}})\, P(H)\, dH \right) dt \ , \tag{A.1}$$

for various n exponents, has to be evaluated, where:

$$P(H) = \frac{2H}{H_{\rm rms}^2}\, \exp\left(-\frac{H^2}{H_{\rm rms}^2}\right) \ ,$$

is the Rayleigh distribution. Here, $\vec{U}$ is the near bed mean velocity 2.41 and $\vec{\tilde{u}_{\rm b}}$ is the instantaneous wave orbital velocity at the bed (Fredsoe & Deigaard, 1992):

$$\vec{\tilde{u}_{\rm b}} = \frac{\pi H}{T}\, \frac{1}{\sinh kD}\, \frac{\vec{k}}{k}\, \cos(\omega t^*) \ = \ \tilde{u_{\rm b}}\, \frac{\vec{k}}{k} \ , \tag{A.2}$$

with $T = 2\pi/\omega$ being the peak period. We will introduce the angle θ between the wave propagation and the x_1-axis, and the angle ϕ between the current and the x_1-axis:

$$k_1 = k\cos\theta \quad , \quad k_2 = k\sin\theta \quad , \qquad U_1 = U\cos\phi \quad , \quad U_2 = U\sin\phi \ , \tag{A.3}$$

where $U = |\vec{U}|$. Then, we can write

$$|\vec{U} + \vec{\tilde{u}_{\rm b}}| = \sqrt{U^2 + \tilde{u_{\rm b}}^2 + 2U\tilde{u_{\rm b}}\cos\psi} \ , \tag{A.4}$$

where $\psi = \phi - \theta$ is the angle between the current and the wave propagation direction.

A number of changes can be done in the integral A.1. First, we define:

$$H \ = \ H_{\rm rms}\,\xi \quad , \quad \varphi = \omega t^* \quad , \quad u_{\rm b} = \frac{\pi H_{\rm rms}}{T\, \sinh(kD)} \ ,$$

and we will have:

$$\tilde{u_{\rm b}} = u_{\rm b}\xi\cos\varphi$$

$u_{\rm b}$ is the wave orbital velocity amplitude at the bottom of a wave with $H = H_{\rm rms}$ (equation 2.45).

We also define:

$$\hat{U}_1 = \frac{U_1}{u_{\rm b}} \quad , \quad \hat{U}_2 = \frac{U_2}{u_{\rm b}} \quad , \quad \hat{U} = \sqrt{\hat{U}_1^2 + \hat{U}_2^2} \ .$$

We will have

$$P(H)\,dH \ = \ 2\xi e^{-\xi^2}\,d\xi \ = \ \hat{P}(\xi)d\xi \ .$$

With all the changes, the integral A.1 will read:

$$\begin{aligned} \vec{I_n} \ &= \ \frac{u_{\rm b}^{n+1}}{2\pi}\int_0^{2\pi}\int_0^{\infty} \\ &[\hat{U}^2 + \xi^2(\cos\varphi)^2 + 2\xi U\cos\varphi\cos\psi]^{n/2}(\hat{\vec{U}} + \xi\cos\varphi\frac{\vec{k}}{k})P(\xi)\ \ d\xi\,d\varphi \ . \end{aligned} \tag{A.5}$$

The change:

$$x = \xi\cos\varphi \quad , \quad y = \xi\sin\varphi \ ,$$

from polar to Cartesian coordinates can be made in equation A.5:

$$\vec{I_n} = \frac{u_{\rm b}^{n+1}}{\pi}\int_{-\infty}^{\infty}\int_{-\infty}^{\infty}[\hat{U}^2 + x^2 + 2xU\cos\psi]^{n/2}(\hat{\vec{U}} + x\frac{\vec{k}}{k})\,e^{-(x^2+y^2)}\,dx\,dy \ ,$$

from where,

$$\vec{I_n} = \frac{u_{\rm b}^{n+1}}{\sqrt{\pi}}\int_{-\infty}^{\infty}[\hat{U}^2 + x^2 + 2xU\cos\psi]^{n/2}(\hat{\vec{U}} + x\frac{\vec{k}}{k})\,e^{-x^2}\,dx$$

follows. If we define the functions

$$F_n(\hat{U},\psi) = \int_{-\infty}^{\infty}[\hat{U}^2 + x^2 + 2xU\cos\psi]^{n/2}\,e^{-x^2}\,dx \ , \tag{A.6}$$

$$G_n(\hat{U},\psi) = \int_{-\infty}^{\infty}[\hat{U}^2 + x^2 + 2xU\cos\psi]^{n/2}\,x\,e^{-x^2}\,dx \ , \tag{A.7}$$

the integral can be finally written as:

$$\vec{I_n} = \frac{b^{n+1}}{\sqrt{\pi}}\,(F_n(\hat{U},\psi)\,\hat{\vec{U}} \ + \ G_n(\hat{U},\psi)\,\frac{\vec{k}}{k}) \ . \tag{A.8}$$

Notice that F_n and G_n have the symmetry properties:

$$F_n(\hat{U},\pi-\psi) \ = \ F_n(\hat{U},\psi) \quad , \quad G_n(\hat{U},\pi-\psi) \ = \ -\,G_n(\hat{U},\psi) \tag{A.9}$$

Thus, we will use these relationships and we will compute F_n, G_n only for $0 \le \psi \le \pi/2$.

A.1 Strong current limit

For $\hat{U} \gg 1$ we have:

$$\begin{aligned} F_n(\hat{U},\psi) &\simeq \hat{U}^n \int_{-\infty}^{\infty} (1+\frac{n\cos\psi}{2\hat{U}}x)\, e^{-x^2}\, dx \\ &= \hat{U}^n \int_{-\infty}^{\infty} e^{-x^2}\, dx \\ &= \sqrt{\pi}\,\hat{U}^n \ , \end{aligned} \tag{A.10}$$

and,

$$\begin{aligned} G_n(\hat{U},\psi) &\simeq \hat{U}^n \int_{-\infty}^{\infty} (1+\frac{n\cos\psi}{2\hat{U}}x)\, x\, e^{-x^2}\, dx \\ &= \frac{n}{2}\hat{U}^{n-1}\cos\psi \int_{-\infty}^{\infty} x^2\, e^{-x^2}\, dx \\ &= \sqrt{\pi}\,\frac{n}{2}\,\hat{U}^{n-1}\,\cos\psi \ . \end{aligned} \tag{A.11}$$

A.2 Weak current limit

By making the transformation $x = \hat{U}z$ we have:

$$F_n(\hat{U},\psi) = \int_{-\infty}^{\infty} [1+z^2+2z\cos\psi]^{n/2}\, e^{-\hat{U}\,z^2}\, dz \ .$$

Given a $z_1 > 0$ the integral can be written as:

$$F_n(\hat{U},\psi) = \int_{-\infty}^{-z_1} ()\, dz \ + \int_{-z_1}^{z_1} ()\, dz \ + \int_{z_1}^{\infty} ()\, dz \ .$$

Let's consider $z_1 = 1$. If $\hat{U} \ll 1$, $e^{-\hat{U}\,z^2} \sim 1$ for z well above z_1. Therefore, the main contribution to F_n will come from the integrals from $-\infty$ to $-z_1$ and from z_1 to ∞. We then will have:

$$\begin{aligned} F_n(\hat{U},\psi) &\simeq \hat{U}^{n+1} \int_{-\infty}^{-z_1} [1+z^2+2z\cos\psi]^{n/2}\, e^{-\hat{U}\,z^2}\, dz \\ &+ \hat{U}^{n+1} \int_{z_1}^{\infty} [1+z^2+2z\cos\psi]^{n/2}\, e^{-\hat{U}\,z^2}\, dz \\ &\simeq 2\,\hat{U}^{n+1} \int_{0}^{\infty} z^n\, e^{-\hat{U}\,z^2}\, dz \\ &= \Gamma\left(\frac{n+1}{2}\right) \ , \end{aligned} \tag{A.12}$$

Furthermore:

$$\begin{aligned} G_n(\hat{U},\psi) &= \hat{U}^{n+2}\int_{-\infty}^{\infty}[1+z^2+2z\cos\psi]^{n/2}\,z\,e^{-\hat{U}\,z^2}\,dz \\ &= \hat{U}^{n+2}\int_{-\infty}^{\infty}|z|^n\,[1+2\frac{\cos\psi}{z}+\frac{1}{z^2}]^{n/2}\,z\,e^{-\hat{U}\,z^2}\,dz\ . \end{aligned}$$

For $\hat{U}\ll 1$ the main contribution to the integral comes from large $|z|$ in the same way than for F_n. Thus,

$$\begin{aligned} G_n(\hat{U},\psi) &\simeq \hat{U}^{n+2}\int_{-\infty}^{\infty}|z|^n\,[1+2\frac{\cos\psi}{z}]^{n/2}\,z\,e^{-\hat{U}\,z^2}\ dz \\ &\simeq n\,\hat{U}^{n+2}\,\cos\psi\int_{-\infty}^{\infty}|z|^n\,e^{-\hat{U}\,z^2}\ dz \\ &= n\,\hat{U}\ \ \Gamma\left(\frac{n+1}{2}\right)\cos\psi\ . \end{aligned} \tag{A.13}$$

A.3 Analytical approximations

The F_n function can be approximated/computed analytically by:

$$F_1(\hat{U},\psi)\ \simeq\ \sqrt{\pi}\hat{U}\ +\ \frac{1}{1+1.6\,\hat{U}+2.5\,\hat{U}^2}\ , \tag{A.14}$$

$$F_2(\hat{U},\psi)\ =\ \sqrt{\pi}\hat{U}^2\ +\ \frac{\sqrt{\pi}}{2}\ , \tag{A.15}$$

$$F_3(\hat{U},\psi)\ \simeq\ \sqrt{\pi}\hat{U}^3\ +\ (2.61-0.92\psi)\,\hat{U}\ +\ \frac{1}{1+2.7\,\hat{U}}\ , \tag{A.16}$$

$$\begin{aligned} F_5(\hat{U},\psi) &\simeq \sqrt{\pi}\hat{U}^5\ +\ (8.66-4.30\psi)\hat{U}^3\ +\ (2.024-0.802\psi)\hat{U}^2 \\ &+ \ (3.38-1.78\psi)\hat{U}\ +\ 2\ , \end{aligned} \tag{A.17}$$

and the G_n by:

$$G_1(\hat{U},\psi)\ \simeq\ \frac{(1+\hat{U})\,\hat{U}\,\cos\psi}{1.0811-0.043\psi+(0.351+0.55\psi)\hat{U}+(1.261-0.098\psi)\hat{U}^2}\ , \tag{A.18}$$

$$G_2(\hat{U},\psi) \;=\; \sqrt{\pi}\hat{U}\,\cos\psi \;\;, \tag{A.19}$$

$$G_3(\hat{U},\psi) \;\simeq\; \frac{3}{2}\sqrt{\pi}\hat{U}\,\cos\psi\,\left(1.128 \;+\; \frac{0.0442 - 0.3016\hat{U} + 1.018\hat{U}^2}{1+\hat{U}}\right) \;\;. \tag{A.20}$$

Notice that these formulae hold for $0 \leq \psi \leq \pi/2$. For $\psi > \pi/2$, as a consequence of the symmetry properties A.9, everything is the same but substituting ψ by $\pi - \psi$.

Appendix B

Bed shear stress integration

The time average of the instantaneous bed shear stress vector 2.43 is presented, from Falqués *et al.* (2002). The bed shear stress in the momentum equations is an analytical approximation of the average over the Rayleigh distributed wave height and over the wave period of the instantaneous bed shear stress vector given by Mei (1989):

$$\vec{\tilde{\tau}}_{\rm b} = \rho\, c_{\rm d}\, |\vec{\tilde{u}}_{\rm B}|\, \vec{\tilde{u}}_{\rm B} \ , \tag{B.1}$$

where $\vec{\tilde{u}}_{\rm B}$ is the instantaneous total flow velocity at the bed (from both currents and waves). By approximating $\vec{\tilde{u}}_{\rm B}$ as the sum of the near bed current velocity and the instantaneous wave orbital velocity at the bottom, we lead to:

$$\vec{\tilde{\tau}}_{\rm b} = \rho\, c_{\rm d}\, |\vec{U} + \vec{\tilde{u}}_{\rm b}|\, (\vec{U} + \vec{\tilde{u}}_{\rm b}) \ , \tag{B.2}$$

where $\vec{\tilde{u}}_{\rm b}$ is the instantaneous wave orbital velocity vector at the bottom. Since there is a probability distribution $P(H)$ of wave amplitudes, equation B.2 has to be averaged over all the wave amplitudes. Furthermore, we are interested in the time averaged bottom shear stress. We thus will have:

$$\vec{\tau}_{\rm b} = \frac{1}{T} \int_0^T \left(\int_0^\infty \rho c_{\rm d} |\vec{U} + \vec{\tilde{u}}_{\rm b}| (\vec{U} + \vec{\tilde{u}}_{\rm b})\, P(H)\, dH \right) dt \ . \tag{B.3}$$

This integral can be computed as:

$$\vec{\tau}_{\rm b} = \rho c_{\rm d}\, \vec{I}_1 = \rho\, c_{\rm d}\, \frac{u_{\rm b}^2}{\sqrt{\pi}} \left(F_1(\hat{U}, \psi)\, \hat{\vec{U}} \ + \ G_1(\hat{U}, \psi)\, \frac{\vec{k}}{k} \right) \ , \tag{B.4}$$

by using the developments in appendix A, where

$$u_{\rm b} = \frac{\pi H_{rms}}{T\, \sinh(kD)} \quad , \quad \hat{\vec{U}} \ = \ \frac{\vec{U}}{u_{\rm b}} \ ,$$

ψ is the angle between the current and the wave incidence and the functions F_1, G_1 are given in appendix A.

- An obvious approximation concerns the strong current limit, $\hat{U} \gg 1$, where:

$$F_1 = \sqrt{\pi}\,\hat{U} \quad , \quad G_1 = 0.5\,\sqrt{\pi}\,\cos\psi \ ,$$

from where:

$$\vec{\tau_b} \,=\, \rho\, c_{\rm d}\,(U\,\vec{U} \,+\, \frac{u_{\rm b}^2}{2}\,\cos\psi\,\frac{\vec{k}}{k}) \,\simeq\, \rho\, c_{\rm d}\,U\,\vec{U} \ . \tag{B.5}$$

- In the weak current limit, $\hat{U} \ll 1$, we have (appendix A):

$$F_1 \,=\, 1 \quad , \quad G_1 \,=\, \hat{U}\,\cos\psi \ ,$$

and, therefore,

$$\vec{\tau_b} \,=\, \rho\,\frac{c_{\rm d}\,u_{\rm b}}{\sqrt{\pi}}\,(\vec{U} + U\cos\psi\,\frac{\vec{k}}{k}) \ . \tag{B.6}$$

- In case of no current, $\hat{U} = 0$, we have $\vec{I}_1 = 0$, since $G_1(0,\psi) = 0$, so that the bottom shear stress vanishes, $\vec{\tau}_b = 0$.

- In the general case, the analytical approximations of F_1 and G_1 allow writting:

$$\begin{aligned}\vec{\tau_{\rm b}} \quad &= \quad \rho\, c_{\rm d}\,U\,\vec{U} + \rho\,\frac{c_{\rm d}}{\sqrt{\pi}}\,\frac{u_{\rm b}\,\vec{U}}{1 + 1.6\,\hat{U} + 2.5\,\hat{U}^2} \\ &+ \quad \rho\,\frac{c_{\rm d}}{\sqrt{\pi}}\,\frac{(u_{\rm b}\,U + U^2)\,\cos\Psi}{1.081 - 0.043\,\Psi + (0.351 + 0.55\,\Psi)\,\hat{U} + (1.26 - 0.098)\,\Psi)\,\hat{U}^2}\,\frac{\vec{k}}{k} \ .\end{aligned} \tag{B.7}$$

Thus, equation 2.44 is found.

Appendix C

Bailard sediment transport integration

C.1 Bailard bedload transport

According to Bailard (1981), the instantaneous bedload transport without the gravitational contribution and without the contribution driven by the waves alone in absence of current is:

$$\vec{q_{\rm bl}} = \frac{\epsilon_{\rm b}\, c_{\rm D}}{g(s-1)\tan\phi_{\rm c}} |\vec{u_{\rm B}}|^2\, \vec{u_{\rm B}} \ , \tag{C.1}$$

where $c_{\rm D}$ is the morphodynamical frictional drag coefficient, $\phi_{\rm c}$ is the angle of repose of the sediment, $\epsilon_{\rm b} \simeq 0.13$ is an efficiency and s is the relative density of the sediment ($s \simeq 2.7$). The original formula of Bailard has been divided by $\rho_{\rm s} g$ in order to express $\vec{q}$ as volume instead of weight per time and length units, with account of $\rho_{\rm s} = s\rho$.

With the same method than in appendix B, we compute the (mean) bedload transport vector as:

$$\vec{q_{\rm bl}} = \frac{\epsilon_{\rm b}\, c_{\rm D}}{g(s-1)\tan\phi_{\rm c}} \frac{1}{T} \int_0^T \left(\int_0^\infty |\vec{U} + \vec{u_{\rm b}}|^2\, (\vec{U} + \vec{u_{\rm b}}) P(H)\, dH \right) dt \ . \tag{C.2}$$

After the definition of the $\vec{I_n}$ integral (appendix A), we can write:

$$\vec{q_{\rm bl}} = \frac{\epsilon_{\rm b}\, c_{\rm D}}{g(s-1)\tan\phi_{\rm c}}\, \vec{I_2} \ , \tag{C.3}$$

and since $\vec{I_2}$ can be computed exactly we have:

$$\vec{q_{\rm bl}} = \frac{\epsilon_{\rm b}\, c_{\rm D}}{g(s-1)\tan\phi_{\rm c}} \left((U^2 + \frac{u_{\rm b}^2}{2})\vec{U} \ + \ u_{\rm b}^2 U \, \cos\psi \, \frac{\vec{k}}{k} \right) \ . \tag{C.4}$$

C.2 Bailard suspended load transport

Again, according to Bailard (1981), the instantaneous suspended load transport without the gravitational contribution and without the contribution driven by the waves alone in absence of current is:

$$\vec{q_{\rm sl}} = \frac{\epsilon_{\rm s}\, c_{\rm D}}{g(s-1)w_{\rm s}} |\vec{u_{\rm B}}|^3\, \vec{u_{\rm B}} \ , \tag{C.5}$$

where $\epsilon_{\rm s}$ is the efficiency for suspended load and $w_{\rm s}$ is the fall celerity of the sediment. The (mean) suspended load transport vector may be computed as:

$$\vec{q_{\rm sl}} = \frac{\epsilon_{\rm s}\, c_{\rm D}}{g(s-1)\, w_{\rm s}} \frac{1}{T} \int_0^T \left(\int_0^\infty |\vec{U} + \vec{u_{\rm b}}|^3\, (\vec{U} + \vec{u_{\rm b}})\, P(H)\, dH \right) dt \ , \tag{C.6}$$

i.e., from appendix A:

$$\vec{q_{\rm sl}} = \frac{\epsilon_s\, c_{\rm D}}{g(s-1)\, w_{\rm s}}\, \vec{I_3} \ , \tag{C.7}$$

which gives:

$$\begin{aligned} \vec{q_{\rm sl}} &= \frac{\epsilon_{\rm s}\, c_{\rm D}}{g(s-1)\, w_{\rm s}} (U^3 + (1.47 - 0.52\psi) u_{\rm b}^2 U + \frac{0.56\, u_{\rm b}^3}{1 + 2.7\hat{U}})\, \vec{U} \\ &+ \frac{\epsilon_{\rm s}\, c_{\rm D}}{g(s-1)\, w_{\rm s}} (1.7 + \frac{0.0663 - 0.453\hat{U} + 1.53\hat{U}^2}{1+\hat{U}})\, u_{\rm b}^3 U\, \cos\psi\ \frac{\vec{k}}{k} \ . \end{aligned} \tag{C.8}$$

The limit cases are:

- strong current,

$$\vec{q_{\rm sl}} = \frac{\epsilon_{\rm s}\, c_{\rm D}}{g(s-1)\, w_{\rm s}} (U^3\, \vec{U} \ + \ \frac{3}{2}\, u_{\rm b}^2 U^2\, \cos\psi\, \frac{\vec{k}}{k}) \ , \tag{C.9}$$

- weak current,

$$\vec{q_{\rm sl}} = \frac{1}{\sqrt{\pi}}\, \frac{\epsilon_{\rm s}\, c_{\rm D}}{g(s-1)\, w_{\rm s}}\, u_{\rm b}^3\, (\vec{U} \ + \ 3\, U\, \cos\psi\, \frac{\vec{k}}{k}) \ . \tag{C.10}$$

C.3 Bailard downslope gravitational transport

According to Bailard (1981), the gravitational contribution of the instantaneous bedload transport is:

$$\vec{q_{\rm gbl}} = -\frac{\epsilon_{\rm b}\, c_{\rm D}}{g(s-1)\tan\phi_{\rm c}^2}\, |\vec{u_{\rm B}}|^3\, \vec{i_{\rm b}}\ \tan\beta \ , \tag{C.11}$$

where $\tan\beta$ is the slope of the bed and $\vec{i_{\rm b}}$ is the unitary vector standing for the downslope direction. The gravitational contribution of the instantaneous suspended load transport is:

$$\vec{q_{\rm gsl}} = -\frac{\epsilon_{\rm s}^2\, c_{\rm D}}{g(s-1)w_{\rm s}^2}\, |\vec{u_{\rm B}}|^5\, \vec{i_{\rm b}}\ \tan\beta \ . \tag{C.12}$$

Thus, the gravitational contribution of the instantaneous total load transport is:

$$\vec{q_{\rm g}} = -\,\tilde{\gamma_{\rm g}}\,\vec{i_{\rm b}}\,\tan\beta \ , \tag{C.13}$$

where:

$$\tilde{\gamma_{\rm g}} = \frac{c_{\rm D}}{g(s-1)}\left(\frac{\epsilon_{\rm b}}{\tan\phi_{\rm c}^2} + \left(\frac{\epsilon_{\rm s}}{w_{\rm s}}\right)^2 |\vec{u_{\rm B}}|^2\right)|\vec{u_{\rm B}}|^3 \ . \tag{C.14}$$

If we consider that $\vec{i_{\rm b}}\,\tan\beta = \vec{\nabla} z_{\rm b}$, equation C.13 gives:

$$\vec{q_{\rm g}} = -\,\tilde{\gamma_{\rm g}}\,\vec{\nabla} z_{\rm b} \ . \tag{C.15}$$

Notice that equation C.15 is valid in the case that all the term of the cross-shore transport are included, i.e., if the undertow and if the effect of wave skewness are considered. If we neglect the cross-shore, we assume that the instantaneous downslope gravitational transport is:

$$\vec{q_{\rm g}} = -\,\tilde{\gamma_{\rm g}}\,\vec{\nabla} h \ , \tag{C.16}$$

where h is the bed level deviation from the initial bathymetry.

The (mean) downslope gravitational transport in the case that all the term of the cross-shore transport are included is:

$$\vec{q_{\rm g}} = -\,\gamma_{\rm g}\,\vec{\nabla} z_{\rm b} \ , \tag{C.17}$$

where, $\gamma_{\rm g}$ is called the Bailard bedslope coefficient and reads:

$$\begin{aligned} \gamma_{\rm g} \quad = \quad & \frac{c_{\rm D}}{g(s-1)}\frac{1}{T}\int_0^T\int_0^\infty \\ & |\vec{U}+\vec{u_{\rm b}}|^3\left(\frac{\epsilon_{\rm b}}{(\tan\phi_{\rm c})^2} \ + \ (\frac{\epsilon_{\rm s}}{w_{\rm s}})^2\,|\vec{U}+\vec{u_{\rm b}}|^2\right) P(H)\,dH\,dt \ . \end{aligned} \tag{C.18}$$

The $\gamma_{\rm g}$ coefficient can be evaluated by means of the F_3 and F_5 integrals (appendix A) as:

$$\gamma_{\rm g} = \frac{c_{\rm D}}{g(s-1)}\left(\frac{\epsilon_{\rm b}}{(\tan\phi_{\rm c})^2}\,\frac{u_{\rm b}^3}{\sqrt{\pi}}F_3 \ + \ (\frac{\epsilon_{\rm s}}{w_{\rm s}})^2\,\frac{u_{\rm b}^5}{\sqrt{\pi}}F_5\right) \ . \tag{C.19}$$

By using the analytical approximations we obtain:

$$\begin{aligned} \gamma_{\rm g} \quad = \quad & \frac{c_{\rm D}}{g(s-1)}\,\frac{\epsilon_{\rm b}}{(\tan\phi_{\rm c})^2}\left(U^3 \ + \ (1.47-0.52\psi)\,u_{\rm b}^2 U \ + \ \frac{0.56\,u_{\rm b}^3}{1+2.7\,\hat{U}}\right) \\ + \quad & \frac{c_{\rm D}}{g(s-1)}\left(\frac{\epsilon_{\rm s}}{w_{\rm s}}\right)^2\left(U^5 \ + \ (4.89-2.43\psi)u_{\rm b}^2U^3\right. \\ & \left. +\,(1.14-0.452\psi)u_{\rm b}^3U^2 \ + \ (1.91-\psi)u_{\rm b}^4U \ + \ 1.13u_{\rm b}^5\right) \ . \end{aligned} \tag{C.20}$$

The limit cases are:

- strong current,

$$\gamma_{\mathrm{g}} = \frac{c_{\mathrm{D}}}{g(s-1)}\, U^3 \left(\frac{\epsilon_{\mathrm{b}}}{(\tan\phi_{\mathrm{c}})^2} + (\frac{\epsilon_{\mathrm{s}}}{w_{\mathrm{s}}})^2\, U^2 \right) \quad , \tag{C.21}$$

- weak current,

$$\gamma_{\mathrm{g}} = \frac{c_{\mathrm{D}}}{g(s-1)}\, \frac{u_{\mathrm{b}}^3}{\sqrt{\pi}} \left(\frac{\epsilon_{\mathrm{b}}}{(\tan\phi_{\mathrm{c}})^2} + 2\,(\frac{\epsilon_{\mathrm{s}}}{w_{\mathrm{s}}})^2\, u_{\mathrm{b}}^2 \right) \quad . \tag{C.22}$$

Appendix D

Comparison between the REF/DIF model and the wave energy equation.

The REF/DIF 1 model based on a parabolic version of the mild slope equation (Kirby *et al.*, 2002) has been incorporated in the 2DH model MORFO55. This new version of MORFO55 is called MORFO55-DIF.

In order to compare the REF/DIF 1 model with our wave energy formulation, the Thornton and Guza dissipation formula (equation 2.38) has been included in MORFO55-DIF, with 3 different methods of discretization, as: (a) REF/DIF 1, (b) REF/DIF S and (c) an hybrid way REF/DIF HW. The comparison has been done in the simple case of plane beach, and normal wave incidence, for the same conditions as Garnier *et al.* (2006*b*).

D.1 Discretization

The mild slope equation (equation 2.17) is discretized by using the Crank-Nicolson technique. Substituting the symbol I by i, and α_{rd} by α, equation 2.98 gives:

$$(\frac{1}{\Delta x} + 0.5\,\alpha_{i+1})\,A_{i+1} = (\frac{1}{\Delta x} - 0.5\,\alpha_i)\,A_i \ , \tag{D.1}$$

The solution for the step $i+1$ is deduced from the step i by using the linear system of the kind:

$$f(\alpha_{i+1})\,A_{i+1} = g(\alpha_i)\,A_i \ . \tag{D.2}$$

From Equation (2.38), $\alpha = \alpha(D, A)$, so as equation D.1 may be written as:

$$f(\alpha(D_{i+1}, A_{i+1}))\, A_{i+1} = g(\alpha(D_i, A_i))\, A_i \ . \tag{D.3}$$

Please note that this equation is a very simplified form of the mild slope equation used by REF/DIF. We choose to write this simple form to understand how the energy dissipation has been discretized. Particularly, the three following methods deal with three different ways to compute $f(\alpha_{i+1})$ which is a priori unknown because it depends on A_{i+1}.

D.1.0.1 (a) REF/DIF 1

In the REF/DIF 1 model (Kirby *et al.*, 2002), the energy dissipation was computed with two steps:

$$\begin{aligned} 1^{\text{st}} \qquad & f(\alpha(D_{i+1}, A_i))\, A_{i+1/2} = g(\alpha(D_i, A_i))\, A_i \,, \\ 2^{\text{nd}} \qquad & f(\alpha(D_{i+1}, A_{i+1/2}))\, A_{i+1} = g(\alpha(D_i, A_i))\, A_i \,. \end{aligned} \tag{D.4}$$

Concretely, a part of the code is written in section D.3.1, noting that in this part of code, `wb` corresponds to ε_{b}/E. The code used is the original REF/DIF 1 code.

D.1.0.2 (b) REF/DIF S

In the REF/DIF S model (Kirby *et al.*, 2004), only one step is done, supposing that in the left hand side of Equation D.3, $\alpha_{i+1} = \alpha_i$:

$$f(\alpha(D_i, A_i))\, A_{i+1} = g(\alpha(D_i, A_i))\, A_i \,. \tag{D.5}$$

From (a), we masked three lines (see section D.3.2).

D.1.0.3 (c) REF/DIF HW

The hybrid method called REF/DIF HW is the same as the case (a), except that the left hand side of Equation D.4, for the first step, depends on D_i (as on A_i) and not on D_{i+1}:

$$\begin{aligned} 1^{\text{st}} \qquad & f(\alpha(D_i, A_i))\, A_{i+1/2} = g(\alpha(D_i, A_i))\, A_i \,, \\ 2^{\text{nd}} \qquad & f(\alpha(D_{i+1}, A_{i+1/2}))\, A_{i+1} = g(\alpha(D_i, A_i))\, A_i \,. \end{aligned} \tag{D.6}$$

From (a), we changed `d(ip1,j)` by `d(ii,j)` in `wb(2,j)` (section D.3.3).

D.2 Results

A comparison of the three methods (a), (b) and (c) is presented in the first six panels of Figure D.1. In each case, when the grid size is small ($\Delta x = 1$ m), the solution is

closed to the one obtained by using the equilibrium state of the time dependent energy equation (the black line).

Looking at the last two panels of Figure D.1, an increasing grid size up to $\Delta x = 2$ m, then $\Delta x = 4$ m, does not falsify the results by using the time dependent energy equation. Nevertheless, for the methods (a) and (b) (first four panels), the results are worse when the grid size is bigger. Particularly, with the method (a) from the REF/DIF 1 model, the waves dissipate too much near the coastline (Panels (a1) and (b1)). On the contrary, with the method (b) from the REF/DIF S model, the waves dissipate too little (Panels (a2) and (b2)).

We will prefer the results by using the hybrid method (c), which fits better whatever the grid size (Panels (a3) and b(3)).

D.3 Code

D.3.1 (a) REF/DIF 1

```
subroutine fdcalc(ifreq,ir)
...
     do 200 i=1,(m-1)
      ip1=i+1
      it=1
...
C  Return here for iterations.
2     if(it.EQ.1)ii=i
      if(it.EQ.2)ii=ip1
...
      do 3 j=1,n
...
      wb(2,j)=cmplx(1.,0.)*1.5*sqrt(pi)*(btgrdm55**3.)*
      &(freqs(1)/(2.*pi))*
      &(cabs(a(ii,j))*2.)**3./(gamrdm55**2.*d(ip1,j)**3.)*
      &(1.-sqrt(1.+((cabs(a(ii,j))*2.)/
      &(gamrdm55*d(ip1,j)))**2.)
      &**(-5.))
...
3     continue
...
      if(it.EQ.2)go to 9
      it=2
      go to 2
9     continue
...
```

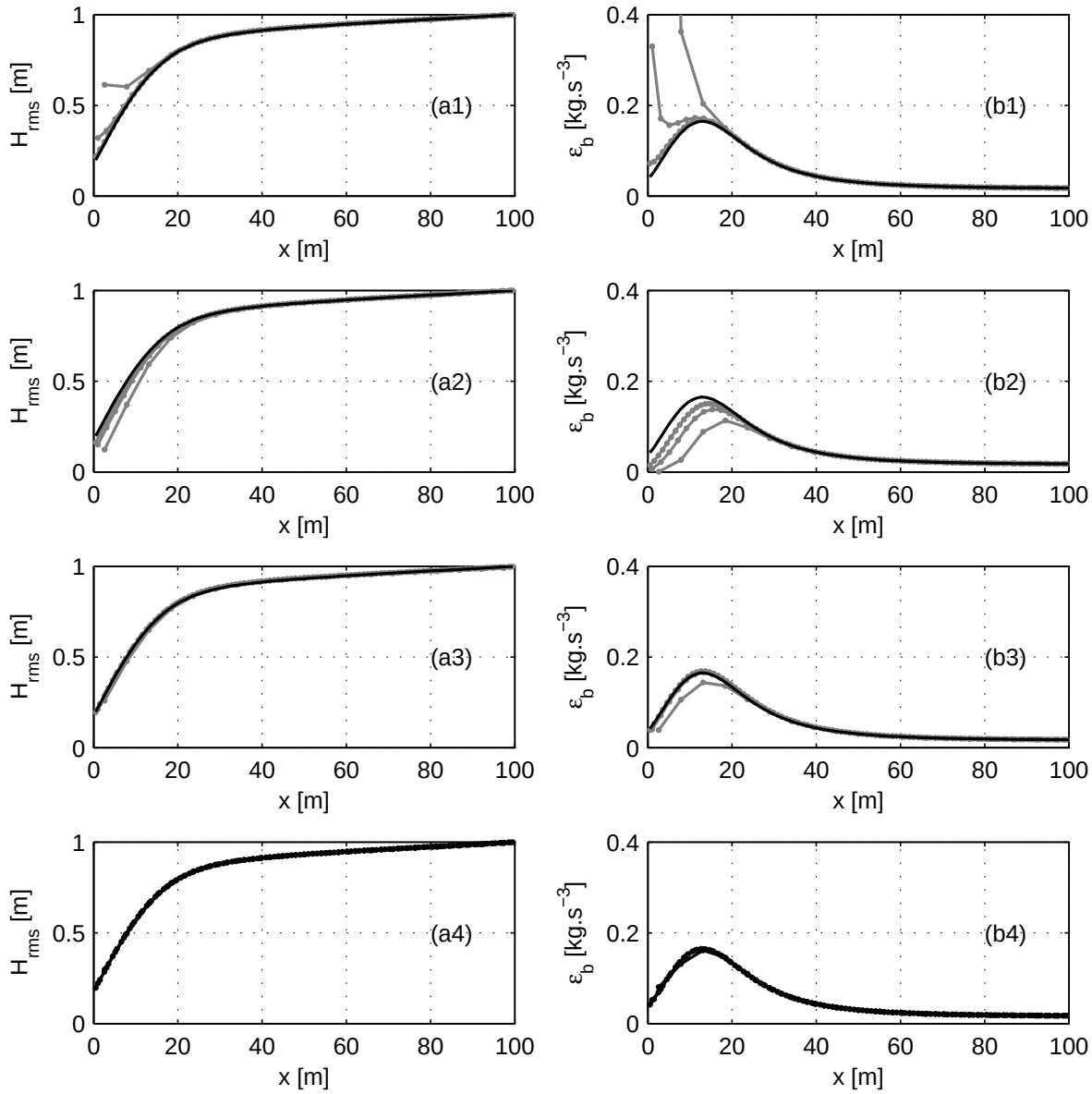

Figure D.1: Basic states profiles. Left (a): wave height, Right (b): dissipation rate. From up to down, the grey lines correspond to the results with the method of: (1) REF/DIF 1 (2) REF/DIF S (3) REF/DIF HW (4) Time dependent wave energy equation (MORFO55), for different grid sizes. For each graph, the black line stands for the solution of the time dependent wave energy equation.

```
200  continue
...
end
```

D.3.2 (b) REF/DIF S

```
subroutine fdcalc(ifreq,ir)
...
     do 200 i=1,(m-1)
      ip1=i+1
      it=1
...
C  Return here for iterations.
2     if(it.EQ.1)ii=i
      if(it.EQ.2)ii=ip1
...
      do 3 j=1,n
...
      wb(2,j)=cmplx(1.,0.)*1.5*sqrt(pi)*(btgrdm55**3.)*
      &(freqs(1)/(2.*pi))*
      &(cabs(a(ii,j))*2.)**3./(gamrdm55**2.*d(ip1,j)**3.)*
      &(1.-sqrt(1.+((cabs(a(ii,j))*2.)/
      &(gamrdm55*d(ip1,j)))**2.)
      &**(-5.))
...
3     continue
...
c       if(it.EQ.2)go to 9
c       it=2
c       go to 2
9     continue
...
200  continue
...
end
```

D.3.3 (c) REF/DIF HW

```
subroutine fdcalc(ifreq,ir)
...
     do 200 i=1,(m-1)
      ip1=i+1
      it=1
```

```
...
C  Return here for iterations.
2     if(it.EQ.1)ii=i
      if(it.EQ.2)ii=ip1
...
      do 3 j=1,n
...
      wb(2,j)=cmplx(1.,0.)*1.5*sqrt(pi)*(btgrdm55**3.)*
      &(freqs(1)/(2.*pi))*
      &(cabs(a(ii,j))*2.)**3./(gamrdm55**2.*d(ii,j)**3.)*
      &(1.-sqrt(1.+((cabs(a(ii,j))*2.)/
      &(gamrdm55*d(ii,j)))**2.)
      &**(-5.))
...
3     continue
...
      if(it.EQ.2)go to 9
      it=2
      go to 2
9     continue
...
200  continue
...
end
```

Appendix E

Wave propagating over a shoal

The hydrodynamics generated by waves normally incoming over a shoal have been investigated in order to compare our wave transformation formulations.

It has been used the option (W2a), (W2b) and (W3), characterized by (section 2.7:

- (W2a) The time-dependent wave energy equation, combined with the local Snell law.
- (W2b) The time-dependent wave energy equation, combined with the global Snell law.
- (W3) The REF/DIF 1 formulation adapted to the MORFO55 model.

Particularly,

- (W2a) does not describe the wave diffraction, and approximates the wave refraction,
- (W2b) does not describe neither the wave diffraction neither the wave refraction by the perturbated topography,
- (W3) describes both the wave diffraction and the wave refraction.

E.1 Experiments

We consider a planar beach of 100 m $\times$ 250 m long. A quasi-rectangular shoal is locate at the position ($x = 50$ m, $y = 125$ m). Its length may vary from 10 m to 160 m. Experiments have been done for the three wave transformation formulations.

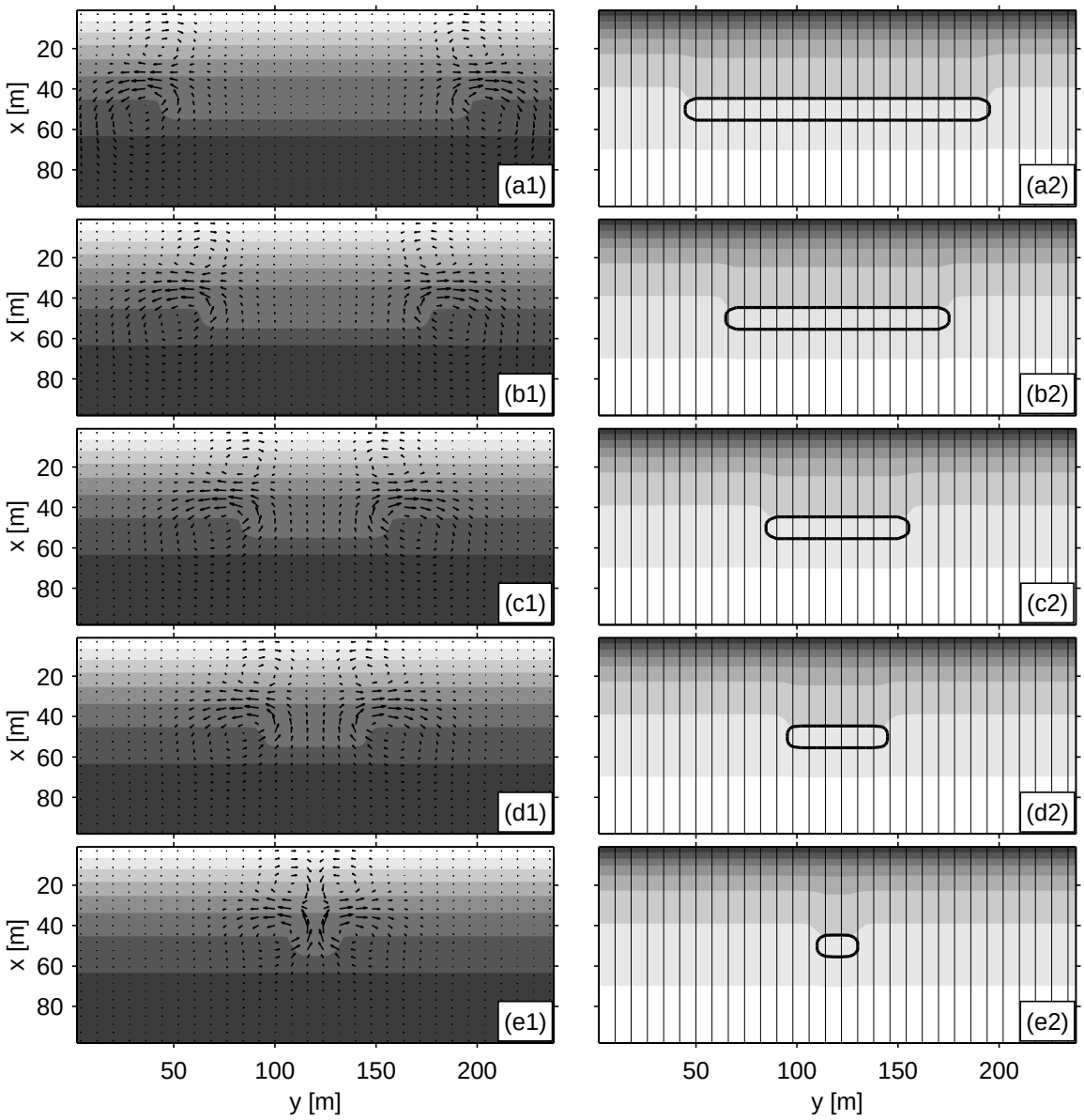

Figure E.1: Shoal experiments. Wave energy equation, global Snell law. Left (1): total depth and current circulation, right (2): wave energy, and wave rays, the thick contour line shows the position of the shoal. From up to down, the longshore span of the shoal is varying: (a) 160 m, (b) 100 m, (c) 60 m, (d) 40 m, (e) 10 m.

E.2 Results

Figure E.1 shows the results of the (W2b) option, for different shoal length. The right plots show that the wave rays are parallel, thus, this formulation does not consider neither the diffraction, nor the refraction. Whatever the length of the shoal, the current circulation may be characterized by a double cell at the y-position of each lateral edge of the shoal. The circulation is symmetric with respect to the $y = 125$ m axis. On the left edge, for instance, the current takes an anticlockwise directed circulation over the shoal, and a clockwise directed circulation in the shoreward part.

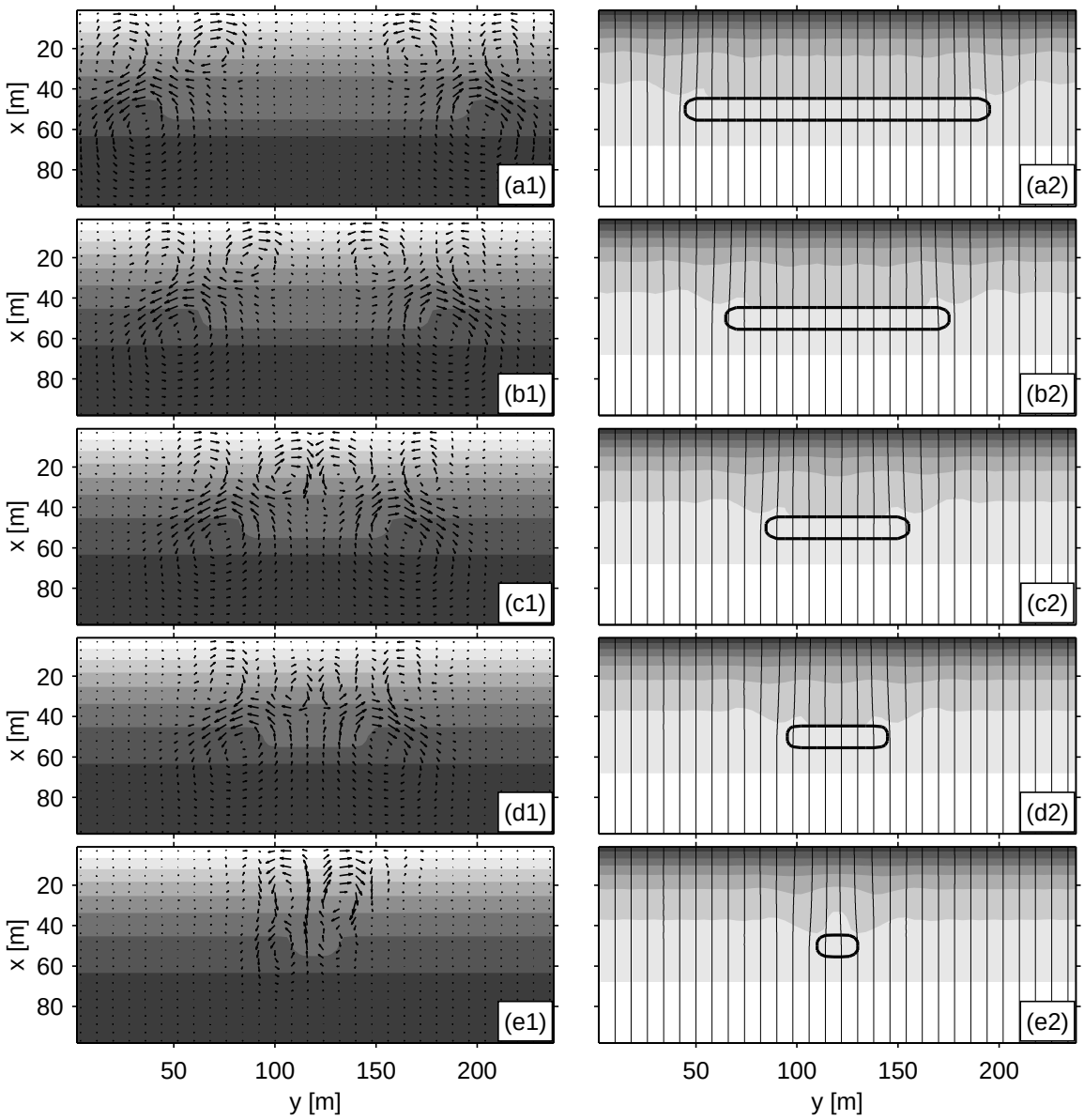

Figure E.2: Shoal experiments. REF/DIF Left (1): total depth and current circulation, right (2): wave energy, and wave rays, the fat contour line shows the position of the shoal. From up to down, the longshore span of the shoal is varying: (a) 160 m, (b) 100 m, (c) 60 m, (d) 40 m, (e) 10 m.

When the diffraction and refraction are included (figure E.2), the wave rays focusing through the centre of the shoal, the current circulation may be characterized by a triple cell (cases (a-d)). At the left edge, for instance, an other clockwise directed circulation cell is formed next to the previous one. The current becomes also more intense near the shore. When the shoal becomes shorter, the two triple cells becomes closer. For the shorter shoal (case (e)), the current becomes onshore in all the section crossing the middle of the shoal.

Figure E.3 also shows the results from (W2a). Figure E.4 is a zoom of the left edge of the shoal. The right plots represent the wave angle, the white colour meaning that the

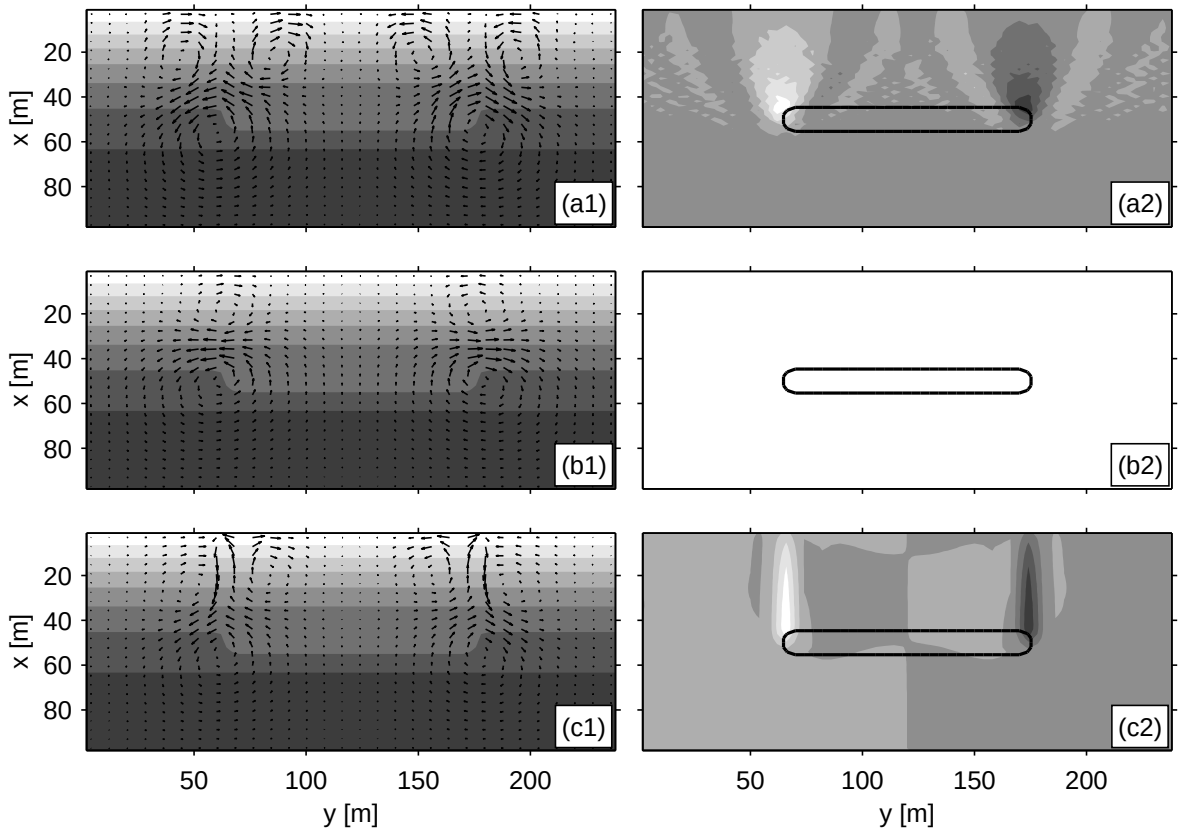

Figure E.3: Shoal experiments, span of the shoal: 100 m. Left (1): total depth and current circulation, right (2): wave angle (colours), the fat contour line shows the position of the shoal. From up to down, computed with: (a) REF/DIF, (b) MORFO55, simple Snell law, (c) MORFO55, local Snell law.

angle is positive, which directly illustrates processes taken into account. Looking at the left plots, a double cell is seen in (W2b) (plot (b1)), whereas a triple cell is seen in (W2a) (plot (c1)) and (W3) (plot (a1)). This suggests that wave refraction may be important. On the other hand, the wave diffraction seems to have a diffusive effect on the current circulation, the size of the cell being larger in (W2a) (plot (c1)) than in (W3) (plot (a1)).

Figure E.5 shows the same results than figure E.3, but in the case of the shoal of 20 m. Same conclusions on the effect of diffraction and refraction on the current circulation may be written.

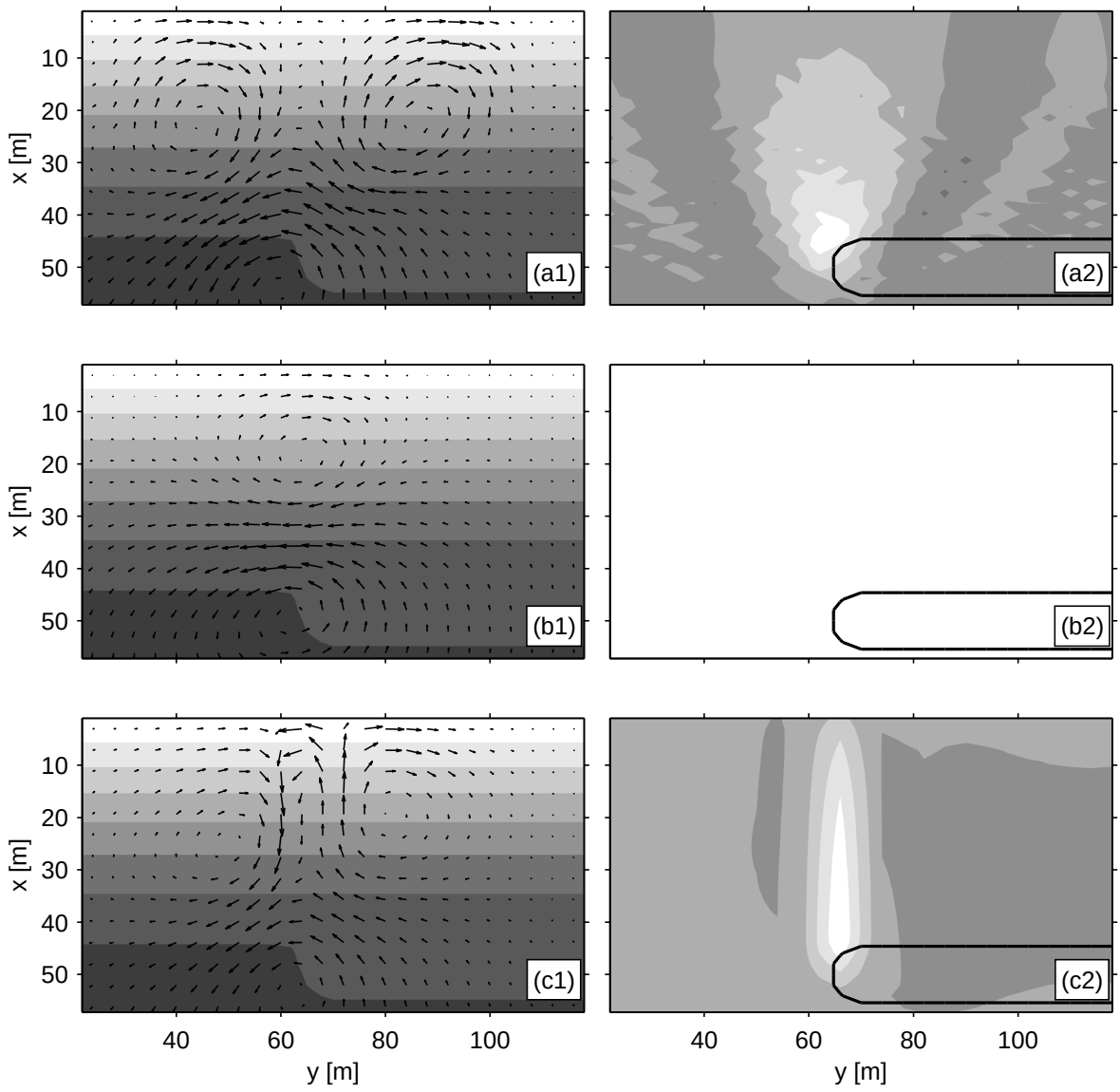

Figure E.4: Zoom of Figure E.3.

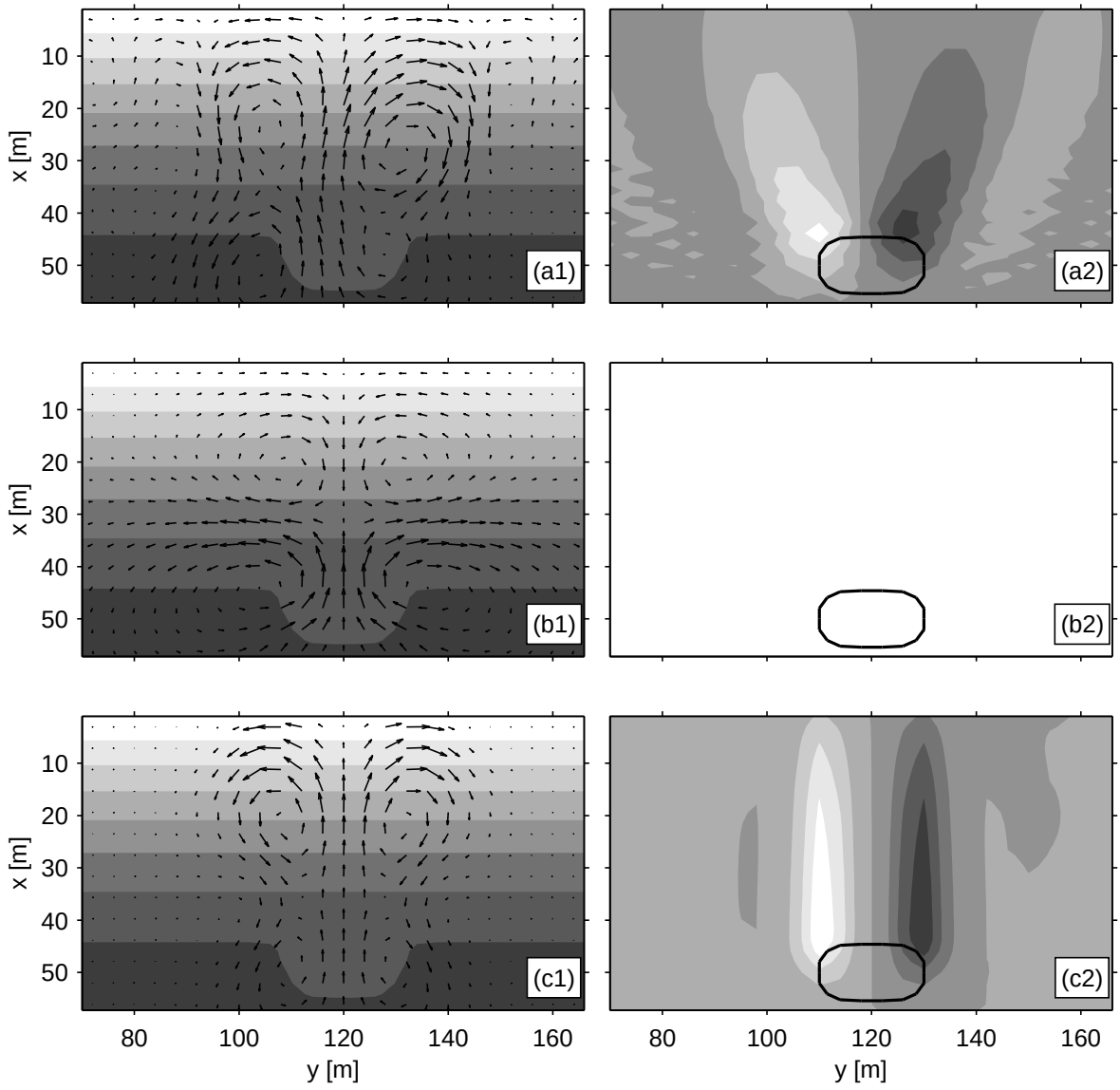

Figure E.5: Shoal experiments, span of the shoal: 10 m. See Figure E.3

Appendix F

Sediment transport analogy

In this section, we make the analogy between the two transport formula used (SVR and CWS) and the transport formula derived by Bailard (1981). The aim is (i) to compare the order of magnitude of the stirring factor used in our model with the corresponding one resulting from the Bailard formula and (ii) to compare the downslope transports.

F.1 SVR and CWS transport formulae

The general formula (equation 2.58) used to describe the total load transport (SVR or CWS) may be written as:

$$\vec{q} = \alpha(\vec{v} - \gamma\, u_{\rm b}\, \vec{\nabla} h) \; = \alpha(\vec{v} - \psi\, \vec{\nabla} h) \;\; , \tag{F.1}$$

where $\vec{v}$ is the depth averaged current vector, h is the bed level deviation from the initial bathymetry, α is the stirring factor, γ the bedslope coefficient and $u_{\rm b}$ the root-mean-square wave orbital velocity amplitude at the bottom defined in equation 2.45.

We introduce here $\psi = \gamma u_{\rm b}$, the bedslope factor. From the basic state figure, we can give an order of magnitude of the stirring factor α and of the bedslope factor for the two sediment transport formulae.

For the SVR transport:

$$\begin{array}{rcccl} \alpha & \sim & 10^{-3} & \mathrm{m} & , \\ \psi & = & 1.5\, u_{\rm b} & \sim \quad 1.5 & \mathrm{m\ s^{-1}} \;\; . \end{array}$$

For the CWS transport:

$$\begin{array}{rcccl} \alpha & \sim & 10^{-3} & \mathrm{m} & , \\ \psi & = & 0.5\, u_{\rm b} & \sim \quad 0.5 & \mathrm{m\ s^{-1}} \;\; . \end{array}$$

F.2 Bailard transport formula

The general transport formula derived by Bailard (Bailard, 1981) is an adaptation of the Bagnold formula (Bagnold, 1963) for steady two-dimensional stream flow to oscillatory flows such as those found in the surf zone. The original Bailard transport formula has been adapted in order to express the sediment flux as volume per time and length units. The resulting instantaneous total load transport of Bailard ($\vec{q_{\mathrm{B}}}$) is composed of the sum of the instantaneous bedload transport ($\vec{q_{\mathrm{Bbl}}}$) and the instantaneous suspended load transport ($\vec{q_{\mathrm{Bsl}}}$):

$$\vec{q_{\mathrm{B}}} = \vec{q_{\mathrm{Bbl}}} + \vec{q_{\mathrm{Bsl}}} \ , \tag{F.2}$$

where, by using the same nomenclature as appendixC:

$$\vec{q_{\mathrm{Bbl}}} = \vec{q_{\mathrm{bl}}} + \vec{q_{\mathrm{gbl}}} \ , \tag{F.3}$$

$$\vec{q_{\mathrm{Bsl}}} = \vec{q_{\mathrm{sl}}} + \vec{q_{\mathrm{gsl}}} \ . \tag{F.4}$$

The instantaneous bedload transport reads:

$$\vec{q_{\mathrm{Bbl}}} = \frac{\epsilon_{\mathrm{b}}\, c_{\mathrm{D}}\, |\vec{u_{\mathrm{B}}}|^2}{g(s-1)\tan\phi_{\mathrm{c}}} \left(\vec{u_{\mathrm{B}}} - \vec{i_{\mathrm{b}}}\, |\vec{u_{\mathrm{B}}}|\, \frac{\tan\beta}{\tan\phi_{\mathrm{c}}} \right) \ , \tag{F.5}$$

where ϵ_{b} is an efficiency ($\epsilon_{\mathrm{b}} \simeq 0.13$), c_{D} is the morphodynamical drag coefficient, $\vec{u_{\mathrm{B}}}$ is the total flow velocity at the bed (from both currents and waves), s is the relative density of the sediment ($s \simeq 2.7$), $\vec{i_{\mathrm{b}}}$ is the unitary vector standing for the downslope direction, $\tan\beta$ is the slope of the bed and $\tan\phi_{\mathrm{c}}$ is the slope of repose of the sediment.

If we assume that the undertow effect is not taken into account in the sediment transport formula, in order to have an order of magnitude of the resulting wave and depth averaged downslope transport flux $q_{\vec{\mathrm{Bbl}}}$, we can make the approximation that $q_{\vec{\mathrm{Bbl}}}$ may write as F.1, with:

$$\begin{aligned} \alpha = \alpha_{\mathrm{bl}} &\sim \frac{\epsilon_{\mathrm{b}}\, c_{\mathrm{D}}\, V^2}{g(s-1)\tan\phi_{\mathrm{c}}} \ , \\ \psi = \psi_{\mathrm{bl}} &\sim \frac{V}{\tan\phi_{\mathrm{c}}} \ . \end{aligned}$$

V is a characteristic velocity, taken as $V \sim 1\,\mathrm{m\,s^{-1}}$. From (Bailard, 1981), we fix $\tan\phi_{\mathrm{c}} \simeq 0.63$. c_{D} may be computed using Soulsby (1997) giving $c_{\mathrm{D}} \sim 0.1$ near the shoreline. It results:

$$\begin{aligned} \alpha_{\mathrm{bl}} &\sim 10^{-3} \quad \mathrm{m} \ , \\ \psi_{\mathrm{bl}} &\sim 1.6 \quad \mathrm{m\,s^{-1}} \ . \end{aligned}$$

The instantaneous suspended load transport reads:

$$\vec{q_{\mathrm{Bsl}}} = \frac{\epsilon_{\mathrm{s}}\, c_{\mathrm{D}}\, |\vec{u_{\mathrm{B}}}|^3}{g(s-1)w_{\mathrm{s}}} \left(\vec{u_{\mathrm{B}}} - \vec{i_{\mathrm{b}}}\, |\vec{u_{\mathrm{B}}}|^2\, \frac{\epsilon_{\mathrm{s}}}{w_{\mathrm{s}}} \tan\beta \right) \ , \tag{F.6}$$

where ϵ_s is an efficiency ($\epsilon_s \simeq 0.01$) and w_s is the fall celerity of the sediment. With the same approximations as for the bedload transport, we deduce the sirring and the bedslope factors for the suspended load transport:

$$\begin{aligned} \alpha = \alpha_{sl} &\sim \frac{\epsilon_s \, c_D \, V^3}{g(s-1)w_s} \ , \\ \psi = \psi_{sl} &\sim \epsilon_s \frac{V^2}{w_s} \ . \end{aligned}$$

Taking $w_s \simeq 0.05 \ \mathrm{m\,s^{-1}}$ (related with the grain size), we obtain:

$$\begin{aligned} \alpha_{sl} &\sim 1.2 \quad 10^{-3} \quad \mathrm{m} \ , \\ \psi_{sl} &\sim 0.2 \quad \mathrm{m\,s^{-1}} \ . \end{aligned}$$

F.3 Conclusion

The order of magnitude of the stirring factor is the same for each sediment transport formula (SVR, CWS, Bailard bedload, Bailard suspended load). The order of magnitude of the bedslope factor is about 1 in each case, nevertheless, it is bigger both for the SVR and the Bailard bedload transport and smaller both for the CWS and the Bailard suspended load transport. The resemblances: SVR/Bailard bedload and CWS/Bailard suspended load has sense because the SVR formula would correspond to more moderated energy beaches whereas the CWS formula would correspond to higher energy beaches and therefore, to a more suspended sediment effect.

Appendix G

Hydrodynamical instabilities

G.1 Shear waves

Shear waves may be considered as far-infragravity oscillations (frequencies lower than the infragravity waves with similar wave numbers), and are defined as wave-like motions generated by an instability of the equilibrium current because of the shear in its horizontal profile.

Indeed, as explains Caballeria (2000), the longshore current intensity increases from zero at the shoreline to a maximum value in the surf zone and decreases to zero in the offshore zone. Sometimes, secondary extrema can also appear. Hence, the current has a sheared profile with one or more inflexion points which provides one or more potential vorticity extrema which is the necessary condition for shear instability.

Numerous experimental and theoretical studies have been made, beyond them we can find, for the former: Bowen & Holman (1989); Falqués & Iranzo (1994); Dodd & Falqués (1996); Caballeria (2000); Baquerizo *et al.* (2001), for the latter: Dodd *et al.* (1992); Reniers *et al.* (1997).

The work presented in this appendix has been the previous work before the study of morphodynamics instabilities of planar beaches (chapter 4). It is based on the linear stability analysis made in Caballeria (2000), extended by using the MORFO55 nonlinear model.

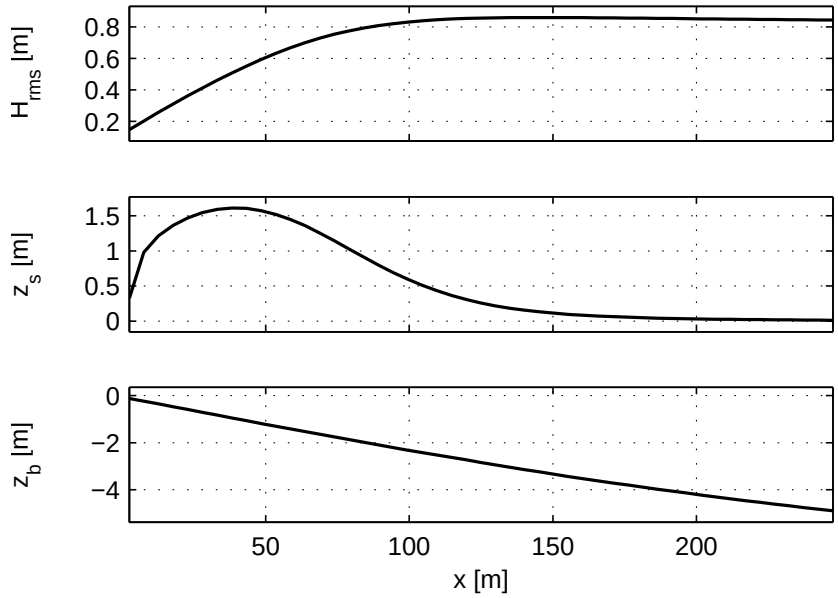

Figure G.1: Shear waves. Basic states.

G.2 Experiments

From Caballeria (2000), shear waves may develop for small values of the dissipative parameter ε_{s} and the frictional parameter r defined as:

$$\varepsilon_{\mathrm{s}} = \frac{1}{\Re} \sim \frac{\nu_{\mathrm{tmax}}}{L\,V}, \tag{G.1}$$

where $\Re$ is the Reynolds number, ν_{tmax} is the maximum eddy viscosity (from equation 2.40), L is a horizontal length scale and V is a characteristic velocity, and,

$$r = \frac{c_{\mathrm{d}}}{\beta_{\mathrm{e}}}, \tag{G.2}$$

where c_{d} is the hydrodynamical drag coefficient and β_{e} is the equivalent slope of the beach.

In order to observe the shear waves the turbulence parameter M and the drag coefficient c_{d} have been decreased from their default value. For this experiment, we chose: $M = 0.3$ and $c_{\mathrm{d}} = 2\,10^{-4}$. They remain reasonable values.

The equilibrium profiles of the wave height, the longshore current and the topography are shown in figure G.1. They may be obtained, by starting the evolution with a non-perturbated bathymetry.

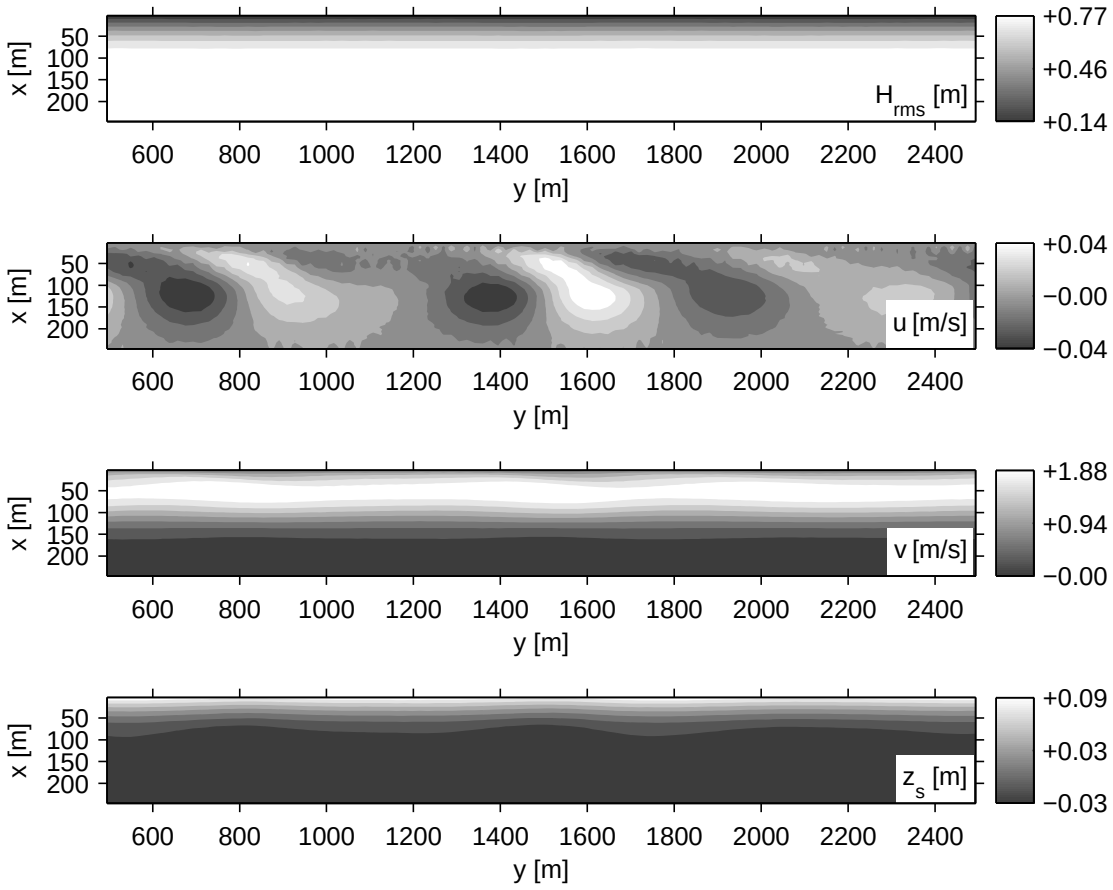

Figure G.2: Shear waves. Evolution time: $t = 106$ min. Top view of, from up to bottom: H_{rms}, u, v, and z_{s}.

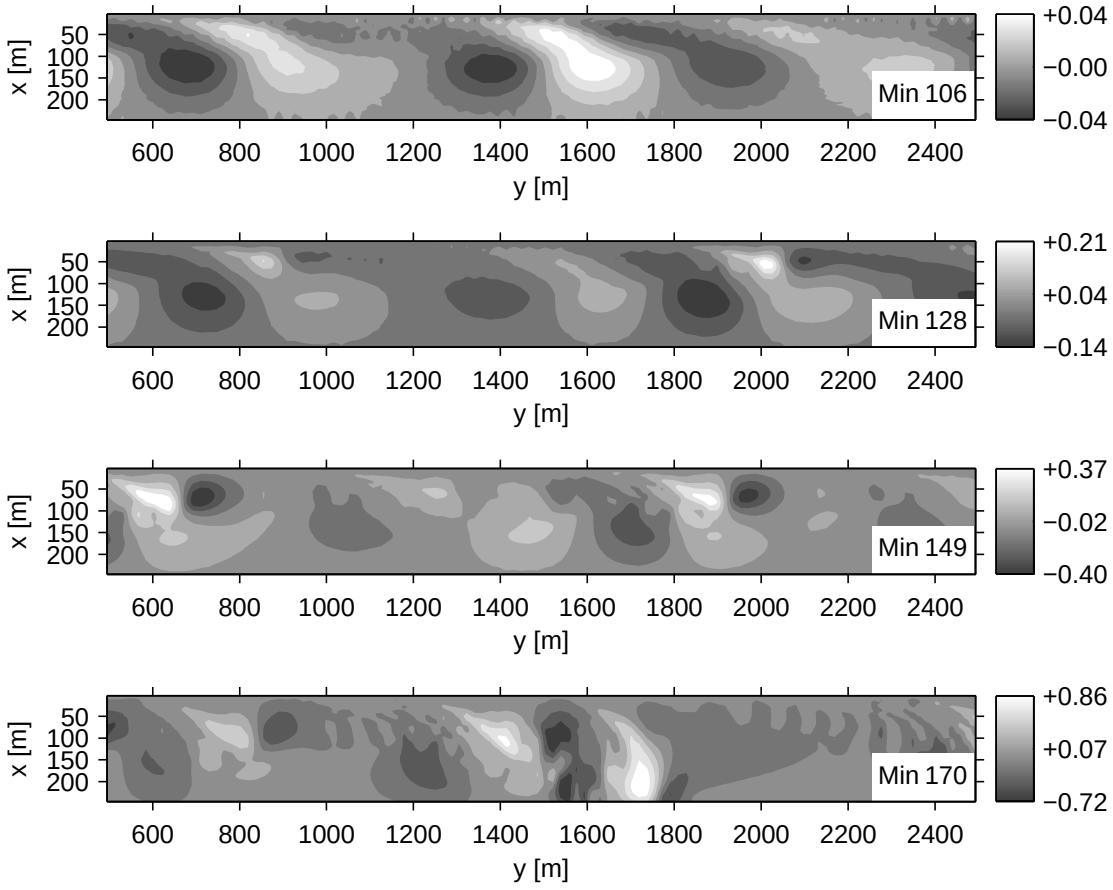

Figure G.3: Shear waves. Evolution from $t = 106$ min to $t = 170$ min. Top view of u.

G.3 Results

Figure G.2 shows a top view of different variables after 106 min of evolution. A clear shear wave pattern is observed. Let us focus on the plot of the cross-shore current u. In this plot, the patterns are more visible because we can see the variation of u from its value at the basic state,i.e., from 0. The shear waves have a regular spacing of about 700 m.

Figure G.3 shows the shows a top view of u, at different instants. The shape of the shear waves is changing and they migrate in the current direction.

Figure G.4 shows the time series of variables from 110 min to 170 min. The shear waves migrate with the period of about 10 min which corresponds to a migration velocity of about 1.2 m/s.

The complete temporal evolution, until the model breaks, is seen in the time series of figure G.5.

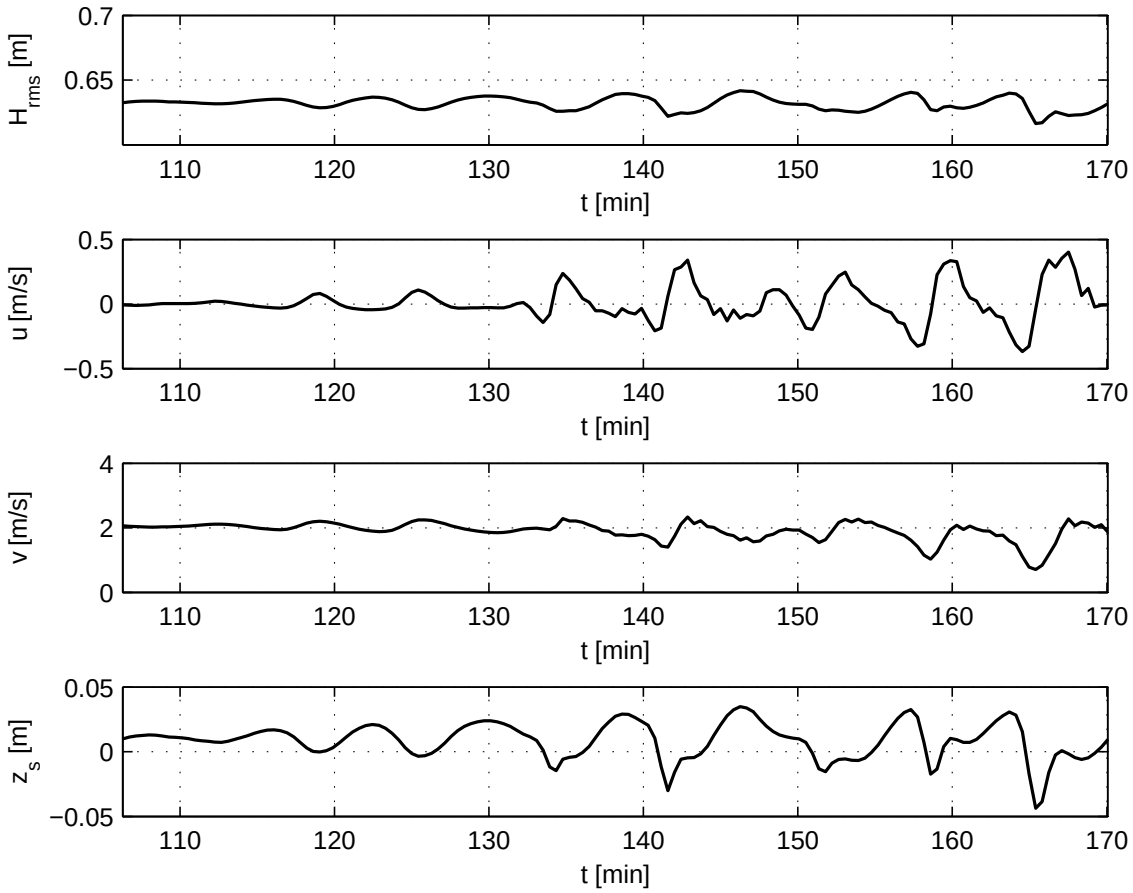

Figure G.4: Shear waves. Time series, from $t = 106$ min to $t = 170$ min, of the variables: H_{rms}, u, v, and z_{s}. (from up to bottom)

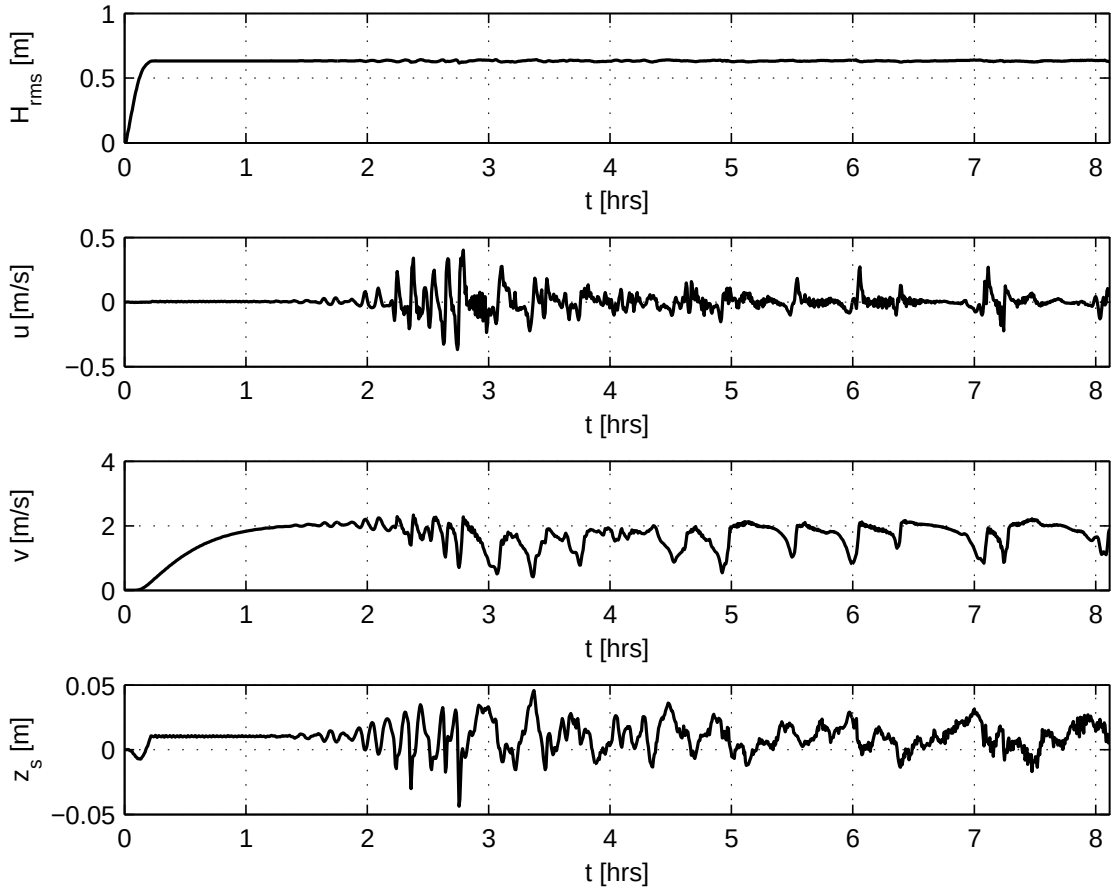

Figure G.5: Shear waves. Time series, from $t = 0$ to $t = 8$ hrs, of the variables: $H_{\rm rms}$, u, v, and $z_{\rm s}$. (from up to bottom)

Bibliography

Ashton, A., Murray, A. B. & Arnault, O. 2001 Formation of coastline features by large-scale instabilities induced by high-angle waves. *Nature* **414**, 296–300.

Bagnold, R. A. 1963 Mechanics of marine sedimentation. In *The Sea* (ed. M.N. Hill), pp. 507–528. New York, U.S.A.: Wiley–Interscience.

Bailard, J. A. 1981 An energetics total load sediment transport model for a plane sloping beach. *J. Geophys. Res.* **86** (C11), 10938–10954.

Bailard, J. A. & Inman, D. L. 1981 An energetics bedload model for a plane sloping beach: local transport. *J. Geophys. Res.* **86** (C3), 2035–2043.

Baquerizo, A., Caballeria, M., Losada, M. A. & Falqués, A. 2001 Frontshear and backshear instabilities of the mean longshore current. *J. Geophys. Res.* **106** (C8), 16997–17011.

Barcilon, A. I. & Lau, J. P. 1973 A model for formation of transverse bars. *J. Geophys. Res* **78** (15), 2656–2664.

Battjes, J. A. 1975 Modeling of turbulence in the surfzone. In *Proc. Symp. Model. Tech.*, pp. 1050–1061. Am. Soc. of Civ. Eng.

Blondeaux, P. 1990 Sand ripples under sea waves. Part 1. Ripple formation. *J. Fluid Mech.* **218**, 1–17.

Bowen, A. J. & Holman, R. A. 1989 Shear instabilities of the mean longshore current. *J. Geophys. Res.* **94** (C12), 18023–18030.

Caballeria, M. 2000 Self-organization in the nearshore: shear waves, transverse and crescentic bars. PhD thesis, Appl. Physics Dept., Univ. Politècnica de Catalunya, Barcelona, Spain.

Caballeria, M., Coco, G., Falqués, A. & Huntley, D. A. 2002 Self-organization mechanisms for the formation of nearshore crescentic and transverse sand bars. *J. Fluid Mech.* **465**, 379–410.

Calvete, D. & de Swart, H. E. 2003 A nonlinear model study on the long-term behavior of shore face-connected sand ridges. *J. Geophys. Res.* **108** (C53169), doi:10.1029/2001JC001091.

Calvete, D., Dodd, N., Falqués, A. & van Leeuwen, S. M. 2005 Morphological development of rip channel systems: Normal and near normal wave incidence. *J. Geophys. Res.* **110** (C10006), doi:10.1029/2004JC002803.

Calvete, D., Falqués, A., de Swart, H. E. & Walgreen, M. 2001 Modelling the formation of shoreface-connected sand ridges on storm-dominated inner shelves. *J. Fluid Mech.* **441**, 169–193.

Castelle, B. 2004 Modélisation de l'hydrodynamique sédimentaire au-dessus des barres sableuses soumises à l'action de la houle: application à la côte aquitaine. PhD thesis, Université Bordeaux I, France.

Castelle, B., Bonneton, P., Dupuis, H. & Senechal, N. 2007 High-energy wave forcing and sandy beach morphology on the French Aquitanian Coast: a review. *Marine Geol.* Under revision.

Christensen, E., Deigaard, R. & Fredsoe, J. 1994 Sea bed stability on a long straight coast. In *Coastal Eng. 1994,* vol. 4, pp. 1865–1879. Am. Soc. of Civ. Eng.

Coco, G., Caballeria, M., Falqués, A. & Huntley, D. H. 2002 Crescentic bars and nearshore self-organization processes. In *Coastal Eng. 2002,* vol. 3, pp. 3765–3777. Am. Soc. of Civ. Eng.

Coco, G., Huntley, D. A. & O'Hare, T. J. 2000 Investigation of a self-organization model for beach cusp formation and development. *J. Geophys. Res.* **105** (C9), 21991–22002.

Damgaard, J., Dodd, N., Hall, L. & Chesher, T. 2002 Morphodynamic modelling of rip channel growth. *Coastal Eng.* **45**, 199–221.

De Melo Apoluceno, D. 2002 Morpho - hydrodynamique des plages à barres en domaine méso à macro-tidal: exemple de la plage du truc vert, gironde, france. PhD thesis, Université Bordeaux I, France.

De Melo Apoluceno, D., Howa, H., Dupuis, H. & Oggian, G. 2002 Morphodynamics of ridge and runnel systems during summer. *J. Coastal Res.,* Special Issue **36**, 222–230.

Deigaard, R. 1997 Comparison between a detailed sediment transport model and an energetics based formula. In *Coastal Dynamics 1997*, pp. 217–226. Am. Soc. of Civ. Eng.

Deigaard, R., Drønen, N., Fredsoe, J., Jensen, J. H. & Jørgesen, M. P. 1999 A morphological stability analysis for a long straight barred coast. *Coastal Eng.* **36** (3), 171–195.

DHI 2004 Recommendations for nourishment strategies. *Tech. Rep.*. HUMOR project, DHI water and environment.

Dingemans, M. W. 1997 *Water Wave Propagation Over Uneven Bottoms. Part 1: Linear Wave Propagation*, *Advanced Series on Ocean Engineering*, vol. 13. Singapore: World Scientific.

Dodd, N. & Falqués, A. 1996 A note on spatial modes in longshore current shear instabilities. *J. Geophys. Res.* **101** (C10), 22715–22726.

Dodd, N., Oltman-Shay, J. & Thornton, E. B. 1992 Shear instabilities in the longshore current: a comparison of observation and theory. *J. Phys. Oceanogr.* **22** (1), 62–82.

Dodd, N., Stoker, A. M., Garnier, R., Vittori, G., De Los Santos, F., Brocchini, M., Soldini, L. & Losada, M. A. 2007 Use of numerical models to study land-based sedimentation and subsequent nearshore morphological evolution. *Coastal Eng.* Submitted.

Evans, O. F. 1938 The classification and origin of beach cusps. *J. Geology* **46**, 615–627.

Fachin, S. & Sancho, F. 2004*a* M-shorecirc: A new morphodynamical model. In *presented at International Coastal Symposium - ICS 2004*. To appear in J. Coastal Res., Special Issue 39.

Fachin, S. & Sancho, F. 2004*b* Morphodynamic instabilities in the surf zone. In *Coastal Eng. 2004*, pp. 2875–2887. Am. Soc. of Civ. Eng.

Falqués, A. 1989 Formación de topografía rítmica en el Delta del Ebro. *Revista de Geofísica* **45** (2), 143–156.

Falqués, A. 2006 Q2d-morfo. a morphodynamic quasi-2dh coastline model. version 1. *Tech. Rep.*. Appl. Physics Deptartment, UPC (Technical University of Catalonia).

Falqués, A. & Calvete, D. 2005 Large scale dynamics of sandy coastlines. Diffusivity and instability. *J. Geophys. Res.* **110** (C03007), doi:10.1029/2004JC002587.

Falqués, A., Calvete, D. & Caballeria, M. 2002 MORFO55/60. modelling system for nearshore morphodynamic patterns. *Tech. Rep.*. HUMOR project, Grup de Morfodinàmica de Costes, Appl. Physics Dept., Univ. Politècnica de Catalunya, Barcelona, Spain.

Falqués, A., Calvete, D. & Caballeria, M. 2004 Morfo60: surf zone morphodynamic instability model. *Tech. Rep.*. HUMOR project, Grup de Morfodinàmica de Costes, Appl. Physics Dept., Univ. Politècnica de Catalunya, Barcelona, Spain.

Falqués, A., Coco, G. & Huntley, D. A. 2000 A mechanism for the generation of wave-driven rhythmic patterns in the surf zone. *J. Geophys. Res.* **105** (C10), 24071–24088.

Falqués, A. & Iranzo, V. 1994 Numerical simulation of vorticity waves in the nearshore. *J. Geophys. Res.* **99** (C1), 825–841.

Falqués, A., Montoto, A. & Iranzo, V. 1996 Bed-flow instability of the longshore current. *Cont. Shelf Res.* **16** (15), 1927–1964.

Fredsoe, J. & Deigaard, R. 1992 *Mechanics of Coastal Sediment Transport*, 1st edn. Singapore: World Scientific.

Garnier, R. 2005 Effect of the wave-driven turbulence on the generation and the nonlinear evolution of nearshore sand bars. In *Advances in Turbulence VIII*. Villanova, Spain.

Garnier, R., Bonneton, P., Falqués, A. & Calvete, D. 2006*a* Modélisation de la formation et de l´évolution non linéaires des barres en croissant de la côte aquitaine. In *IX* emes *Journées Nationales Génie Côtier - Génie Civil*. Brest, France.

Garnier, R., Calvete, D., Falqués, A. & Caballeria, M. 2005*a* Generación y evolución no lineal de barras transversales y oblicuas cerca de la costa. In *VIII Jornadas Españolas de Ingeneria de Costas y Puertos*. Sitges, Spain.

Garnier, R., Calvete, D., Falqués, A. & Caballeria, M. 2005*b* Generation and nonlinear evolution of nearshore oblique bars. In *Coastal Dynamics 2005*. Am. Soc. of Civ. Eng.

Garnier, R., Calvete, D., Falqués, A. & Caballeria, M. 2006*b* Generation and nonlinear evolution of shore-oblique/transverse sand bars. *J. Fluid Mech.* **567**, 327–360.

Garnier, R., Calvete, D., Falqués, A. & Caballeria, M. 2006*c* Modeling ridge and runnel system development from an intertidal shore parallel bar. In *Coastal Eng. 2006*. Am. Soc. of Civ. Eng.

Garnier, R., Dodd, N., Calvete, D., Falqués, A. & Caballeria, M. 2007 Modeling the interaction between transverse and crescentic bar systems. In *Proc. 5^{th} IAHR symposium on River, Coastal and Estuarine Morphodynamics*. Enschede, The Netherlands: International Association for Hydraulic Research, in preparation.

Garnier, R., Falqués, A. & Caballeria, M. 2004 Analysis of the evolution of the shoreline in case of an artificial shoal/pool. *Tech. Rep.*. HUMOR project, Grup de Morfodinàmica de Costes, Appl. Physics Dept., Univ. Politècnica de Catalunya, Barcelona, Spain, work package 4, Coupling between nearshore bedforms and shoreline evolution in unbounded coasts. Task M4.3.3.

Guilcher, A., Godard, A. & Visseaux, E. 1952 Les cretes et sillons obliques de l'estran des Landes de Gascogne. *Comite d'Oceanogr. et d'Etudes des Cotes Bull.* **4** (4), 151–157.

Hino, M. 1974 Theory on formation of rip-current and cuspidal coast. In *Coastal Eng. 1974*, pp. 901–919. Am. Soc. of Civ. Eng.

Horikawa, K. 1988 *Nearshore Dynamics and Coastal Processes*. Tokio, Japan: University of Tokio Press.

Hunter, R. E., Clifton, H. E. & Phillips, R. L. 1979 Depositional processes, sedimentary structures, and predicted vertical sequences in barred nearshore systems, Southern Oregon coast. *J. Sediment. Petrol.* **49** (3), 711–726.

Idier, D. & Astruc, D. 2003 Analytical and numerical modeling of sandbanks dynamics. *J. Geophys. Res.* **108** (C33060), doi:10.1029/2001JC001205.

KIRBY, J. T. & DALRYMPLE, R. A. 1994 Combined refraction/diffraction model REF/DIF1, Version 2.5. Res. Report CACR-94-22. Center for Applied Coastal Research, Univ. of Delaware.

KIRBY, J. T., DALRYMPLE, R. A. & SHI, F. 2002 Combined refraction/diffraction model REF/DIF 1, Version 3.0. Res. Report CACR-02-02. Center for Applied Coastal Research, Univ. of Delaware.

KIRBY, J. T., DALRYMPLE, R. A. & SHI, F. 2004 Refraction-diffraction model REF/DIF S, Version 1.3. Res. Report CACR-04-01. Center for Applied Coastal Research, Univ. of Delaware.

KLEIN, M. D. 2006 Modelling rhythmic morphology in the surf zone. PhD thesis, Tech. Univ. Delft, The Netherlands.

KLEIN, M. D. & SCHUTTELAARS, H. M. 2005 Morphodynamic instabilities of planar beaches: sensitivity to parameter values and process formulations. *J. Geophys. Res.* **110** (F04S18), doi:10.1029/2004JF000213.

KLEIN, M. D., SCHUTTELAARS, H. M. & STIVE, M. J. F. 2002 Linear stability of a double-barred coast. In *Coastal Eng. 2002,* vol. 3, pp. 3396–3408. Am. Soc. of Civ. Eng.

KNAAPEN, M.A.F. 2001 Predicting large waves in erodible sand beds. PhD thesis, Universiteit Twente.

KOMAROVA, N. L. & NEWELL, A. C. 2000 Nonlinear dynamics of sand banks and sand waves. *J. Fluid. Mech.* **415**, 285–321.

KONICKI, K. M. & HOLMAN, R. A. 2000 The statistics and kinematics of transverse bars on an open coast. *Mar. Geol.* **169**, 69–101.

KROON, A., P.HOEKSTRA, HOUWMAN, K.T. & RUESSINK, B.G. 1994 Morphological monitoring of a shoreface nourishment nourtec experiment at terschelling, the netherlands. In *Coastal Eng. 1994*, pp. 2222–2236. Am. Soc. of Civ. Eng.

LAFON, V., APOLUCENO, D. DE MELO, DUPUIS, H., MICHEL, D., HOWA, H. & FROIDEFOND, J. M. 2004 Morphodynamics of nearshore rhythmic sandbars in a mixed-energy environment (sw france): I. mapping beach changes using visible satellite imagery. *Estuarine, Coastal and Shelf Science* **61**, 289–299.

LAFON, V., DUPUIS, H., BUTEL, R., CASTELLE, B., MICHEL, D., HOWA, H. & APOLUCENO, D. DE MELO 2005 Morphodynamics of nearshore rhythmic sandbars in a mixed-energy environment (sw france): 2. physical forcing analysis. *Estuarine, Coastal and Shelf Science* **65**, 449–462.

LAFON, V., DUPUIS, H., HOWA, H. & FROIDEFOND, J. M. 2002 Determining ridge and runnel longshore migration rate using spot imagery. *Oceanologica Acta* **25**, 149–158.

LONGUET-HIGGINS, M. S. 1952 On the statistical distribution of the heights of sea waves. *J. Marine Res.* **XI** (3), 245–266.

Longuet-Higgins, M. S. 1970 Longshore currents generated by obliquely incident sea waves. *J. Geophys. Res* **75** (33), 6778–6801.

Longuet-Higgins, M. S. & Stewart, R. W. 1964 Radiation stresses in water waves: a physical discussion with applications. *Deep Sea Res.* **11**, 529–562.

Marieu, V., Bonneton, P., Ardhuin, F. & Foster, D. 2006 Étude des rides sédimentaires générées par les vagues sur le plateau continental. In *IX* emes *Journées Nationales Génie Côtier - Génie Civil*. Brest, France.

Mei, C. C. 1989 *The Applied Dynamics of Ocean Surface Waves*, *Advanced Series on Ocean Engineering*, vol. 1. Singapore: World Scientific.

Nemeth, A.A. 2003 Modelling offshore sand waves. PhD thesis, Universiteit Twente.

Niederoda, A. W. & Tanner, W. F. 1970 Preliminary study on transverse bars. *Mar. Geol.* **9**, 41–62.

Ortega, M., Garnier, R., Losada, M. A. & Falqués, A. 2007 Transverse/oblique bars in trafalgar beach, cadiz, spain: observation and modelling In preparation.

Pedlosky, J. 1987 *Geophysical Fluid Dynamics*. Berlin, Germany: Springer–Verlag.

Pedreros, R., Howa, H. L. & Michel, D. 1996 Application of grain size trend analysis for the determination of sediment transport pathways in intertidal areas. *Marine Geol.* **135**, 35–49.

Plant, N. G., Ruessink, B. G. & Wijnberg, K. M. 2001 Morphologic properties derived from a simple cross-shore sediment transport model. *J. Geophys. Res.* **106** (C1), 945–962.

Reniers, A. J. H. M., Battjes, J. A., Falqués, A. & Huntley, D. A. 1997 A laboratory study on the shear instability of longshore currents. *J. Geophys. Res.* **102** (C4), 8597–8609.

Reniers, A. J. H. M., Roelvink, J. A. & Thornton, E. B. 2004 Morphodynamic modeling of an embayed beach under wave group forcing. *J. Geophys. Res.* **109** (C01030), doi:10.1029/2002JC001586.

Ribas, F. 2000 Modes normals de la interaccio morfodinamica entre l'onatge incident i la topografia a la zona de rompents. In *Actes de les II Jornades de doctorat del programa de doctorat de Física aplicada i simulació en ciències, Universitat Politècnica de Catalunya*, pp. 9–12.

Ribas, F. 2004 On the growth of nearshore sand bars as instability processes of equilibrium beach states. PhD thesis, Appl. Physics Dept., Univ. Politècnica de Catalunya, Barcelona, Spain.

Ribas, F., Falqués, A. & Montoto, A. 2000 Normal mode analysis of the surf zone morphodynamics. In *Coastal Eng. 2000,* vol. 4, pp. 3229–3242. Am. Soc. of Civ. Eng.

Ribas, F., Falqués, A. & Montoto, A. 2003 Nearshore oblique sand bars. *J. Geophys. Res.* **108** (C43119), doi:10.1029/2001JC000985.

Ribas, F., Garnier, R., Falqués, A., Guillén, J., Ojeda, E. & Calvete, D. 2007 Observation and modeling of crescentic bars in Barcelona embayed beaches. In *Coastal Sediments 2007*. Am. Soc. of Civ. Eng., accepted.

Ribas, F. & Kroon, A. 2006 Observaciones de barras de arena transversales en la playa de Noordwijk (Holanda) usando el sistema de cámaras argus. In *VIII Jornadas Españolas de Ingeneria de Costas y Puertos*. Sitges, Spain.

Ribas, F., Swart, H.E.de, D.Calvete, Falqués, A., Dodd, N. & van Leeuwen, S.M. 2005 Sensitivity of modeled nearshore morphology to wave and sediment transport formulations. In *Coastal Dynamics 2005*. Am. Soc. of Civ. Eng.

Rodriguez, A., Sánchez-Arcilla, A., Redondo, J. M. & Masso, C. 1999 Macroturbulence measurements with electromagnetic and ultrasonic sensors: a comparison under high-turbulent flows. *Experiments in Fluids* **27**, 31–42.

Roos, P. C., Hulsher, S. J. M., Knaapen, M. A. F. & Damme, R. M. J. Van 2004 The cross-sectional shape of tidal sandbanks: modeling and observations. *J. Geophys. Res.* **109** (F02003), doi:10.1029/2003JF000070.

Saint-Cast, F. 2002 Modélisation de la morphodynamique des corps sableux en milieu littoral. PhD thesis, Université Bordeaux I, France.

Schramkowski, G.P., Schuttelaars, H. M. & de Swart, H. E. 2004 Non-linear channel-shoal dynamics in long tidal embayments. *Ocean Dynamics* **54** (3-4), 399–407.

Schuttelaars, H. M. 1997 Evolution and stability analysis of bottom patterns in tidal embayments. PhD thesis, Universiteit Utrecht, Faculteit Wiskunde en Informatica, Utrecht, The Netherlands.

Short, A. D. 1994 Coastal photograph. *J. Coastal Res.* **10** (1), 250.

Short, A. D. 1999 *Handbook of Beach and Shoreface Morphodynamics*. Chichester: Wiley.

Sonu, C. J. 1968 Collective movement of sediment in littoral environment. In *Coastal Eng. 1968*, pp. 373–400. Am. Soc. of Civ. Eng.

Soulsby, R. L. 1997 *Dynamics of Marine Sands*. London, U.K.: Thomas Telford.

Thornton, B. & Guza, R. T. 1983 Transformation of wave height distribution. *J. Geophys. Res.* **88** (10), 5925–5938.

Trowbridge, J. H. 1995 A mechanism for the formation and maintenance of shore-oblique sand ridges on storm-dominated shelves. *J. Geophys. Res.* **100** (C8), 16071–16086.

van Enckevort, I. M. J., Ruessink, B. G., Coco, G., Suzuki, K., Turner, I L., Plant, N. G. & Holman, R. A. 2004 Observations of nearshore crescentic sandbars. *J. Geophys. Res.* **109** (C06028), doi:10.1029/2003JC002214.

van Leeuwen, S. M., Dodd, N., Calvete, D. & Falqués, A. 2006 Physics of nearshore bed pattern formation under regular or random waves. *J. Geophys. Res.* **111** (F01023), doi:10.1029/2005JF000360.

Werner, B. T. & Fink, T. M. 1993 Beach cusps as self-organized patterns. *Science* **260**, 968–971.

Yu, J. & Slinn, D. N. 2003 Effects of wave-current interaction on rip currents. *J. Geophys. Res.* **108** (C33088), doi:10.1029/2001JC001105.

List of symbols

Roman Symbols

a_0	Height of the artificial wall at the shoreline	m
a_1	Parameter for the initial planar/barred beach profile	m
a_2	Longshore bar amplitude	m
A	Wave amplitude (time-averaged)	m
$\bar{A}$	Complex wave amplitude (time-averaged)	m
A_m	Bar amplitude	m
A_S	Total load contribution in α	$-$
A_SB	Bedload contribution in α	$-$
A_SS	Suspended load contribution in α	$-$
B	Breaking coefficient	$-$
c	Wave phase velocity	$\mathrm{m\,s^{-1}}$
$\vec{c}$	Wave phase velocity vector	$\mathrm{m\,s^{-1}}$
c_1	Constant for the CFL condition	$-$
c_d	Hydrodynamical drag coefficient	$-$
c_D	Morphodynamical drag coefficient	$-$
c_g	Wave group velocity	$\mathrm{m\,s^{-1}}$
$\vec{c_\mathrm{g}}$	Wave group velocity vector	$\mathrm{m\,s^{-1}}$
c_m	Migration velocity of the bars	$\mathrm{m\,day^{-1}}$
d_{50}	Median grain size	m
D	Total mean depth	m
D_*	Dimensionless grain size	$-$
D_max	Maximum depth	m
E	Wave energy density (time-averaged)	$\mathrm{J\,m^{-2}}$
f	Discretized variable	$[f]$
f_c	f at the central node	$[f]$
f_p	Intrinsic frequency peak of the wave field	$\mathrm{s^{-1}}$
f_u	f at the u-node	$[f]$
f_v	f at the v-node	$[f]$
g	Gravitational acceleration	$\mathrm{m\,s^{-2}}$
h	Bed level deviation from the initial topography	m
$\|\|h\|\|$	Measure of the bar amplitude over the whole domain	m

$h_{\max}$	Maximum of h	m
$h_{\min}$	Minimum of h	m
H	Wave height (time-averaged)	m
H_{rms}	Root-mean-square average of the wave height	m
H^0_{rms}	H_{rms} at the seaward boundary	m
$\mathcal{H}$	Fourier coefficient of the topographic signal	m
$\lvert\mathcal{H}\rvert_n$	Normalised modulus of $\mathcal{H}$	m
i	Cross-shore space index	–
j	Longshore space index	–
k	Time index	–
k	Wavenumber	m^{-1}
$\vec{k}$	Wave vector	m^{-1}
k^0	Wavenumber at the seaward boundary	m^{-1}
k_l	Wavenumber of the topographic signal (mode l)	m^{-1}
k_{m}	Dominant wavenumber of the topographic signal	m^{-1}
l	Mode index of the rhythmic instabilities	–
L_{m}	Mean horizontal span of the bars	m
L_x	Cross-shore size of the model domain	m
L_y	Longshore size of the model domain	m
M	Turbulence parameter	–
N_t	Final time index	–
N_x	Number of points cross-shore	–
N_y	Number of points longshore	–
p	Sediment porosity	–
$\mathcal{P}$	Production term governing the bar evolution	$\mathrm{m}^2\,\mathrm{s}^{-1}$
$\vec{q}$	Horizontal sediment flux vector	$\mathrm{m}^2\,\mathrm{s}^{-1}$
$\vec{q_{\mathrm{bl}}}$	Bedload transport	$\mathrm{m}^2\,\mathrm{s}^{-1}$
$\tilde{\vec{q}}_{\mathrm{bl}}$	Instantaneous bedload transport	$\mathrm{m}^2\,\mathrm{s}^{-1}$
$\vec{q_{\mathrm{sl}}}$	Suspended load transport	$\mathrm{m}^2\,\mathrm{s}^{-1}$
$\tilde{\vec{q}}_{\mathrm{sl}}$	Instantaneous suspended load transport	$\mathrm{m}^2\,\mathrm{s}^{-1}$
$\vec{q_{\mathrm{g}}}$	Downslope gravitational transport	$\mathrm{m}^2\,\mathrm{s}^{-1}$
$\tilde{\vec{q}}_{\mathrm{g}}$	Instantaneous downslope gravitational transport	$\mathrm{m}^2\,\mathrm{s}^{-1}$
q_x	Cross-shore component of $\vec{q}$	$\mathrm{m}^2\,\mathrm{s}^{-1}$
q_y	Longshore component of $\vec{q}$	$\mathrm{m}^2\,\mathrm{s}^{-1}$
q_{xy}	Rate between the spatial increments	–
$\vec{q_{\mathrm{w}}}$	Wave contribution transport	$\mathrm{m}^2\,\mathrm{s}^{-1}$
$\tilde{\vec{q}}_{\mathrm{w}}$	Instantaneous wave contribution transport	$\mathrm{m}^2\,\mathrm{s}^{-1}$
s	Relative density of the sediment	–
S	Wave steepness	–
$\bar{\bar{S}}'$	Wave radiation stress tensor	$\mathrm{N\,m}^{-1}$
$\bar{\bar{S}}''$	Turbulent Reynolds stress tensor	$\mathrm{N\,m}^{-1}$
S_{m}	Mean horizontal cross-shore span of the bars	m
t	Time	s
t^*	Instantaneous time	s
t_{CFL}	CFL time step	s
t_{CPU}	CPU time	s

T	Wave period	s
T_m	Period of the travelling bars	day
u	Cross-shore component of $\vec{v}$, i.e. v_1	$\mathrm{m\,s^{-1}}$
$\vec{u}$	Three-dimensional velocity vector (time-averaged)	$\mathrm{m\,s^{-1}}$
$\tilde{\vec{u}}$	Instantaneous three-dimensional velocity vector	$\mathrm{m\,s^{-1}}$
u_b	Root-mean-square wave orbital velocity amplitude at the bed	$\mathrm{m\,s^{-1}}$
$\tilde{\vec{u}}_\mathrm{B}$	Instantaneous velocity vector at the bed	$\mathrm{m\,s^{-1}}$
u_crit	Threshold current velocity for the sediment transport	$\mathrm{m\,s^{-1}}$
$\vec{U}$	Near bed mean current vector	$\mathrm{m\,s^{-1}}$
v	Longshore component of $\vec{v}$, i.e. v_2	$\mathrm{m\,s^{-1}}$
$\vec{v}$	Horizontal velocity vector (time- and depth-averaged)	$\mathrm{m\,s^{-1}}$
v_max	Maximum longshore current	$\mathrm{m\,s^{-1}}$
w_s	Fall celerity of sediment	$\mathrm{m\,s^{-1}}$
x	Cross-shore coordinate, i.e. x_1	m
x^*	Coordinate of the normal to the perturbed depth contours	m
x_b	Cross-shore position of the maximum of ε_b	m
x_c	Cross-shore position of the longshore bar	m
y	Longshore coordinate, i.e. x_2	m
z	Vertical coordinate, i.e. x_3	m
z_b	Bed level (time-averaged)	m
$\tilde{z}_\mathrm{b}$	Instantaneous bed level	m
z_b^0	Initial bed level	m
z_s	Sea water level (time-averaged)	m
$\tilde{z}_\mathrm{s}$	Instantaneous sea water level	m
z_s'	Fluctuating contribution in $\tilde{z}_\mathrm{s}$ due to the wave orbital motion	m

Greek Symbols

α	Stirring factor	m
α_rd	Breaking term in REF/DIF	$\mathrm{m^{-1}}$
β_1	Shoreline slope of the initial planar/barred beach profile	–
β_2	Offshore slope of the initial planar/barred beach profile	–
β_m	Bar angle	deg
Δ	Damping term governing the bar evolution	$\mathrm{m^2\,s^{-1}}$
Δt	Time step	s
Δt_m	Morphological time step	s
Δx	Cross-shore grid spacing	m
Δy	Longshore grid spacing	m
γ	Bedslope coefficient	–
γ_b	Breaker index	–
$\tilde{\gamma}_\mathrm{g}$	Instantaneous Bailard bedslope coefficient	–
γ_g	Bailard bedslope coefficient	–
γ_N	Stirring of the sediment by the waves	–
Γ_c	Nondimensional morphological diffusivity	–
Γ	Bedslope term from the BEE	$\mathrm{m^{-1}}$

ε	Dissipation rate	$\mathrm{kg\,s^{-3}}$
ε_b	Dissipation rate due to the wave breaking	$\mathrm{kg\,s^{-3}}$
ε_f	Dissipation rate due to the bottom friction	$\mathrm{kg\,s^{-3}}$
ϵ_b	Efficiency of the bedload transport	$-$
ϵ_s	Efficiency of the suspended load transport	$-$
κ	Seaward boundary parameter	$-$
κ_b	Kinematic viscosity of water	$\mathrm{m^2\,s^{-2}}$
λ	Wavelength	m
λ_m	Bar dominant wavelength	m
λ_mean	Longshore mean spacing of the bars	m
ν_t	Turbulent momentum horizontal diffusivity	$\mathrm{m^2\,s^{-1}}$
ω	Wave frequency (absolute)	$\mathrm{s^{-1}}$
Ω	Dimensionless fall velocity	$-$
ϕ_c	Angle of repose of the sediment	deg
Φ	Wave phase (time-averaged)	$-$
$\tilde{\Phi}$	Instantaneous wave phase	$-$
Φ_f	f corresponding flux	$[f]\,\mathrm{s^{-1}}$
Π	Potential stirring (α/D)	$-$
Ψ	Angle between the current and the propagation direction	deg
ρ	Water density	$\mathrm{kg\,m^{-3}}$
ρ_s	Sediment density	$\mathrm{kg\,m^{-3}}$
σ	Intrinsic wave frequency	$\mathrm{s^{-1}}$
σ_m	Growth rate of the bars	$\mathrm{day^{-1}}$
$\vec{\tau_\mathrm{b}}$	Bed shear stress vector	$\mathrm{N\,m^{-2}}$
τ_m	E-folding time ($1/\sigma_\mathrm{m}$) of the bars	day
θ	Wave angle	deg
θ^0	Wave angle at the seaward boundary	deg
θ^*	Angle between the wave rays and the x^*-axis	deg

Abstract

This thesis performs a nonlinear stability study of the surf zone morphodynamics of sandy beaches. To this end the MORFO55 model based on a wave and depth averaged nonlinear shallow water equations solver with wave driver, sediment transport and bed updating is presented. It is first applied to complex longitudinally non-uniform beaches in order to test different model formulations. Second, it is applied to study the generation of surf zone rhythmic features on alongshore uniform beaches. Shore-attached transverse or oblique bars, crescentic bars and ridge and runnel systems are well known examples of such features. The hypothesis that they emerge by self-organization of the coupling between topography, waves and currents is here tested. In absence of shore-parallel bars, the initial formation of transverse and oblique bars was shown by previous modelling studies of linear stability analysis but is now extended to the finite amplitude regime. In most barred beaches, crescentic bars and ridge and runnel systems appear. Conceptual models based on field observations suggest that ridges and runnels could emerge by the deformation of the alongshore intertidal bar intercepted by crescentic bars. Up to now, only the formation of crescentic bars has numerically succeeded with linear and non linear models. This study shows that a dynamical equilibrium state of each of these rhythmic bar systems may be described with a numerical model. General results are in qualitative agreement with the bar systems observed in nature. A physical explanation for their formation, their evolution and the saturation of their growth is given.

Resumen

Esta tesis se dedica en un estudio de estabilidad no lineal de la morfodinámica de la zona de rompientes de playas de arena. El modelo numérico MORFO55 resuelve las ecuaciones de aguas someras no lineales para la hidrodinámica y actualiza la topografía a partir del transporte de sedimento. En primer lugar, se aplica en el caso de playas complejas longitudinalmente no uniformes con objeto de probar sus distintas formulaciones. En secundo lugar, se usa para estudiar la generación de estructuras rítmicas en playas longitudinalmente uniformes. Entre estos patrones se distinguen las barras transversales y oblicuas, las barras crescenticas y los sistemas de barras/surcos (ridges/runnels). La hipótesis de que emergen a partir de inestabilidades internas del acoplamiento entre la topografía y la hidrodinámica se investiga. Los estudios previos de modelización numérica se limitaban a las etapas iniciales de la generación de las barras. En particular, mostraban que las barras transversales y oblicuas pueden formarse en playas planas mientras que las barras crecenticas aparecen en playas con barra. La formación de los sistemas de barras/surcos se explica con modelos conceptuales de la observación mediante satélite según los cuales emergerían a partir de la deformación de la barra intermareal. Esta tesis estudia el régimen no lineal de la evolución de todos estos sistemas. Particularmente se obtiene un estado final de equilibrio. Los resultados generales coinciden cualitativamente con las barras observadas en la naturaleza. Se da una interpretación física de la formación, de la evolución y de la saturación del crecimiento de las barras.

Résumé

Cette thèse présente une étude de stabilité non linéaire de la morphodynamique en zone de surf des plages sableuses. Le modèle numérique utilisé, MORFO55, résout les équations moyennées de Navier Stokes en eau peu profonde, couplées avec l'équation de conservation du sédiment. D'une part, ce modèle est appliqué aux cas de plages complexes non uniformes dans le but de tester ses différentes formulations. D'autre part, l'étude de la génération de structures rythmiques en zone de surf est réalisée sur des plages uniformes longitudinalement. Les barres transversales et obliques, les barres en croissant ainsi que les systèmes de barres/baïnes sont étudiés, l'hypothèse principale étant que ces structures émergent à partir d'instabilités internes du système morphodynamique par un processus d'auto organisation couplant la topographie et l'hydrodynamique. Les études antérieures de modélisations numériques se limitent à décrire la formation des barres. En particulier, elles démontrent que les barres transversales et obliques apparaissent sur des plages dépourvues de barre longitudinale tandis que les barres en croissant ont tendance à se développer sur des plages à barres. La formation des systèmes barres/baïnes n'a été donnée que par des modèles conceptuels fondés sur l'imagerie satellites, ces systèmes proviendraient de la déformation de la barre intertidale. Cette thèse étudie l'évolution en régime non linéaire de chacun de ces systèmes. En particulier, un état d'équilibre est atteint. Les résultats généraux sont en accord avec l'observation. La formation, l'évolution et la saturation de l'accroissement des barres sont interprétées physiquement.